Late Cenozoic-recent tectonics of the southwestern margin of the Tibetan Plateau, Ladakh, northwest India

by

Wendy Bohon

A Dissertation Presented in Partial Fulfillment
of the Requirements for the Degree
Doctor of Philosophy

Approved April 2014 by the
Graduate Supervisory Committee:

Kip Hodges
Ramon Arrowsmith
Arjun Heimsath
Kelin Whipple
Stephen Reynolds

ARIZONA STATE UNIVERSITY

May 2014

DEDICATION

This work is dedicated to my grandmother, Eunice Waterfield Boyette, who was a model of perseverance and dedication, and to my parents, Dean and Linda Bohon, who always believed I could do anything.

ACKNOWLEDGMENTS

First, I need to give a sincere and hearty thank you to my advisors, Ramon Arrowsmith and Kip Hodges. You have both been incredible sources of inspiration and support, and I am grateful for your guidance during this processes. I would also like to thank my committee, Kelin Whipple, Arjun Heimsath, and Steve Reynolds for providing mentorship and support for the last several (or more!) years. I must also give a special acknowledgement to Matthijs van Soest and Jo-Anne Wartho for their patience and mentorship in the laboratory. I would also like to thank Thijs for many informative and helpful discussions about my data. I must also thank the JMARS team, especially Chris Edwards and Scott Dickenshied, for their help with all aspects of the ASTER remote sensing.

My advisors and other mentors have been amazing, but my fellow graduate students also deserve special recognition for the integral part they have played in my educational journey. Many thanks to all of the students in the Hodges and Arrowsmith research groups- and to the larger surfaces processes crew- especially the folks in Room 603. Special thanks to Matt Jungers and Matt Rossi for help with CRN lab work and data processing. Many thanks to Byron Adams for all of his codes, and for hundreds of hours at the board talking about geothermal gradients. My deepest and sincerest thanks go to Aka Tripathy-Lang for all of the things-without you I wouldn't be here. I would also like to thank the Wednesday night crew for providing much-needed stress-relief, friendship and laughter.

Working in remote parts of the world requires special planning, and I would like to thank C.P. Dorjay for his assistance in organizing our trips and keeping us safe. I would also like to acknowledge all of the wonderful drivers, cooks and helpers who made our fieldwork so safe and enjoyable. Additionally, many thanks to Nathaniel Borneman, Alka Tripathy, Kip Hodges and Ramon Arrowmsith for help in the field. Special thanks to Nateki and Ramon for digging all of the holes! I would also like to acknowledge the Graduate and Professional Student Association at ASU, Sigma Xi and Kip Hodges for funding my fieldwork, and Kip Hodges and Ramon Arrowsmith for funding my lab work.

Finally, I would like to acknowledge my family. Thank you to my mom, dad and sister for always believing in me, no matter what crazy road I decide to travel. Thanks especially to my dad, for inspiring my curiosity about the nature world. A huge thank you is due to my husband, Scott Clarey, and my daughter, Abigail Clarey, for their love and support during this long (and sometimes trying) process. I appreciate all of the sacrifices you've had to make to allow me the time to finish this work. I love you.

ABSTRACT

The Himalayan orogenic system is the youngest and most spectacular example of a continent-continent collision on earth. Although the collision zone has been the subject of extensive research, fundamental questions remain concerning the architecture and evolution of the orogen. Of particular interest are the structures surrounding the 5 km high Tibetan Plateau, as these features record the collisional and post-collisional evolution of the orogen in this area. In this study we examine structures along the southwestern margin of the Tibetan Plateau, including the Karakoram (KFS) and Longmu Co (LCF) faults, and the Ladakh, Pangong and Karakoram Ranges. New low-temperature thermochronology data collected from across the Ladakh, Pangong and Karakoram Ranges improved the spatial resolution of exhumation patterns adjacent to the edge of the plateau. These data show a southwest to northeast decrease in cooling ages, which we believe a wave of increased exhumation due to north-south shortening. We also posit that this shortening is responsible for the orientation of the LCF in India. Previously, the southern end of the LCF was unmapped. We used ASTER remotely sensed images to create a comprehensive lithologic map of the region, which allowed us to map the LCF into India. This mapping shows that this fault has been rotated into parallelism with the Karakoram fault system as a result of N-S shortening and dextral shear on the KFS. Additionally, the orientation and sense of motion along these two systems implies that they are acting as a conjugate fault pair, allowing the eastward extrusion of the Tibet. Finally, we identify and quantify late Quaternary slip on the Tangtse strand of the KFS, which was previously believed to be inactive. Our study found that this fault strand

accommodated ca. 6 mm/yr of slip over the last ca. 33-6 ka. Additionally, we speculate that slip is temporally partitioned between the two fault strands, implying that this part of the fault system is more complex than previously believed.

TABLE OF CONTENTS

Page

CHAPTER 1

INTRODUCTION

1. Motivation

The Himalayan orogenic system is the youngest and most spectacular example of a continent-continent collision on earth. Although the collision zone has been subject of extensive research, fundamental questions remain concerning the architecture and evolution of the orogen. Of particular interest are the structures surrounding the 5 km high Tibetan Plateau; in northwest India, this plateau boundary is demarcated by the continental scale, dextral Karakoram fault system (KFS). Despite being one of the major features of the Himalayan orogen, first-order attributes of the fault system are still not well constrained. For example, slip rate estimates for the fault vary over an order of magnitude. Studies of the decadal slip rate using GPS and InSAR imply that present-day motion along the KFS overall is between 1-3.4 mm/yr (Wright et al., 2004; Jade et al., 2004; Jade et al., 2010), while a single study predicts rates as high as 11+/1 mm/yr (Banerjee et al., 2002). Earlier workers suggested longer-term Quaternary slip rates of ca. 15-32 mm/yr (Armijo et al., 1989; Liu et al, 1992; Avouac and Tapponnier, 1993). Late Quaternary rates have been estimated at ca. 4 mm/yr by Brown et al. (2002) in the central region of the fault system, and ca. 7-12 mm/yr in the southern region (Chevalier et al., 2005, 2012). Working on a strand of the fault in the central section previously believed to be inactive, we determined a higher slip rate (ca. 6 mm/yr) for the time between 33 and 5.7 ka than had previously been inferred. Determining the appropriate Quaternary slip

rate along this structure is imperative, as it has implications for geodynamic models of the India-Eurasian system, regional tectonic evolution, and earthquake hazard.

Additionally, the role that the KFS plays in helping to accommodate Indio-Eurasian collision is hotly debated. Some authors believe the fault developed as a transfer structure, helping accommodate oroclinal bending of the orogen through arc-parallel extension (Ratschbacher et al.,1994; Seeber and Pecher, 1998; Murphy et al., 2000; Murphy and Copeland, 2005), while others believe that it is one of the main transcurrent faults allowing eastward extrusion of the Asian lithosphere (Molnar and Tapponnier, 1975; Tapponnier and Molnar, 1976; Tapponnier et al., 1982; Tapponnier et al., 1986; Peltzer and Tapponnier, 1988). The relationship between the KFS and other major faults in the area, such as the sinistral Longmu Co fault, may hold the key to understanding this long-standing problem (Raterman et al., 2007; Robinson, 2009). However, access to critical areas is curtailed due to rugged terrain and disputed geopolitical boundaries. This necessitates the use of innovative mapping techniques, such as remote sensing, to examine compositional distinctions between rock types in inaccessible regions. By using ASTER remote sensing data we were able to map the continuation of the Longmu Co fault in India where it comes into proximity with the KFS, and, based on field observations and thermochronologic data, infer that the Longmu Co fault and KFS are helping to accommodate the eastward extrusion of Tibet.

Adjacent to the KFS is the Ladakh Batholith, the basement of a continental arc formed during subduction of the Neotethys ocean basin. These continental arcs contain evidence of a long exhumation history and can provide information about key periods in the tectonic and erosional history of the region. Because the Ladakh Batholith is bound in

the south by the Zanskar backthrust system, and in the north by the Main Boundary Thrust and KFS, it is well positioned to record changes in regional stress patterns. Previous thermochronologic work by Kirstein et al. (2006, 2009) and Kirstein (2011) has suggested a long and extremely complex exhumation history for the batholith. While the conclusions drawn from these studies are permissible, we sought to expand the spatial distribution of low-temperature thermochronologic data from the batholith so as better to understand exhumation kinematics and employ 1D thermal-kinematic models of those data to better constrain regional variations in exhumation history. This showed pattern of decreasing exhumation translating from SW to NE.

Below is a brief summary of each chapter. Chapters 2-5 were prepared for publication in peer-reviewed journals, and as such, there is some overlap in the background material.

2. Outline of Chapters 2-5

The remote region of Ladakh in northwest India sits in a geodynamically significant location within the Himalayas; it is at the edge of the Tibetan Plateau and at the junction of many orogenic scale features including the Karakoram fault system (KFS), the Longmu Co fault system, the Main Karakoram Thrust, the Shyok suture and the Bangong suture zone. However, because of its rugged terrain and disputed geopolitical boundaries many scientifically critical areas are inaccessible, and thus geologic maps made of the region are incomplete and often contradictory. In Chapter 2, we outline our method for mapping inaccessible regions like Ladakh using Advanced Spaceborne Thermal Emission and Reflection Radiometer (ASTER) data. Specifically,

we use masked and stretched thermal infrared (TIR) data to make determinations about the composition of rocks within the Ladakh region, and we use this information, coupled with field verification and laboratory analysis, to create a comprehensive lithologic map. This map is consistent with recent geologic maps of accessible locations (Phillips et al., 2008) but also expands the coverage area significantly, especially to the northeast. Using this technique, we were also able to determine the location of the Longmu Co fault in India, and examine compositional variability within the Ladakh Batholith.

In Chapter 3 we turn our focus to the Karakoram fault system (KFS). In the Ladakh region, the KFS birfurcates around the Pangong Range. Previous researchers have assigned all Quaternary fault slip to the northern strand of the fault (Pangong strand), but we found evidence for significant Quaternary slip on the southern strand (Tangtse strand). We performed field mapping to identify features offset by motion along the fault and to determine the amount of offset of each feature. We then utilized cosmogenic radionuclide dating to determine the age of these features. This produced a maximum time integrated slip rate of 5.6 +1.7/-1.1 mm/yr for the Tangtse strand for the period between 33 – 5.7 ka. This is higher than the rate found for the Pangong strand of the fault (4 ± 1 mm/yr; Brown et al., 2002) for the period between 14 ka and 1-2 ka. However, the slip accommodated on the Tangtse strand between 5.7 ka and the present is < 3 m, indicating very little activity on this strand during the last ca. 6 ka. Thus, we posit that slip is temporally distributed between the two fault strands, with one strand being dominant at a time. Presently, the Pangong strand is the dominant strand.

To the southwest of the KFS is the Ladakh Batholith, an Andean style continental arc formed during subduction of the Neotethys ocean basin. We used a combination of

new and previously published U-Th/He data to constrain the uplift and exhumation history of the Ladakh batholith from ca. 26 Ma to ca. 10 Ma. These data showed a decrease in cooling ages across the batholith from southwest to northeast. Modelled thermochronologic data show high exhumation rates across the batholith pre-16 Ma, which then decrease from southwest to northeast.

Chapter 5 focuses on the regional tectonics of the Ladakh area and draws on the knowledge gleaned in Chapters 2-4. We use $^{40}Ar/^{39}Ar$ thermochronology of muscovite and biotite, and U-Th/He thermochronology of zircon and apatite to examine cooling as a result of tectonically induced uplift and subsequent exhumation across the KFS. These data show discrete changes in cooling ages on either side of each fault strand, and decreasing cooling ages across the region that are oldest in the southwest and youngest towards the northeast. This mirrors the trend seen across the Ladakh Batholith in Chapter 4. We speculate that this trend may be the end of wave of increased exhumation caused by an increase in north-south shortening. Additionally, the mapping from Chapter 2 coupled with fieldwork and disturbed thermochronology along the Shyok River lead us to believe that the Longmu Co fault is sinistral oblique in some locations, and has been bent into parallelism with the KFS. The initiation of these two fault strands may have been coincident with the onset of east-west extension across central and southern Tibet. Thus, these faults may be acting as a conjugate fault pair and helping to accommodate the eastward extrusion of Tibet. Generally, conjugate fault pairs create a basin at the end of the retreating wedge, but this isn't observed in this location. We speculate that the increase in north-south shortening responsible for the decrease in cooling ages across the region may also be responsible for closing this gap. Additionally, this shortening, coupled

with dextral movement along the KFS, may be responsible for bending the Longmu Co fault into its current position. Finally, U-Pb crystallization ages of granitoids within the Karakoram Range support a spatially discontinuous comagmatic episode from the Baltoro region to the Ladakh area, and may show evidence for an older, previously unreported magmatic episode.

In Chapter 6 I provide a synthesis of the previous chapters and discuss the possibility for future work in the Ladakh region.

3. References

Armijo R, Tapponnier P, Han T. 1989. Late Cenozoic right-lateral strike-slip faulting in southern Tibet. J. Geophys. Res. 94:2787–838

Avouac, J. P., and Tapponnier, P., 1993, Kinematic model of active deformation in central Asia: Geophysical Research Letters, V. 20, p. 895-898.

Brown, E. T., Bendick, R., Bourles, D. L., Gaur, V., Molnar, P., Raisbeck, G. M., and Yiou, F., 2002, Slip rates of the Karakoram Fault, Ladakh, India, determined using cosmic ray exposure dating of debris flows and moraines: Journal of Geophysical Research, v. 107.

Chevalier, M. L., Ryerson, F. J., Tapponnier, P., Finkel, R. C., Van der Woerd, J., Li, H. B., and Li, Q., 2005, Slip-rate measurements on the Karakoram fault may imply secular variations in fault motion, Science 307, no. 5708, 411-414.

Chevalier, M.-L., Tapponnier, P., Van Der Woerd, J., Ryerson, F.J., Finkel, R.C., and Li, H., 2012. Spatially constant slip rate along the southern segment of the Karakorum fault since 200 ka. Tectonophysics, 530-531: 152-179.

Jade, S., Bhatt, B. C.,Yang, Z., Bendick, R., Gaur, V. K., Molnar, P. , Anand, M. B., and Kumar, D., 2004, GPS measurements from the Ladakh Himalaya, India: Preliminary tests of plate-like or continuous deformation in Tibet, Geological Society of America Bulletin, 116, 1385 – 1391.

Jade, S., Rao, R., Vijayan, H. J., Gaur, M. S. M., Bhatt, V. K., Kumar, B. C., Jaganathan, K., Ananda, S., and Kumar, M. B., 2010, GPS-derived deformation rates in northwestern Himalaya and Ladakh, International Journal of Earth Science, Volume 100, Number 6, 1293-1301.

Kirstein, L.A., Foeken, J.P.T., van der Beek, P., Stuart, F.M., Phillips, R.J., 2009, Cenozoic unroofing history of the Ladakh Batholith, western Himalaya constrained by thermochronology and numerical modeling. Journal of the Geological Society of London 166, 667–678.

Kirstein, L.A., Sinclair, H., Stuart, F.M., Dobson, K., 2006. Rapid Early Miocene exhumation of the Ladakh Batholith, northwestern Himalaya. Geology 34, 1049–1052.

Kirstein, L.A., 2011. Thermal evolution and exhumation of the Ladakh batholith, northwest Himalaya, India. Tectonophysics 503, 222–233.

Liu Qing, J.P. Avouac, P. Tapponnier, and Q. Zhang, 1992. Holocene movement along the southern part of the Karakorum fault, Int. Symposium on the Karakorum and Kunlun mountains Kashgar, China, 91.

Molnar, P., Tapponnier, P., Cenozoic tectonics of Asia, effects of continental collision, Science 189 (1975) 419– 426.

Murphy, M. A., A. Yin, P. Kapp, T. M. Harrison, L. Din, and J. Guo, Southward

propagation of the Karakoram fault system into southwest Tibet: Timing and magnitude of slip, Geology, 27, 719 – 722, 1999.

Murphy, M. A., and Copeland, P., 2005, Transtensional deformation in the central Himalaya and its role in accommodating growth of the Himalayan orogen: Tectonics, v. 24, no. 4.

Phillips, R., 2008, Published Map. In Phillips, R., 2008, Geological map of the Karakoram fault zone, Eastern Karakoram, Ladakh, NW Himalaya, Journal of Maps, v 2008, 21-37.

Peltzer, G., Tapponnier, P., Formation and evolution of strike-slip faults, rifts and basins during the India–Asia collision: an experimental approach, J. Geophys. Res. 93 (1988) 15085– 15177.

Raterman, N.S., Cowgill, E., Lin, D., 2007. Variable structural style along the Karakoram fault explained using triple-junction analysis of intersecting faults. Geosphere 3, 71–85.

Ratschbacher L, Frisch W, Lui G, Chen C,. 1994, Distributed deformation in southern and western Tibet during and after the India-Asia collision. J. Geophys. Res. 99:19817–945.

Robinson, A. C., 2009, Evidence against Quaternary slip on the northern Karakorum Fault suggests kinematic reorganization at the western end of the Himalayan-Tibetan orogen: Earth and Planetary Science Letters, v. 286, no. 1-2, p. 158-170.

Seeber, L., Pecher, A., 1998. Strain partitioning along the Himalayan arc and the Nanga Parbat antiform. Geology 26, 791–794.

Tapponnier, P., Peltzer, G., LeDain, A.Y., Armijo, R., Cobbold, P.R. , Propagating extrusion tectonics in Asia: new insights from simple experiments with plasticine, Geology 10 (1982) 611 –616.

Tapponnier, P., Peltzer, G., Armijo, R., On the mechanics of the collision between India and Asia, in: M.C. Coward, A.C. Ries (Eds.), Collision Tectonics, Spec. Publ.-Geol. Soc. Lond., vol. 19, 1986, pp. 115–157.

Tapponnier, P. Molnar, P., Slip-line field theory and large scale continental tectonics, Nature, 264 (1976) 319–324.

Wright, T. J., Parsons, B., England, P. C., and Fielding, E. J., 2004, InSAR observations of low slip rates on the major faults of western Tibet: Science, v. 305, p. 236-239.

CHAPTER 2

LITHOLOGY FROM SPACE: USING ASTER REMOTE SENSING TO MAP REMOTE TERRESTRIAL AREAS

1. Abstract

An inability to generate lithologic maps of remote regions has stymied many geological research efforts around the globe, but satellite image data offers a readily available tool to surmount this barrier. In this paper, we present a lithologic map of the Ladakh region of the northwestern Indian Himalaya, which is accessible in some places, and wholly inaccessible in others. This juxtaposition allows us to verify our remotely sensed lithologic interpretations, and highlights the utility of using compositional maps generated from satellite data to depict the geology of inaccessible regions.

This contribution outlines a robust method for analysis of Advanced Spaceborne Thermal Emission and Reflection Radiometer (ASTER) data to facilitate lithologic and geologic mapping. Critical to this process is proper data processing and image analysis. It is also important that image interpretations be coupled with laboratory spectral analysis of field samples in order to strengthen the interpretation of the orbital remote sensing data. Using these techniques, we are able to present a comprehensive lithologic map of the region that has been partially verified in the field, and highlight previously undocumented compositional variations in the Ladakh batholith, which is typically mapped as a granitic body with little further subdivision.

2. Introduction

Remote sensing data have been used extensively to map mineral abundances on planetary bodies throughout the Solar System using visible/near infrared and thermal infrared spectroscopy (e.g., Lucey et al., 1998; Bandfield et al., 2000; Bandfield, 2002). Like the planetary bodies where remote sensing techniques have been extensively employed, many environments on Earth are difficult to access due to either extreme topography or political instability and disputed geopolitical borders. However, understanding the geologic relations of these areas may hold the key to unlocking many long-standing science questions, and remote sensing is a powerful tool that can be employed to that end.

The NASA Landsat Thematic Mapper and Enhanced Thematic Mapper Plus (TM/ETM+) datasets are among the most highly utilized multi-spectral imagery, due to the long and continuous data record that the Landsat missions provide spanning more than 40 years (Abrams et al., 2004). However, ASTER (Advanced Spaceborne Thermal Emission and Reflection Radiometer; Yamaguchi et al., 1998) has additional spectral coverage not available from Landsat. Mainly, the increased thermal infrared (TIR) capabilities and improved resolution of ASTER imagery makes it attractive to geoscientists. Landsat offers one TIR spectral band at 120 m/pixel resolution while ASTER offers 5 TIR bands at 90 m/pixel resolution (e.g., Abrams et al., 2004). Detailed analysis of ASTER TIR spectral bands can be used to make inferences about materials exposed at the surface; when coupled with fieldwork and laboratory analysis, these data can be used to create detailed lithologic maps of previously poorly mapped environs.

Here we illustrate the process by which ASTER data can be used to facilitate geologic interpretations by focusing on one such area: the Ladakh region of the northwestern Indian Himalaya (Figure 1). Many parts of the region are roadless, remote, and at high elevations (up to 7000 m). The Ladakh region includes disputed borders among India, Pakistan, and China, such that access permission is not always easy. Only a few areas are reliably accessible to foreign scientists. For that reason, the geology of those areas has been studied extensively and the results have had a disproportionate influence on perceptions of the regional geology. The goal of our study was a more comprehensive understanding of the distributions of bedrock geology in the region that might inform future geologic explorations. Our approach involved the processing of ASTER data using laboratory spectral analyses of representative rock types from the region to match spectral signatures with rock types. While the result does not provide a direct indication of the nature of unit contacts in most instances, field mapping of contact relationships in accessible areas informs tentative interpretations of relationships in more inaccessible areas and helps identify critical areas for future ground studies.

3. Background

3.1 ASTER

The ASTER instrument – a high-resolution, multi-spectral imaging system aboard the TERRA satellite –is used for collecting terrestrial ground surface and atmospheric data (Yamaguchi et al., 1998). It records reflectance spectra representing: 1) three bands of the visible and near-infrared spectrum (VNIR) at wavelengths between 0.5 and 1.0 μm of the electromagnetic spectrum; 2) six bands of the short-wave infrared (SWIR)

spectrum (1.0-2.5 μm); and 3) five bands of the thermal infrared (TIR) spectrum (8-12 μm). The spectrometers collect data at different resolutions for the three groups of wavelengths: VNIR – 15 m/pixel; SWIR – 30 m/pixel; TIR – 90 m/pixel (Abrams et al., 2004; Corrie et al., 2010). All spectral bands have potential geologic applications. VNIR is particularly useful for identifying transition metals and vegetation (e.g., Rowan et al., 1986), while SWIR is useful for identifying hydrous minerals (Hunt, 1977). TIR is primarily used for mapping rock-forming mineral distributions (e.g. Hunt and Salisbury, 1976; Rowan and Mars, 2002; Cooper et al., 2012).

ASTER image analysis has been successfully applied to a variety of different geologic mapping problems in the Himalaya. For instance, Bertoldi et al. (2011) mapped the Buraburi Granite, a previously unknown granitic body in western Nepal, by searching for both the spectral signature for granite and the spectral signature for a lichen that grows specifically on granite. Cooper et al. (2012) used ASTER image analysis to map the position of the South Tibetan fault system in Bhutan by contrasting the primarily carbonate-bearing rocks of the hanging wall with the primarily silica-dominated rocks of the footwall. In the Ladakh region south of the Indus River, Tripathy-Lang et al. (in prep) used ASTER imagery to generate a lithotectonic map of a rugged area containing stratigraphy critical to constraining the timing of collision along the Indus suture zone.

3.2 Geologic setting of Ladakh

The remote Ladakh Himalaya of northwestern India (Figure 1) feature several major tectonic structures. The Indus-Yarlung, Shyok, and Bangong suture zones mark the closure of ocean basins during the accretionary evolution of Tibet and the culminating

event of India-Eurasia collision (e.g., Gansser 1964). The Karakoram fault system, a continental scale dextral strike-slip structure, marks the southwestern margin of the Tibetan Plateau (e.g., Armijo et al., 1989; Searle, 1991), while a portion of the northwestern margin is marked by the sinistral Longmu-Co fault system (Liu, 1993; Raterman et al., 2007; Figure 1). The Ladakh batholith, part of the Transhimalayan plutonic belt (e.g. Honegger et al., 1982), is bounded to the south by the Indus-Yarlong suture zone, and to the north by both the Shyok suture zone and the Karakoram fault system. In one area, where the transpressive Karakoram fault system bifurcates, a NW-SW–ridge of high topography (the Pangong Range) is interposed between the Ladakh Range and the high elevation Karakoram Range to the north. While many geologic maps have been made of the Ladakh region (e.g., Searle, 1996; Dunlap et al., 1998; Ravikant et al., 2006; Phillips, 2008) the results are contradictory and the mapping incomplete. Improved maps of these areas could clarify many long-standing scientific problems. An especially important example is the role the Karakoram fault system plays in accommodating Indian-Eurasian deformation. Central to this debate is the amount of slip that the fault system has accrued. Some researchers (e.g., Avouac and Tapponnier, 1993; Tapponnier et al., 2001) suggest offsets of 1000 km or more, while others (e.g., Lacassin et al., 2004) argue for 400 km or more of total slip. A variety of workers employing different structural and lithologic correlations argue for a total slip closer to 120-170 km (e.g., Searle et al., 1998; Phillips et al., 2004; Robinson, 2009b), or even as low as 66 km (Murphy et al., 2002). Because most of these estimates are determined on the basis of offset lithologic or structural features, an accurate geologic map of the rocks surrounding the fault is imperative for appropriate correlations. In fact, correlations across the fault,

especially in this area, are routinely difficult. Motion along the Karakoram Fault system has offset or obscured major portions of the Shyok and Bangong suture zones, making it unclear which sutures match up across the fault system (Figure 1). This renders reconstruction of this part of the orogen difficult. Additionally, the sinistral Longmu Co fault system is proximal to the Karakoram fault system in the region, but there is controversy as to where these two fault systems intersect (Raterman et al., 2007; McCarthy and Weinberg, 2010; Bohon et al., Chapter 4; Figure 1). This is an important problem to address, as the interaction of these faults over geologic timescales has profound implications for regional tectonics. Some authors speculate that the interaction of these systems has caused a significant bend in the Karakoram fault system (Robinson, 2009a). Other authors (McCarthy and Weinberg, 2010) dismiss this possibility. Critical to the debate is the location of the intersection of the fault systems, which has not been previously mapped.

4. ASTER image analysis

All ASTER images were processed at the Mars Space Flight Facility at ASU using Davinci, which is open source software created specifically for remote sensing image analysis (http://davinci.asu.edu). The images were mosaicked and mapped in JMARS (Java Mission-planning and Analysis for Remote Sensing) for Earth, an open-source Geographical Information System (GIS) application created at Arizona State University (http://jmars.asu.edu).

4.1 Data Acquisition

Data were acquired from the USGS Land Processes Distributed Active Archive Center (https://lpdaac.usgs.gov/). There are no composite scenes available; scenes must be searched for and selected individually.

When undertaking a lithologic mapping project, it is critical to utilize the appropriate processing level of ASTER data. ASTER Level-1A (L1A) datasets are unprocessed digital instrument data that consist of the image and the radiometric and geometric coefficients as well as other auxiliary data, but these additional data are not applied. ASTER Level-1B (L1B) datasets are radiometrically calibrated and geometrically co-registered. AST05 ASTER data comprise a Level 2 product that contains 90 m/pixel resolution NASA temperature-emissivity corrected data applied to atmospherically corrected surface radiance data (Abrams et al., 2004). Atmospheric removal and surface retrievals are imperative because without this, the measured spectra are a combination of both surface and atmospheric absorptions, which complicate the interpretation of the data. Without conducting a temperature emissivity separation on the radiance data, it is not appropriate to compare spectral data from locations with different temperatures, as the temperature of the surface and not the composition will dominate the spectra. Because most rock forming minerals show distinct emissivity spectral features in the thermal infrared (Figure 2), the AST05 product is useful for most lithologic mapping exercises (Abrams et al., 2004).

Often, variations in the detector readout voltages or various instrument instabilities can produce unwanted noise in the data. It is necessary to remove this instrument noise before proceeding with additional processing. The techniques applied to

the ASTER data presented in this work have been extensively documented and applied to other infrared instruments (e.g. the Thermal Emission Imaging System, THEMIS, Christensen et al., 2004) and the effect of the algorithms on the data have been characterized in detail. For more information on the data processing algorithms applied to ASTER see Edwards et al. (2011), Nowicki et al. (2013a), and Nowicki et al. (2013b).

4.2 Data Exclusion Masks

Data exclusion masks were created in order to obscure pixels within each ASTER scene that have significant contributions of material other than the material of interest, in this case exposed rock. Because we want to maximize the amount of compositional diversity due to rock visible in each scene, it is vital to search for and choose ASTER images that have minimal snow, ice and cloud cover. Additionally, if masking for ice and snow is required, ASTER scenes must have been acquired before 2008 because such masks require shortwave infrared data, and the cooler on this system has since failed.

For most scenes, three masks are created (Figure 3). Each has a limit or a range of variables that need to be adjusted for each scene in order to avoid both over- and under-masking distractors. Common values are given below.

1) **The normalized difference vegetation index** mask (NDVI) is used to map vegetation (earthobservatory.nasa.gov; Figure 3b). Generally NDVI values above 0.20 are excluded (Cooper et al., 2013).

$$NDVI = \frac{Band\ 3 - Band\ 2}{Band\ 3 + Band\ 2}$$

2) **The normalized difference snow and ice index** mask (NDSII) is used to mask out snow, ice and liquid surface water (Figure 3c). NDSII values less than 0.5 and greater than 0.9 are usually excluded.

$$NDSII = \frac{Band\ 3 - Band\ 5}{VNIR\ Band\ 1 - SWIR\ Band\ 4}$$

3**) The Cloud** mask (CLOUD; band 1), as the name implies, is used to mask out clouds (Figure 3d). Clouds are often difficult to mask because they radiate to the ground, which can change the spectral signature of nearby ground pixels. Thus, all pixels surrounding clouds should be treated with care. Generally, values in the VNIR that are greater than 40−80 $Wm^{-2}sr^{-1}um^{-1}$ are excluded (Cooper et al., 2013).

Once these masks have been created, they are combined (Figure 3e) and applied to the AST05 Level 2 scene (Figure 3f).

4.3 Image processing

Once each scene has been masked, a decorrelation stretch (DCS) is applied to the multi-band masked ASTER data. In AST05 data, decorrelation stretches maximize the spectral variation (related to the first, second and third principal components) in the scene of interest so that mineralogical differences are exaggerated and easily noted (Gillespie,

1986). In this study, we use the thermal infrared bands in various decorrelation stretches to extract compositional differences. We stretch some combination of three TIR bands, and place each band in the red, blue and green channels of an image. For example, in a 12-11-10 DCS, the green highlights quartz-rich compositions (Figure 4b and e) whereas in the 14-12-10 DCS the green highlights the rocks containing calcite (Figure 4c and f).

4.4 Laboratory Spectra

All spectral data were collected at the ASU Thermal Infrared Spectroscopy Laboratory using a Nicolet Nexus 6700 spectrometer, which allows us to obtain data from the range of 200-4000 cm^{-1} (~2.5 - 50 microns). For information on spectrometer calibration and configuration see Ruff et al. (1997).

Bulk/whole rock samples collected from across the Ladakh batholith were placed in an oven at 80∞C for at least two days to drive off any excess adsorbed water that could compromise spectral clarity and raise the signal to noise of the emission spectroscopy measurement (Ruff et al., 1997). Samples were then placed in the attached emission spectral chamber and the thermal infrared spectra acquired. Hot and warm black body calibration targets were also measured in a full aperture calibration to convert the uncalibrated instrument response to calibrated spectral radiance and emissivity.

Laboratory analysis of hand samples produces high-resolution spectral data that provide information about mineral type and abundance (e.g., Ramsey and Christensen, 1998; Feely and Christensen, 1999). However, spectral data collected from ASTER TIR images only gives information in 5 spectral bands covering only a fraction of the wavelengths of the laboratory instrument. Thus, it is necessary to down-sample any data collected in the laboratory to the same spectral resolution as data collected from the

ASTER images. Nevertheless, the characteristic features of the high-resolution laboratory spectra do not fully disappear when resampled to the lower ASTER resolution (Figure 2).

Even when the down-sampled lab spectra and the spectra collected from ASTER images are from the same location, they may not be alike. Problems relating to sensor resolution and signal-to-noise ratio, acquisition geometry, environmental conditions during data collection (Ehlers, 1991; Kruse et al., 1993), variations in black body calibrations, atmospheric corrections and grain size effects can all affect the shape and clarity of the spectra. Additionally, scaling factors can be an issue. In order to extract spectral information from the ASTER images, spatial averaging (sometimes called pixel averaging) of the target of interest was employed to enhance the signal to noise ratio. This process involves the use of an average of several pixels from a small area to form a composite spectrum. Because each pixel is 90m by 90m, this averages a large area of bedrock with a range of compositions, especially when compared to a hand sample. Because of these potential complications we use a qualitative approach, identifying spectral shape similarities when comparing resampled laboratory spectra and ASTER spectra. In particular, we look for similar amounts of emissivity and similar absorption and reflectance patterns at certain bands (Figure 2).

Another potential issue with spectra collected both in the lab and from the remote sensing data is the presence of weathering/alteration products on the natural surface of the rock. Since remotely sensed data only provides information about the uppermost surface (i.e., several microns for VNIR and up to tens of microns for TIR), any varnish or weathering products on the surface of the rocks can significantly alter the spectral signature. To examine the variability this produced within the granites in our region, we

measured laboratory spectra for three samples that had both fresh and natural surfaces. We then degraded the laboratory spectra to ASTER resolution. In some cases, we found almost no variability between the fresh surface and natural surface spectra. However, with other samples there was a small amount of variability in the spectral shape resulting in some reduction in the ability to adequately distinguish between sub-types of granite.

5. Creating a lithologic map

Here, we guide the reader through our interpretation of the processed ASTER imagery and spectral analysis. The end result of this exercise is a lithologic map of the Ladakh region that, while rooted in remote sensing, is verified by field geology in places (Figure 5). This map broadly classifies rocks by composition but does not assign geologic interpretations to the mapped units.

5.1 Decorrelation stretch analysis

To begin, we used various decorrelation stretches to arrive at a first-order understanding of the distribution of major lithologic units across the region. Because different band combinations highlight different mineral abundances within the rocks, we were able to make educated guesses about bedrock composition simply by comparing the colors on the image. Figure 4 shows two particularly useful decorrelation stretches.

In Figures 4b and 4e, we used a 12-11-10 stretch to focus on variations related to quartz content. In this stretch, carbonates and ultramafic rocks will emit in all bands almost equally, and thus tend to appear washed out. Because bands 12-11-10 lie within the spectral region where there are subtle variations among quartz-rich, felsic,

intermediate, and mafic rocks (Figure 2), this decorrelation stretch is ideal for remotely mapping compositional distinctions in igneous rocks. The most quartz-rich exposures will reflect band 11, and thus appear greener. On the other hand, mafic rocks reflect more of bands 12 and 11, so should appear yellow. Surfaces of intermediate composition will reflect band 10 slightly more than bands 12 and 11, and so appear bluer. Felsic surfaces, while closest to quartz-rich surfaces in terms of absorption features, should appear more blue than green.

In Figure 4c and 4f we used a 14-12-10 decorrelation stretch, which directs band 14 to the red channel, band 12 to the green channel, and band 10 to the blue channel. This stretch is helpful for differentiating carbonate from other rocks, due to a strong absorption feature at band 14 (Figure 2). Because carbonate is absorbed at band 14, it manifests as blue-green in this stretch. Mafic and ultramafic rocks reflect all three wavelengths, and thus appear white or washed out. Quartz-rich and other felsic rocks will absorb bands 12 and 10 and thus appear red. In comparison, intermediate rocks should appear more orange-yellow because they absorb less of bands 12 and 10, and consequently have a larger green and blue component.

5.2 Spectral averaging (pixel averaging)

We produced pixel-averaged spectra for two types of sites: accessible and inaccessible rock units. For rocks that were accessible in the field, we were able to compare their pixel-averaged spectra with regions of similar signature in the decorrelation stretches. In Figure 6, we show pixel-averaged spectra from field-identified rock types LL and PG, which comprise limestone and granite, respectively. We then

compared these spectra with those other locations that we were unable to visit but that were spectrally similar, and were able to identify additional limestone and granite bodies (locations KG, ML and BL in Figure 5b).

However, some distinct compositional differences identified during the decorrelation stretch analysis were for units wholly inaccessible in the field. In these cases, we obtained pixel-averaged spectra of the inaccessible regions from the Ladakh area and compared them to TIR spectra collected from Mountain Pass, California (Rowan and Mars, 2002). The similarity of spectral signatures for each rock type corroborated our assumptions about the composition of the surface in these locations (Figure 7). Using this method, we were able to identify additional carbonates, granites and intermediate rocks. Continuing in this manner, we were able to broadly assess the composition of different units and create a regional lithologic map (Figure 5).

5.3 Comparing laboratory and ASTER spectra

Comparing laboratory spectra versus those obtained from the ASTER imagery enables even further differentiation amongst even the most subtle of color differences in a decorrelation stretch because the color of every pixel is directly influenced by the composition of the exposed surface. Put another way, every color variation has its own unique spectral signature in an ASTER image, which can be difficult to resolve without a more quantitative method by which to assess the data. In the case of the Ladakh batholith, which is usually mapped as a large granitoid unit, there is known compositional variability. It was intruded into metasedimentary and metavolcanic rocks that are exposed on its northern side (Thakur et al., 1981; Dunlap and Wysoczanski, 2002). Also exposed

on the northern flank in this region is the Khardung volcanic sequence (Dunlap and Wysoczanski, 2002), which is a series of felsic pyroclastic flows and volcaniclastic rocks (Weinberg and Dunlap, 2000). Existing data suggest that the batholith itself was primarily formed during two different magmatic phases, and there are also young dike intrusions on the southern side of the batholith (Weinberg et al., 2000; St-Onge et al., 2010; White et al., 2011). As mentioned above, the 12-11-10 decorrelation stretch highlights differences in quartz content (Figure 4), and we exploit that here to tease out compositional variation within the batholith that was undoubtedly produced during the various stages of magmatism.

First, we map compositional differences seen in the ASTER images. In Figure 8 (and Figure 5b), these patterns are apparent: there are large areas near the range crest and along the southern flank that are purple, discontinuous regions throughout the batholith of mostly pink, large northern areas of green, and small isolated patches of orange and red. These different colors should represent different compositions within the batholith. To assess the differences between the pink, purple and green units, we averaged 10 x 10 pixel areas from two different regions within the purple, pink and green zones. The orange and red zones were generally too small and discontinuous for this exercise, so we do not discuss them further. For the purple and pink areas, we chose locations near the range crest and the southern flank (Figure 8). The averaged spectra from within each colored zone were similar to one another but different from the spectra from other zones (Figure 9), indicating that these areas are indeed compositionally distinct. The areas in green are Khardung and Shyok volcanic and metavolcanic rocks that have been described in literature (e.g., Thakur et al., 1981; Dunlap and Wysoczanski, 2002).

A suite of hand samples was collected from within the main body of the Ladakh Batholith, and many of these samples lie within regions that show spectral variability (Figure 8). In the laboratory, we took spectral readings of each sample and then down-sampled these to ASTER resolution (examples of Sample 4 and Sample 8 shown in Figure 9). Next, we averaged the spectral signal from 100 pixels (10 x10) within the ASTER data in the location where the hand sample was collected. Finally, we compared the laboratory down-sampled spectra to the spectra collected from the ASTER image. This showed a relatively good correlation between emissivity within each colored region, with the purple regions always having lower emissivity than the pink regions (Figure 9).

6. Discussion

The lithologic map produced using this combination of field geology and remote sensing interpretation covers significantly more territory than most existing maps (e.g., Ravikant et al., 2006; Phillips, 2008; Figure 5). It also agrees well with previously published maps that are focused on accessible areas. For instance, our ÏMetapelitic schists, volcanics and marblesÓ unit clearly corresponds to the Nubra Formation mapped by Phillips (2008) in the Nubra Valley area. Our map also correctly identifies rocks and contacts that we were unable to access, but that have been accessed by other groups. Sinha et al. (1999) trekked across the Karakoram Range from the Nubra Valley to the Karakoram Pass in Tibet, which allowed them to create a lithostratigraphic map along that transect. Our remote sensing-based mapping in the same region does a reasonable job of reproducing the major contacts and rock types shown on their map (Figure 10).

Additionally, our mapping has allowed us to add to the body of geologic knowledge for this area. For instance, we are able to distinguish internal variability within a large granitic body in the region - the Ladakh batholith (Figure 1). Bouihol et al. (2013) used isotope geochemistry and U-Pb geochronology to deduce the magmatic evolution of portions of the Ladakh Batholith. Unfortunately, the samples they worked on were only collected from within the pink regions the batholith, or in regions of the batholith where there was no distinguishable color pattern. Nonetheless, their dataset allows us to speculate on the origin of the compositional differences. Based on the isotopic and trace element signatures of the granitoids evaluated within our study area, Bouihol et al. (2013) suggested that some of these intrusions were the result of juvenille magmas derived from the subducting plate. The distinction between the pink and unmapped regions could be the result of geochemical differences within the subducting plate, differences in mantle source region or mixing (Bouihol et al., 2013). Samples from other regions of the batholith have a more evolved compositional signature, which implies that these melts were crustal mixtures, probably incorporating either sediments or Indian lower crust (Bouihol et al., 2013). We speculate that the purple regions within our study area may be regions of more evolved magmatic composition, correlating to the evolved samples found in other parts of the batholith. This correlates well with the emissivity spectra derived from each region.

We also were able to locate the trace of the Longmu Co Fault southwest of the region where it has been previously mapped (Raterman et al., 2007), mainly due to the clarity of the contact between the northern silicic rocks and the southern carbonate rocks in the ASTER imagery (Figure 4e and f; Figure 11). This carbonate unit, which marks the

fault trace and is distinctive in the ASTER imagery, may hold the key to a geologic mystery – the location of the southern Longmu Co fault in India. Using ASTER remote sensing we are able to follow this contact from its previously mapped extent in Tibet to the western bank of the Skyok River (Figure 11). From there, the unit becomes discontinuous, but appears to rotate into parallelism with the Karakoram fault system and continue along the Nubra Valley to at least the village of Panamik (Figure 5). This is well beyond the intersection suggested by Raterman et al. (2007). If the Longmu Co fault does not intersect the Karakoram fault just north of the Pangong Range as speculated by Raterman et al. (2007), then it is unlikely that motion along the Longmu Co fault is responsible for the formation of the bend in the Karakoram Range.

7. Conclusions

ASTER thermal infrared data, when coupled with careful field studies and laboratory analysis, can be a powerful tool for informing lithologic mapping in remote or inaccessible locations. However, ASTER scenes must be chosen and processed appropriately. Acquiring the proper type of data and masking out non-essential pixels are necessary steps for proper analysis of such data. Additionally, applying decorrelation stretches can provide important information about compositional subtleties. By using a combination of masks, decorrelation stretches with band combinations and laboratory analyses we have successfully compiled a regional lithologic map for the remote and rugged Ladakh region of NW India. This map has allowed us to make inferences about the intersection of the Karakoram and Longmu Co faults, as well as speculate about compositional variation within Ladakh Batholith.

8. References

Abrams, M., Hook, S., & Ramachandran, B. (2004). ASTER User Handbook, Version 2. Jet Propulsion Laboratory, California Institute of Technology. http://asterweb.jpl.nasa.gov/content/03_data/04_Documents/aster_user_guide_v2.pdf

Armijo R, Tapponnier P, Han T. 1989. Late Cenozoic right-lateral strike-slip faulting in southern Tibet. J. Geophys. Res. 94:2787–83.

Avouac, J. P., and Tapponnier, P. (1993), Kinematic model of active deformation in central Asia: Geophysical Research Letters, V. 20, p. 895-898.

Bandfield, J. L., V. E. Hamilton, and P. R. Christensen, (2000) A global view of Martian surface compositions from MGS-TES, Science, 287, 1626 – 1630.

Bandfield, J. L. (2002) Global mineral distributions on Mars, J. Geophys. Res. 107, 10.1029/2001JE001510

Bard, J. (1983). Metamorphism of an obducted island arc; example of the Kohistan Sequence (Pakistan) in the Himalayan collided range. Earth and Planetary Science Letters 65(1), 133-144.

Bertoldi, L., Massironi, M., Visoná, D., Carosi, R., Montomoli, C., Gubert, F., Naletto, G., and Pelizzo, M.G. (2011), Mapping the Buraburi granite in the Himalaya of western Nepal: Remote sensing analysis in a collisional belt with vegetation cover and extreme variation of topography: Remote Sensing of Environment, v. 115, p. 1129– 1144.

Bouilhol, P., Jagoutz, O., Hanchar, J.M., Dudas, F.O., 2013. Dating the India–Eurasia collision through arc magmatic records. Earth Planet. Sci. Lett. 366, 163–175.

Christensen, P. R., B. M. Jakosky, H. H. Kieffer, M. C. Malin, H. Y. McSween, Jr., K. Nealson, G. L. Mehall, S. H. Silverman, S. Ferry, M. Caplinger, and M. Ravine (2004), The Thermal Emission Imaging System (THEMIS) for the Mars 2001 Odyssey Mission, *Space Science Reviews*, *110*(1), 85-130.

Cooper, F.J., Adams, B.A., Edwards, C.S. and Hodges, K.V., (2012). Large normalsense displacement on the South Tibetan fault system in the eastern Himalaya. Geology, 40, 971–974.

Corrie RK, Ninomiya Y, Aitchison JC (2010), Applying advanced spaceborne thermal emission and reflection radiometer (ASTER) spectral indices for geological mapping and mineral identification on the Tibetan Plateau. Int Arch Photogramm Remote Sens Spat Info Sci, 464–469.

Dunlap, W.J., Weinberg, R.F., Searle, M.P. (1998). Karakoram fault zone rocks cool in two phases. Journal of the Geological Society 155, 903–912.

Dunlap, W.J., Wysoczanski, R., (2002). Thermal evidence for early Cretaceous metamorphism in the Shyok suture zone and age of the Khardung volcanic rocks, Ladakh, India. Journal of Asian Earth Sciences 20, 481–490.

Edwards, C. S., K. J. Nowicki, P. R. Christensen, J. Hill, N. Gorelick, and K. Murray (2011), Mosaicking of global planetary image datasets: 1. Techniques and data processing for Thermal Emission Imaging System (THEMIS) multi-spectral data, *J. Geophys. Res.*, *116*(E10), E10008.

Ehlers, M., 1993, Integration of GIS, remote sensing, photogrammetry and cartography: the geoinformatics approach. GIS GEO-Informations-Systeme, 6, 18-23.

Feely, K. C., and P. R. Christensen (1999), Quantitative compositional analysis using

thermal emission spectroscopy: Application to igneous and metamorphic rocks, *J. Geophys. Res., 104*, 24,195-124,210.

Gansser, A., 1980, The significance of the Himalayan suture zone, *Tectonophysics, 62*, 37-52.

Gillespie, A. R., Kahle, A. B., & Walker, R. E. (1986). Color enhancement of highly correlated images: I. Decorrelation and HSI contrast stretches. Remote Sensing of Environment, 20, 209 – 235.

Honegger, K., Dierich, V., Frank, Gansser, A., Thoni, M. & Trommsdroff, V., 1982, Magmatism and metamorphism in the Ladakh Himalayas (the Indus-Tsangpo Suture Zone). Earth and Planetary Science Letters, 60, 253–292

Hunt, G. R. (1977). Spectral signatures of particulate minerals in the visible and near infrared. Geophysics, 42(3), 501 – 513.

Hunt, G. R., & Salisbury, J. W. (1976). Mid-infrared spectral behavior of metamorphic rocks, Technical Report AFRCL-TR-76-0003, US Air Force Cambridge Research Laboratory, Cambridge, MA

Kruse, F. A., Lejkoff, A. B., Boardman, J. W., Heidebrecht, K. B., Shapiro, A. T., & Barloon, P. J., et al. (1993). The spectral image processing system (SIPS)– interactive visualization and analysis of imaging spectrometer data. Remote Sensing of Environment, 44, 145–163.

Lacassin, R., Valli, F. , Arnaud, N., Leloup, P.H. , Paquette, J.L. , Haibing, L., Tapponnier, P., Chevalier, M.-L. , Guillot, S., Maheo, G., Zhiqin, X., (2004). Large-scale geometry, offset and kinematic evolution of the Karakorum fault, Tibet, Earth Planet. Sci. Lett. 219, 255 – 269.

Liu, Q., 1993, Pal»oclimat et contraintes chronologiques sur les mouvements r»cent dans l'Ouest du Tibet: Failles du Karakorum et de Longmu Co–Gozha Co, lacs en pull-apart de Longmu Co et de Sumxi Co [ThÀse de Doctorat]: Paris, Universit» Paris VII, 360 p.

Lucey PG, Blewett DT, Hawke BR (1998) Mapping the FeO and TiO2 content of the lunar surface with multispectral imagery. J Geophys Res 103:3679-3699 Earth Planet. Sci. Lett. 142, 311–330.

McCarthy, M. R., and R. F. Weinberg, (2010) Structural complexity resulting from pervasive ductile deformation in the Karakoram shear zone, Ladakh, NW India, Tectonics, 29.

Murphy, M. A., Yin, A., Kapp, P., Harrison, T. M., Manning, C. E., Ryerson, F. J., Ding L., and Guo, J.H. (2002). Structural evolution of the Gurla Mandhata detachment system, southwest Tibet: implications for the eastward extent of the Karakoram fault system, Geological Society of America Bulletin, 114, pp. 428–447.

Nowicki, K. J., **C.** S. Edwards, P. R. Christensen, Post-Projection Removal of Row- and Column-Correlated Noise in Line-Scanning Data: Application to THEMIS infrared Data, (in press 2013a), IEEE-Whispers Transactions.

Nowicki, K. J., C. S. Edwards, P. R. Christensen, Removal of Salt-and-Pepper Noise in THEMIS Infrared Radiance and Emissivity Spectral Data of the Martian Surface (in press, 2013b), IEEE-Whispers Transactions.

Phillips, R. (2008). Published Map. In Phillips, R. (2008). Geological map of the Karakoram fault zone, Eastern Karakoram, Ladakh, NW Himalaya, Journal of Maps, v 2008, 21-37.

Phillips, R. J., Parrish, R. R., and Searle, M. P. (2004). Age constraints on ductile deformation and long-term slip rates along the Karakoram fault zone, Ladakh: Earth and Planetary Science Letters, v. 226, no. 3-4, p. 305-319.

Ramsey, M. S., and P. R. Christensen (1998), Mineral abundance determination: Quantitative deconvolution of thermal emission spectra, *J. Geophys. Res.*, *103*, 577-596, doi:10.1029/97JB0278

Raterman, N.S., Cowgill, E., Lin, D. (2007). Variable structural style along the Karakoram fault explained using triple-junction analysis of intersecting faults. Geosphere 3, 71–85.

Ravikant, V., Wu, F.-Y., Ji, W.-Q. (2009). Zircon U–Pb and Hf isotopic constraints on petrogenesis of the Cretaceous–Tertiary granites in eastern Karakoram and Ladakh, India. Lithos 110, 153–166.

Robinson, A. C. (2009a). Evidence against Quaternary slip on the northern Karakorum Fault suggests kinematic reorganization at the western end of the Himalayan-Tibetan orogen: Earth and Planetary Science Letters, v. 286, no. 1-2, p. 158-170.

Robinson, A. C. (2009b). Geologic offsets across the northern Karakorum fault: Implications for its role and terrane correlations in the western Himalayan-Tibetan orogen: Earth and Planetary Science Letters, v. 279, no. 1-2, p. 123-130.

Rowan, L. C., Wetlaufer, P. H., Goetz, A. F. H., Billlingsley, F. C., & Stewart, J. H. (1974). Discrimination of rock types and detection of hydrotermally altered areas in south – central Nevada. U.S. Geological Survey Professional Paper, 883, 1 – 35.

Rowan LC, Mars JC. 2003. Lithologic mapping in the Mountain Pass, California area using advanced spaceborne thermal emission and reflection radiometer (ASTER) data. Remote sensing of Environment 84: 350–366.

Rowan, L. C., & Mars, J. C. (2003). Lithologic mapping in the Mountain Pass, California area using Advanced Spaceborne Thermal Emission And Reflection Radiometer (ASTER) data. Remote Sensing of Environment, 84, 350–366.

Ruff, S. W., Christensen, P. R., Barbera, P. W., & Anderson, D. L. (1997). Quantitative thermal emission spectroscopy of minerals: A laboratory technique for measurement and calibration. Journal of Geophysical Research, 102(B7), 14899– 14913.

Searle, M.P., 1991. Geology and Tectonics of the Karakoram Mountains. John Wiley and Sons, Chichester, UK, p. 358.

Searle, M.P., Weinberg, R.F., Dunlap, W.J. (1998). Transpressional tectonics along the Karakoram fault zone, northern Ladakh: constraints on Tibetan extrusion. In: Holdsworth, R.E., Strachan, R.A., Dewey, J.F. (Eds.), Continental Transpressional and Transtensional Tectonics, 135. Geological Society, Special Publication, London, pp. 307–325.

Searle, M.P., Windley, B.F., Coward, M.P., Cooper, D.J.W., Rex, A.J., Rex, D.C., Li, T., Xiao, X.C., Jan, M.Q., Thakur, V.C., Kumar, S. (1987). The closing of Tethys and the tectonics of the Himalayas. Geological Society of America Bulletin 98, 678–701.

St-Onge, M.R., Rayner, N., Searle, M.P. (2010). Zircon age determinations for the Ladakh batholith at Chumathang (Northwest India): implications for the age of the India–Asia collision in the Ladakh Himalaya. Tectonophysics 495, 171–183.

Sinha, A.K., Upadyay, R., Chandra, R., 1999. Contributions to the geology of the eastern Karakoram, India. Geological Society of America, Special Publication 328, 33-48.

Thakur, V. C., & Misra, D. K. (1984). Tectonic framework of the Indus and Shyok suture zones in eastern Ladakh, northwest Himalaya. *Tectonophysics*,*101*(3), 207-220.

Tapponnier, P., Xu, Z.Q., Roger, F., Meyer, B., Arnaud, N., Wittlinger, G., and Yang, J.S. (2001). Oblique stepwise rise and growth of the Tibetan Plateau: Science, v., 294, p. 1671-1677.

Weinberg, R.F., Dunlap, W.J. (2000). Growth and deformation of the Ladakh batholith, northwest Himalayas: implications for timing of continental collision and origin of calc-alkaline batholiths. Journal of Geology 108, 303–320.

Weinberg, R.F., Dunlap, W.J., Whitehouse, M. (2000). New field, structural and geochronological data from the Shyok and Nubra valleys, northern Ladakh: linking Kohistan to Tibet. In: Khan, .A., Treloar, P.J., Searle, M.P., Jan, M.Q. (Eds.), Tectonics of the Nanga Parbat Syntaxis and the Western Himalaya. Geological Society of London Special Publication, vol. 170, pp. 253– 275.

White, L.T., Ahmad, T.,Ireland, T.R., Lister, G.S., Forster,M.A. (2011). Deconvolving episodic age spectra from zircons ofthe Ladakh Batholith, northwest Indian Himalaya. Chemical Geology 289, 179–196.

Yamaguchi, Y., A. B. Kahle, H. Tsu, T. Kawakami, and M. Pniel (1998). Overview of Advanced Spaceborne Thermal Emission and Reflection Radiometer (ASTER), *Ieee T Geosci Remote*, *36*(4), 1062-1071, doi: 10.1109/36.700991.

9. Figures

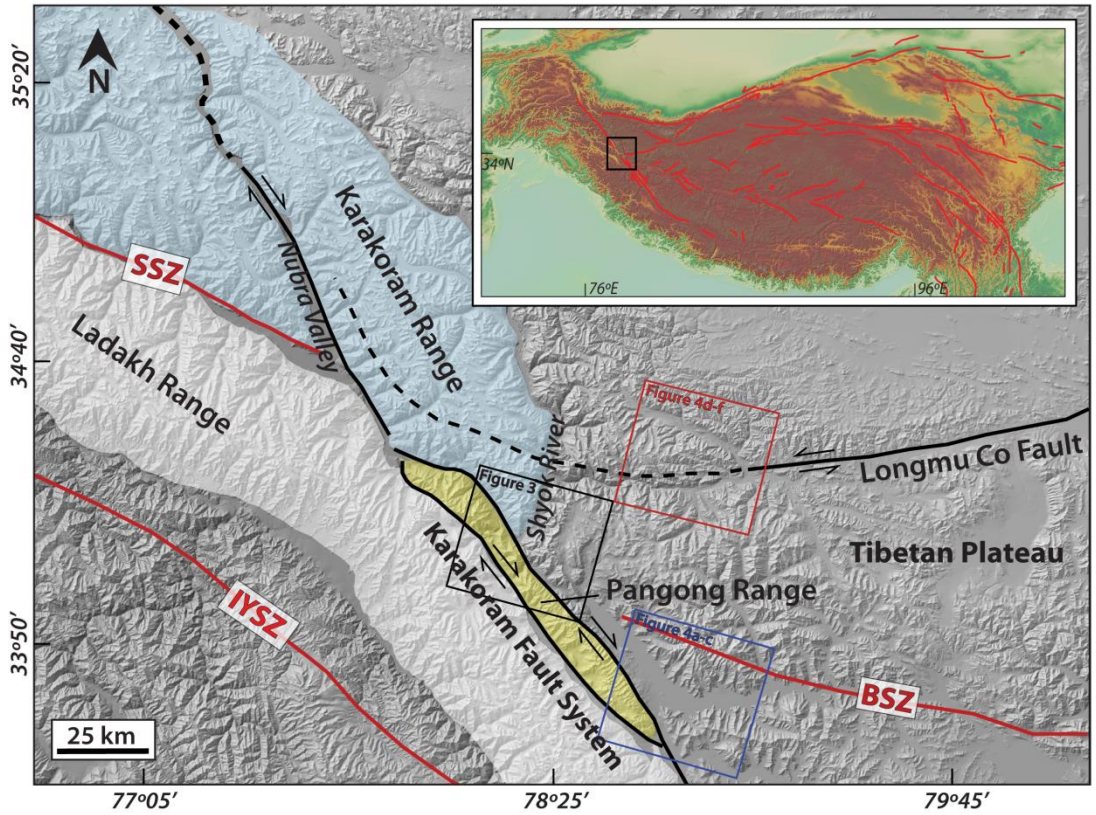

Figure 1. Simplified tectonic map of major features of the Ladakh region of northwest India over a hillshade DEM. Major faults are indicated by black lines and suture zones are indicated by red lines (SSZ - Shyok suture zone; IYSZ - Indus-Yarlung suture zone; BSZ - Bangong suture zone). The major mountain ranges discussed in this work have been shaded. Other structural provences and important locations are marked. The locations of Figures 3, 4a-c and 4d-f are indicated by colored boxes. Inset map shows transform faults within the Himalayan orogen (modified from Taylor and Yin, 2009). The black box in the inset shows the study location.

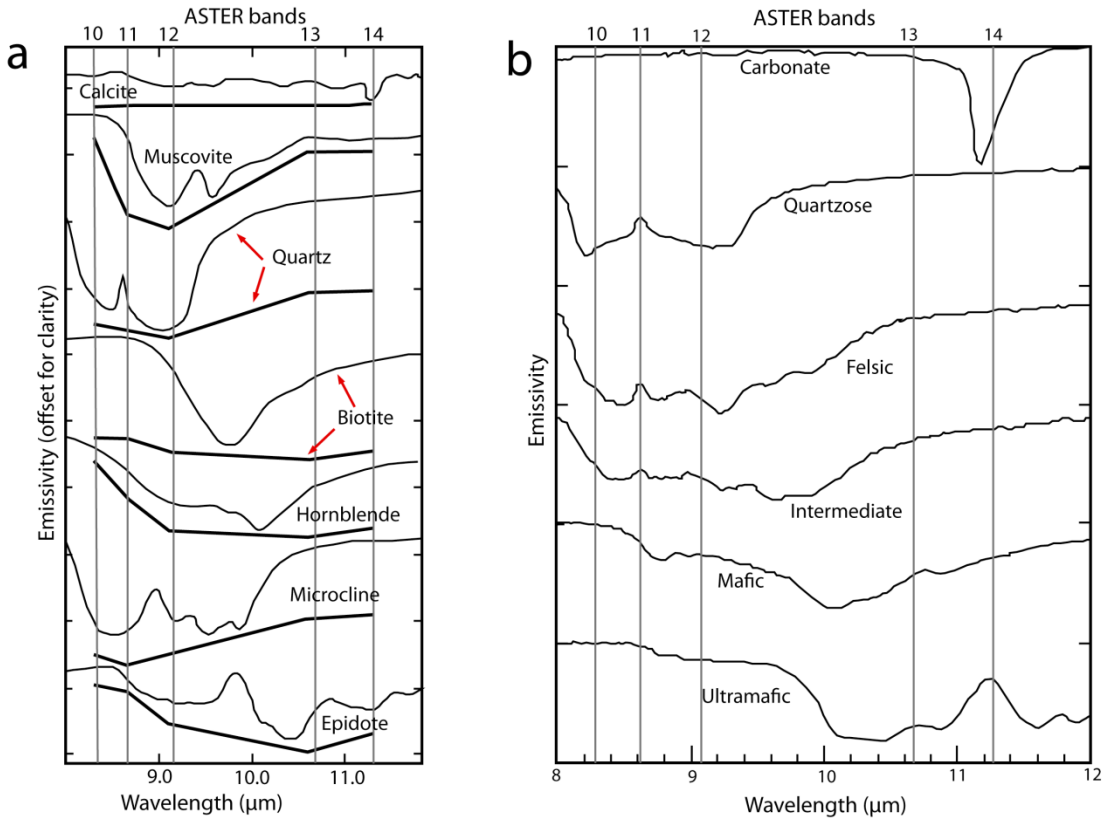

Figure 2. Emissivity spectra. Aster bands are indicated by thin gray lines. a) Emissivity spectra of common rock forming minerals from the ASTER standard product emissivity image (AST05). The top line in each pair is the laboratory derived spectrum and the darker bottom line is the same spectrum degraded to ASTER resolution. After Rowan and Mars (2002). b) Emissivity spectra for various rock types. Note that certain rock types have unique absorptions in some wavelengths. After Ninomiya et al. (2005).

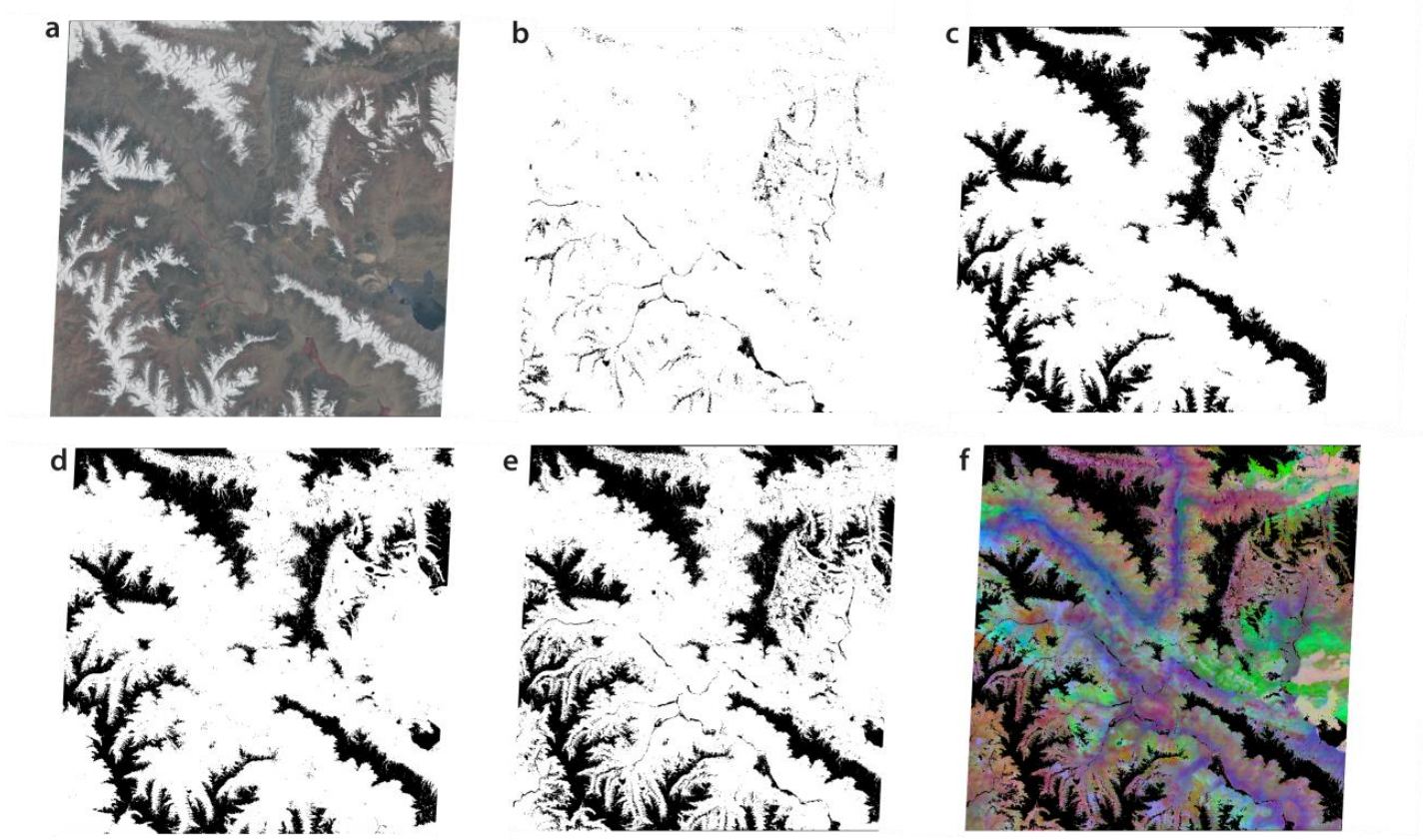

Figure 3. Examples of masks applied to an ASTER scene which shows the central Pangong Range. Black areas indicate pixels that have been "masked" or excluded from the scene. a) False color image for reference, b) NDVI - masks vegetation, c) NDSII - masks snow, ice and water d) CLOUD - masks clouds (and also some snow and ice), e) composite of all masks, f) composite of all masks applied to the same image to which a decorrelation stretched has been applied with bands 12-11-10 in the red, green and blue channels, respectively. Location of ASTER scene marked by a white box in Figure 1.

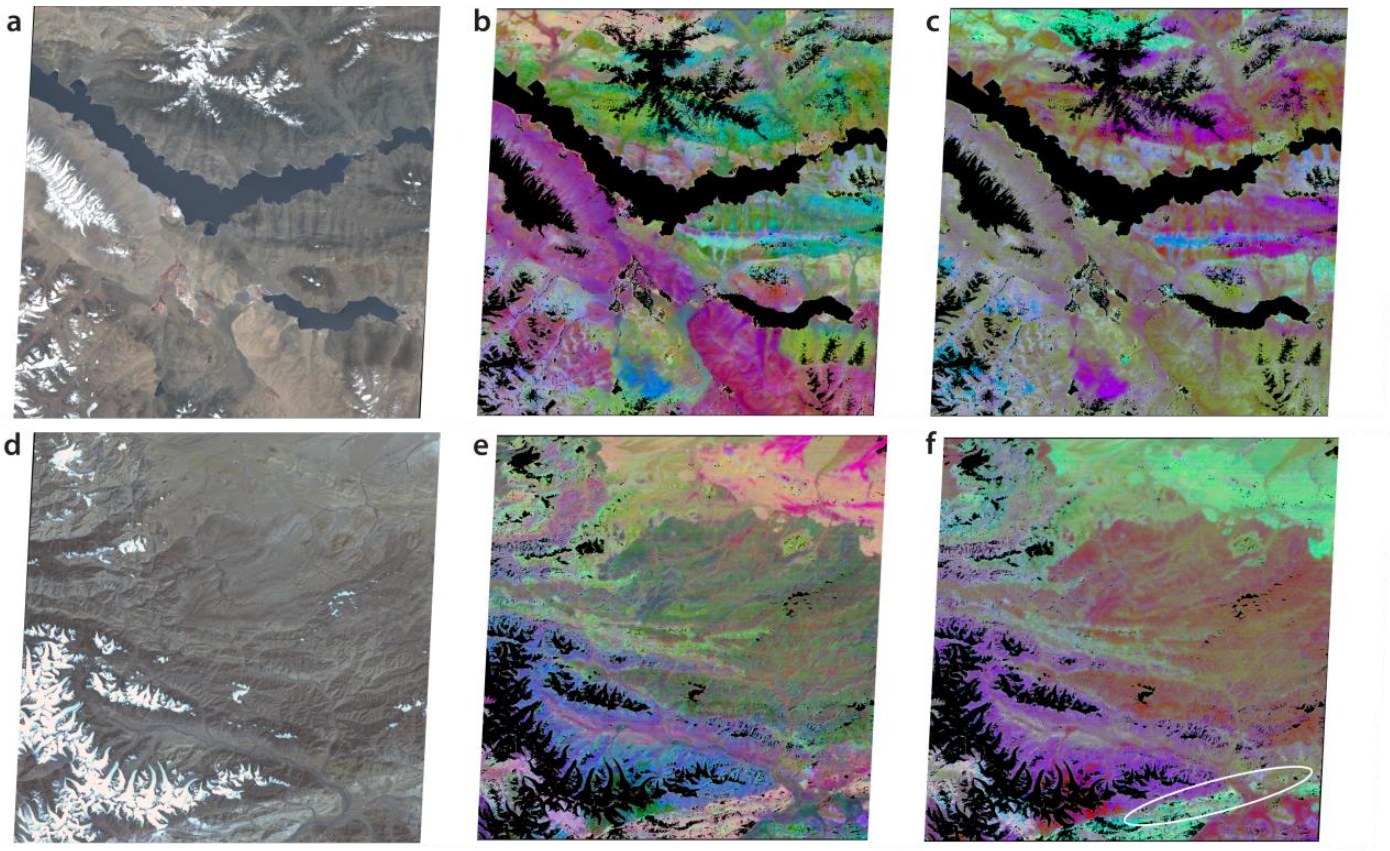

Figure 4. Two different ASTER scenes from the Ladakh region. The location of Figures 4a-c is shown as a blue box in Figure 1, and the location of Figures 4c-e is outlined by a red box. The images a and d are false color images (for reference). In images b and e we use a 12-11-10 stretch. In this stretch, carbonates and ultramafic rocks reflect all bands, and so appear peach/tan. Quartz-rich rocks will appear greenish and more mafic rocks will appear yellow. In images c and f we used a 14-12-10 decorrelation stretch, which is ideal for locating carbonate due to its strong absorption feature at band 14 (Figure 2). Because carbonate is absorbed at band 14, it manifests as blue-green in this stretch. Mafic and ultramafic rocks appear white or washed out and felsic rocks will appear red. In Figures 4d and e note the crispness of the contact along the Longmu Co fault where the carbonate unit is juxtaposed against silicic rocks. (Circled with a white ellipse in 4f).

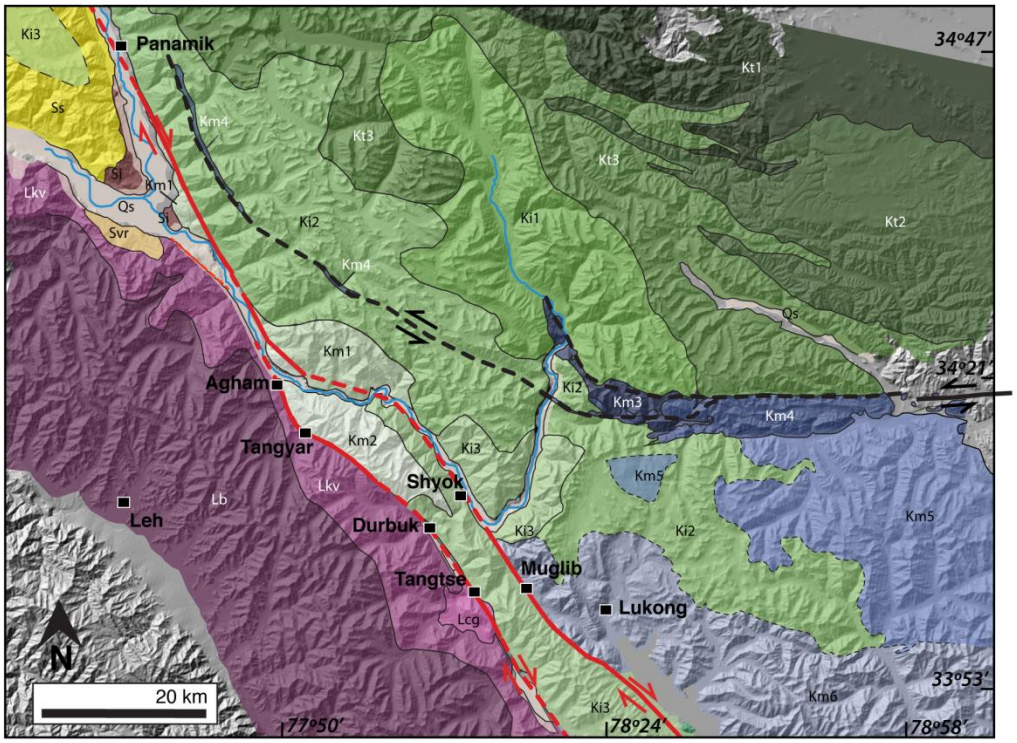

Karakoram Fault
Longmu Co Fault

Qs Quaternary sediments

Ladakh Complex

- Lcg Chilam granite
- Lkv Khardung volcanic units
- Lb Plutons of the Ladakh batholith

Suture Zone Complex

- Ssm Saltoro molasse
- Svr Volcanic rocks
- Si Intrusive igneous rocks

Karakoram Complex

Tethyan sedimentary domain

- Kt1 Predominantly calcareous sedimentary rocks with some chert
- Kt2 Predominantly volcaniclastic and clastic sedimentary rocks
- Kt3 Predominantly clastic sedimentary rocks

Karakoram batholith and proximal country rocks

- Ki1 Plutons interspersed with metasmorphic rocks
- Ki2 Karakoram granitic rocks; gradational contact with Ki3
- Ki3 Amphibolites, calc-silicates and migmatites with granitic intrusions

Metamorphic domain

- Km1 Metapelitic schists, volcanics and marbles
- Km2 Schists, calc-silicates marble & amphibolite bands
- Km3 Calcareous schists and calc-silicate gneisses, highly strained
- Km4 Impure marbles, highly strained
- Km5 Clastic metasedimentary rocks
- Km6 Volcanoclastic and clastic sedimentary rocks with ophiolitic blocks and carbonate bands

Unmapped regions

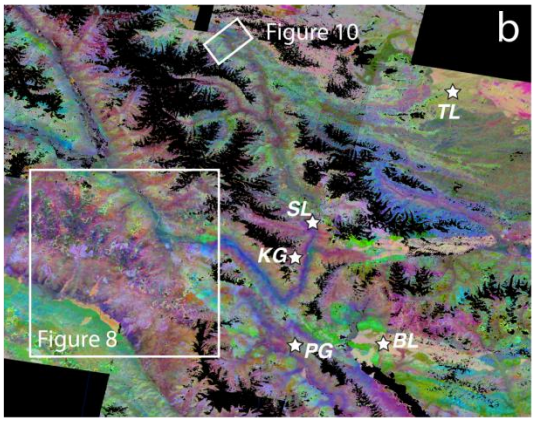

Figure 5. a) Lithologic map of the Ladakh region created from a combination of field work and ASTER remote sensing data overlaid on a 30 m hillshade map. Black squares mark villages. The units on the left correspond to Figure 5a. The black box shows the extent of Figure 3. b) ASTER decorrelation stretch 12-11-10 showing the same extent as the map in 5a. This stretch highlights differences in the amount of quartz present in the rocks. In this case pink indicates silicic rocks, blue indicates more mafic rocks and tan/peach shows carbonates. Various stretches were used while mapping to accentuate differences in mineral composition. The black areas are regions of snow, ice, water, clouds, or vegetation that have been removed.

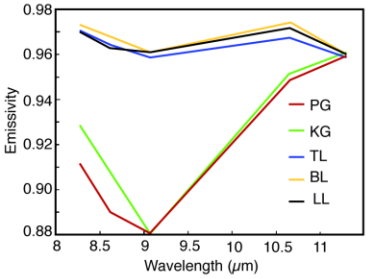

Figure 6. Examples of spectra from ASTER images. PG and LL were verified in the field as being a granite and a limestone, respectively. We were not able to access the rocks of KG, TL and BL. However, based on similar spectral characteristics to our field located outcrops we were able to assign lithologies to these units. Note the similarities in spectral shape between units of the same rock type. PG - Granite in the Pangong Range; KB - Granite in the Karakoram Range; TL - Tibetan limestone; BL - limestone in the Bangong Suture area; SL - limestone/skarn along the Shyok River. Locations shown in Figure 5b.

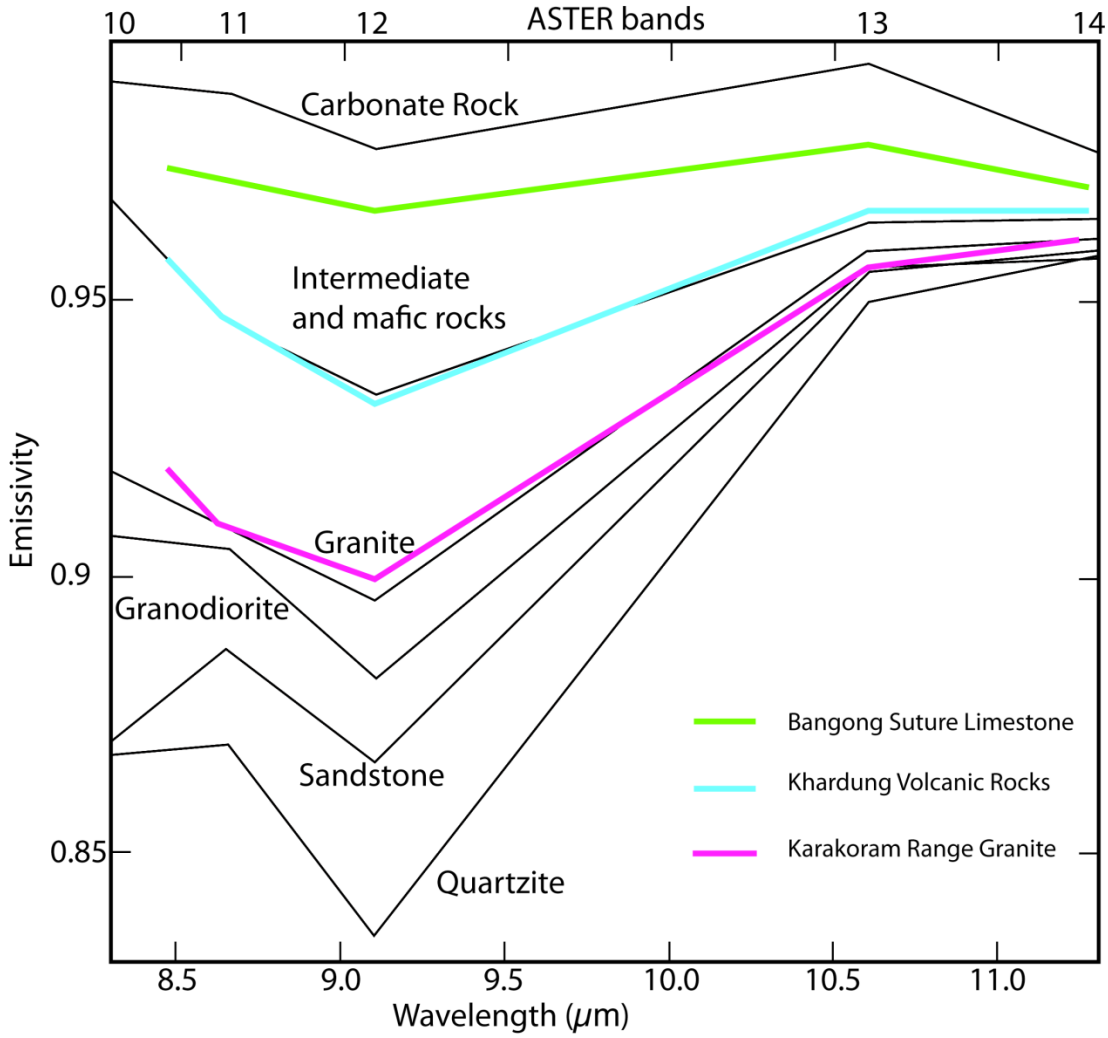

Figure 7. Emissivity spectra. Black lines show the emissivity spectra of common rock types derived from the ASTER emissivity image (AST05) from Mountain Pass, California (Rowan and Mars, 2002). The colored lines show spectra derived from the AST05 images from the Ladakh region of NW India.

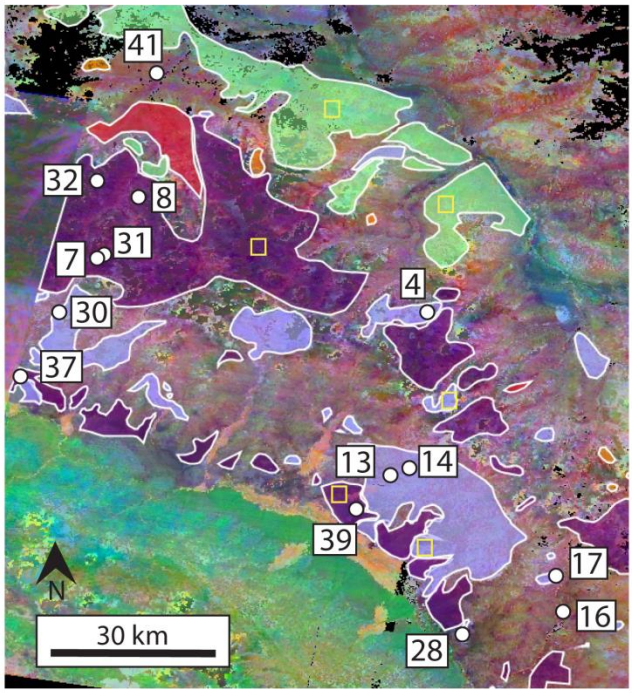

Figure 8. ASTER image of the central Ladakh Batholith showing areas of compositional variability. A decorrelation stretch has been applied with bands 12, 11 and 10 set in the red, green and blue channels, respectively. Overlain are mapped interpretations of compositional differencs based on color differences. Three main color fields are mapped (purple, pink and green) as well as two secondary fields (red and orange). Locations of samples collected in the field are indicated by the white dots, numbers are the sample names. Locations of colored regions sampled for Figure 9 are indicated by boxes outlined in yellow. For illustrative purposes these boxes are larger than the 10 x 10 pixels average in each location.

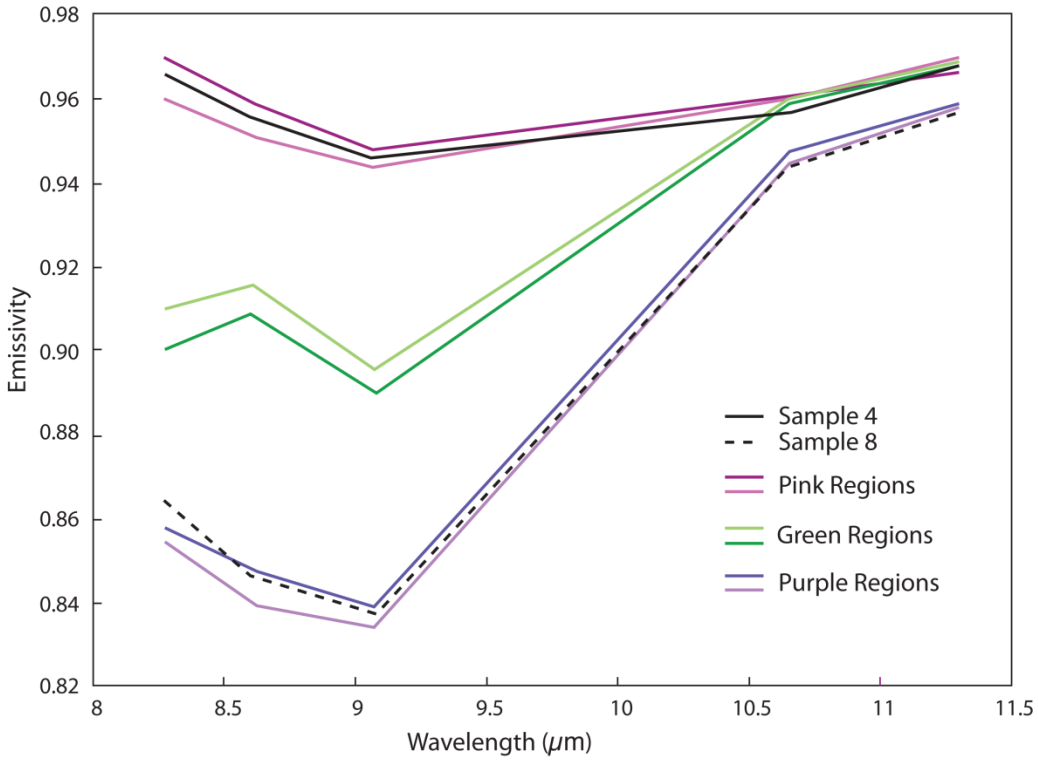

Figure 9. Spectra collected from ASTER data from the 3 different color regions within the Ladakh Batholith (Figure 8). Two samples from each color were pixel averaged (10 x 10 pixels)-sampled regions shown in Figure 8. The difference in spectra between the different regions indicate compositional differences within the batholith. Also plotted are spectra from two different areas that were sampled in the field (Figure 8). Sample 4 is from a "pink" area, while Sample 8 is from a "purple" area.

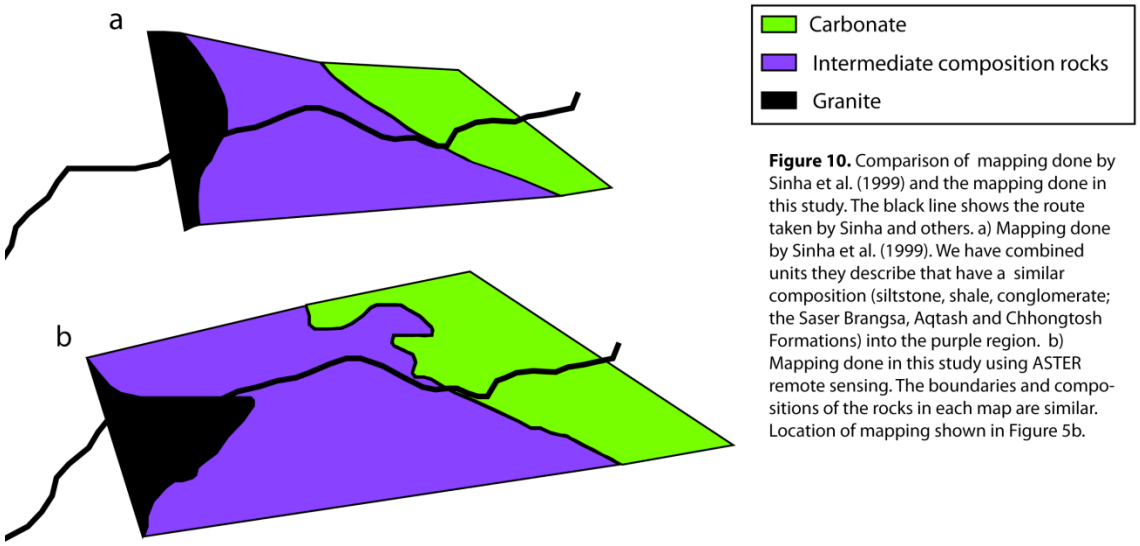

Figure 10. Comparison of mapping done by Sinha et al. (1999) and the mapping done in this study. The black line shows the route taken by Sinha and others. a) Mapping done by Sinha et al. (1999). We have combined units they describe that have a similar composition (siltstone, shale, conglomerate; the Saser Brangsa, Aqtash and Chhongtosh Formations) into the purple region. b) Mapping done in this study using ASTER remote sensing. The boundaries and compositions of the rocks in each map are similar. Location of mapping shown in Figure 5b.

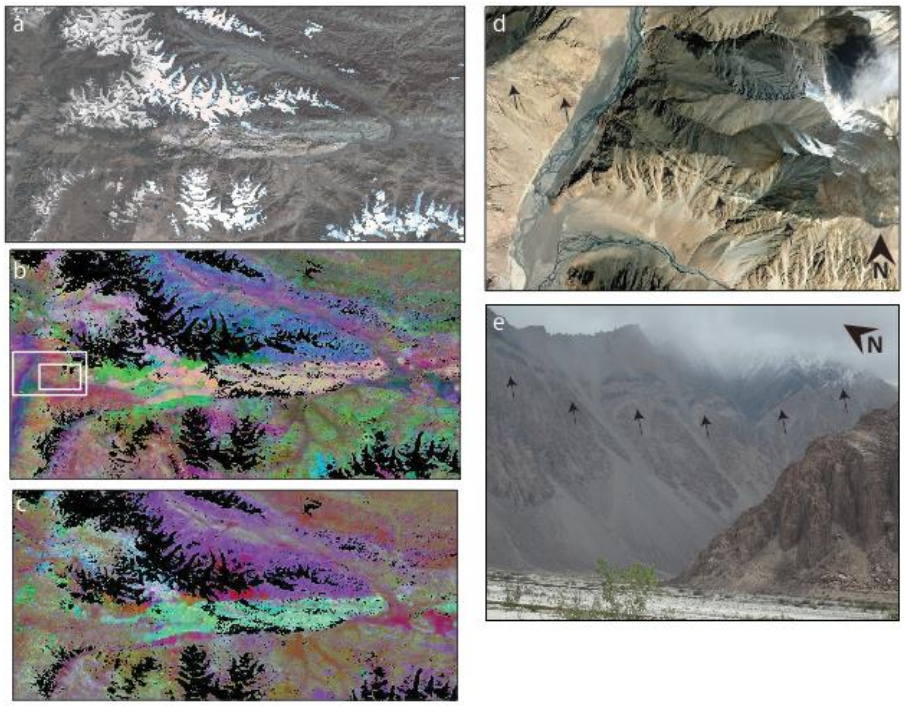

Figure 11. Stretched ASTER images, a Google Earth image and a field photo of the trace of the Longmu Co Fault. a) False color image for reference, b) 12-11-10 stretch. The peach/white unit is a carbonate tracer unit marking the Longmu Co fault system. The large white box shows the location of Figure 11d, the small white box shows the location of Figure 11e. c) 14-12-11 stretch of the same region. d) Google Earth image of the Longmu Co fault which is marked by the Km4 unit, indicated by arrows, e) Field photo of the Longmu Co fault in the same area as Figure 11d. Note the black and white banding of unit Km4 (marked by arrows).

CHAPTER 3

REFINING ESTIMATES OF QUATERNARY SLIP ALONG THE KARAKORAM FAULT SYSTEM, LADAKH, NORTHWEST INDIA

1. Abstract

The NW-SE–striking, dextral Karakoram fault system (KFS) stretches for more than 1200 km and is one of the major tectonic features of the Himalayan orogenic system. Published estimates of Quaternary slip along the fault range from 1 to 30 mm/yr. The slip rate along this structure has implications for geodynamic models of the India-Eurasian system, regional tectonic evolution, and earthquake hazard. In the Ladakh region of NW India, the KFS expresses as northern and southern strands bounding the Pangong Range. A lack of documented Quaternary offset along the southern fault strand has led previous researchers to assume that Quaternary KFS slip in this region was partitioned exclusively to the northern fault strand. We present new evidence of late Quaternary deformation along the southern strand that requires a revised interpretation of the Quaternary slip history of the KFS fault system in NW India. We estimate an average late Quaternary slip rate for the KFS between 33.9 ka and 5.7 ka of 4.4 to 7.5 mm/yr, higher than previously published estimates. However, the slip rate apparently dropped to ~ 4mm/yr afterwards, consistent with previously published estimates. These revisions at least partially mitigate apparent along-strike inconsistencies between Quaternary slip-rate estimates for the KFS in NW India and western Tibet.

2. Introduction

Assessing the role played by major transcurrent faults in orogenic systems – as relatively minor discontinuities in an otherwise diffusely deforming medium, or as first-order boundaries effectively separating microplates – is an important step toward achieving a better understanding of the rheological behavior of continental crust during orogenesis. Tests of competing hypotheses regarding the role of transcurrent faulting in these settings derive from the predictions they make regarding fault-system longevity, total amounts of slip, and secular variations in slip rate. However, measuring and comparing slip rates over different time scales using different techniques is problematic, especially along the Karakoram fault system (KFS) in NW India (Murphy et al., 2002, 2010; Phillips et al., 2004; Searle and Phillips, 2007; Valli et al., 2008; Streule et al., 2009; Searle et al., 2010; Wang et al., 2012; Figure 1). Thought to have initiated in the Miocene, the KFS has accommodated substantial dextral slip during Himalayan-Tibetan orogenesis but estimates of the overall slip vary over an order of magnitude, from 120-170 km (e.g., Searle et al., 1998; Phillips et al., 2004; Robinson, 2009) to 1000 km or more (e.g., Avouac and Tapponnier, 1993; Tapponnier et al., 2001). Debate about estimates of Miocene-Pliocene slip rates along the fault is understandable; a lack of consensus regarding Quaternary slip rates less so. Based on all available Middle Pleistocene-recent slip rate data for the fault system, Houlie et al. (2013) posit that the KFS experiences substantial variations in seismic activity over millennial scales due to changing stress levels on the fault, which are partially controlled by varying seisimicity on the subducting Indian plate beneath western Tibet. They conclude that the KFS is

currently in a period of reduced activity. Most GPS and InSAR data imply that present-day motion along the KFS overall is between 1-3.4 mm/yr (Wright et al., 2004; Jade et al., 2004; Jade et al., 2010), although one earlier study estimated rates as high as 11+/1 mm/yr (Banerjee et al., 2002). Longer-term late Quaternary slip rates of ca. 15-32 mm/yr have been estimated by reconstructing offset geomorphic markers associated with the Last Glacial Maximum (Armijo et al., 1989; Avouac and Tapponnier, 1993). Geomorphically derived late Quaternary rates were estimated at ca. 4 mm/yr by Brown et al. (2002) along one portion of the KFS, but Chevalier et al. (2005, 2012) estimated rates of ca. 7-12 mm/yr 250 km along strike to the southeast.

Here we present new Quaternary rate constraints for a section of the KFS exposed along the Pangong Range of NW India (Figure 1). It has been known for many years that the Pangong Range is a transpressional range developed between two major strands of the KFS (e.g., Searle, 1998). Previous researchers have argued that Quaternary slip along the KFS in this area was restricted to the northeastern strand. We present evidence that the southwestern strand also has been active during the Quaternary, with a demonstrable dextral offset of 160 m. This amount of offset is comparable to that determined by Brown et al. (2002) for the northeastern strand, which formed the basis for their estimate of the Quaternary slip rate for the KFS. Our detailed study of the slip history of the southwestern strand was designed to test the hypothesis that both strands may have moved synchronously, such that their combined slip rates might be closer to that estimated for the KFS by Chevalier and co-workers (2005; 2012).

3. The Karakoram Fault System in Ladakh and Adjacent Tibet

The NW-SE striking, oblique, dextral KFS stretches for ~ 1000 km from the Pamirs of Central Asia at least as far southeast as the Gurla Mandata area of Tibet. It effectively serves as the southwestern boundary of the Tibetan Plateau. Some of the best exposures of the KFS occur in the Ladakh region of India, where the system bifurcates around the narrow, NW-SE–trending Pangong Range (Figure 1). Streule et al. (2009) suggested that the Pangong Transpressional Zone (PTZ) represents deeper structural levels of the Karakoram metamorphic and igneous complex that underlies most of the Karakoram Range to the NNW, and they followed earlier workers (e.g., Searle et al., 1998; Phillips and Searle, 2007) in interpreting the PTZ as having been extruded along the Karakoram fault system.

The NE and SW boundaries of the PTZ are referred to as the Pangong and Tangtse strands of the KFS, respectively (Figure 1). Phillips and Searle (2007) described a variety of deformation features along both strands, including SC fabrics, asymmetric boudins, and stretching lineations consistent with the known dextral oblique shear sense of the KFS. No significant low-temperature tectonites have been found in the bedrock outcrops of the Tangtse strand, but they are well developed along the Pangong strand. Described in detail by Rutter et al. (2007), they include marble cataclasites and clay-bearing fault gouges that overprinted pre-existing ductile fabrics during transpressive uplift.

The youngest deformation features in the Pangong Range are Quaternary fault scarps that bound the range itself. The only previous study of these features was done by Brown et al. (2002; Figure 1), who documented late Quaternary right-lateral slip along

the Pangong strand using two offset debris flows (displaced 1-2 m and 40 ± 5 m). These features were dated using cosmogenic radionuclides, which yielded ages of 1-2 ka for the debris flow offset less and 11-14 ka for the debris flow showing the larger offset. Together, these results are consistent with a time-averaged slip rate of 4 ± 1 mm/yr. However, Brown et al. reported finding no evidence of Quaternary deformation along the Tangtse strand of the KFS. This, and the lack of cataclastic rocks in bedrock outcrops along that strand, have led a variety of workers (e.g., Rutter et al., 2007) to infer that all of the recent slip on the KFS through the Pangong region has been concentrated along the Pangong strand. Our recent work along a relatively remote section of the Tangtse strand demonstrates that this is not the case.

4. Late Quaternary Slip along the Tangtse strand

Most previous investigations of the Tangtse strand focused on exposures near the village of Tangtse (Figure 1), where – in places not obscured by very young fluvial sediments – it juxtaposes PTZ rocks against igneous rocks of the Upper Cretaceous-Paleocene Ladakh arc to the south. As we traced this structure to the northwest, where it ultimately marks a boundary between the PTZ and older Quaternary units, we found evidence of Quaternary deformation, particularly in the fault-controlled Tangyar Valley, near the NW terminus of the Tangste strand where it converges with the Pangong strand (Figure 1).

Near the village of Agham, the Tangtse strand changes orientation along strike from south to north from a steeply dipping, oblique-dextral fault to a shallowly east-dipping (30°- 50°) thrust fault that places Karakoram metamorphic complex marbles over

poorly consolidated alluvium of possible Quaternary age (Figure 2). The local thrust fault geometry of this otherwise steeply dipping fault reinforces the structural complexity of the previously poorly mapped northwestern end of the Pangong Range: despite the long, Miocene-Quaternary history of the Tangtse strand as a predominantly dextral-slip structure, the thrust sense motion observed for the SW fault termination may suggest a very recent local reversal in vergence of the structure

Further SE along the valley, we conducted detailed field mapping of landforms disrupted by fault movement (Figure 3a and 3b): an offset alluvial fan surface (Q4-6), a debris-flow–dominated surface, and a series of fluvial terraces including the modern stream channel (Q1-3). The Q5 alluvial fan surface has incised terraced risers that have been offset 160 ± 10 m horizontally and 24 ± 4 m vertically with the east side up (P1-P1'), consistent with the transpressional sense of motion for the fault system in this region. These offset amounts are maximum values, and the uncertainty is related to measurement error only.

Field mapping shows that this surface and the southwest-facing scarp exposed by fault offset are progressively more eroded towards the southeast (Figure 4 between P1 and P1'). The amount of scarp degradation and debris covering the inferred fault trace is consistent with an extended period of inactivity along the fault since the creation of the modern landform. In order to explore progressive slip along the fault, we generated a series of reconstructions of the offset Q5 surface (Figure 4). These reconstructions were created by using drainage patterns, prominent landforms, and relative elevations as markers. Our procedure involved backslipping of the Q5 surface to match features across the fault consistent with the offset and geomorphic modification of the scarp (Figure 4).

We started with the modern landform and backslipped the Q5 surface in three steps. In Step 1 (Figure 4b) the landform was backslipped 50 m horizontally and 8 m vertically. The first marker used to facilitate the reconstruction of this step was an area of reworked Q5o alluvium southwest of the fault trace which had no upslope source-we matched this with a region of Q5o northeast of the fault trace. We also identified a channel to the northeast of the fault trace that was overdeepened as compared to the apparent continuation of the channel across the fault. About 52 m northwest on the southwest side of the fault trace we observed a channel with a similar channel shape and depth that had no clear upstream equivalent. Given the similarities in the channels as well as the similar amount of offset to the Q5o reworked alluvium we also judged this channel to be a piercing point. In Step 2 (Figure 4c), the landforms were offset 105 m horizontally and 17 m vertically. The main markers used for reconstruction were elevations across the fault trace, however, we identified series of drainages and ridges that matched across the fault. The most prominent of these is marked by a purple dot in Figure 4c. In Step 3 the feature was backslipped a total of 160 m horizontally and 24 m vertically. This final step matches the steep southeastern to southern facing edges of the alluvial fan surface across the fault. Based on measurements made in the field we consider the error on this offset to be ± 5m. However, because of the curvature of the alluvial scarps north and south of the fault trace and the amount of degradation of each scarp we expand this error to ± 10m. This accounts for the full range of measurement error from the field and in subsequent satellite based mapping.

To the southeast of the alluvial fan surface is a lower, younger debris flow-dominated surface with levees roughly perpendicular to the fault trace (Figure 3). Some

of the debris flow levees appear to have been offset or deflected across the fault trace, with displacements between 1 and 3 m. However, other levees show no evidence of fault disruption (See Figure 3a for uninterpreted image). This implies that some debris flows were emplaced before or recently after surface faulting, while others were created after the last major surface rupturing event. Inset into the north-central part of the debris flow surface are a set of fluvial terraces (Q1-3) that show no evidence of offset, implying that they are younger than the last significant earthquake.

A complicating factor in the assessment of this landscape is that a trail – used by humans and animals – is evident along the fault trace in many locations. Earlier workers, having seen this trail from a distance, may have assumed an anthropogenic origin for all linear features cutting across fans coming off the SW side of the Pangong Range. Such an assumption could explain why other workers might have missed geomorphic signs of Quaternary activity. Detailed field study, however, clearly demonstrates that the trail deviates from strict adherence to the fault trace. Our documentation of offset features and fault-modified topography, all indicative of a consistent, right-lateral, oblique sense of fault motion, confirms Quaternary activity.

5. Methods

Like Brown and co-workers did while studying the Pangong strand, we turned to cosmogenic radionuclide (CRN) dating to constrain the ages of neotectonic landforms on the Tangtse strand in the Tangyar Valley. We collected samples from a cosmogenic

profile pit (CSPF) on the Q5 surface, as well as samples from boulders within the debris-flow field.

All quartz purification and sample chemistry for CRN dating were processed in the WOMBAT laboratory at Arizona State University using conventional mineral separation, quartz purification, and digestion techniques (Kohl and Nishizumi, 1992). We amalgamated, crushed and sieved each sample to obtain the 250–1000 μm fraction of rock. To clean the samples, sieved portions of the sediment were placed in aqua regia for at least 12 hours and then leached several times in a combination of HF and HNO_3. Quartz was then extracted using heavy liquid mineral separation. Quartz separates were spiked with ^{9}Be and digested using HF, $HCLO_4$ and HNO_3. We removed interfering cations and anions using column chromatography. Beryllium was extracted, oxidized, mixed with niobium powder and loaded into cathodes. $^{10}Be/^{9}Be$ ratios were measured via accelerator mass spectrometry at the Purdue Rare Isotope Measurement Laboratory at Purdue University (http://www.physics.purdue.edu/primelab/; Table 1).

6. Constraints on the Timing of Late Quaternary Activity

We can get a broad sense of the landscape age and evolution by evaluating the glacial history of the valley, because the offset geomorphic features in the Tangyar Valley were developed after glaciation. Quaternary glaciation in the region has been documented and dated by Dortch et al. (2010). Their work indicates that the valleys of the region were significantly modified and the valley floor piedmont landforms were reset during major late Quaternary glacial advances. Dortch et al. (2010) dated three stages of Quaternary glaciation in the nearby Shyok and Nubra valleys. The Tangyar

features occur at a similar elevation (4950 m), valley position, geomorphic setting, and in the same modern climate regime as features assigned by Dortch and co-workers to the ca. 107-157 ka Deshkit 3 glacial stage. However, we cannot preclude the possibility that they correlate instead to features belonging to the ca. 81±6 ka Deshkit 2 glacial stage. We thus assume the maximum age for the Quaternary geomorphic features cut by the Tangtse strand is between 157 and 75 ka. If the alluvial fan shown in Figure 2 is only slightly younger than 75 ka and offset 160 ± 10 m, the magnitude of its offset would imply a Quaternary slip rate if ca. 2.3 mm/a. An age slightly younger than 157 ka would imply a slip rate of ca. 1.1 mm/yr. This latter value is an absolute minimum slip rate for the Tangtse strand. While this approach allows for broad-brush assessments, CRN dating provides much better constraints on the age of offset landforms and thereby provides more robust slip rate values.

The landform with the largest offset is the Q5 surface of the alluvial fan (Figure 3a and 3b). To date this landform, a ^{10}Be profile pit was dug into the side of the alluvial fan terrace in an area that appeared to be geomorphically stable (Figure 5). Many clasts collected from the surface and near surface had partially-developed to well-developed pedogenic calcite coatings, also indicating reasonable surface stability. While lateral erosion of the alluvial riser is possible, it is unlikely to change the age results of the CRN dating, as it would expose more of the interior of the stable landform. The stratigraphy of the pit was logged and photographed (Figure 5), and quartz rich clasts (primarily quartzite and grandiorite) were preferentially sampled from horizons every ~40-60 cm from the surface to a depth of 190 cm (Table 1). These sampling horizons were generally limited to ± 3 cm. After the data was processed (see above) we used a Monte Carlo

simulation to generate 100 best-fit solutions for our ^{10}Be depth concentrations to determine the range of likely surface ages. We used the median value as our preferred age and the minimum and maximum best-fit solutions as our upper and lower bounds. (Methods are described in detail in the supplementary material; see also Braucher et al., 2009). The CRN data from the Q5 surface yielded a range of possible surface ages between 30.7 and 37.0 ka with a preferred age of 33.9 ka (Figure 6). If we use the 33.9 ka preferred age for the Q5 surface as a maximum constraint on the 160 ± 10 m horizontal and 24 ± 4 m vertical offsets of Q5, this implies a rate for the offset along this strand of ca. 4.6 to 4.9 mm/a integrated over the past 33.9 ka. However, it should be noted that the erosion rate parameter assumed to calculate the surface age was low. Dating of surfaces using CRN requires "reasonable inference of negligible erosion" (Gosse et al., 2001), however, some erosion of surfaces is expected. Thus, by choosing a low rate we account for some erosion of the surface, but do not violate one of the underlying assumptions of the CRN dating. Regardless, a low erosion rate will produce a minimum surface age and thus a maximum slip rate (see Supplemental Materials). It is possible that erosion on this surface is higher than our input value, which would increase the age of the Q5 surface bringing it closer to that of the ages found using the glacial bounds.

The debris flow-dominated surface to the southeast of the alluvial fan also shows evidence of offset (Figure 3a and 3b). Five boulders (Samples B1-4 and B6) from levees within the debris flow-dominated surface yielded exposure ages ranging from 5.7 ± 0.50 ka to 73 ± 6.5 ka; four yielded dates ≤ 12.6 ± 1.1 ka (Table 1). A good constraint on the slip rate for this surface is provided by the youngest ^{10}Be boulder age of 5.7 ka from sample B2. This sample was collected on a debris flow levee mapped as having been

offset between 1 and 3 meters, implying a slow horizontal offset over the past 5.7 ka: between about 0.2 and 0.5 mm/a of slip.

This suggests a temporal variation in slip rate between the two dated landforms with faster slip rates pre-5.7 ka. To better determine the older, faster slip rate we subtract the amount of offset accommodated by the debris flow surface and the time over which it accrued to find the faster, time-integrated slip rate for the offset Q5 surface. Applying this correction and employing the probabilistic approach outlined in Zechar and Frankel (2009), we find 5.6 +1.9/-1.2 mm/yr to be a maximum slip rate for this fault strand over the time interval 5.7 – 33.9 ka. (See supplementary material for a further discussion of the methodology.)

7. Implications

If the rate of deformation of the KFS in the study area were constant over any specified time interval during the Quaternary when both the Pangong and Tangtse strands were active, then the total slip rate for the system must be calculated as the sum of the slip rates on the two strands. Our data show that both strands were plausibly active during the same time interval. However, the debris flow offsets studied along the Tangtse strand record significantly less slip than did debris flow offsets studied by Brown et al. (2000) on the Pangong strand– ca. 3 m versus ca. 40 m of offset. Thus, it appears that the Pangong Strand has been the dominant strand during at least the last 12.6 ka. We speculate that one dextral fault strand was generally active at a time, but that the other strand may experience rare episodes of rupturing during that same interval, in some instances with kinematics locally different from dextral-oblique. (Such a scenario could

explain the Quaternary thrust-sense kinematics of the Tangtse strand near the NW end of the Pangong Range.) If we are correct, the Tangtse Strand was dominant before the deposition of the debris flow surface in our area dated at ≤12.6 ka. A similar variation in temporal slip accommodation is posited for the relationship between the sub-parallel San Jacinto and San Andreas fault systems in southern California (e.g., Sharp, 1981; Bennett et al., 2004). Explanations that have been put forth for rupture variation on parallel fault strands include changes in regional stress, the evolution of fault zone geometry (Bennett et al., 2004; Li and Liu, 2006) and preferred rupture propagation direction (Dor et al., 2006).

8. Conclusions

Slip rates proposed by Brown et al. (2002) for the Karakoram fault system in the Pangong region of Ladakh, India (ca. 4 mm/yr), are predicated on the assumption that the slip along the KFS in this region over the past ca. 14 kyr was accommodated exclusively along the Pangong strand of the fault system. Detailed mapping of a second major strand of the KFS in this region demonstrates that it too experienced significant late Quaternary slip, such that the 4 mm/yr value of Brown and co-workers is an underestimate for the period before slip was concentrated on the Pangong strand (≤12.6 ka). Our work suggests the prior slip rate along the Tangtse strand was as high as 5.6 +1.9/-1.2 mm/yr, which approaches the lower limit of the rates found by Chevalier et al. (2005) in the south. Evidence for partitioning of slip through time suggests that the late Quaternary history of this fault system is more complex than previously believed. Ultimately, a more

comprehensive, along-strike neotectonic dataset will be required to fully understand the temporal evolution of deformation on the Karakoram fault system.

9. References

Anderson, R. S., Repka, J. L., and Dick, G. S., 1996, Explicit treatment of inheritance in dating depositional surfaces using in situ 10Be and 26Al, Geology, 24, 47–51.

Armijo, R., Tapponnier, P., and Tonglin, H., 1989, Late Cenozoic right-lateral strike-slip faulting in southern Tibet: Journal of Geophysical Research–Solid Earth and Planets, v. 94, p. 2787–2838.

Avouac, J. P., and Tapponnier, P., 1993, Kinematic model of active deformation in central Asia: Geophysical Research Letters, V. 20, p. 895-898.

Balco G, Stone JO, Lifton NA, Dunai TJ. 2008. A complete and easily accessible means of calculating surface exposure ages or erosion rates from 10Be and 26Al measurements. Quaternary Geochronology 8: 174–195.

Banerjee, P., B¸rgmann, R., 2002, Convergence across the northwest Himalaya from GPS measurements, Geophysical Research Letters 29, 13.

Bennett, R. A., A. M. Friedrich, and K. P. Furlong (2004), Codependent histories of the San Andreas and San Jacinto fault zones from inversion of fault displacement rates, Geology, 32, 961 – 964

Braucher, R., P. Del Castillo, L. Siame, A. J. Hidy, and D. L. Bourles, 2009, Determination of both exposure time and denudation rate from an in situ-produced 10Be depth profile: A mathematical proof of uniqueness. Model sensitivity and applications to natural cases, Quat. Geochronol., 4, 56–67.

Brown, E. T., Bendick, R., Bourles, D. L., Gaur, V., Molnar, P., Raisbeck, G. M., and Yiou, F., 2002, Slip rates of the Karakoram Fault, Ladakh, India, determined using cosmic ray exposure dating of debris flows and moraines: Journal of Geophysical Research, v. 107.

Cerling, T.E., Craig, H., 1994. Geomorphology and in-situ cosmogenic isotopes. Annual Reviews of Earth and Planetary Sciences 22, 273-317.

Chevalier, M. L., Ryerson, F. J., Tapponnier, P., Finkel, R. C., Van der Woerd, J., Li, H. B., and Li, Q., 2005, Slip-rate measurements on the Karakoram fault may imply secular variations in fault motion, Science 307, no. 5708, 411-414.

Chevalier, M.-L., Tapponnier, P., Van Der Woerd, J., Ryerson, F.J., Finkel, R.C., and Li, H. (2012). Spatially constant slip rate along the southern segment of the Karakorum fault since 200 ka. Tectonophysics, 530-531: 152-179.

Dor, O., Rockwell, T.K., Ben-Zion, Y., 2006b. Geological observations of damage asymmetry in the structure of the San Jacinto, San Andreas and Punchbowl faults in southern California: a possible indicator for preferred rupture propagation direction. Pure and Applied Geophysics 163 (2–3), 301–349.

Dortch, J.M., Owen, L.A., Caffee, M.W., 2010. Quaternary glaciation in the Nubra and Shyok valley confluence, northernmost Ladakh, India. Quat. Res. 74, 132-144.

Gosse, J. C., Phillips, F. M., 2001, Terrestrial in situ cosmogenic nuclides: theory and application. Quaternary Science Reviews 20, 1475–1560.

Houlie, N., and Phillips, R.J., 2013, Quaternary rupture behaviour of the Karakoram Fault and its relation to the dynamics of the continental lithosphere, NW Himalaya-Western Tibet, Tectonophysics, 599, 1-7.

Jade, S., Bhatt, B. C.,Yang, Z., Bendick, R., Gaur, V. K., Molnar, P. , Anand, M. B., and Kumar, D., 2004, GPS measurements from the Ladakh Himalaya, India: Preliminary tests of plate-like or continuous deformation in Tibet, Geological Society of America Bulletin, 116, 1385 – 1391.

Jade, S., Rao, R., Vijayan, H. J., Gaur, M. S. M., Bhatt, V. K., Kumar, B. C., Jaganathan, K., Ananda, , S., and Kumar, M. B., 2010, GPS-derived deformation rates in northwestern Himalaya and Ladakh, International Journal of Earth Science, Volume 100, Number 6, 1293-1301.

Kohl, C.P. and Nishizumi, K., 1992, Chemical isolation of quartz for measurement of in situ produced cosmogenic nuclides., Geochemica et Cosmochemica Acta, 56: 3583–3587.

Li, Q., and M. Liu (2006), Geometrical impact of the San Andreas Fault on stress and seismicity in California, Geophys. Res. Lett., 33, L08302.

Murphy, M. A., Yin, A., Kapp, P., Harrison, T. M., Manning, C. E., Ryerson, F. J., Ding L., and Guo, J.H., 2002, Structural evolution of the Gurla Mandhata detachment system, southwest Tibet: implications for the eastward extent of the Karakoram fault system, Geological Society of America Bulletin, 114, pp. 428–447.

Murphy, M. A., V. Sanchez, and M. H. Taylor (2010), Syncollisional extension along the India-Asia suture zone, south central Tibet: Implications for crustal deformation of Tibet, Earth Planet. Sci. Lett., 290(3–4), 233–243.

Phillips, R. J., Parrish, R. R., and Searle, M. P., 2004, Age constraints on ductile deformation and long-term slip rates along the Karakoram fault zone, Ladakh: Earth and Planetary Science Letters, v. 226, no. 3-4, p. 305-319.

Phillips, R. J., and Searle, M. P., 2007, Macrostructural and microstructural architecture of the Karakoram fault: Relationship between magmatism and strike-slip faulting: Tectonics, v. 26.

Robinson, A. C, 2009, Geologic offsets across the northern Karakorum fault: Implications for its role and terrane correlations in the western Himalayan-Tibetan orogen: Earth and Planetary Science Letters, v. 279, no. 1-2, p. 123-130.

Rutter, E. H., Faulkner, D. R., Brodie, K. H., Phillips, R. J., Searle, M. P., 2007, Rock deformation processes in the Karakoram Fault zone, Eastern Karakoram, Ladakh, NW India, Journal of Structural Geology v. 29, 1315-1326.

Searle, M. P., Weinburg, R. F. and Dunlap, W. J., 1998, Transpressional tectonics along the Karakoram fault zone, northern Ladakh: Constraints on Tibetan extrusion, in Holdsworth, R.E., et al., eds., Contential transpression and transtension tectonics: Geological Society [London] Special Publication 135, p. 307-326.

Searle, M.P., Parrish, R.R., Thow, A.V., Noble, S.R., Phillips, R.J. & Waters, D.J. 2010. Anatomy, age and evolution of a collisional mountain belt: the Baltoro granite batholith and Karakoram MetamorphicComplex, Pakistani Karakoram. Journal of the Geological Society, London, 167, 183-202.

Sharp, R. V. (1981), Variable rates of late Quaternary strike slip on the San Jacinto fault zone, southern California, J. Geophys. Res., 86, 1754 –1762.

Struele, M. J., Phillips, R. J., Searle, M. P., Waters, D. J., Horstwood, M.S.A., 2009, Evolution and chronology of the Pangong Metamorphic Complex adjacent to the Karakoram fault, Ladakh: constraints from thermobarometry, metamorphic modeling

and U-Pb geochronology, Journal of the Geological Society; September 2009; v. 166; no. 5; p. 919-932.

Tapponnier, P., Xu, Z.Q., Roger, F., Meyer, B., Arnaud, N., Wittlinger, G., and Yang, J.S., 2001, Oblique stepwise rise and growth of the Tibetan Plateau: Science, v., 294, p. 1671-1677.

Wang, H., Wright, T.J. (2012). Satellite geodetic imaging reveals internal deformation of western Tibet. Geophys. Res. Lett. 39, L07303.

Wright, T. J., Parsons, B., England, P. C., and Fielding, E. J., 2004, InSAR observations of low slip rates on the major faults of western Tibet: Science, v. 305, p. 236-239.

Valli, F., HervÈ Leloup, P., Paquette, J.-L., Arnaud, N., Li, H., Tapponnier, P., Lacassin, R., Guillot, S., Liu, D., Deloule, E., Xu, Z., MahÈo, G., 2008. New U**e**Th/Pb constraints on timing of shearing and long-term slip-rate on the Karakorum fault. Tectonics 27.

Zechar, J.D., Frankel, K.L., 2009. Incorporating and reporting uncertainties in fault slip rates. J. Geophys. Res. 114.

10. Figures

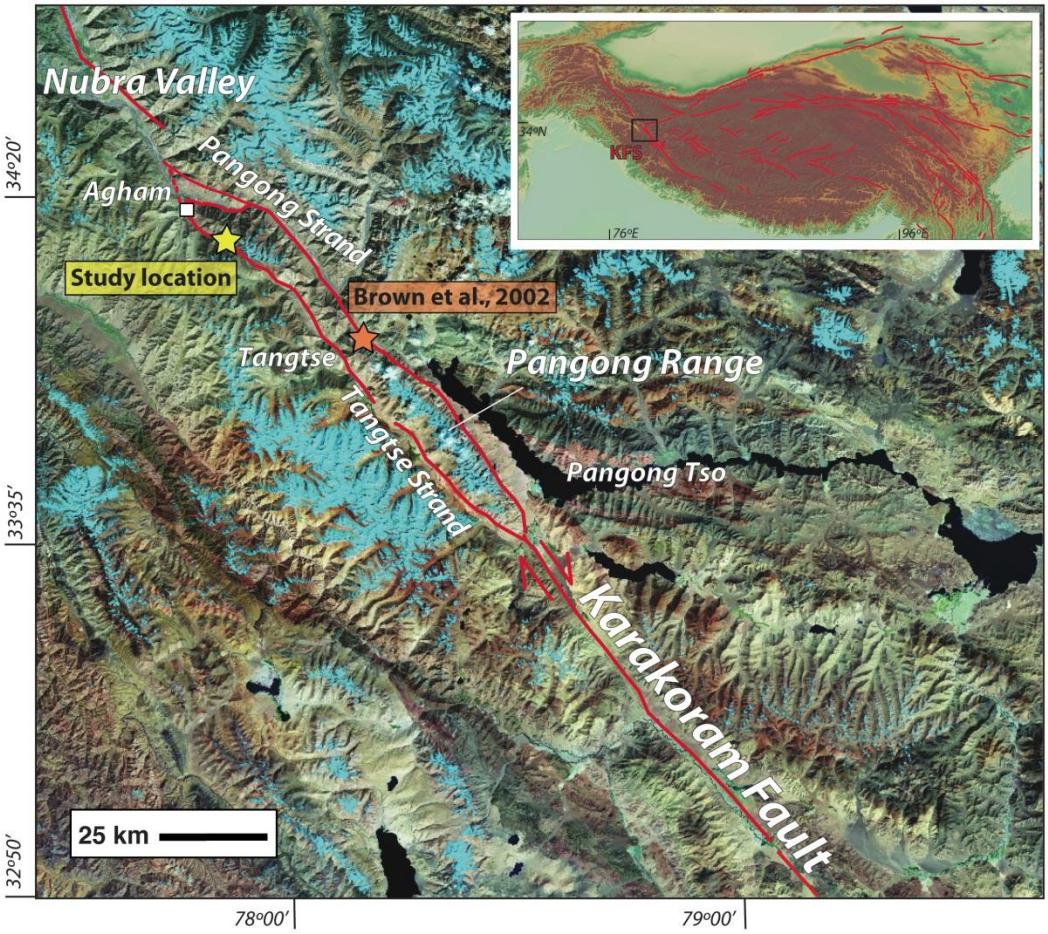

Figure 1. Central sector of Karakoram Fault with locations of slip rate studies. The orange star marks the location of the study by Brown et al., 2002, and the yellow star marks the location of this study in the Tangyar Valley. The white box shows the location of Figure 2. The background is Geocover Landsat 2000; https://zulu.ssc.nasa.gov/mrsid/mrsid.pl. The inset shows strike-slip faults of the India-Eurasia collision (modified from Taylor and Yin, 2009). Black box shows the extent of the Landsat image.

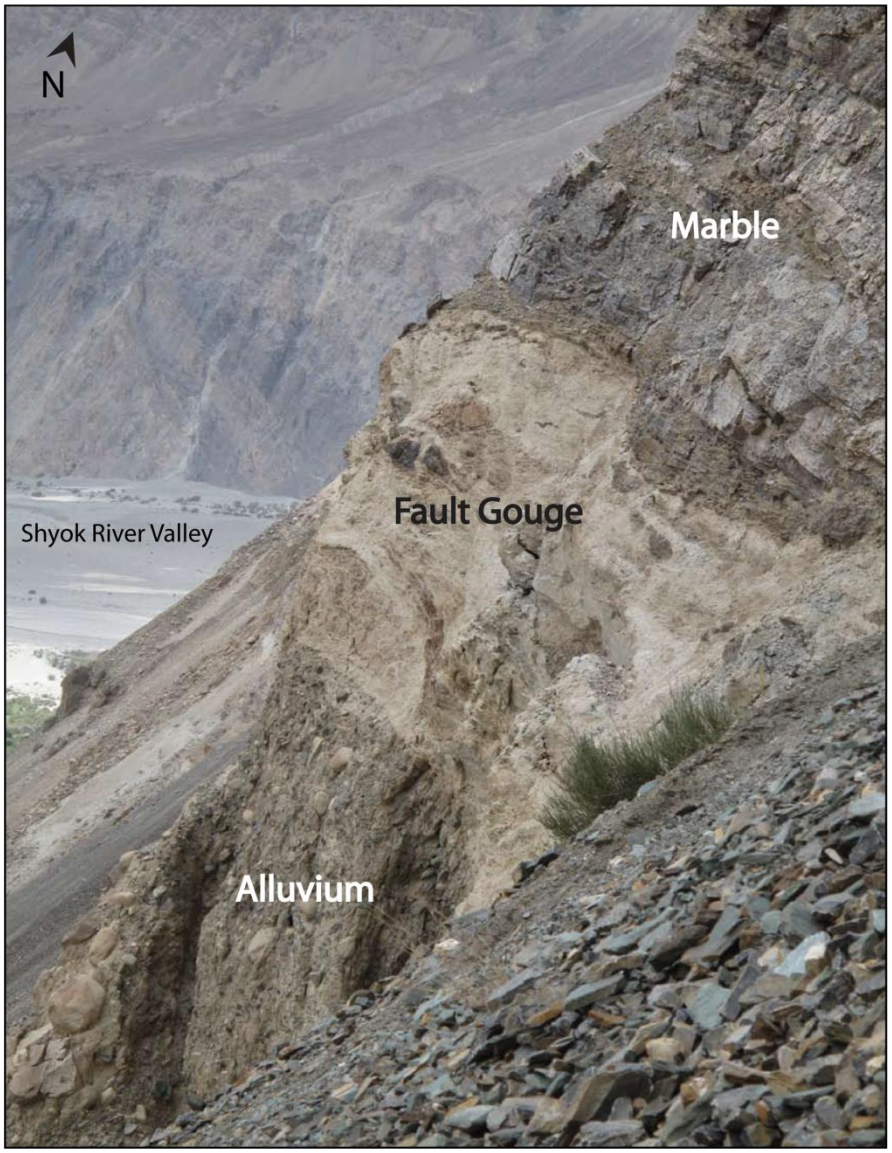

Figure 2. Exposure of the Karakoram fault system just east of Agham (Figure 1). In this location the KFS is a shallowly east-dipping (30°- 50°) thrust fault that places Karakoram metamorphic complex marbles over poorly consolidated alluvium. Fault gouge is ~2.5 m thick. View is to the north.

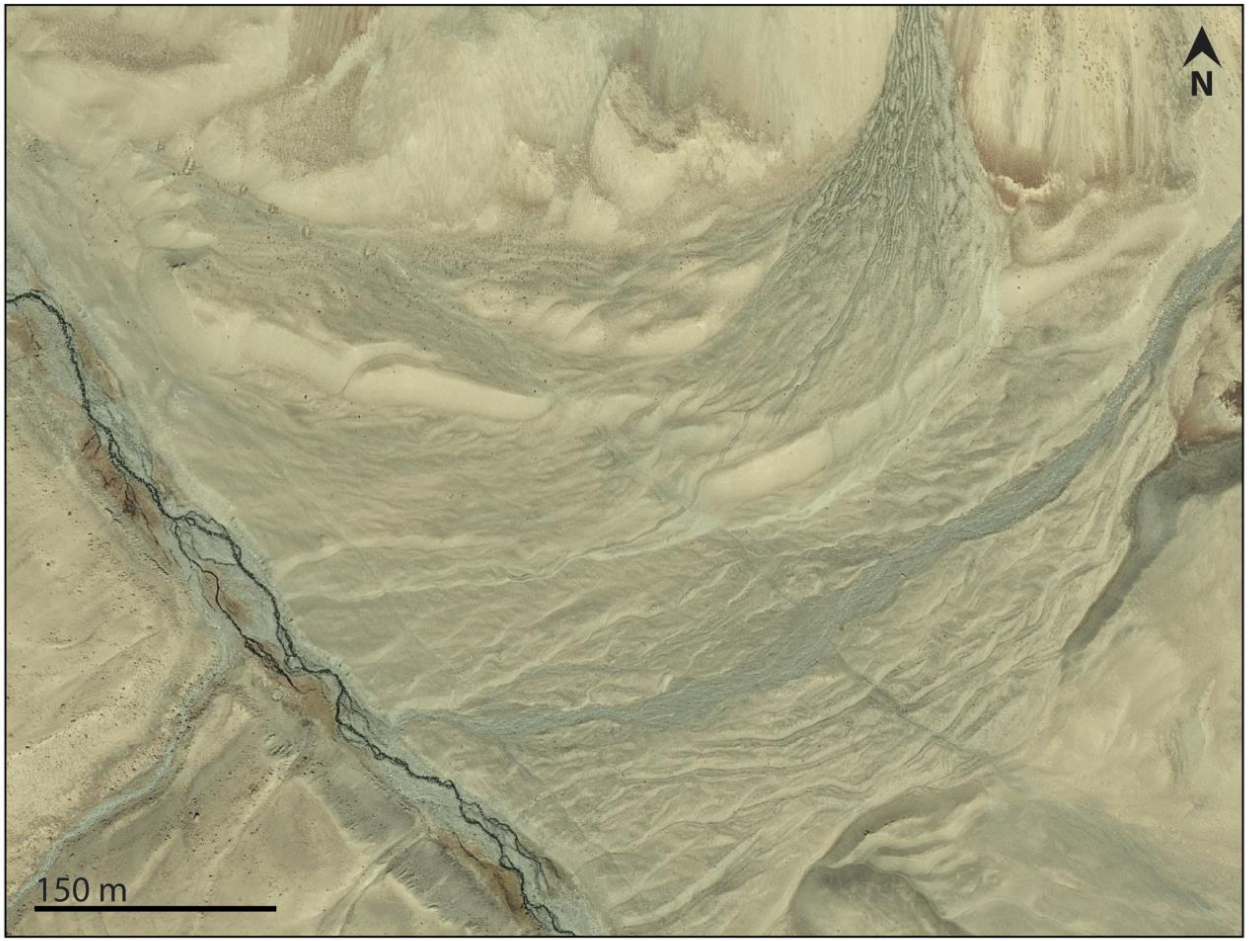

Figure 3a. Uninterpreted Google Earth image of offset landforms in the Tangyar Valley. See Figures 3b and 4 for geomorphic interpretations.

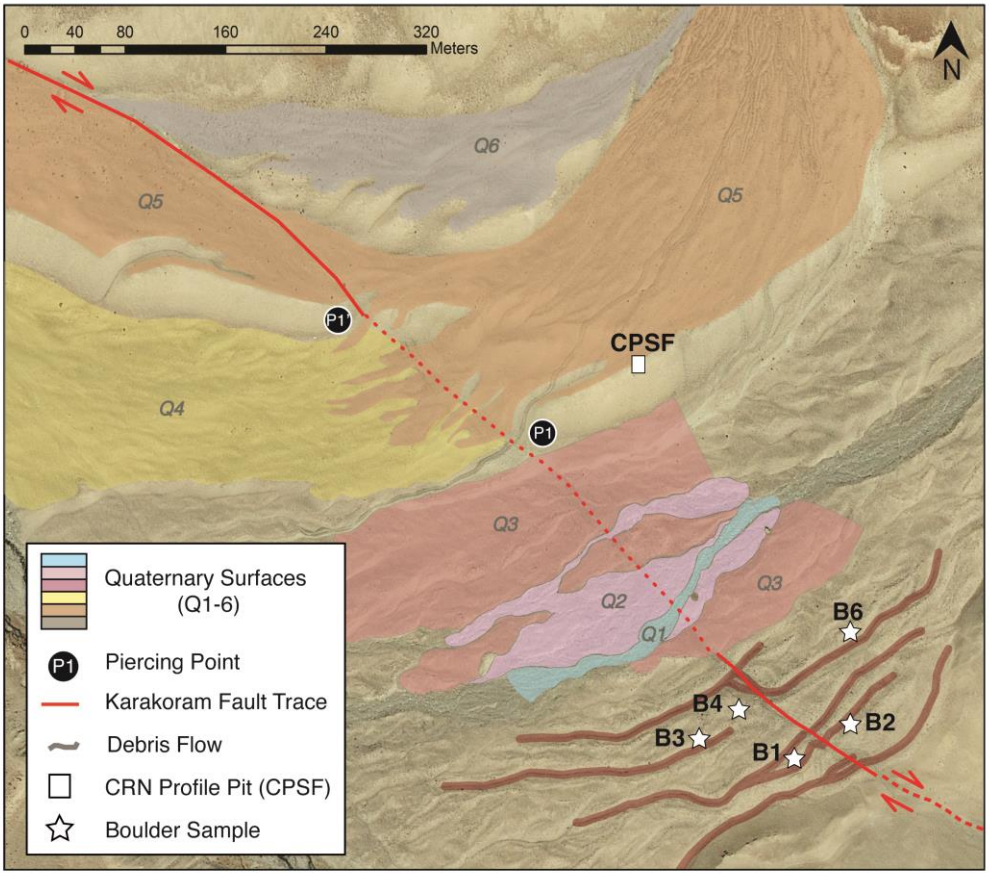

Figure 3b. Google Earth image showing the location and relationship of important surfaces along the Tangtse strand of the Karakoram fault system. In the northwest is an offset alluvial fan system, to the southeast are fluvial terraces that have not been affected by fault motion and in the southeast corner is a debris-flow dominated surface that shows some evidence of offset by the fault. The box and stars show the location of samples collected for cosmogenic radionuclide dating (Table 1). P and P' show a piercing point across the fault.

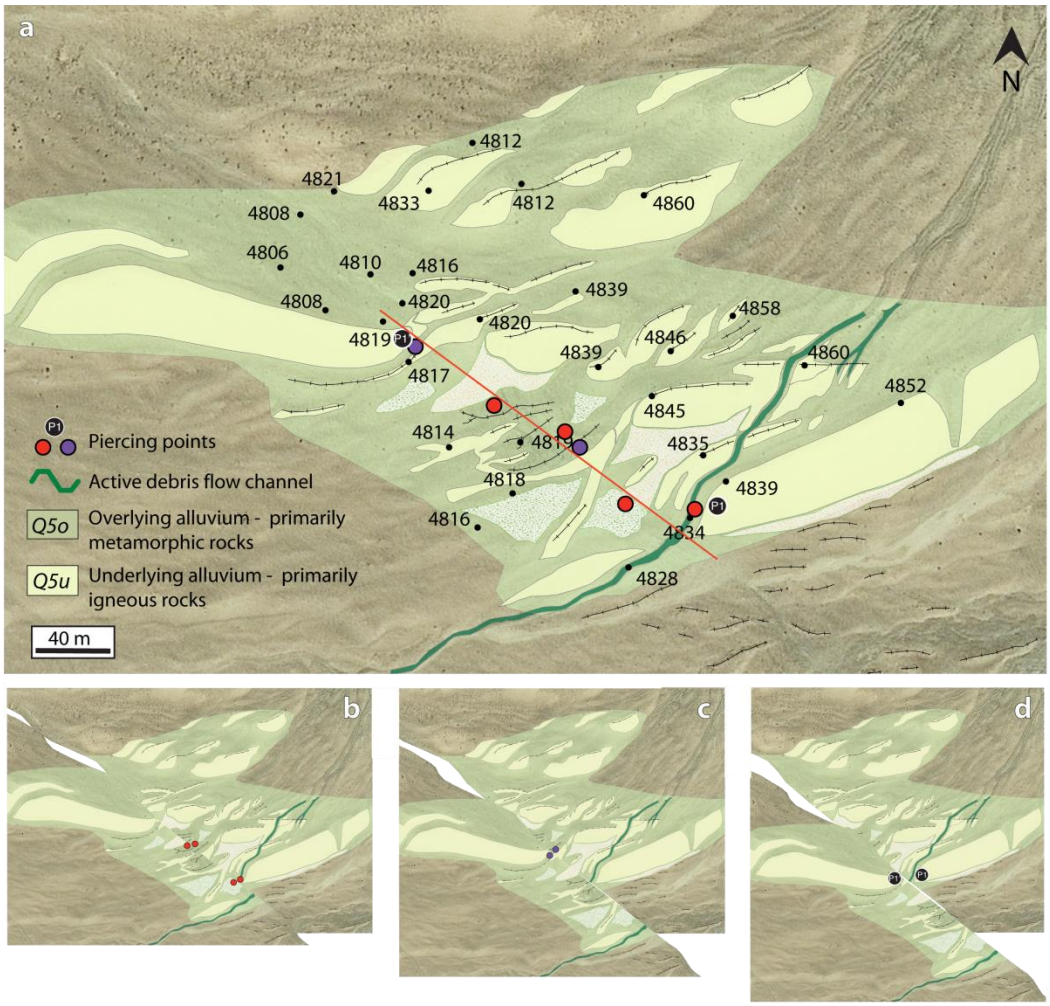

Figure 4. Google Earth image with geomorphic mapping showing elevations (m), units and landform reconstruction of the Q5 surface. This figure highlights the complexity of scarp degradation and shows the debris covering the fault trace. The Q5 surface has terraced risers that have been offset by the Karakoram fault system 160 ± 5 m horizontally and 24 ± 4 m vertically with the east side up. Colored units are alluvial deposits that make up the Q5 surface. Dotted white and tan units are reworked *Q5u* and dotted white and green units are reworked *Q5o*. Hatched lines indicate ridge lines. Red dots show examples of piercing points used to reconstructed time step b, purple dots show examples of piercing points used to reconstruction time step c, black dots show piercing point used to reconstruct the original landform. a) Present day landform, b) landform backslipped along the fault 50 m horizontally and 8 m vertically, c) landform offset 105 m horizontally and 17 m vertically, d) original landform, backslipped a total of 160 m horizontally and 24 m vertically.

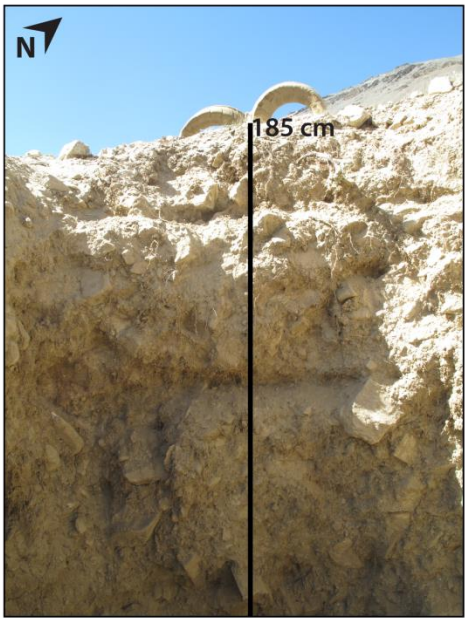

Figure 5. Field photo of cosmogenic radionuclide profile pit CPSF. This pit was excavated into the southeastern side of the upper terrace level of surface Q5 (Figure 3b). Samples were collected from depths of 0-2.5 cm, 38-43 cm, 107-114 cm, 142-150 cm and 183-190 cm.

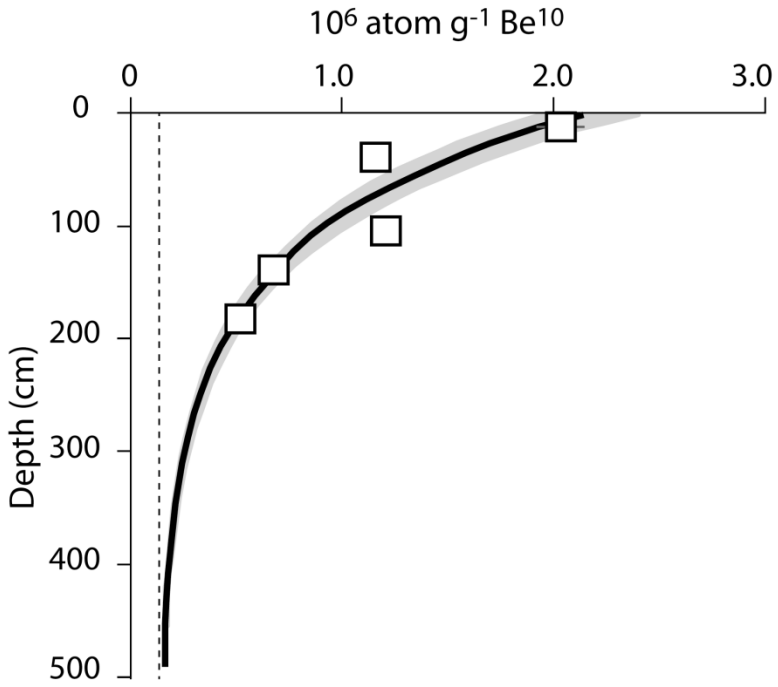

Figure 6. Cosmogenic depth profile CPSF from surface Q5 (Table 1). Boxes show sample location depth. Dashed line indicates inheritance (from Brown et al., 2002). The solid black line shows the best fit profile solution which gives a preferred surface age of 33.9 ka. The grey bounds around the best fit profile solution indicate the range of possible surfaces ages (30.5-37.0 ka) as calculated using the methods outlined in Braucher et al. (2009; Supplemental Material). Both vertical sampling errors and horizontal analytical errors are contained within the size of the sampling location boxes (with the exception of the top sample).

Table 1: Cosmogenic radionuclide data

Sample	Latitude	Longitude	Elevation (m)	Depth (cm)	Shielding Correction	10Be, 10^3 atom/g*	Error 10Be, 10^3 atom/g^	Age (ka; from Braucher et al., 2009)	
CPSF 0-1	34°14'25.4"	077°55'12.8"	4532	1	0.989	2150	210	33.9	
CPSF 15-17	34°14'25.4"	077°55'12.8"		40		1263	50		
CPSF 42-45	34°14'25.4"	077°55'12.8"		109		1321	70		
CPSF 56-59	34°14'25.4"	077°55'12.8"		145		787	14		
CPSF 72-75	34°14'25.4"	077°55'12.8"		187		552	12		
								Age (ka) Lal (1991)/Stone (2000)	**Uncertainty (yrs)**
B1	34°14'16.4"	077°55'19.1"	4570	2	0.991	724	35	7.5	654
B2	34°14'17.1"	077°55'20.9'	4569	2	0.991	587	56	5.7	497
B3	34°14'.16.4"	077°55'15.1'	4522	3	0.991	970	16	10.7	932
B4	34°14'17.0"	077°55'17.6"	4520	2	0.994	5714	1412	73.4	6490
B6	34°14'19.5"	077°55'21.2"	4537	2	0.983	1108	73	12.6	1099

*Calculated using a ^{10}Be production rate of 72 atom $g^{-1}yr^{-1}$.

^Error includes that associated with the AMS measurement. AMS measurement normalized to the ^{10}Be standard 07KNSTD.

CHAPTER 4

THERMOCHRONOLOGIC CONSTRAINTS ON THE MIOCENE EXHUMATION OF THE CENTRAL LADAKH BATHOLITH, NW INDIA

1. Abstract

The Ladakh Batholith is part of the Transhimalayan igneous province that extends from Afghanistan to Bhutan. Situated in the Ladakh region of northwest India, the batholith is framed by the dextral, Miocene-Recent Karakoram fault system and Cretaceous Shyok suture zone to the north, and the early Tertiary Indus-Yarlong suture zone to the south. As such, it is in a position to record changes in regional stress patterns related to the evolution of the orogenic system since the collision of India with Eurasia. To examine spatial and temporal trends in exhumation across the batholith, we used a combination of new and previously published (U-Th)/He data and constrained the uplift and exhumation history of the Ladakh Batholith from ca. 26 Ma to ca. 10 Ma. These thermochronologic data show a decrease in cooling ages from southwest to northeast. One-dimensional thermal modeling of these data indicates that exhumation rates decreased in the southwestern and central Ladakh range at ca. 16 Ma, but it was another 4-5 Ma before the northeastern Ladakh batholith slowed to the same rates. We suggest that the diachroneity of exhumation across the batholith implies that changes in regional stresses related to a relative decrease in north-south shortening caused a wave of decreased exhumation to sweep across the region from southwest to northeast.

2. Introduction

Stretching for more than 2500 km across southern Tibet and adjacent regions of India and Pakistan, the Transhimalayan igneous province represents a series of Andean-style continental arcs and fragments of intraoceanic arcs formed along or welded to the southern margin of Eurasia during subduction of the Neotethys ocean basin in advance of early Tertiary Indio-Eurasia collision (Honegger et al., 1982; Scharer et al., 1984; St. Onge et al., 2010; Bouilhol et al., 2013) Although emplaced in Mesozoic to early Tertiary time, these arc rocks record evidence of a long exhumation history that extends into the middle and late Tertiary.

With an outcrop extent of 20,000-30,000 km^2 in northwestern India and northeastern Pakistan, the Ladakh Batholith sits adjacent to some of the most significant Miocene-Recent structural features in the Himalayan-Tibetan orogenic system (Figure 1), including the dextral-oblique Karakoram fault system (e.g., Searle, et al., 1998; Phillips et al., 2004). In the Ladakh region of northwest India, the batholith is adjacent to the former Eurasian plate margin and the southwestern edge of the Tibetan Plateau. Thus, it is ideally situated to record processes related to both collision and post-collisional orogenic evolution. By utilizing low temperature thermochronology, which can quantify exhumation patterns related to rock uplift, we can gain insight into key periods in the tectonic history of the region that are recorded within the rocks of the batholith.

Previous thermochronologic work on the Ladakh Batholith by Kirstein et al. (2006, 2009) and Kirstein (2011) has suggested a long and complex exhumation history. Inspired by these previous studies, we endeavored to: 1) expand the spatial distribution of low-temperature thermochronologic data from the batholith to characterize the

exhumation patterns across the range; and 2) employ 1D thermal models of those data (following the method of Thiede and Ehlers, 2013) to better understand regional variations in exhumation history and how these relate to the evolution of the orogen in this area.

3. Geologic Setting

In the Ladakh region of northwestern India (Figure 1), the Ladakh Batholith was intruded into the Cretaceous Shyok Formation, metasedimentary and metavolcanic rocks exposed on the northern side of the batholith (Thakur et al., 1981; Dunlap and Wysoczanski, 2002; Chapter 2). Also exposed in this region are the 67.4 - 60.5 Ma Khardung volcanic sequence (Dunlap and Wysoczanski, 2002), a series of felsic pyroclastic flows and volcaniclastic rocks that are considered to be the extrusive equivalent to the Ladakh Batholith (Weinberg and Dunlap, 2000).

The batholith is bounded in the north by the Karakoram fault system, Khalsar thrust (Srimal et al., 1987), and Shyok suture zone (Figure 1). The Karakoram fault system comprises a series of active dextral-oblique strike slip faults, thought to have initiated in this area around ~15 Ma (Phillips et al., 2004), and to have accommodated 120-150 km of lateral motion (Searle, 1998). Adjacent to the Ladakh Batholith, the Karakoram fault system bifurcates around the Pangong Range, a slice of the middle crust exhumed between two fault strands (e.g., Searle et al., 1998; Phillips and Searle, 2007; Figure 1). The steeply north-dipping Khalsar thrust (Figure 1) is locally exposed near the village of Khalsar and has been tentatively correlated by Weinberg et al. (2000) with the Main Karakoram thrust system to the west. The Shyok suture zone marks the collision

between the southeastern Eurasian margin and Kohistan-Ladakh island arc. According to most workers, this event predated the final Indian-Eurasian collision (Achache et al., 1984; Bard, 1983; Brookfield and Reynolds, 1981; Searle, 1991; Matte et al., 1996; Weinberg et al., 2000), although this interpretation has recently been a point of controversy (see Bouilhol et al., 2013). In Ladakh, the Shyok suture zone intersects the Karakoram fault system near the Nubra Valley (Figure 1), but lateral motion along the Karakoram fault system has obscured much of the suture zone in the region. This has led to debate regarding the location of the Shyok suture zone in Ladakh, as well the appropriate correlation of the suture zone across the Karakoram fault system to the east (Searle 1996; Matte et al., 1996; Lacassin et al., 2004; Phillips et al., 2004; Figure 1).

In the south, the batholith is bounded by the Indus-Yarlung suture zone, which most workers regard as marking the final collision between Greater India and Eurasia (Gansser 1964, 1980; Allegre et al. I984; Searle et al. 1987) at ~50 Ma (e.g., Patriat and Achache, 1984; Klootwijk et al., 1992; Rowley, 1996; Tripathy-Lang et al., 2013; Figure 1). The Indus- Yarlung suture zone separates the Kohistan-Ladakh island arc terranes in the north from the Himalaya to the south. A series of south-dipping faults of the Zanskar backthrust system place Indus Basin molasse over the Ladakh Batholith (Searle, 1986; Searle et al., 1997). Some authors think these faults are a westward continuation of the Great Counter Thrust and have been active since ~20 Ma (e.g., Yin, 2006; Henderson et al., 2010). Recent work by Tripathy-Lang et al. (2009) instead suggests that back-thrusting in the Ladakh region may be restricted to between 11 and 7 Ma.

4. Previous Work on Ladakh Batholith Exhumation

Based on U-Pb zircon geochronology of a variety of plutons, it appears that the bulk of the Ladakh Batholith intruded in different magmatic phases between ca. 103-83 Ma and ca. 65 and 50 Ma, and that the last significant magmatic pulse occurred ca. 46-47 Ma (Weinburg and Dunlap, 2000; Singh et al., 2007; Ravikant et al., 2009; St-Onge et al., 2010; White et al., 2011).

Published thermochronologic constraints for the batholith include some $^{40}Ar/^{39}Ar$ mica and K-feldspar dates (Searle et al., 1989; Dunlap et al., 1998). The limited data suggest bedrock cooling below nominal mica and K-feldspar closure temperatures (ca. 490˚C – 230˚C; Hodges, 2014) during the Middle to Late Oligocene. Kirstein et al. (2006, 2009) published (U–Th)/He zircon (ZrnHe), fission-track apatite (ApFT), and (U–Th)/He apatite (ApHe) data for a number of samples collected across the batholith. These samples were primarily collected along the southern side of the batholith as well along the route from Leh to Khardung (Figure 1). Collectively these data help constrain bedrock cooling below nominal closure temperatures of 170˚C (ZrnHe), 110˚C (ApFT), and 70˚C (ApHe; Hodges, 2014). While the ZrnHe data imply system closure progressively from ca. 31 Ma in the south to ca. 22 Ma in the north, ApFT data are more variable across the range (Figures 2 and 3). The maximum ApFT ages (ca. 35-30 Ma) were for samples near the southern margin of the batholith. While the oldest ApHe dates of Kirstein et al. (2006) are also from the southern margin (ca. 19 Ma), her youngest (ca. 12 Ma) are from the range crest (Figures 2 and 3). Given these patterns, Kirstein et al. (2009) inferred northward tilting and doming of the batholith as a result of collision between India and Eurasia (ca. 50 Ma), followed by southward tilting of the batholith

during the large scale tectonic and magmatic changes accompanying the uplift of the Tibetan Plateau (ca 30-15 Ma). They further hypothesized that higher relief in the north produced by southward tilting led to increased erosion, thereby explaining some of the younger thermochronologic ages along the northern margin. Finally, these authors surmised that Late Miocene motion along the south-vergent Main Karakoram thrust (presumed to be exposed near the southern margin of the Karakoram Range to the north) and the Zanskar backthrust system, as well as sediment mantling of the southern slopes of the batholith, may also help account for the observed thermochronologic and denudation patterns.

Kirstein (2011) presented the results of an Al-in-amphibole geobarometric study of hornblende-bearing units in the batholith. Assuming that all of these undated units crystallized at approximately the same time, she noted a decrease in emplacement pressure from south to north. In light of these results, she reinterpreted previously published thermochronologic data to indicate significant exhumation of the southern part of the batholith in the Oligocene and significant exhumation of the northern part of the batholith in the Middle to Late Miocene.

5. Methods

To broaden the geographic distribution of low-temperature thermochronologic data in the batholith – and thus evaluate the possibility of variability in exhumation history along the NW-SE trend of the Ladakh Range – we collected samples along transects to the northwest and southeast of the one collected by Kirstein et al. (2006, 2009; Figure 2). We refer to these as transects A, B, and C, where A corresponds to the

northwest transect, B is the transect of Kirstein and co-workers, and C is the southeast transect. Along Transect A, we collected thirteen samples of granite or granodiorite between the villages of Basgo and Hundar. Along Transect C, we collected seven samples of granite or granodiorite between Martselang and Durbuk. Of the three, only Transect A represents an entire traverse across the range because outcrops of the batholith are not accessible along the northeastern margin of the range as they are covered by the extrusive Khardung volcanic sequence.

5.1 Swath Topography

In order to illustrate relief across the studied transects and our sampling elevations, we extracted swath profiles from 90-m Shuttle Radar Topography Mission (SRTM) data using a boxcar filter. The swath centers correspond to straight-line distances between the lables A-A', B-B', and C-C' on Figure 2. We averaged topography over arbitrarily defined swath widths of 4000 m and created separate digital elevation models of maximum, minimum and mean elevations. We then used the profiler tool in ArcMap to create profiles across the swaths. Thermochronologic samples that fell outside of the 3 main transects were projected onto the nearest transect (Figures 4, 5 and 6).

5.2 Low-Temperature Thermochronology

Single crystals of zircons and apatites were separated from collected samples for (U-Th)/He thermochronology using conventional magnetic and gravimetric techniques. All mineral processing was done at Arizona State University (ASU). Individual zircon and apatite grains were selected for analysis based on their size, clarity, crystal habit, and

lack of inclusions. They were photographed, measured, sealed into Nb tubes, and loaded into an Australian Scientific Instruments *Alphacron* helium extraction and analysis system housed in the Noble Gas, Geochronology and Geochemistry Laboratory (NG^3L) at ASU. Gasses were extracted by heating individual grains with an infrared (980 nm) diode laser and purified using reactive getters. After spiking with ^3He for isotope-dilution analysis, helium isotopic compositions were measured on a Balzers *Prisma QMS 200* quadrupole mass spectrometer. The degassed crystals were then dissolved, spiked with ^{235}U and ^{230}Th from isotope-dilution analysis, and digested in appropriate acids in preparation for U and Th analysis. (Zircon digestions involved heating at elevated temperatures and pressures.) Parent element measurements were made on either a Thermo *X-series* inductively coupled plasma mass spectrometer (ICP-MS) in the W.M. Keck Foundation Laboratory for Environmental Geochemistry at ASU, or on a Thermo *iCAP-Q* ICP-MS in the NG^3L facility. Analytical procedures closely follow those outlined by Schildgen et al. (2009) for apatite and van Soest et al. (2011) for zircon.

For each sample, we dated between two and six crystals of both apatite and zircon. As is frequently the case for (U-Th)/He data, replicate single-crystal ApHe and ZrnHe dates from our Ladakh samples sometimes showed a dispersion in excess of what analytical imprecision would explain. Possible explanations for such behavior include radiation damage retarding ^4He diffusion in apatites (e.g., Shuster et al., 2006), U+Th zoning that affects the validity of alpha ejection corrections (Hourigan, et al., 2005), the effects of alpha implantation (Spiegel, et al., 2009), and the effects of undetected high U + Th inclusions such as zircon in larger apatite crystals.

Our approach to determining a ‘best’ ApHe or ZrnHe closure age for a sample

was as follows. First, we employed the Hampel identifier method (Davies and Gather, 1993) to identify dates that were clearly discrepant. (For this study, we employed an outlier limit of four median absolute deviations from the median of the measured dates.) Next, for each ApHe or ZrnHe population, we calculated an error-weighted mean, its standard deviation, and the mean squared weighted deviation (MSWD) of the weighted mean. The MSWD is then compared to predicted ca. 95% confidence limits for the expected MSWD value of 1.0 for a weighted mean of a population of this size (Wendt and Carl, 1991). If the calculated MSWD was within that ca. 95% confidence range, we report the weighted mean date and its 2σ uncertainty in our data table (Table 1). If it were not, we magnified the calculated value for 2σ by the square root of the MSWD and quote the result in Table 1 as the best-estimate of the uncertainty of the weighted-mean date.

5.3 One-Dimensional Thermal Modeling

Many recent studies have featured thermal modeling of thermochronologic datasets in an effort to constrain spatial and temporal variations in bedrock exhumation rates in the Himalaya on the timescales of millions of years (e.g., Whipp, et al., 2007; Robert, et al., 2011; Coutand, et al., 2014). Deformation can lead to significant lateral heat transport in active orogenic wedges, and thus 2D or even 3D thermal models may be attractive to address some important questions (Braun, et al., 2012). Nevertheless, many questions regarding exhumation rates can be adequately addressed using 1-D models, particularly when the data being modeled are for low-temperature thermochronometers (Whipp et al., 2007; Thiede and Ehlers, 2013). We followed the approach of Thiede and Ehlers (2013) to explore variations in exhumation rate with time across the Ladakh

Batholith. This involved Monte Carlo forward modeling of thermochronometer closure behavior over time, presuming input thermal parameters (Table 2), variable exhumation, and using a modified 1D version of the PECUBE software of Braun et al. (2012).

In order to determine how the exhumation rate changed through time, we allowed rates to vary randomly between 0 and 4 km/Ma at times 50, 30, 25, 20, 16, 12, 8, 4 and 0 Ma. Rates were permitted to change at the preset time intervals, but could not change between intervals. We assumed that collision and related uplift and exhumation began at roughly 50 Ma and thus began the model at that time. However, the time period between 50 Ma and our oldest modeled ZrnHe date (ca. 26 Ma) is unconstrained, so we only report results for after 26 Ma. Errors on our (U-Th)/He cooling ages were expanded to 10% of the mean in order to equally weight cooling ages within our modeled solutions. Many laboratories calculate uncertainties as 10% of the mean (based on the long-term reproducibility of age standards rather than on analytical imprecision alone), so this is within acceptable community standards.

The resulting models (n=300,000 for each sample) were then statistically compared to measured closure ages, and reasonable fits were used to estimate exhumation rate as a function of time for specific samples as well as reasonable uncertainties in those rates. Fits were evaluated by using the reduced chi-squared test. The misfit of a sample is determined to be the mean of all of the individual chronometer chi-squared values from within that sample. In this case, a chi-squared value of ≤ 10 is considered an acceptable fit. Acceptable exhumation rate histories are reported in Figure 6 as the mean and standard deviation of the exhumation rate at each time interval.

6. Results

An interesting characteristic of both our (U-Th)/He thermochronologic data and those of Kirstein et al. (2009) is the lack of any strong correlation between apparent age and sample elevation (Figure 7). This precludes the common practice of using age-elevation relationships to interpret exhumation rates, and argues against spatially uniform exhumation across the Ladakh Range. Additionally, there is no correlation between effective uranium concentration (eU) and ApHe age in these samples, which limits the possibility that radiation damage significantly skewed our results for some crystals.

Our ZrnHe dates and those of Kirstein et al. (2009) range from 30.8 ± 5.8 Ma to 16.07 ± 2.56 Ma (Figure 2). The oldest cooling ages are clustered along the southwest flank of the batholith, while younger dates show a wider spatial distribution. All ZrnHe cooling ages between ca. 31 Ma and 24 Ma are located in the southwestern and central portions of the range, and the majority of ages between ca. 23 and 14 Ma are located in the northeastern and central portions of the range.

Our ApHe dates range from 16.9 ± 2.1 Ma to 10.3 ± 1.4 Ma in no simple geographic pattern (Figure 2). They are similar to those reported by Kirstein et al. (2009), except that their ApHe dates for samples along the southwest flank of the batholith (Samples Taru 3593, Leh 3295 and Tikse 3325; Transect B) are significantly older (21.8-18.5 Ma) than ours from the same part of the batholith (14.42-11.20 Ma). One significant difference between our (U-Th)/He analytical protocols and those of Kirstein et al. (2006, 2009) is that we ran individual crystals, whereas they ran multigrain aliquots. Their procedure precludes the identification of outliers in a dataset and significantly increases the uncertainty associated with alpha ejection corrections. While we include the older

dates in our discussions of the Ladakh data below, it should be noted that these older ApHe dates may be unreliable.

Our data and those of Kirstein et al. (2006, 2009) constrain the cooling and exhumation histories for three SW to NE transects across the Ladakh Range (A, B and C; Figure 4, 5 and 6). Differences among cooling age patterns of individual transects speak to the variability of exhumation histories from the southeast to the northwest. ZrnHe dates from Transects A and B show strong correlations with position along the lengths of the transects, with apparent ages progressively decreasing from SW to NE (Figure 4 and 5). The spatial distribution of zircon apparent ages is more limited in Transect C (ca. 20 km as opposed to ca. 40 km), and the Transect C data do not indicate a clear correlation between cooling age and along-transect position (Figure 6). ApHe dates for Transects B and C decrease from SW to NE. Apatite dates for Transect A are sparse, relatively restricted geographically, and do not show the same trend (Figure 4).

7. Thermal Modeling of Exhumation Histories

In order to clarify how these cooling ages relate to the exhumation history of the batholith, we modeled the thermal evolution of selected samples along each transect. Specifically, we chose one sample representing each of the southwestern, central and northeastern portions of the batholith in Transects A and C. Along Transect A we used Samples N1, N7 and N11 and along Transect C we used samples S1, S4 and S6. These samples were chosen because they had the largest number of reasonable model fits. Note that we only modeled samples from our dataset in order to ensure uniform processing technique and outlier exclusion. Because the model is essentially unconstrained before

the first chronometer, we concentrate on the timing of changes in exhumation, rather than on model calculated exhumation rates between the model initiation time and the first chronometer age. Figure 8 illustrates the results of this exercise.

Exhumation rates for samples from the southwestern margin and central region decrease at ca. 16 Ma. However, the exhumation rate of the sample from the northeastern margin of Transect A does not decrease until ca. 12 Ma, while the exhumation rate for the northeastern margin sample from Transect C drops more gradually over the 12-16 Ma interval.

8. Discussion

Although the thermochronologic data presented in this work do not speak to the pre-Oligocene history of the batholith, the Khardung volcanic sequence on the NE side of the Ladakh Batholith provide evidence for northeast tilting of the batholith about a northwest-southeast horizontal axis sometime after their deposition (67.4 - 60.5 Ma; Dunlap and Wysoczanski, 2002). The total amount of northeast tilting since deposition is constrained to 30∞- 60∞ indicated by the dip of the unit (Weinberg and Dunlap, 2000). Kirstein et al. (2009) inferred that the most likely cause of this northward rotation was postcollisional northward underthrusting of India beneath Eurasia. However, continuation of such rotation during the past ca. 26 Ma would not produce the cooling age patterns and exhumation rate evolution our data and those of Kirstein et al. (2006, 2009) imply. Kirstein et al. (2009) proposed that this post-26 Ma pattern in cooling ages was related instead to southward tilting of the batholith.

We suggest that a better explanation for the cooling age pattern is a progressive

decline in exhumation rate from southwest to northeast between 16 and 12 Ma. One interpretation that suits this observation involves an early (pre-16 Ma) phase of uniform shortening across the region –related to post-collisional India-Eurasia convergence – followed by a structural reorganization that permitted a decay in uplift and exhumation beginning in the SW part of the batholith and migrating northeastward with time. We regard it as potentially important that this second stage in the Miocene exhumation history of the Ladakh Range began at approximately the same time as the initiation of the transpressional Karakoram fault system to the northeast. Across the Karakoram fault system, east-west extension began to dominate the strain field of Tibet at about the same time (e.g., Coleman and Hodges, 1995; Edwards and Harrison, 1997; Williams et al., 2001; Cottle et al., 2009; Kali et al., 2010; Lee et al., 2011). We suggest that eastward displacement of crust within the Tibetan extensional domain after 16 Ma enabled northeastward propagation of the locus of local shortening, uplift, and erosion, leaving in its wake a northeastward-propagating domain of lower exhumation rate. As we show in a subsequent chapter, evidence exists that the wave of decreased exhumation continued propagating northward into the Pangong and Karakoram Ranges after 12 Ma.

9. Conclusions

New low-temperature thermochronology data improve the spatial resolution of cooling age data within the central Ladakh Range. Thermal-kinematic modeling using these data shows a decrease in exhumation rates in the central and southwestern side of the batholith starting at ca. 16 Ma. However, exhumation rates do not begin to decrease until ca. 12 Ma along the northeastern batholith margin. We posit that this signal is

indicative of a northeastward-propagating domain of lower exhumation rate produced as a result of changes in the relative amounts of northeast-southwest shortening. Because the timing of the change in exhumation rate is coeval with the onset of east-west extension in Tibet we theorize that far-reaching changes in regional stress patterns caused a decrease in rock uplift rate and a subsequent decrease in exhumation rates across the Ladakh Batholith.

10. References

Achache, J., Courtillot, V., & Xiu, Z. Y., 1984. Paleogeographic and tectonic evolution of southern Tibet since middle Cretaceous time: New paleomagnetic data and synthesis. Journal of Geophysical Research, 89(B12), 10311-10.

Aitchison, J. C, Abrajevitch, A. et al. 2002. New insights into the evolution of the Yarlung Tsangpo suture zone, Xizang (Tibet), China. Episodes, 25(3), 90-94.

Allegre, CJ O., V. Courtillot, P. Tapponnier, A. Hirn, M. Mattauer, C. Coulon, J. J. Jaeger, 1984. Structure and evolution of the Himalaya–Tibet orogenic belt, p. 17-22.

Bard, J., 1983. Metamorphism of an obducted island arc; example of the Kohistan Sequence (Pakistan) in the Himalayan collided range. Earth and Planetary Science Letters 65(1), 133-144.

Bouilhol, P., Jagoutz, O., Hanchar, J. M., and Dudas, F. O., 2013. Dating the India–Eurasia collision through arc magmatic records: Earth and Planetary Science Letters, v. 366, p. 163-175.

Braun, J., van der Beek, P., Valla, P., Robert, X., Herman, F., Glotzbach, C., Pedersen,

V., Perry, C., Simon-Labric, T., and Prigent, C., 2012. Quantifying rates of landscape evolution and tectonic processes by thermochronology and numerical modeling of crustal heat transport using PECUBE: Tectonophysics, v. 524, p. 1-28.

Brookfield, M. E., & Reynolds, P. H., 1981. Late Cretaceous emplacement of the Indus suture zone ophiolitic melanges and an Eocene-Oligocene magmatic arc on the northern edge of the Indian plate. Earth and Planetary Science Letters, *55*(1), 157-162.

Brookfield, M. E., & Reynolds, P. H., 1990. Miocene $^{40}Ar/^{39}Ar$ ages from the Karakorum Batholith and Shyok Melange, northern Pakistan, indicate late Tertiary uplift and southward displacement. *Tectonophysics*, *172*(1), 155-167.

Coleman ME, Hodges KV., 1995. Evidence for Tibetan Plateau uplift before 14 Myr ago from a new minimum estimate for east-west extension. Nature, 374:49–52.

Cottle, J.M., Jessup, M.J., Newell, D.L., Horstwood, M.S.A., Noble, S.R., Parrish, R.R., Waters, D.J., and Searle, M.P., 2009, Geochronology of granulitized eclogite from the Ama Drime Massif: Implications for the tectonic evolution of the South Tibetan Himalaya: Tectonics, v. 28, doi: 10.1029/2008TC002256

Coutand, I., Whipp, D. M., Grujic, D., Bernet, M., Fellin, M. G., Bookhagen, B., Landry, K. R., Ghalley, S. K., and Duncan, C., 2014. Geometry and kinematics of the Main Himalayan Thrust and Neogene crustal exhumation in the Bhutanese Himalaya derived from inversion of multithermochronologic data: Journal of Geophysical Research: Solid Earth, v. 119, no. 2, p. 2013JB010891.

Davies, L., Gather, U., 1993. The identification of multiple outliers. Journal of the American Statistical Association 88 (423), 782–792, 88 (423).

Dunlap, W.J., Weinberg, R.F., Searle, M.P., 1998. Karakoram fault zone rocks cool in two phases. Journal of the Geological Society 155, 903–912.

Dunlap, W.J., Wysoczanski, R., 2002. Thermal evidence for early Cretaceous metamorphism in the Shyok suture zone and age of the Khardung volcanic rocks, Ladakh, India. Journal of Asian Earth Sciences 20, 481–490.

Edwards MA, Harrison TM, 1997. When did the roof collapse? Late Miocene N-S extension in the High Himalaya revealed by Th-Pb monazite dating of the Khula Kangri granite. Geology 25:543–46

Gansser A., 1964. The Geology of the Himalayas. New York: Wiley Interscience. pp. 289.

Gansser, A., 1980, The significance of the Himalayan suture zone:Tectonophysics, v. 62, p. 37–52.

Henderson, A.L., Najman, Y., Parrish, R., Boudagher-Fadel, M., Barford, D., Garzanti, E., and Ando, S., 2010, Geology of the Cenozoic Indus Basin sedimentary rocks: Paleoenvironmental interpretation of sedimentation from the western Himalaya during the early phases of India-Eurasia collision: Tectonics, v. 29.

Hodges, K. V., 2014, Thermochronology in Orogenic Systems, *in* Holland, H. D., and Turekian, K. K., eds., Treatise on Geochemistry, Second Edition, Volume 4: Oxford, Elsevier, p. 281-308.

Honegger, K., Dietrich, V., Frank, W., Gansser, A., Thoni, M., Trommsdorff, V., 1982. Magmatism and metamorphism in the Ladakh Himalayas (the Indus-Tsangpo

suture zone). Earth and Planetary Science Letters 60, 253–292.

Hourigan, J. K., Reiners, P. W., and Brandon, M. T., 2005, U-Th zonation dependent alpha-ejection in (U-Th)/He chronometry: Geochimica et Cosmochimica Acta, v. 69, p. 3349-3365.

Jamieson, S.S.R., Sinclair, H.D., Kirstein, L.A., Purves, R.S., 2004. Tectonic forcing of longitudinal valleys in the Himalaya: morphological analysis of the Ladakh batholith, North India. Geomorphology 58, 49–65.

Kirstein, L.A., 2011. Thermal evolution and exhumation of the Ladakh batholith, northwest Himalaya, India. Tectonophysics 503, 222–233.

Kirstein, L.A., Sinclair, H., Stuart, F.M., Dobson, K., 2006. Rapid early Miocene exhumation of the Ladakh batholith, western Himalaya. Geologic Society of America 34, 1049–1052.

Kirstein, L.A., Foeken, J.P.T., van der Beek, P., Stuart, F.M., Phillips, R.J., 2009. Cenozoic unroofing history of the Ladakh batholith, western Himalaya, constrained by thermochronology and numerical modeling. Geological Society of London 166, 667–678.

Klootwijk, C. T., Gee, J. S., Peirce, J. W., Smith, G. M., & McFadden, P. L., 1992. An early India-Asia contact: paleomagnetic constraints from Ninetyeast Ridge, ODP leg 121. *Geology*, *20*(5), 395-398.

Lacassin, R., Valli, F. , Arnaud, N., Leloup, P.H. , Paquette, J.L. , Haibing, L., Tapponnier, P., Chevalier, M.-L. , Guillot, S., Maheo, G., Zhiqin, X., 2004, Large-scale geometry, offset and kinematic evolution of the Karakorum fault, Tibet, Earth Planet. Sci. Lett. 219, 255 – 269.

Lee, J., Hager, C., Wallis, S. et al., 2011. Middle to late Miocene extremely rapid exhumation and thermal reequilibration in the Kung Co rift, southern Tibet. Tectonics, 30, 1–26.

Matte, P., Tapponnier, P., Arnaud, N., Bourjot, L., Avouac, J.P., Vidal, P., Liu, Q., Pan, Y., Wang, Y., 1996. Tectonics of Western Tibet, between the Tarim and the Indus. Earth Planet. Sci. Lett. 142, 311–330.

Patriat, P., and J. Achache, 1984. India-Eurasia collision chronology has implications for crustal shortening and driving mechanism of plates,Nature, 311, 615 – 621.

Phillips, R. J., Parrish, R. R., and Searle, M. P., 2004, Age constraints on ductile deformation and long-term slip rates along the Karakoram fault zone, Ladakh: Earth and Planetary Science Letters, v. 226, no. 3-4, p. 305-319.

Phillips, R. J., and Searle, M. P., 2007, Macrostructural and microstructural architecture of the Karakoram fault: Relationship between magmatism and strike-slip faulting: Tectonics, v. 26

Ravikant, V., Wu, F.-Y., Ji, W.-Q., 2009. Zircon U–Pb and Hf isotopic constraints on petrogenesis of the Cretaceous–Tertiary granites in eastern Karakoram and Ladakh, India. Lithos 110, 153–166.

Robert, X., van der Beek, P., Braun, J., Perry, C., and Mugnier, J. L., 2011, Control of detachment geometry on lateral variations in exhumation rates in the Himalaya: Insights from low-temperature thermochronology and numerical modeling: Journal of Geophysical Research-Solid Earth, v. 116, p. doi: 10.1029/2010jb007893.

Rowley, D. B., 1996, Age of initiation of collision between India and Asia: A review of

stratigraphic data: Earth and Planetary Science Letters, v. 145, p. 1–13.

Schârer, U., Xu, R.H., Allegre, C.J., 1984. U–Pb geochronology of Gangdese (Transhimalaya) Plutonism in the Lhasa-Xigaze Region, Tibet. Earth and Planetary Science Letters 69 (2), 311–320.

Schildgen, T. F., K. V. Hodges, K. X. Whipple, M. S. Pringle, M. C. van Soest, and K. Cornell, 2009, Late Cenozoic structural and tectonic development of the western margin of the Central Andean Plateau in southwest Peru, Tectonics, 28.

Searle, M.P., Weinberg, R.F., Dunlap, W.J., 1998. Transpressional tectonics along the Karakoram fault zone, northern Ladakh: constraints on Tibetan extrusion. In: Holdsworth, R.E., Strachan, R.A., Dewey, J.F. (Eds.), Continental Transpressional and Transtensional Tectonics, 135. Geological Society, Special Publication, London, pp. 307–325.

Searle, M.P., 1991. Geology and Tectonics of the Karakoram Mountains. John Wiley and Sons, Chichester, UK, p. 358.

Searle MP, Parrish RR, Hodges KV, Hurford A, Ayres MW, Whitehouse MJ, 1997. Shisha Pangma leucogranite, south Tibetan Himalaya: field relations, geochemistry, age, origin, and emplacement. J. Geol. 105:295–31.

Searle, M. P., B. F. Windley, M. P. Coward, D. J. W. Cooper, A. J. Rex, T. Li, X. Xiao, M. Q. Jan, V. C. Thakur, and S. Kumar, 1987, The closing of the Tethys and the tectonics of the Himalaya, Geol. Soc. Am. Bull., 98, 678 – 701.

Searle, M. P., and Rex, A. J., 1989, Thermal model for the Zanskar Himalaya: Journal of Metamorphic Geology, v. 7, p. 127–134.

Searle, M. P., and Fryer, B. J., 1986, Garnet, tourmaline, and muscovite-bearing

leucogranites, gneisses and migmatites of the Higher Himalaya from Zanskar, Kulu, Lahoul and Kashmir, in Coward, M. P., and Ries, A. C., eds., Collision tectonics: Geological Society [London] Special Publication 19, p. 185–201.

Shuster, D. L., Flowers, R. M., and Farley, K. A., 2006, The influence of natural radiation damage on helium diffusion kinetics in apatite: Earth and Planetary Science Letters, v. 249, p. 148-161.

Singh, S., Kumar, R., Barley, M.E., Jain, A.K., 2007. SHRIMP U–Pb ages and depth of emplacement of Ladakh Batholith, Eastern Ladakh, India. Journal of Asian Earth Sciences 30 (3–4), 490–503.

Spiegel, C., Kohn, B., Belton, D., Berner, Z., and Gleadow, A., 2009, Apatite (U-Th-Sm)/He thermochronology of rapidly cooled samples: The effect of He implantation: Earth and Planetary Science Letters, v. 285, no. 1-2, p. 105-114.

Srimal, N., Basu, A. R. & Kyser, T. K. 1987. Tectonic inferences from oxygen isotopes in volcano plutonic complexes of the India-Asia collision zone, NW India. Tectonics, 6, 261-273.

St-Onge, M.R., Rayner, N., Searle, M.P., 2010. Zircon age determinations for the Ladakh batholith at Chumathang (Northwest India): implications for the age of the India–Asia collision in the Ladakh Himalaya. Tectonophysics 495, 171–183.

Thiede, J.C., Ehlers, T.A., 2013. Large spatial and temporal variations in Himalayan denudation. Earth Planet. Sci. Lett. 371–372

Tripathy, A. K., Hodges, K. V., van Soest, M. C., and Ahmad, T., 2010, Timing and duration of backthrusting in the Indus Group: a detrital zircon (U-Th)/He approach, American Geophysical Union, Fall Meeting, San Francisco, Abstract

T43C-2130.

Thakur, V. C., & Misra, D. K., 1984. Tectonic framework of the Indus and Shyok suture zones in eastern Ladakh, northwest Himalaya. *Tectonophysics,101*(3), 207-220.

van Soest, M., Monteleone, B.D., Hodges, K.V., Boyce, J.W., 2011. Laser depth profiling studies of helium diffusion in Durango fluorapatite, Geochim. Cosmochim. Acta, 75, pp. 2409–2419.

Weinberg, R.F., Dunlap, W.J., 2000. Growth and deformation of the Ladakh Batholith, Northwest Himalayas: implications for timing of continental collision and origin of calc-alkaline batholiths., Journal of Geology 108, 303–320.

Weinberg, R.F., Dunlap, W.J., Whitehouse, M., 2000. New field, structural and geochronological data from the Shyok and Nubra valleys, northern Ladakh: linking Kohistan to Tibet. In: Khan, .A., Treloar, P.J., Searle, M.P., Jan, M.Q. (Eds.), Tectonics of the Nanga Parbat Syntaxis and the Western Himalaya. Geological Society of London Special Publication, vol. 170, pp. 253– 275.

Wendt, I., & Carl, C., 1991. The statistical distribution of the mean squared weighted deviation. *Chemical Geology: Isotope Geoscience Section*, *86*(4), 275-285.

Whipp, D. M., Ehlers, T. A., Blythe, A. E., Huntington, K. W., Hodges, K. V., and Burbank, D. W., 2007, Plio-Quaternary exhumation history of the central Nepalese Himalaya: 2. Thermo-kinematic and thermochronometer age prediction model: Tectonics, v. 26, doi:10.1029/2006TC001991.

White, L.T., Ahmad, T.,Ireland, T.R., Lister, G.S., Forster,M.A., 2011. Deconvolving episodic age spectra from zircons ofthe Ladakh Batholith, northwest Indian Himalaya. Chemical Geology 289, 179–196.

Williams, H., Turner, S., Kelley, S., and Harris, N., 2001, Age and composition of dikes in southern Tibet: New constraints on the timing of east-west extension and its relationship to postcollisional magmatism: Geology, v. 29, p. 339–342.

Yin, A., 2006. Cenozoic tectonic evolution of the Himalayan orogen as constrained by along-strike variation of structural geometry, exhumation history, and foreland sedimentation. *Earth-Science Reviews*, *76*(1), 1-131.

11. Figures

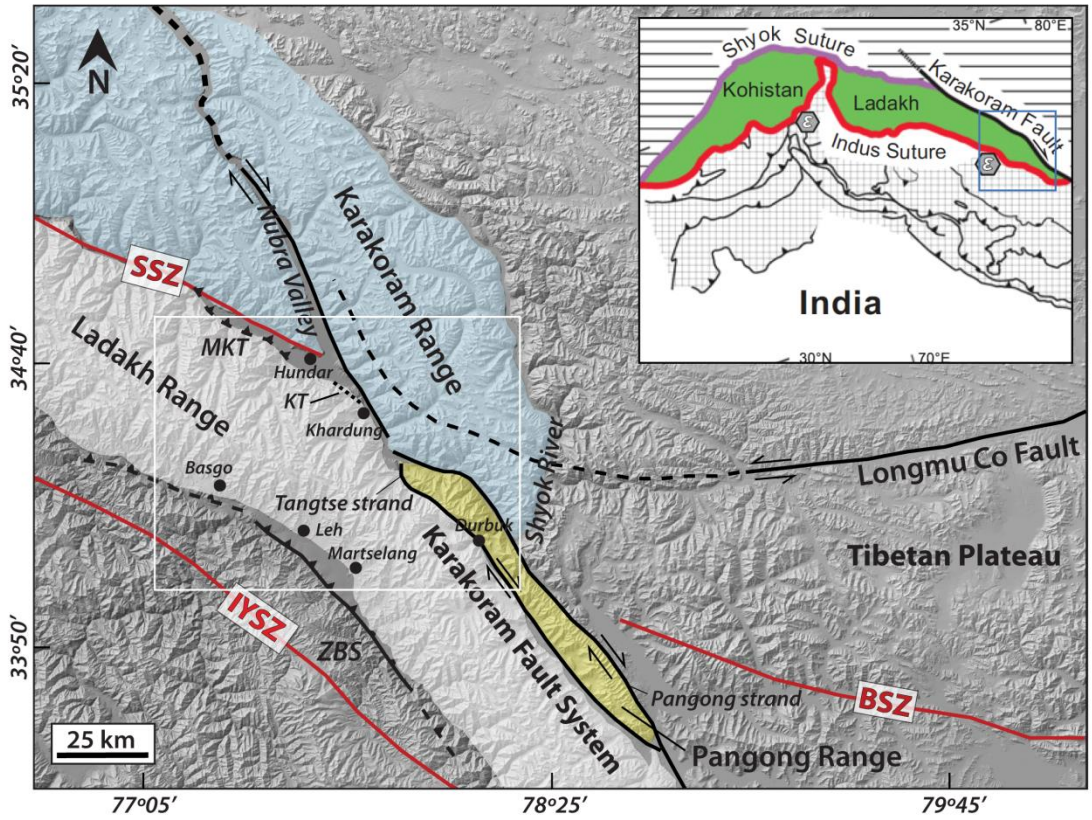

Figure 1. Simplified tectonic map of the Ladakh region of nothwest India. Colored regions show major ranges. Red lines indicate suture zones. Black lines show major faults. Cities are marked with circles. The inset shows the structural position of the Ladakh Batholith within the Khoistani-Ladakh Arc (from Bouihol et al., 2013). Blue box in inset shows study location. White box shows the location of Figure 2. MKT - Main Karakoram Thrust; KT - Khalsar Thrust; SSZ - Shyok suture zone; BSZ - Bangong suture zone; IYSZ - Indus-Yarlung suture zone; ZBS - Zanskar backthrust system.

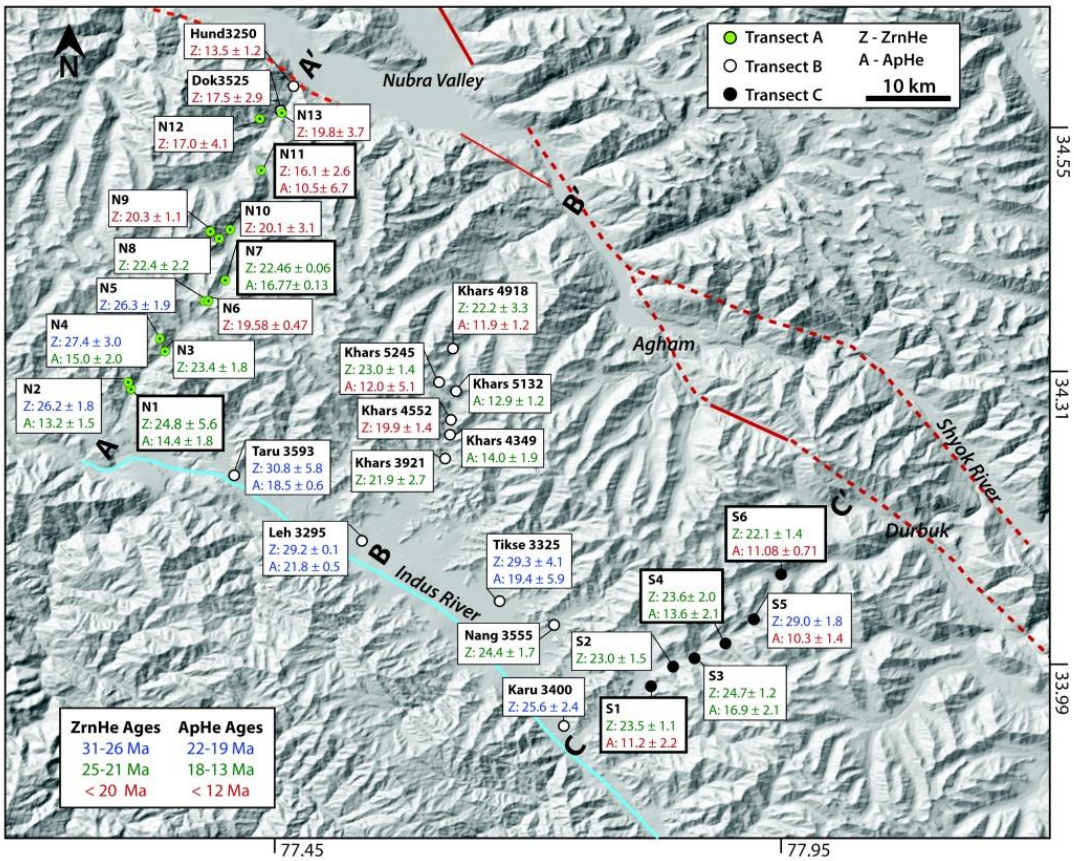

Figure 2. Hillshade map of the central Ladakh Batholith. The Karakoram fault system is marked with a red line. Three thermochronologic sampling transects extend across the Ladakh Range; Transects A, B and C. The samples along Transect B and other samples indicated with a white circle were reported by Kirstein et al. (2006, 2009). The cooling ages of each chronometer have been grouped and color coded by age range - blue ages are oldest, red ages are youngest and green ages are intermediate in age. The approximate location of the Indus River (used in Transects A, B and C) is marked in blue. The samples with darker outlined boxes were used in the thermal-mechanical models. In general, all cooling ages decrease from southwest to northeast across the range. Reported data are weighted mean ages and 2σ uncertainty.

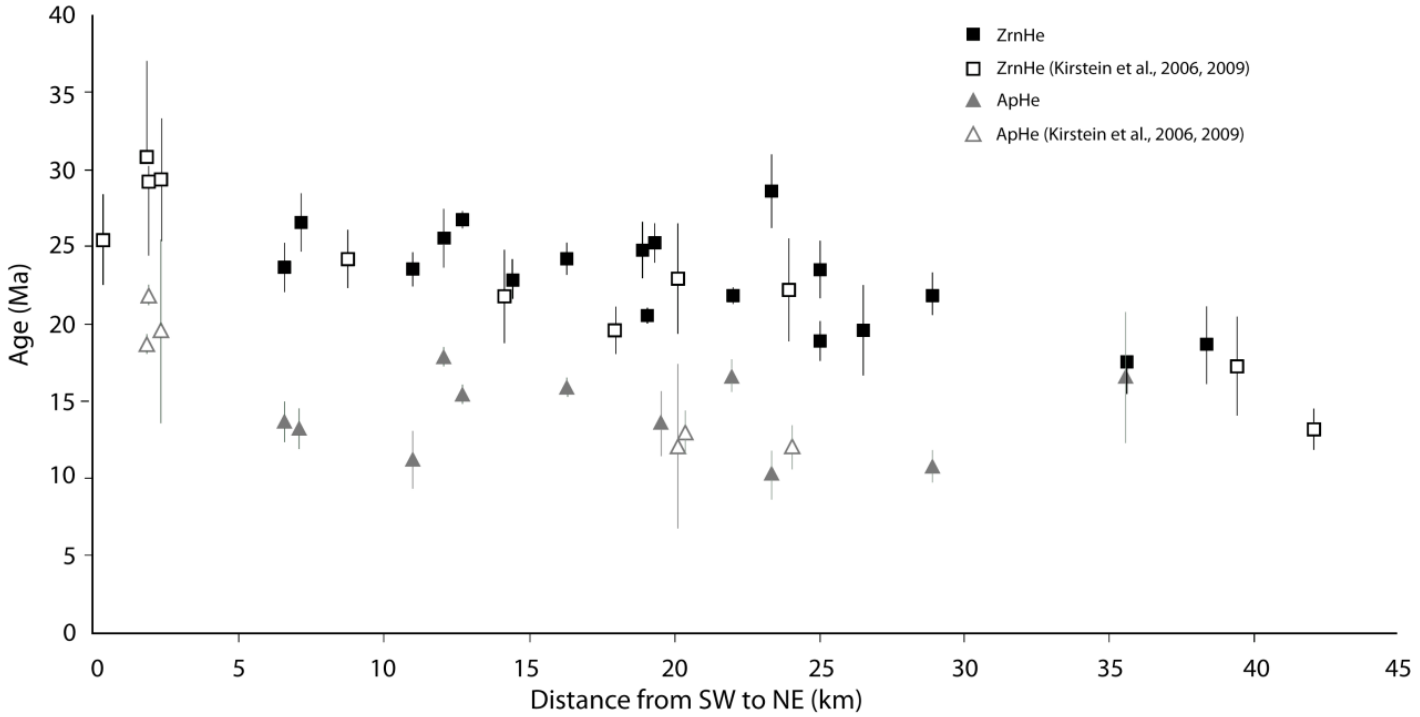

Figure 3. Thermochronology data from all 3 transects plotted by distance from the Indus River. Overall, the data show a decrease in cooling ages across the batholith from southwest to northeast.This trend is seen most clearly in the ZrnHe data. Erros are plotted at 2σ. ZrnHe - zircon U-Th/He; ApHe - apatite U-Th/He.

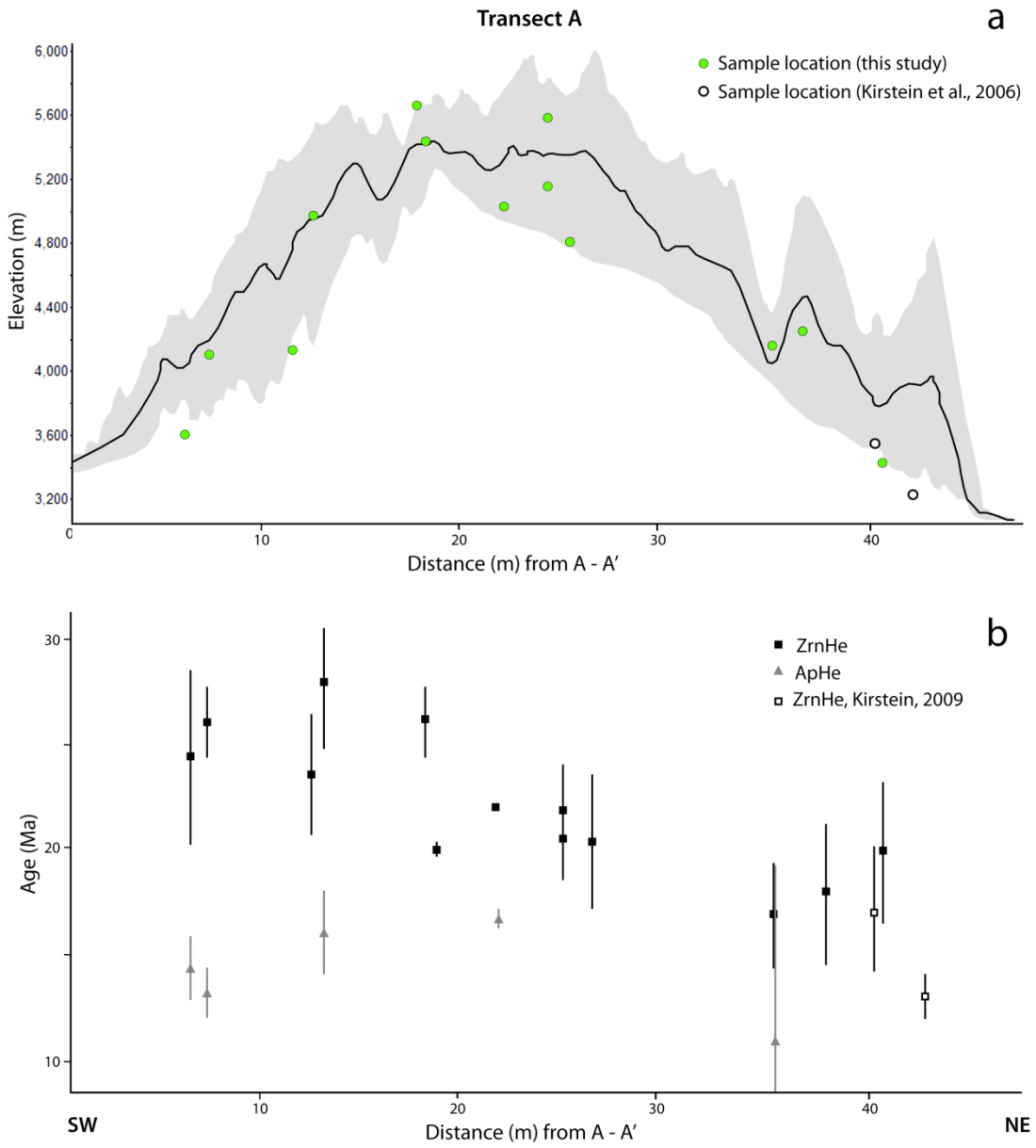

Figure 4. Transect A across the Ladakh Range (see Figure 2). a) Topographic swath profile along the northern transect showing maximum , minimum and mean elevation. Sample locations are indicated by circles. b) ZrnHe (square) and ApHe (triangle) ages plotted by distance along transect. The ZrnHe ages show a clear decrease in cooling age from southwest to northeast. The ApHe data do not mirror this trend, and, with the exception of one sample, seem to show the opposite age pattern. ZrnHe - zircon U-Th/He; ApHe - apatite U-Th/He

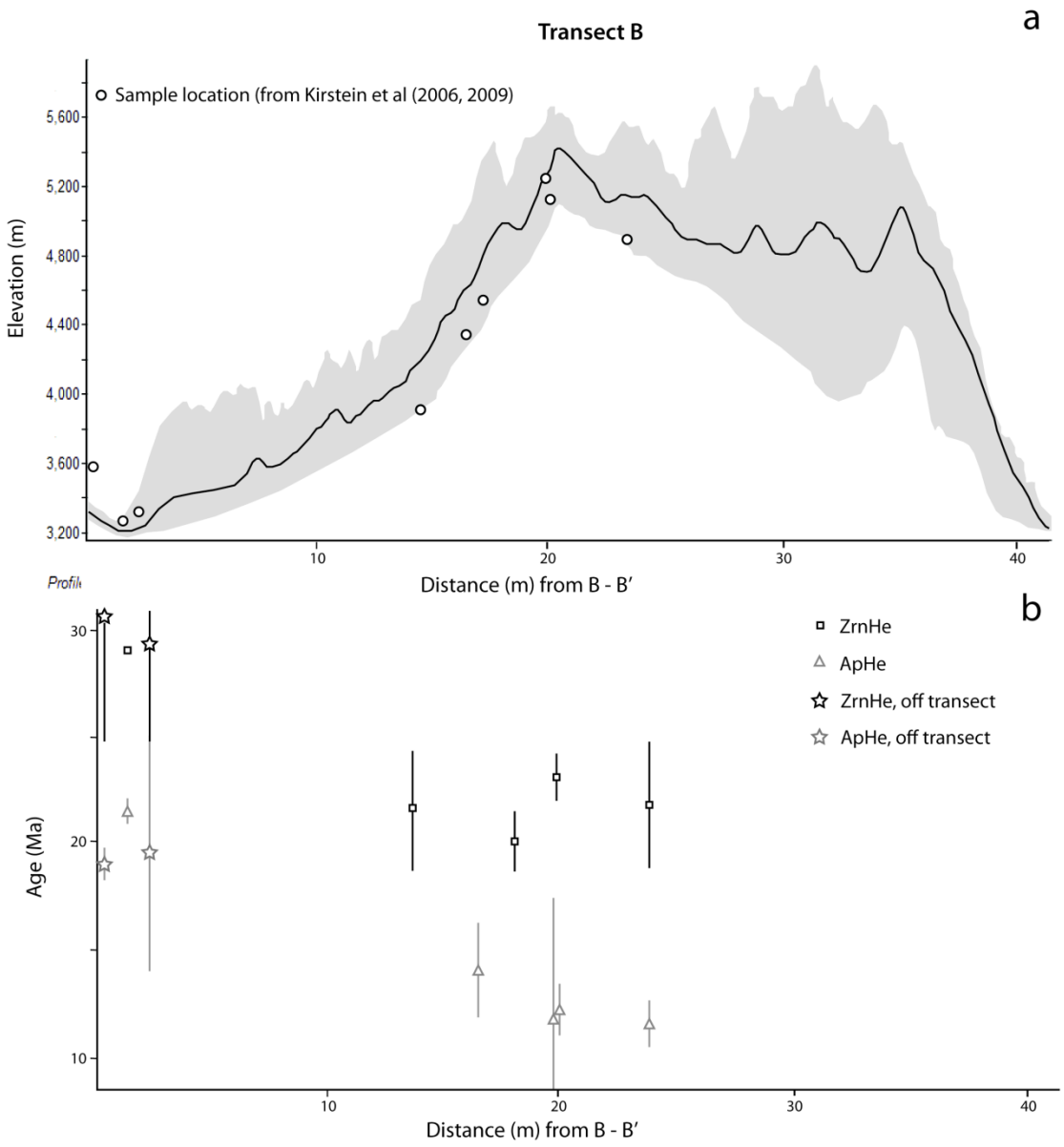

Figure 5. Transect B across the Ladakh Range (see Figure 2). Samples along this transect were collected and reported by Kirstein et al., 2006, 2009. a) Topographic swath profile along the transect showing maximum , minimum and mean elevation. Sample locations are indicated by circles. b) ZrnHe (square) and ApHe (triangle) ages are plotted by distance along transect. Stars indicate samples that were projected onto this transect. Both ZrnHe and ApHe cooling ages decrease towards the northeast. However, this trend is strongly controlled by 3 samples at the southwestern end of the transect. ZrnHe - zircon U-Th/He; ApHe -apatite U-Th/He

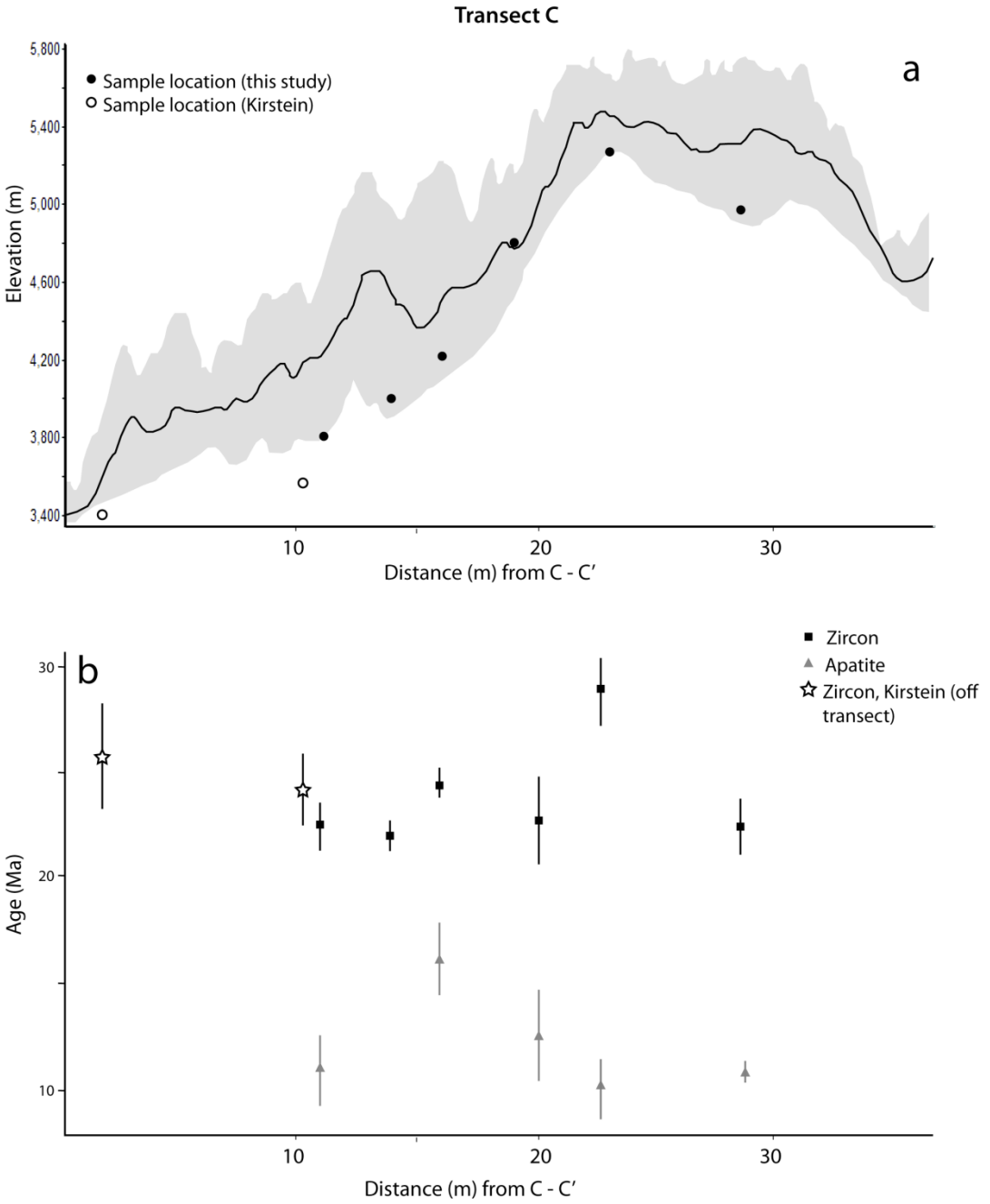

Figure 6. Transect C across the Ladakh Range (see Figure 2). a) Topographic swath profile along the transect showing maximum , minimum and mean elevation. Sample locations are indicated by circles. b) ZrnHe (square) and ApHe (triangle) ages plotted by distance along transect. Stars are samples from Kirstein, 2009 that have been projected onto this transect. There is no obvious age pattern across the range. ZrnHe - zircon U-Th/He; ApHe - apatite U-Th/He

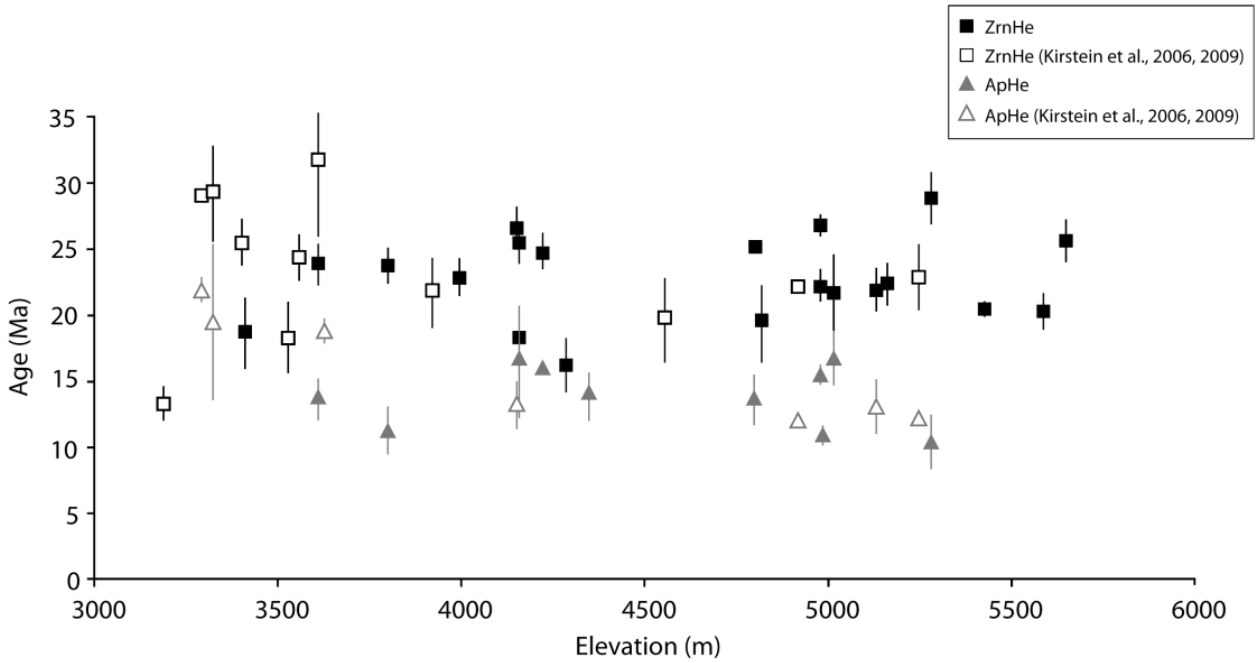

Figure 7. Cooling ages from this study and Kirstein et al. (2006, 2009) plotted against elevation. Errors are plotted at 2σ. ZrnHe - zircon U-Th/He; ApHe - apatite U-Th/He.

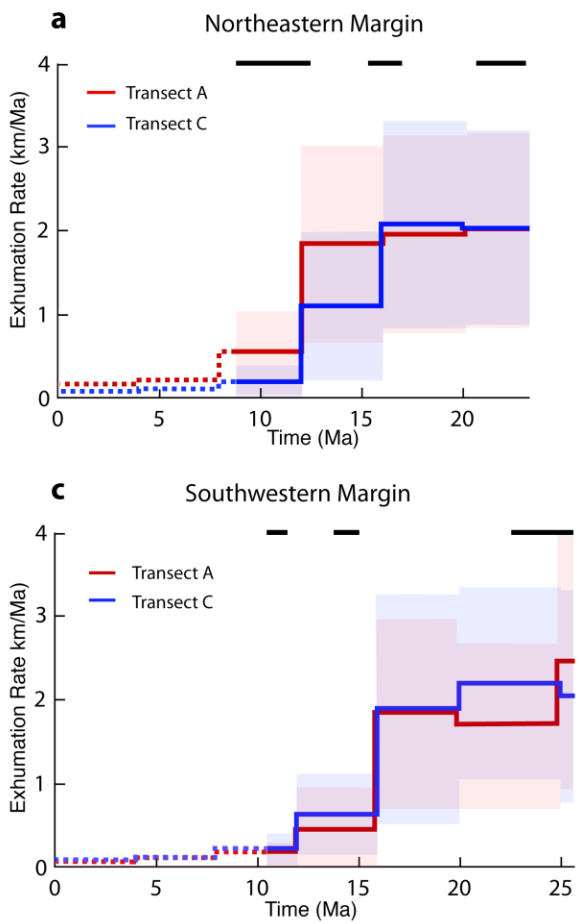

Figure 8. Modeled exhumation rate versus time. In each plot, one representative sample has been taken from Transects A and C. Samples used in these models are darkly outlined in Figure 2. The colored lines show the mean exhumation rate for each sample. The colored boxes represent 1 standard deviation of the mean for each time step (colors correspond to the colored lines). The thick black lines at the top of each plot indicate the periods of the model that are constrained by ZrnHe and ApHe data. Areas unconstrained by data are dashed. a) Samples from the northeastern part of the transect. For Transect A this is near the northern margin of the batholith (Sample N11). For Transect C this is closer to the north/central part of the batholith (Sample S6). b) Samples from the central part of the batholith (Samples N7 and S4), c) Samples from the southwestern margin of the batholith (Samples N1 and S1). Based on these models, exhumation decreased first in the southwestern and central portions of the batholith, but continued to stay high along the northeastern margin for an additional ~3 My.

Table 1: Apatite and zircon (U-Th)/He data

	Sample	Latitude	Longitude	Elevation	^{4}He *	±2s	^{238}U *	±2s	^{232}Th*	±2s	Raw Data	±2s	Ft	^Corr. Date	±2s	Weighted Mean Date	±2s
				(m)	(fmol)		(fmol)		(fmol)		(Ma)			(Ma)	(Ma)	(Ma)	
Transect A																	
N1	a1	34.272	77.294	3610	4.1E+00	1.2E-01	1.9E+02	4.0E+00	6.1E+02	1.3E+01	9.68	0.32	0.676458	14.31	0.23	14.4	1.8
	a3				6.3E+00	1.9E-01	2.6E+02	5.5E+00	1.2E+03	2.2E+01	8.99	0.30	0.728251	12.34	0.21		
	a5				5.1E+00	1.3E-01	2.8E+02	5.2E+00	5.7E+02	9.8E+00	9.65	0.29	0.664666	14.52	0.22		
	z1				3.9E+02	9.4E+00	9.2E+03	1.5E+02	3.3E+04	2.8E+02	17.86	0.47	0.802984	22.23	0.30	24.8	5.6
	z2				3.0E+02	7.4E+00	8.6E+03	1.4E+02	1.3E+04	1.3E+02	20.10	0.56	0.793006	25.34	0.35		
	z4				*1.5E+02*	4.0E+00	*2.4E+03*	4.0E+01	*8.9E+03*	7.6E+01	*26.61*	0.74	*0.732645*	*36.29*	*0.50*		
	z5				*2.9E+02*	6.9E+00	*2.1E+03*	3.4E+01	*1.6E+04*	1.3E+02	*37.68*	0.95	*0.62685*	*60.05*	*0.76*		
	z6				1.2E+02	2.9E+00	3.4E+03	5.2E+01	9.3E+03	9.3E+01	16.78	0.44	0.759634	22.08	0.29		
N2	*a1*	34.279	77.291	4152	*1.5E+00*	5.7E-02	*5.2E+02*	9.9E+00	*5.7E+02*	1.1E+01	*1.733*	0.073	*0.639699*	*2.709*	*0.057*	13.2	1.5
	a2				3.2E+00	1.2E-01	2.0E+02	4.0E+00	4.2E+02	8.4E+00	8.60	0.36	0.672778	12.78	0.27		
	a3				9.8E-01	5.2E-02	7.9E+01	2.5E+00	1.7E+02	4.3E+00	6.44	0.38	0.55556	11.59	0.34		
	a5				4.5E+00	1.2E-01	2.0E+02	4.1E+00	7.4E+02	1.2E+01	9.24	0.27	0.65411	14.12	0.21		
	z1				9.0E+01	2.4E+00	3.1E+03	4.9E+01	2.4E+03	2.3E+01	19.26	0.59	0.779689	24.69	0.38	26.2	1.8
	z2				1.5E+02	3.6E+00	4.1E+03	6.6E+01	4.1E+03	4.6E+01	22.66	0.64	0.81249	27.88	0.39		
	z3				2.1E+02	5.2E+00	7.0E+03	1.1E+02	4.9E+03	4.3E+01	20.36	0.57	0.780668	26.07	0.37		
N3	z1	34.31	77.328	4154	1.4E+02	3.4E+00	4.4E+03	7.1E+01	3.5E+03	3.2E+01	20.03	0.58	0.795492	25.17	0.36	23.4	3.7
	z2				*1.9E+02*	4.5E+00	*7.9E+03*	1.3E+02	*4.0E+03*	3.6E+01	*16.30*	0.47	*0.815835*	*19.98*	*0.29*		
	z3				1.6E+02	3.8E+00	5.3E+03	8.5E+01	3.9E+03	3.6E+01	19.57	0.55	0.826258	23.68	0.33		
	z5				6.4E+01	1.6E+00	2.0E+03	3.3E+01	2.0E+03	2.7E+01	19.86	0.57	0.72556	27.36	0.39		
N4	a1	34.323	77.323	4980	1.8E+00	6.9E-02	8.1E+01	2.7E+00	2.6E+02	6.0E+00	9.91	0.43	0.653771	15.15	0.33	15.0	2.0
	a2				4.0E+00	1.3E-01	1.7E+02	4.4E+00	5.1E+02	1.0E+01	10.88	0.41	0.71135	15.30	0.29		
	a3				4.7E+00	1.3E-01	1.6E+02	3.9E+00	7.7E+02	1.4E+01	10.72	0.34	0.689671	15.53	0.24		
	z1				*2.7E+02*	6.4E+00	*1.0E+04*	1.7E+02	*7.9E+03*	7.7E+01	*17.04*	0.47	*0.761062*	*22.38*	*0.31*	27.4	3.0
	z2				1.8E+02	4.3E+00	5.2E+03	9.3E+01	4.1E+03	4.2E+01	21.92	0.63	0.791726	27.67	0.40		
	z3				2.3E+02	5.6E+00	7.0E+03	1.1E+02	5.7E+03	5.8E+01	21.81	0.61	0.801817	27.19	0.38		
N5	z4	34.3608	77.368	5645	4.7E+02	1.1E+01	1.4E+04	2.3E+02	8.9E+03	7.8E+01	23.13	0.65	0.834143	27.72	0.39	26.3	1.9
	z5				3.8E+02	9.2E+00	1.2E+04	1.9E+02	5.6E+03	5.2E+01	22.73	0.64	0.842888	26.96	0.38		
	z6				3.0E+02	7.4E+00	1.0E+04	1.6E+02	5.5E+03	5.2E+01	20.35	0.57	0.823519	24.71	0.35		
N6	z1	34.361	77.372	5426	4.2E+02	1.0E+01	1.9E+04	5.4E+02	1.2E+04	2.5E+02	15.04	0.52	0.764526	19.67	0.34	19.58	0.47
	z2				*5.7E+02*	1.4E+01	*1.8E+04*	3.1E+02	*1.5E+04*	1.4E+02	*20.89*	0.60	*0.808501*	*25.83*	*0.37*		
	z3				3.2E+02	7.7E+00	1.5E+04	2.7E+02	8.0E+03	6.9E+01	14.70	0.42	0.7529	19.52	0.28		
N7	a1	34.382	77.389	5014	4.2E-01	2.3E-02	2.5E+01	1.9E+00	1.9E+01	1.3E+00	11.03	0.95	0.691283	15.95	0.69	16.77	0.13
	a2				1.0E+00	4.2E-02	6.4E+01	2.2E+00	2.4E+01	1.3E+00	11.20	0.60	0.665276	16.83	0.45		
	a3				3.2E+00	1.3E-01	2.0E+02	5.3E+00	6.8E+01	2.3E+00	11.83	0.58	0.707159	16.72	0.41		
	z4				8.1E+02	1.9E+01	3.3E+04	5.5E+02	1.3E+04	1.3E+02	17.67	0.49	0.788026	22.41	0.31	22.46	0.06
	z5				8.8E+02	2.1E+01	3.3E+04	5.8E+02	1.5E+04	1.4E+02	18.65	0.53	0.829901	22.47	0.32		
	z6				8.9E+02	2.1E+01	3.5E+04	6.1E+02	1.4E+04	1.3E+02	18.09	0.51	0.804185	22.49	0.32		

N8	z1	34.424	77.383	5159	7.0E+02	1.7E+01	2.5E+04	3.9E+02	1.1E+04	1.1E+02	20.05	0.56	0.816418	24.55	0.34	22.4	2.2
	z2				2.9E+02	7.1E+00	1.3E+04	2.0E+02	6.2E+03	6.4E+01	16.07	0.45	0.807533	19.89	0.28		
	z3				4.4E+02	1.0E+01	2.0E+04	3.1E+02	5.3E+03	4.3E+01	16.23	0.46	0.781306	20.77	0.29		
	z5				1.5E+03	3.5E+01	5.0E+04	7.7E+02	2.2E+04	1.8E+02	20.46	0.57	0.859085	23.81	0.33		
	z6				2.1E+03	5.1E+01	7.0E+04	1.6E+03	3.9E+04	5.3E+02	21.09	0.66	0.838602	25.14	0.40		
N9	z1	34.431	77.374	5584	5.6E+02	1.4E+01	2.2E+04	3.5E+02	1.0E+04	8.9E+01	18.07	0.51	0.839894	21.51	0.30	20.3	1.1
	z2				3.7E+02	8.8E+00	1.6E+04	2.6E+02	7.4E+03	7.9E+01	16.16	0.46	0.802991	20.12	0.29		
	z3				5.0E+02	1.2E+01	2.0E+04	3.2E+02	1.5E+04	1.3E+02	16.71	0.47	0.85237	19.60	0.27		
N10	z1	34.433	77.394	4815	5.9E+02	1.4E+01	2.1E+04	3.4E+02	1.0E+04	1.1E+02	19.70	0.56	0.802453	24.54	0.35	20.1	3.1
	z2				3.1E+02	7.3E+00	1.6E+04	2.7E+02	6.6E+03	6.6E+01	13.34	0.38	0.796634	16.74	0.24		
	z3				4.7E+02	1.1E+01	2.3E+04	3.7E+02	7.8E+03	7.7E+01	14.87	0.43	0.791642	18.78	0.27		
	z5				2.7E+02	6.6E+00	9.8E+03	1.5E+02	4.4E+03	3.7E+01	19.00	0.55	0.780074	24.34	0.35		
	z6				3.6E+02	8.5E+00	1.5E+04	2.3E+02	7.6E+03	6.4E+01	16.53	0.46	0.796719	20.74	0.29		
N11	a1	34.492	77.425	4156	2.5E+00	1.5E-01	1.1E+02	3.0E+00	4.6E+02	8.7E+00	9.10	0.58	0.639258	14.22	0.45	10.5	6.7
	a2				*5.3E+00*	1.7E-01	*2.9E+02*	5.8E+00	*1.5E+03*	2.9E+01	*6.51*	0.23	*0.733892*	*8.86*	*0.16*		
	a3				1.9E+00	7.1E-02	6.4E+01	2.4E+00	2.5E+02	6.1E+00	12.00	0.53	0.643231	18.65	0.41		
	z1				1.1E+02	2.8E+00	5.4E+03	8.8E+01	3.7E+03	3.8E+01	14.15	0.40	0.778484	18.17	0.26	16.1	2.7
	z2				2.3E+00	1.3E-01	7.3E+01	2.9E+00	3.4E+02	4.7E+00	11.75	0.69	0.686088	17.12	0.51		
	z3				*1.1E+02*	2.6E+00	*6.3E+03*	1.0E+02	*3.7E+03*	3.8E+01	*11.41*	0.32	*0.78537*	*14.52*	*0.21*		
N12	z1	34.545	77.424	4285	2.7E+02	6.5E+00	1.2E+04	1.9E+02	1.1E+04	1.1E+02	14.63	0.39	0.80755	18.11	0.24	17.0	4.1
	z2				1.5E+03	3.7E+01	7.3E+04	1.3E+03	1.0E+05	1.1E+03	12.42	0.34	0.843168	14.73	0.20		
	z3				*2.9E+02*	7.2E+00	*9.2E+03*	1.5E+02	*1.0E+04*	9.2E+01	*19.42*	0.54	*0.762736*	*25.45*	*0.35*		
	z5				1.2E+02	2.8E+00	5.8E+03	9.0E+01	7.9E+03	6.6E+01	11.68	0.31	0.738016	15.83	0.21		
	z1	34.551	77.446	3411	2.9E+02	7.1E+00	1.2E+04	1.9E+02	7.9E+03	7.8E+01	16.59	0.47	0.776214	21.37	0.30	19.8	3.7
N13	z2				2.2E+02	5.3E+00	9.8E+03	1.6E+02	8.5E+03	8.5E+01	14.39	0.40	0.746059	19.28	0.27		
	z3				1.3E+02	3.1E+00	6.4E+03	1.1E+02	5.8E+03	6.2E+01	12.93	0.36	0.770122	16.78	0.23		
	z5				*1.1E+02*	2.8E+00	*3.8E+03*	6.0E+01	*3.4E+03*	3.1E+01	*18.52*	0.53	*0.717389*	*25.80*	*0.37*		
Transect C																	
S1	a1	33.972	77.819	3800	7.0E-01	4.0E-02	4.0E+01	1.5E+00	5.8E+01	3.0E+00	9.45	0.42	0.74341	12.71	0.92	11.2	2.2
	a2				3.0E-01	2.0E-02	3.2E+01	1.1E+00	9.3E+01	1.6E+02	5.06	0.40	0.4793	10.55	0.60		
	z1				3.1E+02	7.3E+00	1.2E+04	3.0E+02	5.0E+03	4.6E+02	17.83	0.66	0.80456	22.15	0.72	23.5	1.1
	z2				1.3E+03	2.9E+01	5.0E+04	9.5E+02	1.5E+04	2.3E+02	18.19	0.38	0.81011	22.45	0.66		
	z3				6.2E+02	1.5E+01	2.2E+04	4.4E+02	9.8E+03	3.2E+02	20.27	0.36	0.82974	24.42	0.74		
	z4				6.1E+02	1.4E+01	2.3E+04	4.1E+02	6.7E+03	1.0E+02	19.27	0.56	0.79689	24.17	0.70		
	z5				2.2E+02	5.0E+00	7.5E+03	1.8E+02	3.7E+03	1.6E+02	19.98	0.48	0.80891	24.69	0.80		
S2	z1	33.992	77.8411	3995	3.1E+02	7.3E+00	1.2E+04	3.0E+02	5.0E+03	6.5E+03	17.83	0.62	0.80456	22.15	0.72	23.0	1.5
	z2				1.1E+03	2.5E+01	3.6E+04	6.9E+02	1.6E+04	1.2E+02	20.94	0.58	0.79062	26.48	1.26		
	z3				2.7E+02	6.3E+00	9.6E+03	2.0E+02	4.0E+03	1.0E+02	19.53	0.58	0.78202	24.97	0.76		
	z4				3.0E+02	6.9E+00	1.2E+04	2.4E+02	4.6E+03	1.7E+02	17.12	0.38	0.81030	21.12	0.62		
	z5				3.0E+02	7.0E+00	1.2E+04	2.9E+02	5.5E+03	1.4E+02	17.90	0.42	0.75497	23.70	0.78		
	z6				2.0E+02	4.7E+00	7.8E+03	2.1E+02	4.9E+03	1.5E+01	17.05	0.36	0.74250	22.95	0.76		
S3	a1	34	77.863	4222	1.6E+01	4.2E-01	7.7E+02	1.6E+01	5.8E+02	6.8E+00	13.62	0.28	0.760596	17.90	0.56	16.9	2.1
	a2				2.6E+00	8.0E-02	1.8E+02	5.4E+00	1.4E+02	8.4E+00	9.32	0.46	0.59190	15.75	0.68		
	a3				1.7E+01	2.8E-01	6.4E+02	1.2E+01	5.3E+02	1.6E+01	17.46	0.42	0.76672	22.77	0.86		

	a4				2.0E+01	5.2E-01	9.0E+02	1.5E+01	1.1E+03	7.3E+00	13.20	0.58	0.81909	16.12	0.46		
	a5				1.0E+01	2.8E-01	5.7E+02	1.0E+01	4.0E+02	1.6E+02	11.97	0.64	0.75903	15.77	0.48		
	z1				2.6E+02	6.0E+00	8.4E+03	1.5E+02	6.8E+03	1.7E+02	20.33	0.68	0.82366	24.67	0.68	24.7	1.2
	z2				3.0E+02	7.3E+00	1.4E+04	2.8E+02	6.4E+03	3.0E+02	15.42	0.58	0.83641	18.44	0.56		
	z3				8.0E+02	1.9E+01	2.6E+04	5.2E+02	1.1E+04	1.7E+02	21.56	0.62	0.81239	26.53	0.76		
	z4				2.2E+02	4.9E+00	6.7E+03	1.5E+02	7.2E+03	2.4E+02	20.15	0.62	0.82717	24.35	0.70		
	z5				3.7E+02	8.4E+00	1.3E+04	3.0E+02	9.8E+03	3.0E+01	19.27	0.40	0.81915	23.51	0.70		
S4	a1	34.015	77.894	4800	9.7E+00	2.6E-01	4.1E+02	1.0E+01	1.0E+03	1.3E+01	11.60	0.70	0.74955	15.47	0.50	13.6	2.1
	a2				2.4E+00	1.2E-01	1.5E+02	3.8E+00	3.7E+02	1.1E+01	8.05	0.28	0.70746	11.37	0.58		
	a3				8.3E+00	2.2E-01	4.5E+02	9.0E+00	4.1E+02	2.5E+01	11.72	0.40	0.77587	15.10	0.46		
	a4				8.2E+00	2.2E-01	4.3E+02	1.2E+01	1.3E+03	9.9E+00	8.90	0.24	0.77290	11.52	0.36		
	a5				2.2E+00	8.0E-02	1.6E+02	1.0E+01	2.8E+02	2.7E+01	7.58	0.64	0.65529	11.56	0.70		
	a6				1.2E+01	3.2E-01	4.4E+02	1.0E+01	1.2E+03	4.4E+02	12.93	0.52	0.77461	16.69	0.54		
	z1				5.2E+02	1.2E+01	2.0E+04	5.1E+02	1.6E+04	2.5E+02	17.19	0.68	0.832195	20.65	0.68	23.3	2.0
	z2				3.5E+02	8.0E+00	1.1E+04	2.9E+02	8.2E+03	2.4E+02	20.21	0.78	0.82242	24.57	0.78		
	z3				3.9E+02	9.1E+00	1.3E+04	3.1E+02	7.9E+03	2.7E+02	20.92	0.74	0.82289	25.41	0.82		
	z4				4.7E+02	1.1E+01	2.0E+04	5.1E+02	9.1E+03	5.1E+02	16.69	0.28	0.81880	20.38	0.70		
	z5				6.2E+02	1.4E+01	1.9E+04	4.8E+02	1.8E+04	2.4E+02	20.46	0.24	0.84861	24.10	0.74		
	z6				4.0E+02	9.0E+00	1.3E+04	2.7E+02	8.3E+03	1.3E+01	21.35	0.24	0.82422	25.89	0.76		
S5	a1	34.0396	77.923	5280	2.3E+00	8.0E-02	1.4E+02	1.1E+01	4.8E+02	2.3E+00	7.06	0.26	0.68028	10.38	0.58	10.3	1.4
	a2				3.9E-01	4.0E-02	2.6E+01	2.0E+00	7.7E+01	8.8E+00	6.93	0.26	0.55402	12.50	1.28		
	a3				1.7E+00	8.0E-02	1.3E+02	2.8E+00	3.9E+02	6.8E+00	6.02	0.50	0.70372	8.56	0.40		
	a4				2.4E+00	1.4E-01	1.9E+02	3.8E+00	4.1E+02	9.5E+00	6.54	0.56	0.67695	9.65	0.58		
	a5				3.7E+00	1.0E-01	2.2E+02	4.8E+00	5.9E+02	1.8E+02	8.08	0.70	0.68558	11.79	0.36		
	z1				2.6E+02	5.7E+00	7.4E+03	1.5E+02	6.7E+03	1.2E+02	22.40	0.50	0.82101	27.27	0.78	29.0	1.8
	z2				*2.5E+02*	*6.0E+00*	*9.9E+03*	*2.0E+02*	*5.6E+03*	*9.8E+02*	*17.42*	*0.24*	*0.82374*	*21.14*	*0.62*		
	z3				1.3E+03	2.9E+01	3.0E+04	5.2E+02	4.4E+04	2.5E+02	24.23	0.58	0.82727	29.28	0.80		
	z4				6.5E+02	1.5E+01	1.7E+04	3.3E+02	9.9E+03	1.9E+02	26.65	0.78	0.84117	31.67	0.94		
	z5				2.6E+02	6.2E+00	7.5E+03	1.8E+02	5.3E+03	1.1E+02	23.14	0.42	0.81745	28.30	0.92		
S6	a1	34.085	77.95	4983	2.5E+01	6.4E-01	9.0E+02	1.6E+01	4.9E+03	5.4E+01	9.78	0.40	0.805010	12.14	0.36	11.08	0.71
	a2				1.2E+01	3.0E-01	4.9E+02	9.4E+00	2.7E+03	8.9E+01	8.20	0.66	0.70061	11.70	0.34		
	a3				1.7E+01	4.2E-01	7.1E+02	1.3E+01	3.7E+03	4.4E+01	8.50	0.38	0.81368	10.44	0.3		
	a5				1.1E+01	3.0E-01	5.1E+02	1.2E+01	2.3E+03	5.9E+01	8.04	0.36	0.77979	10.31	0.32		
	a7				1.0E+01	2.6E-01	4.1E+02	9.8E+00	2.2E+03	2.6E+02	8.41	0.56	0.75887	11.09	0.36		
	z1				3.2E+02	6.8E+00	1.1E+04	2.4E+02	1.1E+04	2.2E+02	17.87	0.48	0.83053	21.51	0.60	22.1	1.4
	z2				3.0E+02	6.8E+00	9.6E+03	1.9E+02	8.1E+03	3.7E+02	19.96	0.62	0.82407	24.21	0.68		
	z3				*1.2E+03*	*2.5E+01*	*3.0E+04*	*5.6E+02*	*1.6E+04*	*2.3E+02*	*26.73*	*0.58*	*0.83517*	*32.00*	*0.84*		
	z4				3.2E+02	7.5E+00	1.2E+04	2.3E+02	9.8E+03	1.2E+03	17.86	0.58	0.84671	21.09	0.68		
	z5				*4.3E+02*	*1.0E+01*	*4.0E+04*	*1.0E+03*	*2.2E+04*	*3.3E+02*	*7.35*	*0.38*	*0.82351*	*8.92*	*0.60*		
	z6				4.8E+02	1.1E+01	1.7E+04	4.1E+02	1.2E+04	0.0E+00	18.71	0.42	0.83953	22.28	0.70		

*Absolute measured abundances. 4He measurement used to calculate the "raw date," which was not corrected for the effects of 4He loss due to alpha particle recoil. The mean Fτ correction calculated following Farley et al. (1996) for apatite and Hourigan et al. (2005) for zircon.
^ The Fτ corrected date of the crystal. This age was recalculated with a Fτ corrected 4He measurement.
Statistically significant outliers that were excluded from consideration are shown in italics.

CHAPTER 5

LATE CENOZOIC TECTONICS OF THE SOUTHWESTERN MARGIN OF THE TIBETAN PLATEAU FROM LOW-TEMPERATURE THERMOCHRONOLOGY AND ONE-DIMENSIONAL THERMAL MODELING

1. Abstract

The western margin of the Tibetan Plateau is bound by the predominantly sinistral, generally NE-striking Longmu Co fault system and the predominantly dextral, generally NW-striking Karakoram fault system. The two fault systems come close to intersecting each other in the Ladakh region of northwest India. New mapping based on multispectral remote sensing imagery augmented by field mapping suggests that the main strand of the Longmu Co fault system changes strike as it approaches the region of intersection to become roughly parallel to the Karakoram fault, a relationship consistent with large-scale drag folding. U-Pb geochronology indicates that the Karakoram fault system in this area initiated at ca. 15 Ma (Phillips et al., 2004) coincident with the onset of east-west extension in central and southern Tibet. If the Longmu Co Fault were also to have initiated ca. 15 Ma, then the KFS and the LCF systems may have been acting as a conjugate pair since the onset of extension. (U-Th)/He and $^{40}Ar/^{39}Ar$ closure dates for minerals from bedrock samples collected from between the two fault strands show a progressive decrease from southwest to northeast. We posit that this trend is the result of a progressive, late Cenozoic northward sweep of shortening across the region, which was followed by a northeastward-propagating domain of lower exhumation rate. One-dimensional thermal-kinematic models of multi-chronometer datasets support this idea,

with models showing exhumation rates that decrease across the region from southwest to northeast. We infer that the observed large-scale bending of the Longmu Co fault reflects both this shortening and dextral shear along the Karakoram fault system.

2. Introduction

Major transcurrent fault systems surrounding the Tibetan Plateau have played a fundamental role in the late Cenozoic evolution of the Himalayan-Tibetan orogenic system. In the Ladakh region of northwest India, the southwestern edge of the plateau is defined by the intersection of two of these systems: the Karakoram fault (KFS) and the Longmu Co fault system (LCF; Figure 1). The NW-SE striking Karakoram fault exhibits primarily dextral motion; however, it contains a significant component of oblique motion along its central segment. The NE-SW striking Longmu Co fault is a sinistral strike-slip fault that is considered to be the southwestern extension of the Altyn-Tagh fault (Liu, 1993; Raterman et al., 2007). The slip along these late Cenozoic structures is consistent with E-W extension across the central and southern plateau (e.g., Robinson, 2009), and the best estimates for KFS initiation mirrors the beginning of this extension (ca. 15 Ma; Phillips et al., 2004; Wallis et al., 2014). This suggests that the primary role of the KFS and LCF systems since ca. 15 Ma is to accommodate the eastward extrusion of Tibet.

One aim of this study is to determine the differential exhumation history of the Pangong Range (PR), the Karakoram Range (KR) and the Ladakh Range (LR; Figure 1). Recognizing spatial and temporal changes in the exhumation patterns of these ranges, which are in the vicinity of the KFS and LCF, will allow for better constraints on how this part of the orogen has evolved to accommodate changing stress fields during

collision, as well elucidate the timing and sense of motion of the KFS in the Ladakh region. A related goal is to understand the interaction of the LCF and KFS systems and the role they play in accommodating coeval north-south shortening and east-west extension across this part of the orogenic system.

Here we present U-Pb, $^{40}Ar/^{39}Ar$, and (U-Th)/He data from samples collected across the Ladakh region, spanning the area between the two fault systems. We present cooling ages from these samples, and perform 1-D thermal-kinematic modeling to explore the exhumation history across the KFS. These data, coupled with field observations and maps made utilizing ASTER remote sensing, inform our geologic and structural interpretations of the Ladakh region.

3. Geologic Setting

The Ladakh region of NW India is of particular interest because it exposes the boundary between the 5-km high Tibetan Plateau and the Himalaya proper. This boundary is presently demarcated by the Karakoram fault system. North of the KFS in this region is the Karakoram Range, which stretches from the Pamirs in the northwest to the Shyok River in the southeast. To the southwest of the KFS is the Shyok suture zone, which marks the collision between the Lhasa Terrain and the Kohistan-Ladakh Arc. This closure likely occurred during the Cretaceous (Treloar et al., 1989), although estimates for closure timing have been posited to be as young as 40 Ma (Bouilhol et al., 2013). South of the Shyok suture zone is the Ladakh Range, dominated by the calc-alkaline Ladakh batholith, part of the 2500 km long Transhimalayan Plutonic Belt (e.g., Honegger et al., 1982; Scharer et al., 1984). Flanking the Ladakh batholith to the south is the Indus-

Yarlung suture zone, which marks the final collision between greater India and Eurasia (Gansser 1964, 1980; Allegre et al. I984; Searle et al. 1987) at ~50 Ma (e.g., Patriat and Achache, 1984; Klootwijk et al., 1992). The Indus-Yarlung suture zone separates the Transhimalayan Plutonic Belt in the north from the Tibetan Sedimentary series to the south. Between the Ladakh batholith and the Karakoram Range lies the elongate Pangong Range. Below, we review the history and relationships of key features in more detail.

4. Ranges

4.1 Ladakh Range

The calc-alkaline Ladakh batholith (LB) is part of the Transhimalayan Plutonic Belt that extends from Afghanistan to Bhutan. The batholith itself trends NW and is approximately 600 km long and 40 km wide. It is composed primarily of Andean-type, Late Paleocene-Early Eocene continental arc plutonic rocks (Searle, 1991) which range in composition from diorite to granite. To the north, the LB is overlain by the Khardung volcanic unit-- considered its extrusive equivalent (e.g., Srimal 1986a; Srimal et al. 1987; Weinberg et al., 2000; Figure 2). The Ladakh Range is bounded to the south by the Indus-Yarlung suture zone and to the north by the Karakoram fault system and the Khalsar Thrust (Srimal et al., 1987; Figure 2). The Khalsar Thrust has been interpreted as a reactivated part of the Shyok suture zone (Rex et al, 1988; Weinberg et al., 2000). Published thermochronologic constraints include $^{40}Ar/^{39}Ar$ mica and K-feldspar dates (Searle et al., 1989; Dunlap et al., 1998). These data imply that the bedrock cooled below ca. 490-230ºC (Hodges, 2014) during the Middle to Late Oligocene. Apatite fission track studies suggest the LB had cooled to below 120ºC by Miocene times (Clift et al. 2002;

Kirstein et al. 2006). Tilted units of the Khardung volcanic unit indicate that the batholith was rotated northward during the initial collision between India and Asia (Kirstein et al., 2006, 2009). Thermochronologic data and thermal-kinematic modeling suggest that during the Oligocene-late Miocene the batholith either experienced southward tilting (Kirstein et al., 2006, 2009) or a northward sweep of exhumation related to denudation created by shortening (Chapter 4). The Chilam granite, which is located on the northern edge of the Ladakh batholith (Figure 2), is separated from the main body of the batholith by the Khardung volcanic unit. Dunlap and co-workers (1998) argued on the basis of its mineralogy that the Chilam granite is part of the Ladakh suite of intrusive rocks.

4.2 Pangong Range

The Pangong Range (Figure 1) consists of granulite to amphibolite facies metasedimentary and metaigneous rocks intruded by igneous rocks ranging in composition from diorite to leucogranite (Searle et al., 1998; Weinberg and Searle, 1998; Rolland et al., 2009). U-Pb crystallization ages of igneous rocks within the Pangong Range reflect multiple episodes of magmatic intrusion and anatectic melting, and these rocks are sometimes referred to as the Pangong injection complex. Most leucogranites within the Pangong Range were intruded between ca. 20-14 Ma (Searle et al., 1998; Phillips et al., 2004; Jain and Singh, 2008; Ravikant et al., 2009; Reichardt et al., 2010; Leloupe et al., 2011; Boutonnet et al., 2012) but other granitoids have crystallization ages between ca. 74-55 Ma (Jain and Singh, 2007; Ravikant et al, 2009; Reichardt et al., 2010) and ca. 108-104 Ma (Searle et al., 1998; Phillips and Searle, 2007; Boutonnet et al., 2012). A few of the larger plutons in the range have been named. The Tangtse Pluton,

located on the western side of the range was intruded between ca. 18 and 15 Ma (Phillips et al., 2004; Reichardt et al., 2010). The Durbuk Pluton, northwest of the Tangtse pluton, yields a similar crystallization age of ca. 20-15 Ma (Ravikant et al., 2009). These U-Pb zircon crystallization ages are also similar to those obtained for the Karakoram igneous complex to the north-northeast (Weinberg et al., 2000; Phillips et al., 2004; Weinberg et al., 2000; this study). Streule et al. (2009) suggested that the Pangong metamorphic complex (all metamorphic rocks contained between the two fault strands) represents deeper structural levels of the Karakoram metamorphic and igneous complex that underlies most of the Karakoram Range. Rolland and Pecher (2001) determined that metamorphic rocks within the PR originated from a depth of >20 km. Wallis et al. (2014) determined that peak metamorphism in the region occurred prior to the initiation of the KFS as a result of crustal thickening and magmatism, but agree with previous workers that the Pangong Range was exhumed from depths of 19-20 km. We follow these workers (e.g., Searle et al., 1998; Phillips and Searle, 2007; Struele et al., 2009) in interpreting the Pangong Range as having been extruded along the Karakoram fault system.

Based on $^{40}Ar/^{39}Ar$ thermochronology of amphiboles and biotites, Dunlap et al. (1998) found that the Karakoram fault zone rocks show two phases of rapid cooling – one from ca. 17 to 13 Ma and another starting at 8 Ma and continuing until at least 7 Ma. Additional cooling ages from hornblende samples across the PR (Rolland et al., 2009; McCarthy and Weinberg, 2010), suggest that the range was actively exhuming through the ca. 500ºC isotherm by at least 13.5 Ma and that most of its exhumation occurred before 10 Ma (McCarthy and Weinberg, 2010).

4.3 Karakoram Range

The Karakoram Range is bound in the north by the Pamirs, and in the south by the Gilgit, Indus and Shyok Rivers. Much of what is known regarding the geology of the Karakoram Range is based on studies undertaken in Pakistan prior to the modern era of political instability in the region (Searle, 1991). There have been a few studies of the Karakoram Range in NW India, mostly focused on exposures found adjacent to the Pangong Range and east of the Shyok River in an extension of the Karakoram Range known as the Chang-Chenmo Range (Figure 1). The Karakoram Range to the northeast of the KFS (Figure 1) exposes igneous and metamorphic rocks representing a Late Jurassic – Middle Cretaceous Andean-style arc predating the closure of the Neo-Tethys ocean basin (e.g., Searle, 1999). The igneous rocks of this range have intruded rocks of the Karakoram metamorphic complex in the south (Roy, 2010) and Karakoram Tethyan basin sedimentary rocks in the north (Srimal et al., 1987; Sinha et al., 1999; Figure 2). The Karakoram Tethyan Carboniferous-Permian sequence consists of six lithostratigraphic units composed mainly of sedimentary and volcanic rocks (Sinha et al., 1999). Granites and leucogranites exposed within the Karakoram Range represent multiple phases of magmatism during the Middle Cretaceous, Paleocene-Eocene and Miocene (Parrish and Tirrul, 1989; Schârer et al., 1990; Searle et al., 1992; Searle et al., 1998; Weinberg et al., 2000; Fraser et al., 2001; Phillips et al., 2004; Ravikant et al., 2009; this study). The area to the north of the Chang-Chenmo Range (Figure 1) has not been deeply exhumed, as adjacent Asian passive margin strata are well preserved and relatively flat-lying (Norin 1946 in Dunlap 1998; Figure 1). However, in Karakoram

Range in Pakistan, evidence of deep exhumation since ca. 20 Ma exists (Searle et al., 1989).

The Karakoram metamorphic complex, found NE of the Pangong Range between the Shyok River and Pangong Tso, consists of metamorphosed Paleozoic-Mesozoic sedimentary rocks (McCarthy and Weinberg, 2010). Described units include psammites, marbles, amphibolites, and various types of schists, including garnet-biotite- staurolite schist (Dunlap et al., 1998; McCarthy and Weinberg, 2010; Wallis et al., 2014), as well a prominent leucogranite sheet. Wallis et al. (2014) found that rocks in the Pangong Range and the Karakoram Metamorphic Complex record a similar pressure, suggesting that they were metamorphosed during a regional metamorphic event.

5. Faults

5.1 Karakoram fault system

The Karakoram fault is a NW-SE striking dextral, strike-slip fault system that extends ~1000 km from the Pamirs to at least the Gurla Mandata region, and forms the southwestern boundary of the Tibetan Plateau. Its northern end is a structurally complex region of thrust faults and younger, transtensional basins (Burtman and Molnar, 1993; Strecker et al., 1995; Robinson, 2009a). The nature of the southern terminus of the KFS is debated. Some work asserts that the fault terminates at the Pulan Basin adjacent to the Gurla Mandata detachment system (Murphy et al., 2002), whereas other work suggest that it continues past Gurla Mandata into the Himalaya (Murphy and Copeland, 2005; Murphy et al., 2014). Other authors contend that its strain is transferred to a reactivated segment of the Indus-Yarlung suture zone (Lacassin et al., 2004).

In the Ladakh region of northwest India, the KFS bifurcates around the Pangong Range (Figures 1 and 2). The northern and southern strands of the KFS are referred to as the Pangong and Tangtse strands, respectively (discussed below and in Chapters 2 and 3). Phillips and Searle (2007) described a variety of moderate temperature deformation fabrics along both strands, including S-C foliations, asymmetric boudins, and stretching lineations consistent with the known dextral shear sense of the KFS. Much debate has centered on the age of initiation of the fault system in this area. U-Pb geochronology of leucogranite dikes that both predate and postdate mylonitic fabric of the Tangtse strand suggests that moderate temperature shearing began after 15.7 Ma and was completed by ca. 13.7 Ma (Phillips et al., 2004). However, based on field relationships from different outcrops and alternate interpretations of metamorphic and structural data, other authors posit that the initiation age of the fault is closer to ca. 23-18 Ma (Weinberg and Mark, 2008; Weinberg et al., 2009; Sen et al, 2009; Rolland et al., 2009; Leloup et al. 2011; Boutonnet et al., 2012; Sen et al., 2014).

The total offset along the KFS and its slip history are also controversial topics, with escape tectonic models (e.g., Avouac and Tapponnier, 1993; Tapponnier et al., 2001) implying 1000 km or more of offset, and other models suggesting 400 km or less (e.g., Searle et al., 1998; Lacassin et al., 2004; Phillips et al., 2004; Robinson, 2009b). These contrasting interpretations, and disagreements regarding the initiation age of the KFS (Phillips et al., 2004; Lacassin et al., 2004; Phillips and Searle, 2007; Valli et al., 2007, 2008; Rolland et al., 2009; Leloup et al. 2011, Boutonnet et al., 2012; Sen et al., 2014), lead to estimates of Miocene-Recent integrated slip rates ranging from < 5 mm/yr to > 25 mm/yr. Quaternary slip rates continue to be the subject of debate. Early workers

concentrating on the southeastern part of the KFS in southern Tibet (e.g., Liu et al., 1992; Avouac and Tapponnier, 1993) suggested Quaternary slip rates of ca. 32 mm/yr. More recently, Chevalier et al. (2005, 2012) have estimated lower rates, from ca. 5-9 mm/yr in the northwest to ca. 7-12 mm/yr in the southeast. In the Ladakh region of India, Brown and co-workers (2002) determined a slip rate of 4 ± 1 mm/yr on the Pangong strand of the KFS. Recent work by Bohon et al. (Chapter 3) found evidence for as much as 6 mm/yr of additional slip on the Tangtse strand between ca. 34 ka and ca. 6 ka, with evidence for minimal recent slip (< 12.6 ka). Robinson (2009a) found no evidence of slip over the past 150 kyr on the KFS along the far northwestern segment of the KFS in western Tibet. Over much shorter timescales, GPS and InSAR data show that present-day motion along the KFS overall is between 1-3 mm/yr (Jade et al., 2004; Wright et al., 2004; Jade et al., 2010) with one early study suggesting rates as high as ca. 11 mm/yr (Banerjee and Burgmann, 2002).

For most of its length, the KFS trends 325º. However, it deviates from this orientation near the northern end of the Pangong Range (~N 34.5∞). The mechanism for the formation of this bend in the fault system is debated. Raterman et al. (2007) speculated that this deviation from the average strike reflects the impingement of the KFS as it intersects the Longmu Co fault system (LCF). The bend in the KFS, in their estimation, is the result of either left-lateral motion along the LCF causing deformation at the fault intersection, or bend initiation causing development of the southwestern LCF system. They also note that the amount of displacement mapped along the LCF (25-32 km) is suspiciously similar to the amount of bend in the KFS when measured perpendicular to strike (27 km). An alternate but similar idea from Robinson (2009a) is

that, rather than creating the bend in the KFS, the initiation of the LCF caused either strain transfer or impingement of the KFS to essentially terminate slip along the northern section of the fault. Conversely, McCarthy and Weinberg (2010) argue that the bend in the Karakoram fault system is the natural result of transpression, which caused the bifurcation of the fault and the uplift of the Pangong Range. Their observations of large scale folding within the Karakoram Range and adjacent valleys, dextral thrusting in the Pangong Range, and the relative amounts of exhumation between the Pangong and Karakoram metamorphic complexes led them to conclude that the Pangong Range is obliquely thrust over the Karakoram metamorphic complex as a result of the northward indentation of the rigid Ladakh batholith. They argue that their observations do not support hypotheses wherein interactions between the LCF system and the KFS caused the bend in the KFS.

5.2 Pangong strand (northern strand)

The KFS splits into 2 distinct strands near the village of Agham (Figure 2). From there, the Pangong strand continues southeast toward Shyok Village. It continues past Muglib and along the southwestern side of Pangong Tso before rejoining with the southern Tangtse strand near the southeastern end of the Pangong Range. Low-temperature deformation fabrics along the Pangong strand have been described in detail by Rutter et al. (2007), and include marble cataclasites and clay-bearing fault gouges that overprinted pre-existing ductile fabrics during transpressive uplift of the Pangong Range. Southeast of Muglib, Quaternary landform offsets are described by Brown et al. (2002). Those workers found recent slip rates to be 4 ± 1 mm/yr.

5.3 Tangtse strand (Southern strand)

The Tangtse splits from the Pangong strand northwest of the Pangong Range and continues in a southeasterly direction through the villages of Agham, Tangyar, Durbuk and Tangtse (Figure 2). From there it follows the southwest side of the Pangong Range before bending east to rejoin the Pangong strand. No significant low-temperature deformation fabrics have been found in the bedrock outcrops of the Tangtse strand. This lack of cataclastic rocks in bedrock outcrops along this strand have led workers (e.g., Phillips et al., 2004; Rutter et al., 2007) to infer that all of the modern slip on the KFS through the Pangong region is concentrated along the Pangong strand and that the Tangtse strand is inactive. However, where the Tangtse strand passes out of the bedrock and through sediments toward the northwestern end of the Pangong Range, the structure clearly has a signature of Quaternary slip. However, this strand appears to have had a much lower slip rate since that time relative to the Pangong strand.

5.4 Longmu Co fault system

The sinistral Longmu Co Fault system (LCF; Figure 1) is speculated to be a southwestern extension of the Altyn-Tagh Fault system (Liu, 1993; Raterman et al., 2007). It separates the Tianshuihai terrain to the north from the Qiangtang terrain to the south (Matte et al., 1996). Late Miocene-Pliocene structural reorganization of the western Altyn Tagh and Karakoram faults is thought to have caused initiation of the Longmu Co fault to allow eastward growth of the Tibetan Plateau (Raterman et al., 2007). Whereas the fault has experienced at least 25-32 km of total slip (Raterman et al., 2007), InSAR

results show no current motion along the main strand of the fault, although they do indicate between 5-10 mm/yr of motion along a northern splay (Wright, 2004). Raterman et al. (2007) estimate a Quaternary slip rate of 8 ± 3 mm/yr and a geodetic slip rate of 3 ± 1 mm/yr for the LCF. Based on possible slip rates for the LCF and the amount of bending of the KFS, they suggest an initiation age for the LCF of 10-3 Ma.

6. Satellite imagery based mapping

Many geologic maps have been made of the Ladakh region (e.g., Searle, 1996; Dunlap et al., 1998; Ravikant, 2006; Phillips, 2008), but the published results are contradictory or incomplete because geopolitical disputes and high, rugged topography have precluded detailed geologic mapping in a variety of critical areas. Even the most recent, comprehensive maps (e.g., Phillips, 2008) focus only on the more accessible geology proximal to the trace of the Karakoram fault system. Advanced Spaceborne Thermal Emission and Reflection Radiometer (ASTER) imagery has allowed us to expand earlier results into a more regional geologic map of the entire Ladakh area (see Chapter 2).

The ASTER instrument is a high-resolution, multi-spectral imaging system aboard the TERRA satellite that is used for collecting terrestrial ground surface and atmospheric data (Yamaguchi et al., 1998). We employed decorrelation stretches of thermal infrared, AST05 (Level 2) data – with a resolution of 90 m/pixel – to build our maps. In order to convert spectral response to rock type, we obtained laboratory infrared spectra for critical rock types throughout the accessible parts of the study area, and we used them to devise unit classification schemes. Additional details of our remote sensing

analytical methods may be found in Chapter 2. The resulting lithologic map (Figure 2) correlates well with existing maps for accessible areas but extends the mapped area significantly to the east and northeast. Our ASTER-derived mapping units sometimes correspond to previously used map units, but frequently they do not. In Figure 3, we show correlations between our mapped units and those of Phillips, 2008.

We separated the region into three sections based on tectonic location; the Karakoram, Ladakh, and Suture Zone Complexes (Figure 2). The Karakoram Complex is further subdivided into the Tethyan sedimentary domain, the Karakoram batholith and proximal country rocks region, and the Metamorphic domain. We were able to clearly distinguish and map three basic units within the Tethyan sedimentary domain: a cherty calcareous sedimentary unit (Kt1), a clastic and volcanoclastic sedimentary unit (Kt2) and a clastic sedimentary unit (Kt3). Notably, the southernmost exposures of the Longmu Co fault zone mapped by Raterman et al. (2007) are marked by a unit of calcareous schists, calc-silicate gneisses and a unit impure marbles, both of which are highly strained. We tentatively interpret these units to be a slice of the Karakoram Tethyan sequence that experienced contact metamorphism as a consequence of intrusion of granitic rocks of the Karakoram batholith. We posit that the northernmost of these units is lying along a splay off the Longmu Co fault that strikes north-northwest along the upper reaches of the Shyok River. Beyond a point at about 78˚20'E, the calcareous schists and calc-silicate gneiss exposures cannot be distinguished in the ASTER data and we were unable to trace the fault splay to the NW as it strikes into mixed granitic and metamorphic rocks. The second continuation of the marble unit can be followed approximately 60 km westward and northwestward as a dismembered body entirely

surrounded by Karakoram batholith granites (Ki2; described below). This belt of rock was encountered in the Shyok Valley as part of our field reconnaissance of the area shown in Figure 4. The strongly deformed nature of these outcrops and their similarity with units mapped along the Longmu Co fault system farther east led us to interpret these outcrops as marking the trace of the main strand of the Longmu Co fault system as it passes through Karakoram Range. We tentatively correlate these rocks with the Saser Formation as mapped by Phillips (2008) north of the intersection of the Shyok Suture zone and the KFS.

The Karakoram batholith and proximal country rocks consists of a series of three units distinguished by varying amounts of igneous intrusion into the metamorphic country rocks. In the Ki1 unit large granitic plutons have been intruded into Tethyan sedimentary rocks. To the south, a massive granitoid batholith (Ki2) gradually transitions into amphibolites, calc-silicates and migmatites with many small-scale (meter to sub-meter) granitic intrusions (Ki3). Unlike most authors (e.g., Dunlap et al., 1998; Phillips, 2008; Leloupe et al., 2011), we did not attempt to subdivide the complex suite of rocks within the central and southern Pangong Range; instead, we classify them all simply as Ki3.

The Metamorphic domain consists primarily of rocks exposed within the Chang Chenmo Range, the northern Pangong Range and along the Nubra Valley. Within the Chang Chenmo Range unit Km5 is composed of clastic and metasedimentary rocks. South of the Km5 unit is the Bangong-Nujiang suture zone and the Karakoram Metamorphic Complex (e.g. Phillips, 2008), which on our map are grouped together into unit Km6 - volcanoclastic and clastic sedimentary rocks with ophiolitic blocks and

carbonate bands. Along the northern section of the Pangong Range we define a unit of schists, calc-silicates, marble and amphibolite bands (Km2). Just north of the Km2 unit and along the Nubra Valley are outcrops of metapelitic schists, metavolcanics and occasional marbles that we designate as Km1. This unit corresponds to the Nubra Formation mapped by Phillips (2008; Figure 3).

The Ladakh Complex and the Suture Zone Complex both lie south of the Karakoram fault system. The Ladakh Complex is subdivided into three units; the plutons of the Ladakh batholith (Lb), the felsic, extrusive Khardung volcanic unit (Lkv) and the Chilam granite (Lcg). The Suture Zone Complex consists of the Saltoro molasse (Ssm), Volcanic rocks (Svr) and intrusive igneous rocks found at the southern tip of the Shyok Range and across the Shyok River near Tirit (Si). Additionally, rocks that appear very similar to the Ki3 unit are found within the Shyok Range. The relationship of these rocks to the surrounding units is unclear-they may be Ki3 rocks in a faulted relationship with rocks of the Shyok Range, or they may be a separate unit that surficially appears similar to Ki3 in both its spectral characteristics and in outcrop. Further investigation of this unit to determine its appropriate correlation is warranted.

7. Geochronology and Thermochronology

The regional lithologic map described above provides a context for geochronologic and thermochronologic sampling and helps to inform our interpretation of the results. Below, we present U-Pb, $^{40}Ar/^{39}Ar$, and (U-Th)/He data from samples collected across the Ladakh region (Figure 5).

7.1 U-Pb geochronology

7.1.1 Sampling strategy

Most rock units within the Eastern Karakoram Range are not well dated. We took advantage of our reconnaissance geologic work along the Shyok River – a region that has been off-limits to foreign scientists until only recently – to collect two samples; a granite (SY3) and a diorite (IC2) for U-Pb geochronology in an effort to constrain intrusive ages. Sample SY3 was collected from a large pluton within unit Ki2. Sample IC2 is proximal to sample SY3 (Figure 2), but sample IC2 was collected from an outcrop of diorite from unit Ki3.

7.1.2 Method

Zircon crystals were obtained from whole rock samples using conventional crushing, sieving, gravimetric and magnetic separation techniques. All mineral separation was done at ASU. Grains of appropriate size (>150 μm) were hand-picked and incorporated into a mount that was polished and cleaned before analysis. U-Pb geochronology was completed at the Arizona LaserChron Center (www.geo.arizona.edu/alc) at the University of Arizona using Laser-Ablation Multicollector-Inductively Coupled Plasma Mass Spectrometry (LA-MC-ICPMS; Gehrels et al., 2006, 2008). Cathodoluminescence (CL) images were acquired prior to sampling in order to inform ablation spot placement. The zircons were ablated with a New Wave UP193HE Excimer laser using a spot diameter of 30 μm. The ablated material was carried in helium to a Nu HR ICPMS where U, Th, and Pb isotopes were simultaneously measured.

The analytical data are reported in Table 1. Uncertainties for all dates in this paper are reported at the 2σ level. In this table we include only analytical errors. Data that were >10% discordant, as well as any $^{206}Pb/^{238}U$ dates with an error greater than 10%, were excluded from the results.

7.1.3 Sample SY3 data and interpretation

In sample SY3, some grains show simple magmatic oscillatory zoning, but most have xenocrystic cores that are easily recognizable under cathodoluminescence (CL) because of their color difference, irregular geometry and the truncation of intracrystalline zoning. Thirty-seven grains were analyzed, with sixty total analyses – 37 cores and 23 rims (Table 1; Figure 6). Two core measurements were excluded because of discordance. Eleven core dates range from ca. 2708-556 Ma, whereas the remaining cores dates are distributed throughout the Paleozoic and early Mesozoic (Table 1; Figure 6). We interpret the core dates as indicative of inheritance. In particular, the Archean and Proterozoic ages suggest Indian crustal contamination (Zhu et al., 2009; 2011). The rim dates cluster well, with fifteen yielding an error-weighted mean age of 14.58 ± 0.21 Ma (MSWD = 0.57; Figure 6), which we interpret to be the crystallization age of the granite. Similar Middle Miocene U-Pb ages have been reported for granites scattered throughout the Pangong Range **(**Searle et al., 1998; Phillips et al., 2004; Leloupe et al., 2011; Boutonnet et al., 2012**)** and at least one granite from the eastern Karakoram Range (Weinberg et al., 2000). Similar ages have been reported for a variety of granitic units in the central and western Karakoram Range (Searle et al., 1989, 1992; Parrish and Tirrul, 1989; Phillips et al., 2013).

7.1.4 Sample IC2 data and interpretation

The zircon suite from sample IC2 is complex both structurally and isotopically. While a few crystals display only oscillatory zoning indicative of a single phase of igneous crystallization, a few others show distinctive xenocrystic cores similar to sample SY3 zircons. But most IC2 zircons show complicated growth patterns involving igneous growth – sometimes polyphase – followed by local recrystallization, metamorphism, or both (Figure 7). In an attempt to unravel this history, we analyzed 24 grains, and dated 23 cores and 19 rims (42 total analyses; Table 1; Figure 7). Concordant core dates ranged from 789 ± 22 Ma to 50.8 ± 7.2 Ma, while rim dates ranged from 165 ± 11 Ma to 32.9 ± 1.4 Ma. Some of the observed spread in the dates of both the cores and rims may be because the laser spot size during analysis was, in most cases, larger than the scale of zoning between igneous and metamorphic growth zones. Both core and rim dates cluster at ca. 160-165 Ma, which we regard as our best current estimate for the intrusive age of the granite. We interpret older dates as indicative of inheritance and younger dates as indicative of Pb disturbance by metamorphism.

7.2 $^{40}Ar/^{39}Ar$ Thermochronology

7.2.1 Sampling strategy

Although the KFS is generally considered a dextral fault, there is a significant component of oblique slip along its central portion (e.g., Searle et al., 1998; Dunlap et al., 1998; Phillips and Searle, 2007; Struele et al., 2009). This vertical component of fault motion can be explored by utilizing mineral systems that record cooling as a result of

tectonically induced uplift and subsequent exhumation. To determine the relative amounts of exhumation across both strands of the Karakoram fault system, we collected a suite of samples roughly perpendicular to the trace of the Karakoram fault from the Chilam Granite (Lcg) in the southwest, across the Pangong Range (from unit Ki3), and ~30 km north along the Shyok River, into the Karakoram Range (Figure 5; Tables 2 and 3; units Ki1, Ki2 and Ki3). Within the Pangong Range we collected samples along two transects (Figure 5) - the Durbuk-Shyok transect in the northwest (Samples DGA, DGB and IC6) and the Tangtse-Muglib transect in the southeast (Samples TGA, TGC, TGD and LG1). We also collected a sample from within the Karakoram Range near Panamik (Sample NBGRB), ~100 km northwest of the main transect location. Samples were collected from similar elevations to limit the effects of elevation on chronometer dates. In this section, we focus on $^{40}Ar/^{39}Ar$ thermochronology of muscovite (MsAr) and biotite (BtAr), which can constrain bedrock cooling below the nominal bulk closure temperatures that range from 300-400˚C for these systems (Hames and Bowring, 1994; Harrison et al., 1985).

7.2.2 Method

Unaltered biotite and muscovite grains were hand-picked for stepwise degassing analysis. Grains from each sample were cleaned using acetone, methanol and deionized water and then wrapped in individual packets of aluminum foil. These packets were interspersed in the irradiation package with biotite age standard HD-B1 (24.18 ± 0.18 Ma; Schwarz and Trieloff, 2007), which is used to monitor and correct for variations in the neutron flux gradient, and sent to the McMaster University nuclear reactor for neutron

irradiation. After irradiation, samples were loaded into an aluminum palette and baked for one day at 120ºC to remove atmospheric argon adhered to the palette and samples. Gas released by laser heating was purified with a system of getters, and the remaining gas was measured on a Noblesse magnetic sector mass spectrometer. Intercalibration between the Faraday and ion counter was achieved by using multiple air shots. Due to the potential for young mineral ages and low K content (and thus low amounts of released gas) each sample was distributed between 3 sample holes, and the total amount of gas was summed at the end of the extraction.

Three dates were calculated for most minerals: 1) a total gas date, which is a weighted mean of the dates for each increment; 2) a plateau date (Figure 8), which is the weighted mean of three or more adjacent increments of gas that compose at least 50% of the gas released; and 3) an isochron date, which is calculated by a linear regression analysis of steps from the experiment on an inverse isotope correlation plot of $^{36}Ar/^{40}Ar$ vs. $^{39}Ar/^{40}Ar$ (Table 2; see also Supplementary Material). For experiments yielding a plateau, the plateau date was taken as our best estimate of the age of cooling age of the mineral through its nominal closure temperature. Most minerals yielded a statistically significant plateau date, but four did not (SY1 biotite, IC1 biotite, TGD biotite and CHGRA biotite). Evaluation of the linearity of these minerals on inverse isotope correlation diagrams (see Supplemental Materials) implied a relatively straightforward behavior but, statistically speaking, they did not define isochrons. For these experiments, we assumed that the nominal 'isochron dates' (derived from linear regression fits) were correct, but magnified the statistically derived uncertainties for those dates by the square root of the mean square weighted deviation (MSWD; Wendt and Carl, 1991) to account

for excess scatter. Data reduction was done using the *Mass Spec* software developed at the Berkeley Geochronology Center. Irradiation parameters and errors are reported in the Supplemental Material (Table A, supplemental materials). All errors are reported at the 95% confidence level as 2σ.

7.2.3 MsAr and BtAr data and interpretation

We obtained ten biotite dates and four muscovite dates from samples across the region (Figure 5; Table 2). While the diffusion kinematics of biotite are well understood (e.g., Harrison et al., 1985), the propensity of the mineral to contain excess argon is also known (Rama et al., 1965; Pankhurst et al., 1973; Roddick et al., 1980; Kelley, 2002). Conversely, muscovite is less prone to both weathering and excess argon contamination, but the kinetics of the system are not as not as well constrained (compare Hames and Bowring, 1994, to Harrison et al., 2009). In our samples containing both muscovite and biotite, the biotite dates are consistently older. We interpret this as indicative of the presence of excess argon that cannot be resolved using the inverse isochron method (Roddick, et al., 1980). Other groups working in this region have reported similar problems with excess argon (Bhutani et al., 2004; Thanh et al., 2009), with one study (Boutonnet et al., 2012) also encountering BtAr older than MsAr dates from the same samples. Regardless, our biotite and muscovite dates lie within the range of those reported by others who have worked in this region (Dunlap, 1998; Searle, 1998; Boutonnet et al., 2012).

Our sampling transects are intersected by the Tangtse and Pangong strands of the KFS as well as the interpreted position of the Longmu Co fault system. This provides a

convenient context for discussing our thermochronologic results; in Figure 9, we present the results in bins that represent (from south to north) the northern edge of the Ladakh Range, the Pangong Range, the Karakoram Range south of the Longmu Co fault trace, and the Karakoram Range north of the Longmu Co fault trace.

Our southernmost sample (from the Chilam granite) yielded a BtAr date of 11.23 ± 0.50 Ma. This result is similar to other biotite $^{40}Ar/^{39}Ar$ dates reported for the area (Searle et al., 1998; Dunlap et al., 1998). In contrast, BtAr dates from samples collected across the Tangtse strand of the fault, within the Pangong Range, are younger, ranging from 7.311 ± 0.090 Ma to 10.27 ± 0.28 Ma. MsAr samples from within the Pangong Range yield ages of 9.790±0.073 Ma and 9.037 ± 0.040 Ma. Three BtAr dates from the Karakoram Range south of the Longmu Co fault trace ranged from 7.58 ± 0.16 and 9.030 ± 0.030 Ma. Two MsAr samples from within this block yielded plateau ages of 7.401 ± 0.028 Ma and 7.316 ± 0.049 Ma. Although no muscovite was found in the SY1 sample collected from north of the Longmu Co fault trace, BtAr from that sample was dated at 10.34 ± 0.22 Ma.

In general, Figure 9 illustrates a progressive northward decrease in age of BtAr and MsAr dates from the northernmost Ladakh Range through the part of the Karakoram Range lying south of the Longmu Co fault trace. This pattern is consistent with that observed for parts of the Pangong Range by Boutonnet et al. (2012), but our data within that range are more tightly clustered. There may be a slight suggestion of an offset in our BtAr dates across the Tangtse strand of the KFS, but this offset is difficult to resolve given the sparcity of data south of the strand and the relatively large uncertainty of the single Chilam granite date. Evidence for a significant offset in BtAr dates across the

Longmu Co fault trace is more robust, implying a component of south-side-up oblique slip on this structure after ca. 8 Ma.

7.3 (U-Th)/He Thermochronology

Previously published thermochronologic datasets for the study area have aimed to elucidate the older, higher-temperature parts of its cooling history (e.g., Honegger et al., 1982; Searle et al., 1989; Dunlap et al., 1998; Searle et al., 1998; Weinberg and Dunlap, 2000; Phillips et al., 2004; Jain and Singh, 2008; Ravikant et al., 2009; Reichardt et al., 2010; Leloupe et al., 2011; Boutonnet et al., 2012). By instead utilizing lower-temperature thermochronometers, we can explore the more recent tectonic history of the area. We turned to the (U-Th)/He thermochronology of zircon (ZrnHe) and apatite (ApHe) for this purpose. We obtained ZrnHe dates from 12 samples and ApHe dates from 14 samples along the two transects.

7.3.1 Method

Grains were obtained from whole rock samples using conventional crushing, sieving, magnetic and gravimetric separation techniques. All mineral separation was done at ASU. Individual zircon and apatite crystals were chosen for analysis based on size, clarity, crystal habit and lack of inclusions. They were imaged, measured, placed in Nb tubes and loaded into an Australian Scientific Instruments *Alphachron* extraction and analysis system in the Noble Gas, Geochronology and Geochemistry Laboratory (NG^3L) at ASU. ^4He was extracted by heating individual grains with an infrared diode laser. The released gas was purified by reactive getters and measured using a quadrupole mass

spectrometer. After lasing, the grains were removed, digested, and spiked with ^{235}U and ^{230}Th. Parent element measurements were made on either a Thermo *X-series* inductively coupled plasma mass spectrometer (ICP-MS) in the W.M. Keck Foundation Laboratory for Environmental Geochemistry at ASU, or on a Thermo *iCAP-Q* ICP-MS in the NG^3L facility. Analytical procedures closely follow those outlined by Schildgen et al. (2009) for apatite and van Soest et al. (2011) for zircon. Zircon (U-Th)/He (ZrnHe) and apatite (U-Th)/He (ApHe) dates reflect the time at which a crystal cooled through the ~195ºC isotherm and ~85ºC isotherm, respectively (average bulk closure temperatures calculated for these samples employing the method of Dodson (1973).

Between two and eight single crystals were analyzed for each reported ZrnHe or ApHe date. Occasionally, analyses for a single sample showed a distribution of dates exceeding what is expected from analytical imprecision. This could be the result of radiation damage (e.g., Shuster et al., 2006; Flowers et al., 2009; Guenthner et al., 2013), alpha ejection correction issues due to U+Th zoning (Hourigan et al., 2005), or unrecognized inclusions within the grain. To address excess dispersion and eliminate statistical outliers in the data, we employ the Hampel identifier method (Davies and Gather, 1993) using an outlier limit of 4 median absolute deviations from the median of the measured dates. For each sample, we determine an error-weighted mean and its standard deviation, as well as the mean squared weighted deviation (MSWD) of the weighted mean. The calculated MSWD is then compared to the expected MSWD. If the calculated MSWD is within ca. 95% confidence range of the expected MSWD, we report the weighted mean and its 2σ uncertainty. If it was not, we magnified the calculated value for 2σ by the square root of the MSWD and quote the result in Table 3 as the best

estimate of the uncertainty of the weighted-mean date.

7.3.2 ZrnHe and ApHe data and interpretation

Samples from the Chilam granite have ZrnHe cooling ages ranging from 6.85 ± 0.73 to 6.4 ± 0.1 Ma (Table 3; Figures 5 and 9). In the Pangong Range, ZrnHe dates range from ca. 5.76 ± 0.26 to 5.42 ± 0.29 Ma. Karakoram block ZrnHe dates range from 4.94 ± 0.18 to 3.82 ± 0.61 Ma south of the trace of the Longmu Co fault and are 4.64 ± 0.27 Ma north of the trace. ApHe dates follow a similar geographic pattern. South of the Tangtse strand, this chronometer yields dates ranging from 5.49 ± 0.13 to 5.2 ± 0.81 Ma. Within the Pangong Range, ApHe dates varied between 4.70 ± 0.19 Ma and 4.00 ± 0.37 Ma. The youngest apatite dates were obtained for samples collected in the Karakoram Range south of the Longmu Co fault (3.97 ± 0.97 Ma to 2.26 ± 0.45 Ma), and apatite for the sample collected north of the fault trace was slightly older (3.58 ± 0.63 Ma).

Overall patterns of (U-Th)/He dates are nearly identical to those for the $^{40}Ar/^{39}Ar$ dates presented earlier, showing a trend of northward younger cooling ages towards the northeast (Figure 9). For the low-temperature thermochronometers, the evidence for a disruption in the overall pattern at the Tangtse strand is stronger than it is based on BtAr data, but the biotite argon and zircon and apatite helium data all indicate differential north-side-up, oblique slip on that fault since ca. 4 Ma. More surprisingly, the thermochronologic data ensemble indicates even younger exhumation of the Karakoram Range south of the Longmu Co fault, where ApHe dates are as young as 2.36 ± 0.45 Ma. As was the case for the BtAr data, the ZrnHe data also indicate south-side up oblique slip on the Longmu Co fault. However, ApHe dates are statistically indistinguishable on

either side of the fault. The simplest interpretation of this result is that the oblique slip component of Longmu Co offset had ceased by ca. 3.2 Ma or had diminished to the point that it cannot be resolved using ApHe data.

The findings of north-side up offset along both strands of the KFS is inconsistent with the commonly espoused interpretation of the Pangong Range as a transpressional uplift within the KFS (e.g. Searle, 1998), which would require south-side up offset along the Pangong strand of the fault. Thus, it appears that transpressional exhumation of the Pangong Range had ceased by at least ca. 5 Ma when the ZrnHe data show north-side up motion along the Pangong fault strand. This is consistent with the findings of Searle et al. (1998), Dunlap (1998) and McCarthy and Weinberg (2010) that the majority of relative Pangong Range exhumation had to be completed prior to 10 Ma. This also necessitates that the sense of motion of the Pangong fault strand has changed from primarily oblique south-side up to oblique north-side up.

8. One Dimensional Thermal Modeling

8.1 Method

In an effort to interpret spatial and temporal variations in bedrock exhumation rates on the timescales of millions of years based on the thermochronologic data, we pursued one-dimensional thermal modeling of a representative sample from each of the four major lithotectonic blocks of our transect: the Ladakh Range (S1), the Pangong Range (TGA) the Karakoram Range south of the Longmu Co fault (SY3); and the Karakoram Range north of the Longmu Co fault (SY1). We also modeled Sample CHGRA within the Ladakh Range immediately adjacent to the Tangtse strand of the

KFS. We chose samples that yielded the most reasonable fit modeling solutions for each block.

We followed the approach of Thiede and Ehlers (2013), which involves Monte Carlo forward modeling of closure behavior in thermochronometers over time assuming input thermal parameters (Table 4) and using a modified 1D version of the Pecube software of Braun et al. (2012). We ran the model to predict ZrnHe and ApHe cooling ages for the southern three blocks (closure temperatures of 195ºC and 85ºC, respectively). Errors on our cooling ages were expanded to 10% of the calculated date. During model runs we allowed exhumation rates to vary randomly between 0 and 4 km/Ma at times 20, 15, 12, 6, 5, 4, 3, 2 and 0 Ma. These rates were allowed to change at the predetermined time intervals, but could not change between intervals.

We ran the model for 50,000 iterations and then compared the results to the measured closure ages. Reasonable fits were determined by using the reduced chi-squared test. The misfit of a sample is determined to be the mean of all of the individual chronometer chi-squared values from within that sample. For this work, a chi-squared value of ≤ 10 was considered an acceptable fit. Reasonable fits were used to estimate exhumation rate as a function of time for each sample and to report reasonable uncertainties in those. Acceptable exhumation rate histories are reported in Figure 10 as the mean and one standard deviation of the mean at each time interval. Because the model is essentially unconstrained before the first chronometer, we concentrate on the timing of changes in exhumation, rather than on model calculated exhumation rates between the model initiation time and the first chronometer age.

8.2 Results

By 6.5 Ma exhumation rates within the Chilam granite are already low (Figure 10). However, exhumation is high to the northeast in the Pangong and Karakoram Ranges until ca. 5 Ma when rates begin to gradually decrease within the Pangong Range. At 4 Ma, exhumation rates decrease to the north of the LCF, while rates within the Karakoram Range between the LCF and KFS do not begin to decrease until ca. 3 Ma. Thus, exhumation rates appear to decrease across the Chilam-Pangong-Karakoram transect from southwest to northeast, with different sides of the fault system responding to the decrease at different times. The package of rocks between the LCF and KFS continued to exhume relatively quickly, even after exhumation has decreased to the northeast and southwest. However, the lower thermochronometers across this boundary are within error of each other, so this result is not robust.

9. Discussion

The rocks adjacent to and between the strands of the KFS display discrete differences in their cooling and exhumation histories. Previous studies (Raterman et al., 2007) and lithologic mapping (Chapter 2) indicate that the KFS and the LCF come into close proximity in the region crossed by our thermochronologic transect. Below, we explore the potential role that interactions between these fault systems may have on influencing these regional patterns of uplift and exhumation.

Whereas Raterman et al. (2007) trace the LCF into the vicinity of the KFS, their hypothesis necessitates that the Longmu Co and Karakoram faults intersect at or near the northern tip of the Pangong Range. Our field observations, thermochronologic data and

lithologic mapping do not support a single major fault strand in this location - especially not one that has accommodated 25-32 km of motion (Figure 2).

Interestingly, our photointerpretive mapping of the region (using ASTER and Quickbird imagery) shows a distinctive carbonate band traceable from the mapped section of the LCF (Raterman et al, 2007), across the Shyok River and into the Karakoram Range (Figures 2 and 4; Chapter 2; Km3 and Km4). In the field, an exposure of this unit (Km4) in the Karakoram Range on the west bank of the Shyok River confirms that it is banded marble, skarn and chert in a fault contact relationship with the granitic rocks to the south. The nature of the contact between this unit and the granitic and metamorphic rocks to the north was obscured. The trace of this unit is not continuously mappable northwestward through the Karakoram Range, but its projected continuation aligns well with linear valleys and outcrops of a similar unit (Figure 2), mapped by Phillips (2008) as the Saser Formation. While Phillips (2008) interprets this as a secondary strand of the Karakoram fault system, we interpret it instead as the trace of the Longmu Co fault that has been rotated into parallelism with the Karakoram fault. Along the eastern side of the Shyok River, just to the south of the Km4 (between N34º17’06 / W78º18’05 and N34º11’39 / W78º16’39), both the metamorphic rocks and the igneous intrusions of units Ki2 and Ki3 have been folded into large anticlinal structures with fold hinges trending ~340º (Figure 2). Our thermochronologic data show a decrease in sample age coincident with this region of folding (Figures 5 and 9). At the southern end of this series of folds - ~10 km from the trace of the KFS system - the rocks abruptly change character, showing little to no folding and becoming more fractured. A similar but less well-defined series of folds may be present on the western side of the Shyok River

between N34º14’45 / W78º16’20 and N34º10’11/ W78º14’57; however this was only observed in satellite imagery. The orientation of these folds implies roughly NE-SW shortening of the area to the south of the LCF system. This shortening is counterintuitive based solely on the conjugate sense slip directions and orientation of the LCF and KFS, which would produce SE-NW extension. However, oblique motion along the LCF without linkage to the KFS would produce folding in this orientation. We propose that units Km3 and Km4 mark the trace of the southern Longmu Co fault system in India, and that this fault, in the vicinity of the Shyok River, is not purely translational but rather oblique (Figure 11).

The observation that that the strain field of the Tibetan Plateau is predominantly extensional despite the overall contractional nature of the Himalayan-Tibetan orogenic system has been the topic of extensive discussion (e.g., Armijo et al., 1986; Molnar, 1992; Kapp and Guynn, 2004; Chen and Yang, 2004; Zhang et al., 2004; Selverstone, 2005; Murphy et al., 2010; Lee et al., 2011). Earthquake moment tensors from the Tibetan Plateau show that almost half of the extension is accommodated by strike slip faulting, whereas the other half is taken up by normal faulting (Molnar and Lyon-Caen, 1989). Conjugate strike-slip faults are intimately linked to normal faults both north and south of the suture (e.g. Molnar and Tapponnier, 1978). This relationship highlights the role that strike-slip faults play in accommodating coeval north-south shortening and east-west extension (Kong and Bird, 1996; Yin, 2000; Lee et al., 2011).

Tibetan Plateau extension has been ongoing in the Himalayan orogen since at least as far back as ca. 15 Ma (e.g., Coleman and Hodges, 1995; Edwards and Harrison, 1997; Williams et al., 2001; Cottle et al., 2009; Kali et al., 2010; Lee et al., 2011). This is

pertinent because the KFS seems to have initiated at about the same time as Tibetan Plateau extension (ca. 15 Ma; Phillips et al., 2004), and development of the KFS. Because the KFS is dextral and the LCF is sinistral, coeval motion of the fault systems would allow for eastward extrusion of material between them. Thus, it seems reasonable to argue that the opposing shear senses of the KFS and LCF systems may enable strain compatibility between the extending plateau region and the mountainous regions to the west such as the Pamir. If this is correct, we suspect that the Longmu Co fault system may have initiated earlier than proposed by Raterman et al. (2007), around 15 Ma or perhaps even earlier.

Extension accommodated by conjugate faults systems generally produces a basin or gap at the trailing edge of the retreating wedge (e.g., Taylor et al., 2003). However, thrust faulting, vertical axis rotation of the surrounding region or shortening could potentially close that gap (Taylor et al., 2003). In the case of the KFS and LCF, there is no gap observed near where the systems come into proximity. Thus, we posit that roughly north-south shortening across the region has created a "trailing zipper", closing the gap between the two fault systems (Figure 11). The curvature of the carbonate band (Km4) associated with the trace of the LCF (mapped as the Saser Formation by Phillips, 2008) may reflect bending related to both KFS slip and the closure of the gap. This closure accompanies transmission of shortening across the Ladakh - Pangong - Karakoram Range region, which is evident in our low-temperature thermochronologic data. The compilation of three southwest-northeast transects across the Ladakh batholith show a decrease in the cooling age of ZrnHe and ApHe thermochronometers towards the northeast from ca. 30 Ma to ca. 11 Ma (see Chapter 4). We posited in Chapter 4 that this is the result of a

decrease in shortening and consequent decrease in uplift sweeping across the area from southwest to northeast, leaving a reduction of exhumation in its wake. When combined with the data from this study, the trend toward younger cooling ages in the northeast becomes even more apparent. The average thermochronologic ages within the Chilam granite, Pangong Range and southern Karakoram Range show a cessation of rapid cooling that starts in the southwest and migrates towards to the northeast (Figure 12). In other words, north-south shortening controlled uplift rates across the region until ca. 16 Ma, when exhumation rates in the Ladakh Range begin to decline. Our data do not show a decrease in exhumation rates within the Chilam granite, but this is likely because the decrease occurred before the closure of ZrnHe within the granite at ca. 6.5 Ma. At ca. 5 Ma, rates dropped in the Pangong Range. Interestingly, exhumation rates in the Karakoram Range to the north of the LCF begin to decrease at ca. 4 Ma, before rates to the south of the fault trace (ca. 3 Ma). However, as previously mentioned this trend is not robust and should be viewed with caution. However, if this apparent trend is real, it implies that shortening was still acting to exhume the rocks between the LCF and KFS as recently as ca. 3 Ma. It also supports the supposition that, in this region, the LCF accommodates substantial oblique motion.

10. Conclusions

East-west extension across the central and southern Tibetan plateau began at ca. 15 Ma, which is coincident with best estimates for the initiation of the central Karakoram fault system. If the Longmu Co fault also initiated at this time, these systems have acted as a conjugate fault pair since the onset of extension, allowing the eastward extrusion of

Tibet. The expected accommodation space created by eastward extrusion is absent in this area, likely due to zippering of the gap between the two fault systems as a result of north-south shortening. A carbonate unit, which represents the trace of the LCF in India, and which was documented though ASTER remote sensing image analysis (Chapter 2), has been rotated into parallelism with the KFS as a result of this closure and dextral shear along the KFS. Additionally, the bend in the KFS, often attributed to sinistral motion along the LCF, may also be caused by the closure of this gap. This process accompanies transmission of shortening across the Ladakh - Pangong – Karakoram region, which is evident in new and previously published $^{40}Ar/^{39}Ar$ and (U-Th)/He data. These data show cooling ages across the region that are oldest in the southwest and youngest towards the northeast. Thermal modeling shows a decrease in exhumation rate at 16 Ma. starting along the southwestern edge of the Ladakh batholith and translating towards the northeast across the Karakoram and Longmu Co faults. We suggest that eastward displacement of crust within the Tibetan extensional domain after 16 Ma enabled northeastward propagation of the locus of local shortening, uplift, and erosion, leaving in its wake a northeastward-propagating domain of lower exhumation rate.

11. References

Avouac, J. P., and Tapponnier, P., 1993, Kinematic model of active deformation in central Asia: Geophysical Research Letters, V. 20, p. 895-898.

Allegre, CJ and 34 others, 1984, Structure and evolution of the Himalayan-Tibet orogenic belt. Nature 307:17–22

Armijo, R., Tapponnier, P., Mercier, J.L., Han, T.L., 1986. Quaternary extension in southern Tibet—field observations and tectonic implications. J. Geophys. Res. 91, 13803–13872.

Avouac, J. P., and Tapponnier, P., 1993, Kinematic model of active deformation in central Asia: Geophysical Research Letters, V. 20, p. 895-898.

Banerjee, P., Burgmann, R., 2002, Convergence across the northwest Himalaya from Brown, E. T., Bendick, R., Bourles, D. L., Gaur, V., Molnar, P., Raisbeck, G. M., and Yiou, F., 2002, Slip rates of the Karakoram Fault, Ladakh, India, determined using cosmic ray exposure dating of debris flows and moraines: Journal of Geophysical Research, v. 107.

Bhutani, R., K. Pande, and N. Desai, 2003. Age of the Karakoram fault activation: 40Ar/39Ar geochronological study of Shyok suture zone in northern Ladakh, India, Curr Sci., 84(11), 1454–1458.

Bhutani, R., Pande, K., Venkatesan, T.R., 2004. Tectono-thermal evolution of the India Asia collision zone based on 40Ar/39Ar thermochronology in Ladakh, India. Proceedings Indian Academy of Sciences 113, 737–754.

Bouilhol, P., Jagoutz, O., Hanchar, J. M., and Dudas, F. O., 2013. Dating the India–Eurasia collision through arc magmatic records: Earth and Planetary Science Letters, v. 366, p. 163-175.

Boutonnet, E., P. H. Leloup, N. Arnaud, J.-L. Paquette, W. J. Davis, and K. Hattori, 2012, Synkinematic magmatism, heterogeneous deformation, and progressive strain localization in a strike slip shear zone. The case of the right-lateral Karakorum fault, Tectonics, 31.

Braun, J., van der Beek, P., Valla, P., Robert, X., Herman, F., Glotzbach, C., Pedersen, V., Perry, C., Simon-Labric, T., and Prigent, C., 2012. Quantifying rates of landscape evolution and tectonic processes by thermochronology and numerical modeling of crustal heat transport using PECUBE: Tectonophysics, v. 524, p. 1-28.

Brown, E. T., R. Bendick, D. L. Bourle`s, V. Gaur, P. Molnar, G. M. Raisbeck, and F. Yiou, 2002, Slip rates of the Karakorum fault, Ladakh, India, determined using cosmic ray exposure dating of debris flows and moraines, J. Geophys. Res., 107(B9), 2192.

Burtman, V. S., Molnar, P., 1993, Geological and geophysical evidence for deep subduction of continental crust beneath the Pamir, Geological Society of America, Special paper 281.

Chen, W.P. and Yang, Z. H. 2004. Earthquakes beneath the Himalayas and Tibet; evidence for strong lithospheric mantle. Science, 304, 1949–1952.

Chevalier, M. L., Ryerson, F. J., Tapponnier, P., Finkel, R. C., Van der Woerd, J., Li, H. B., and Li, Q., 2005, Slip-rate measurements on the Karakoram fault may imply secular variations in fault motion, Science 307, no. 5708, 411-414.

Chevalier, M.-L., Tapponnier, P., Van Der Woerd, J., Ryerson, F.J., Finkel, R.C., and Li, H., 2012. Spatially constant slip rate along the southern segment of the Karakorum fault since 200 ka. Tectonophysics, 530-531: 152-179.

Clift, P. D., A. Carter, M. Krol, and E. Kirby, 2002, Constraints on India-Eurasia collision in the Arabian Sea region taken from the Indus Group, Ladakh Himalaya, India, *in* Clift, P. D., Kroon, D., Gaedicke, C., and Craig, J., eds., The Tectonic and

Climatic Evolution of the Arabian Sea Region, London, Geological Society of London Special Publication 195, 97-116.

Coleman ME, Hodges KV., 1995. Evidence for Tibetan Plateau uplift before 14 Myr ago from a new minimum estimate for east-west extension. Nature, 374:49–52.

Cottle, J.M., Jessup, M.J., Newell, D.L., Horstwood, M.S.A., Noble, S.R., Parrish, R.R., Waters, D.J., and Searle, M.P., 2009, Geochronology of granulitized eclogite from the Ama Drime Massif: Implications for the tectonic evolution of the South Tibetan Himalaya: Tectonics, v. 28, doi: 10.1029/2008TC002256.

Davies, L., Gather, U., 1993. The identification of multiple outliers. Journal of the American Statistical Association 88 (423), 782–792, 88 (423).

Dodson, M.H., 1973. Closure temperature in cooling geochronological and petrological systems: Contributions to Mineralogy and Petrology, v. 40, p. 259-274.

Dunlap, W.J., Weinberg, R.F., Searle, M.P., 1998. Karakoram fault zone rocks cool in two phases. Journal of the Geological Society 155, 903–912.

Edwards MA, Harrison TM, 1997. When did the roof collapse? Late Miocene N-S extension in the High Himalaya revealed by Th-Pb monazite dating of the Khula Kangri granite. Geology 25:543–46

Flowers, R. M., R. A. Ketcham, D. L. Shuster and K. A. Farley (2009), Apatite (U-Th)/He thermochronometry using a radiation damage accumulation and annealing model, Geochim. Cosmochim. Acta, 73, 2347-2365.

Fraser, J.E., Searle, M.P., Parrish, R.R. & Noble, S.R., 2001, Chronology of deformation, metamorphism, and magmatism in the southern Karakoram Mountains, Geological Society of America Bulletin, 113, 1443–1455.

Gansser A. 1964. The Geology of the Himalayas, New York: Wiley Interscience. p. 289

Gansser, A., 1980, The significance of the Himalayan suture zone, *Tectonophysics, 62*, 37-52.

Gehrels, G. E., V. Valencia, and J. Ruiz (2008), Enhanced precision, accuracy, efficiency, and spatial resolution of U-Pb ages by laser ablation multicollector inductively coupled Plasma mass spectrometry, Geochem. Geophys. Geosyst., 9, Q03017, doi:10.1029/2007GC001805.

Gehrels, G. E., V. Valencia, and A. Pullen (2006), Detrital zircon geochronology by Laser-Ablation Multicolector ICPMS at the Arizona LaserChron Center, in Geochronology: Emerging Opportunities, Paleontological Society Short Course, October 21, 2006, Philadelphia, PA, edited by T. Olszewski et al., Paleontol. Soc. Pap., I2, 1-10.

Guenthner, W., Reiners, P., Ketcham, R.A., Nasdala, L. and Giester, G. 2013: Helium diffusion in natural zircon: radiation damage, anisotropy, and the interpretation of zircon (UTh)/He thermochronology; American Journal of Science, v. 313, p. 145-198.

Hames, W. E., and S. Bowring, 1994, An empirical evaluation of the argon diffusion geometry in muscovite, Earth Planet. Sci. Lett., 124, 161–169.

Harrison, T. M., Celerier, J., Aikman, A. B., Hermann, J., and Heizler, M. T., 2009, Diffusion of ^{40}Ar in muscovite: Geochimica et Cosmochimica Acta, v. 73, no. 4, p. 1039-1051.

Hodges, K. V., 2014, Thermochronology in Orogenic Systems, *in* Holland, H. D., and Turekian, K. K., eds., Treatise on Geochemistry, Second Edition, Volume 4: Oxford,

Elsevier, p. 281-308.

Hourigan, J. K., Reiners, P. W., and Brandon, M. T., 2005, U-Th zonation dependent alpha-ejection in (U-Th)/He chronometry: Geochimica et Cosmochimica Acta, v. 69, p. 3349-3365.

Honegger, K., Dierich, V., Frank, Gansser, A., Thoni, M. & Trommsdroff, V., 1982, Magmatism and metamorphism in the Ladakh Himalayas (the Indus-Tsangpo Suture Zone). Earth and Planetary Science Letters, 60, 253–292.

Jade, S., Bhatt, B. C.,Yang, Z., Bendick, R., Gaur, V. K., Molnar, P. , Anand, M. B., and Kumar, D., 2004, GPS measurements from the Ladakh Himalaya, India: Preliminary tests of plate-like or continuous deformation in Tibet, Geological Society of America Bulletin, 116, 1385 – 1391.

Jade, S., Rao, R., Vijayan, H. J., Gaur, M. S. M., Bhatt, V. K., Kumar, B. C., Jaganathan, K., Ananda, S., and Kumar, M. B., 2010, GPS-derived deformation rates in northwestern Himalaya and Ladakh, International Journal of Earth Science, Volume 100, Number 6, 1293-1301.

Jain, A., and S. Singh, 2008, Tectonics of the southern Asian Plate margin along the Karakoram Shear Zone: Constraints from field observations and U-Pb SHRIMP ages, Tectonophysics, 451, 186–205.

Kali, E., Leloup, P.H., Arnaud, N., Mahéo, G., Liu, D., Boutonnet, E., VanderWoerd, J., Xiaohan, L., Liu-Zeng, J., Haibing, L., in press. Exhumation history of the deepest central Himalayan rocks (Ama Drime range): key P–T–D–t constraints on orogenic models. Tectonics. doi:10.1029/2009TC002551.

Kapp, P., Guynn, J.H., 2004. Indian punch rifts Tibet. Geology 32, 993–996.

Kelley, S., 2002. Excess argon in K–Ar and Ar–Ar geochronology. Chemical Geology 188, 1–22.

Kirstein, L.A., Foeken, J.P.T., van der Beek, P., Stuart, F.M., Phillips, R.J., 2009, Cenozoic unroofing history of the Ladakh Batholith, western Himalaya constrained by thermochronology and numerical modeling. Journal of the Geological Society of London 166, 667–678.

Kirstein, L.A., Sinclair, H., Stuart, F.M., Dobson, K., 2006. Rapid Early Miocene exhumation of the Ladakh Batholith, northwestern Himalaya. Geology 34, 1049–1052.

Klootwijk, C. T., Gee, J. S., Peirce, J. W., Smith, G. M., & McFadden, P. L., 1992. An early India-Asia contact: paleomagnetic constraints from Ninetyeast Ridge, ODP leg 121. *Geology*, *20*(5), 395-398.

Kong, X., and P. Bird, Neotectonics of Asia: Thin-shell, finite-element models with faults, in The Tectonics of Asia, edited by A. Yin and T. M. Harrison, pp. 18 – 35, Cambridge Univ. Press, New York, 1996.

Lacassin, R., Valli, F. , Arnaud, N., Leloup, P.H. , Paquette, J.L. , Haibing, L., Tapponnier, P., Chevalier, M.-L. , Guillot, S., Maheo, G., Zhiqin, X., 2004, Large-scale geometry, offset and kinematic evolution of the Karakorum fault, Tibet, Earth Planet. Sci. Lett. 219 255 – 269.

Lee, J., Hager, C., Wallis, S. et al., 2011. Middle to late Miocene extremely rapid exhumation and thermal reequilibration in the Kung Co rift, southern Tibet. Tectonics, 30, 1–26.

Leloup, P.H., Boutonnet, E., Davis, W.J., Hattori, K., 2011. Long-lasting intracontinental

strike-slip faulting: new evidence from the Karakorum shear zone in the Himalayas. Terra Nova 23, 92-99.

Liu Qing, J.P. Avouac, P. Tapponnier, and Q. Zhang, 1992. Holocene movement along the southern part of the Karakorum fault, Int. Symposium on the Karakorum and Kunlun mountains Kashgar, China, 91.

Liu, Q., 1993, Pal»oclimat et contraintes chronologiques sur les mouvements r»cent dans l'Ouest du Tibet: Failles du Karakorum et de Longmu Co–Gozha Co, lacs en pull-apart de Longmu Co et de Sumxi Co [ThÀse de Doctorat]: Paris, Universit» Paris.

Mah»o, G., J. Blichert-Toft, C. Pin, S. Guillot, A. PÕcher, 2009, Partial melting of mantle and crustal sources beneath South Karakoram, Pakistan: Implications for the Miocene geodynamic evolution of the India-Asia convergence zone, J. Petrol., 50, 427–449.

Matte, P., Tapponnier, P., Arnaud, N., Bourjot, L., Avouac, J.P., Vidal, P., Liu, Q., Pan, Y., Wang, Y., 1996. Tectonics of Western Tibet, between the Tarim and the Indus. Earth Planet. Sci. Lett. 142, 311–330.

McCarthy, M. R., and R. F. Weinberg, 2010, Structural complexity resulting from pervasive ductile deformation in the Karakoram shear zone, Ladakh, NW India, Tectonics, 29.

Molnar, P., and H. Lyon-Caen, Fault plane solutions of earthquakes and active tectonics of the Tibetan Plateau and its margins, Geophys. J. Int., 99, 123 – 153,1989.

Molnar, P., and P. Tapponnier, Active tectonics of Tibet, J. Geophys. Res., 83, 5361 – 5373, 1978.

Molnar P, England P, Martinod J. 1993. Mantle dynamics, the uplift of the Tibetan

Plateau, and the Indian monsoon. Rev. Geophys. 31:357–96

Murphy, M. A., Yin, A., Kapp, P., Harrison, T. M., Manning, C. E., Ryerson, F. J., Ding L., and Guo, J.H., 2002, Structural evolution of the Gurla Mandhata detachment system, southwest Tibet: implications for the eastward extent of the Karakoram fault system, Geological Society of America Bulletin, 114, pp. 428–447.

Murphy, M. A., and Copeland, P., 2005, Transtensional deformation in the central Himalaya and its role in accommodating growth of the Himalayan orogen: Tectonics, v. 24, no. 4.

Murphy, M.A., Saylor, J.E., Ling, D., 2009. Landscape evolution of southwest Tibet based on integrated paleoelevation reconstructions and structural history. Earth Planet. Sci. Lett. 282, 1–9.

Murphy, M. A., Taylor, M. H., Gosse, J., Silver, C. R. P., Whipp, D. M., and Beaumont, C., 2014, Limit of strain partitioning in the Himalaya marked by large earthquakes in western Nepal: Nature Geoscience, v. 7, p. 38-42.

Norin, E., 1946. Geological explorations in western Tibet: Reports from the scientific expedition to the northwestern provinces of China under the leadership of Sven Hedin. The Sino-Swedish expedition, publication 29, III., Geology 7.

Pankhurst, R.J., Moorbath, S., Rex, D.C. and Turner, G., 1973. Mineral age patterns in ca. 3700 My old rocks from West Greenland. Earth Planet. Sci. Lett., 20: 157-170.

Parrish, R. R., and R. Tirrul, 1989, U-Pb age of the Baltoro granite, Northwest Himalaya, and implications for monazite U-Pb systematics, Geology, 17, 1076–1079.

Patriat P, Achache J. 1984. India-Eurasia collision chronology has implications for crustal shortening and driving mechanism of plates. Nature 311:615–21

Phillips, R., 2008, Published Map. In Phillips, R., 2008, Geological map of the Karakoram fault zone, Eastern Karakoram, Ladakh, NW Himalaya, Journal of Maps, v 2008, 21-37.

Phillips, R. J., Parrish, R. R., and Searle, M. P., 2004, Age constraints on ductile deformation and long-term slip rates along the Karakoram fault zone, Ladakh: Earth and Planetary Science Letters, v. 226, no. 3-4, p. 305-319.

Phillips, R. J., and Searle, M. P., 2007, Macrostructural and microstructural architecture of the Karakoram fault: Relationship between magmatism and strike-slip faulting: Tectonics, v. 26.

Phillips, R.J., Searle, M.P. & Parrish, R.R. 2013. The geochemical and temporal evolution of the continental lithosphere and its relationship to continental-scale faulting: The Karakoram Fault, eastern Karakoram, NW Himalayas. Geochemistry Geophysics Geosystems, 14, 583-603.

Rama, S.N., Hart, S.R., Roedder, E., 1965. Excess radiogenic argon in fluid inclusions. Journal of Geophysical Research 70, 509–511.

Raterman, N.S., Cowgill, E., Lin, D., 2007. Variable structural style along the Karakoram fault explained using triple-junction analysis of intersecting faults. Geosphere 3, 71–85.

Ravikant, V. (2006), Utility of Rb-Sr geochronology in constraining Miocene and Cretaceous events in the eastern Karakoram, Ladakh, India, J. Asian Earth Sci., 27, 534–543, doi:10.1016/j.jseaes.2005.05.007.

Ravikant, V., Wu, F.-Y., Ji, W.-Q., 2009. Zircon U–Pb and Hf isotopic constraints on petrogenesis of the Cretaceous–Tertiary granites in eastern Karakoram and Ladakh,

India. Lithos 110, 153–166.

Reichhardt, H., Weinberg, R.F., Andersson, U.B., Fanning, C.M., 2010. Hybridization of granitic magmas in the source: the origin of the Karakoram Batholith, Ladakh, NW India. Lithos 116, 249–272.

Rex, A. J., M. P. Searle, R. Tirrul, M. B. Crawford, D. J. Prior, D. C. Rex, and A. Barnicoat, 1988, The geochemical and tectonic evolution of the central Karakoram, North Pakistan, Phil. Trans. R. Soc. Lond., A326, 229–255.

Robinson, A. C., 2009a, Evidence against Quaternary slip on the northern Karakorum Fault suggests kinematic reorganization at the western end of the Himalayan-Tibetan orogen: Earth and Planetary Science Letters, v. 286, no. 1-2, p. 158-170.

Robinson, A.C., 2009b. Geologic offsets across the northern Karakorum fault: Implications for its role and terrane correlations in the western Himalayan-Tibetan orogen: Earth and Planetary Science Letters, v. 279, no. 1-2, p. 123-130.

Roddick, J. C., Cliff, R. A., and Rex, D. C., (1980), The evolution of excess argon in Alpine biotites - A ^{40}Ar-^{39}Ar analysis: Earth and Planetary Science Letters, v. 48, p. 185-208.

Rolland, Y., et al., 2009, Syn-kinematic emplacement of the Pangong metamorphic and magmatic complex along the Karakorum Fault (N Ladakh), J. Asian Earth Sci., 34, 10–25.

Rolland, Y., and Pecher, A., 2001, The Pangong granulites of the Karakoram fault (western Tibet): Vertical extrusion within a lithosphere-scale fault?: Comptes Rendus de l'Academie des Sciences, Serie Ii Fascicule á Sciences de la Terre et des

Planetes, v. 332, p. 363–370.

Roy, P., Jain, A., Singh, S., 2010, Microstructures of mylonites along the Karakoram Shear Zone, Tangste Valley, Pangong Mountains, Karakoram, J. Geol. Soc. India, 75, 679–694.

Rutter, E. H., Faulkner, D. R., Brodie, K. H., Phillips, R. J., Searle, M. P., 2007, Rock deformation processes in the Karakoram Fault zone, Eastern Karakoram, Ladakh, NW India, Journal of Structural Geology v. 29, 1315-1326.

Schârer, U., P. Copeland, T. M. Harrison, and M. P. Searle, 1990, Age, cooling history and origin of postcollisional leucogranites in the Karakoram batholith, a multisystem isotope study, J. Geol., 98, 233–251.

Schildgen, T. F., K. V. Hodges, K. X. Whipple, M. S. Pringle, M. C. van Soest, and K. Cornell, 2009, Late Cenozoic structural and tectonic development of the western margin of the Central Andean Plateau in southwest Peru, Tectonics, 28.

Schwarz, W.H., Trieloff, M., 2007a. Intercalibration of ^{40}Ar–^{39}Ar age standards NL-25, HB3gr hornblende, GA1550, SB-3, HD-B1 biotite and BMus/2 muscovite. Chemical Geology 242, 218–231.

Searle, M. P., M. A. Khan, J. E. Fraser, and S. J. Gough, 1999, The tectonic evolution of the Kohistan-Karakoram collision belt along the Karakoram Highway transect, north Pakistan, Tectonics, 18, 929–949.

Searle, M.P., Weinberg, R.F., Dunlap, W.J., 1998. Transpressional tectonics along the Karakoram fault zone, northern Ladakh: constraints on Tibetan extrusion. In: Holdsworth, R.E., Strachan, R.A., Dewey, J.F. (Eds.), Continental Transpressional and Transtensional Tectonics, 135. Geological Society, Special Publication, London,

pp. 307–325.

Searle, M.P., 1991. Geology and Tectonics of the Karakoram Mountains. John Wiley and Sons, Chichester, UK, p. 358.

Searle, M.P., Owen, L.A., 1999. The evolution of the Indus River in relation to topographic uplift, erosion, climate and geology of western Tibet, the Transhimalayan and High Himalayan Ranges. In: Meadows, A., Meadows, P. (Eds.), The Indus River. Oxford University Press, Oxford, UK, pp. 210–230.

Searle, M. P., M. A. Khan, J. E. Fraser, S. J. Gough, and M. Q. Jan, The tectonic evolution of the Kohistan-Karakoram collision belt along the Karakoram Highway transect, north Pakistan, Tectonics, 18, 929 – 949, 1999.

Searle, M.P., Windley, B.F., Coward, M.P., Cooper, D.J.W., Rex, A.J., Rex, D.C., Li, T., Xiao, X.C., Jan, M.Q., Thakur, V.C., Kumar, S., 1987, The closing of Tethys and the tectonics of the Himalayas. Geological Society of America Bulletin 98, 678–701.

Searle, M. P., and Rex, A. J., 1989, Thermal model for the Zanskar Himalaya: Journal of Metamorphic Geology, v. 7, p. 127–134.

Searle, M. T., Geological evidence against large-scale pre-Holocene offsets along the Karakoram Fault: Implications for the limited extrusion of the Tibetan, Tectonics, 15, 171 – 186, 1996.

Searle, M. P., M. B. Crawford, and A. J. Rex (1992), Field relations, geochemistry, origin and emplacement of the Baltoro granite, central Karakoram, R. Soc. Edin. Trans., 83, 519–538.

Sen, K., Mukherjee, B.K., Sachan, H.K., 2009. Field and microstructural analysis of the Pangong Granodiorite, Ladakh (NW India): implications for tectonics along the

Karakoram Fault Zone. Curr. Sci. 96, 1124**e**1130.

Sen, K., Mukherjee, G., Collins, A, 2014. Interplay of deformation and magmatism in the Pangong Transpression Zone, Eastern Ladakh, India: Implications for remobilization of the trans-Himalayan arc and initiation of the Karakoram Fault, Journal of Structural Geology, Vol. 62, p. 13-24.

Shuster, D. L., Flowers, R. M., and Farley, K. A., 2006, The influence of natural radiation damage on helium diffusion kinetics in apatite: Earth and Planetary Science Letters, v. 249, p. 148-161.

Sinha, A.K., Upadyay, R., Chandra, R., 1999. Contributions to the geology of the eastern Karakoram, India. Geological Society of America, Special Publication 328, 33-48.

Srimal, N., Basu, A.R. & Kyser, T.K. 1987. Tectonic inferences from oxygen isotopes in volcano-plutonic complexes of the India-Asia collision zone, NW India. Tectonics, 6, 261–273.

Srimal, N.,1986, India–Asia collision: implication fromthe geology of the eastern Karakoram, Geology 14, 523–527.

Strecker, M. R., Frisch, W., Hamburger, M.W., Ratschbacher, L., Semiletkin, S., Zamoruyev, A., and Sturchio, N., 1995, Quaternary deformation in the eastern Pamirs, Tadzhikistan and Kyrgyzstan: Tectonics, v. 14, p. 1061–1079.

Struele, M. J., Phillips, R. J., Searle, M. P., Waters, D. J., Horstwood, M.S.A., 2009, Evolution and chronology of the Pangong Metamorphic Complex adjacent to the Karakoram fault, Ladakh: constraints from thermobarometry, metamorphic modeling and U-Pb geochronology, Journal of the Geological Society; September 2009; v. 166; no. 5; p. 919-932.

Tapponnier, P., Xu, Z.Q., Roger, F., Meyer, B., Arnaud, N., Wittlinger, G., and Yang, J.S., 2001, Oblique stepwise rise and growth of the Tibetan Plateau: Science, v., 294, p. 1671-1677.

Taylor, M., Yin, A., Ryerson, F.J., Kapp, P., Ding, L., 2003. Conjugate strike-slip faulting along the Bangong–Nujiang suture zone accommodates coeval east–west extension and north–south shortening in the interior of the Tibetan Plateau. Tectonics 22, 1044.

Thanh, N.X., 2009. Petrology and geochronology of igneous and metamorphic rocks in the Shyok suture of Ladakh Himalaya, India. Unpublished PhD thesis, Okayama University of Science, Japan, p. 180.

Thiede, J.C., Ehlers, T.A., 2013. Large spatial and temporal variations in Himalayan denudation. Earth Planet. Sci. Lett. 371–372.

Treloar, P. J.,D. C. Rex, P.G.Guise,M. P. Coward,M. P. Searle, B. F. Windley, M. G. Petterson, M. Q. Jan, and I. W. Luff (1989), K-Ar and Ar-Ar geochronology of the Himalayan collision in NW Pakistan: constraints on the timing of suturing, deformation, metamorphism and uplift, Tectonics, 8, 881–909.

Wallis, David, Phillips, R.J., Lloyd, G.E., (2014) Evolution of the Eastern Karakoram Metamorphic Complex, Ladakh, NW India, and its relationship to magmatism and regional tectonics, Tectonophysics, doi:10.1016/j.tecto.2014.03.023

Weinberg, R.F. & Searle, M.P. 1998. The Pangong Injection Complex, Indian Karakoram: a case of pervasive granite flow through hot viscous crust. Journal of the Geological Society, London, 155, 883–892.

Weinberg, R.F., Dunlap, W.J., 2000. Growth and deformation of the Ladakh batholith,

northwest Himalayas: implications for timing of continental collision and origin of calc-alkaline batholiths. Journal of Geology 108, 303–320.

Weinberg, R.F., Dunlap, W.J., Whitehouse, M., 2000. New field, structural and geochronological data from the Shyok and Nubra valleys, northern Ladakh: linking Kohistan to Tibet. In: Khan, .A., Treloar, P.J., Searle, M.P., Jan, M.Q. (Eds.), Tectonics of the Nanga Parbat Syntaxis and the Western Himalaya. Geological Society of London Special Publication, vol. 170, pp. 253– 275.

Weinberg, R. F., and G. Mark, 2008, Magma migration, folding, and disaggregation of migmatites in the Karakoram Shear Zone, Ladakh, NW India, Geol. Soc. Am. Bull., 120, 994–1009.

Weinberg, R. F., G. Mark, and H. Reichardt, 2009, Magma ponding in the Karakoram shear zone, Ladakh, NW India, Geol. Soc. Am. Bull., 121, 278–285.

Weinberg, R. F., and G. Mark, 2008, Magma migration, folding, and disaggregation of migmatites in the Karakoram Shear Zone, Ladakh, NW India, Geol. Soc. Am. Bull., 120, 994–1009, doi:10.1130/B26227.1.

Wendt, I., and Carl, C., 1991, The statistical distribution of the mean squared weighted deviation: Chemical Geology, v. 86, p. 275-285.

Whipp, D. M., Ehlers, T. A., Blythe, A. E., Huntington, K. W., Hodges, K. V., and Burbank, D. W., 2007, Plio-Quaternary exhumation history of the central Nepalese Himalaya: 2. Thermo-kinematic and thermochronometer age prediction model: Tectonics, v. 26.

Williams, H., Turner, S., Kelley, S., and Harris, N., 2001, Age and composition of dikes in southern Tibet: New constraints on the timing of east-west extension and its relationship to postcollisional magmatism: Geology, v. 29, p. 339–342.

Wright, T. J., Parsons, B., England, P. C., and Fielding, E. J., 2004, InSAR observations of low slip rates on the major faults of western Tibet: Science, v. 305, p. 236-239.

Valli, F., Arnaud, N., Leloup, P.H., Sobel, E.R., Mah»o, G., Lacassin, R., Guillot, S., Li, H., Tapponnier, P., Xu, Z., 2007. Twenty million years of continuous defromation along the Karakorum fault, western Tibet: a thermochronological analysis. Tectonics 26.

Valli, F., Herv» Leloup, P., Paquette, J.-L., Arnaud, N., Li, H., Tapponnier, P., Lacassin, R., Guillot, S., Liu, D., Deloule, E., Xu, Z., Mah»o, G., 2008. New U**e**Th/Pb constraints on timing of shearing and long-term slip-rate on the Karakorum fault. Tectonics 27.

van Soest, M., Monteleone, B.D., Hodges, K.V., Boyce, J.W., 2011. Laser depth profiling studies of helium diffusion in Durango fluorapatite, Geochim. Cosmochim. Acta, 75, pp. 2409–2419.

Yamaguchi, Y., A. B. Kahle, H. Tsu, T. Kawakami, and M. Pniel (1998). Overview of Advanced Spaceborne Thermal Emission and Reflection Radiometer (ASTER), *Ieee T Geosci Remote*, *36*(4), 1062-1071, doi: 10.1109/36.700991.

Yin, A., Mode of Cenozoic east-west extension in Tibet suggests a common origin of rifts in Asia during the Indo-Asian collision, J. Geophys. Res., 105, 21, 745 – 21,759, 2000.

Zhang, H., Harris, N., Parrish, R., Kelley, S., Li, Z., Rogers, N., Argles, T., King, J.,

2004. Causes and consequences of protracted melting of the mid-crust exposed in the North Himalayan antiform. Earth and Planetary Science Letters 228, 195–212.

Zhu, D.C., Mo, X.X., Niu, Y.L., Zhao, Z.D., Yang, Y.H., and Wang, L.Q., 2009, Zircon U-Pb dating and in-situ Hf isotopic analysis of Permian peraluminous granite in the Lhasa terrane, southern Tibet: Implications for Permian collisional orogeny and paleogeography: Tectonophysics, v. 469, p. 48–60.

12. Figures

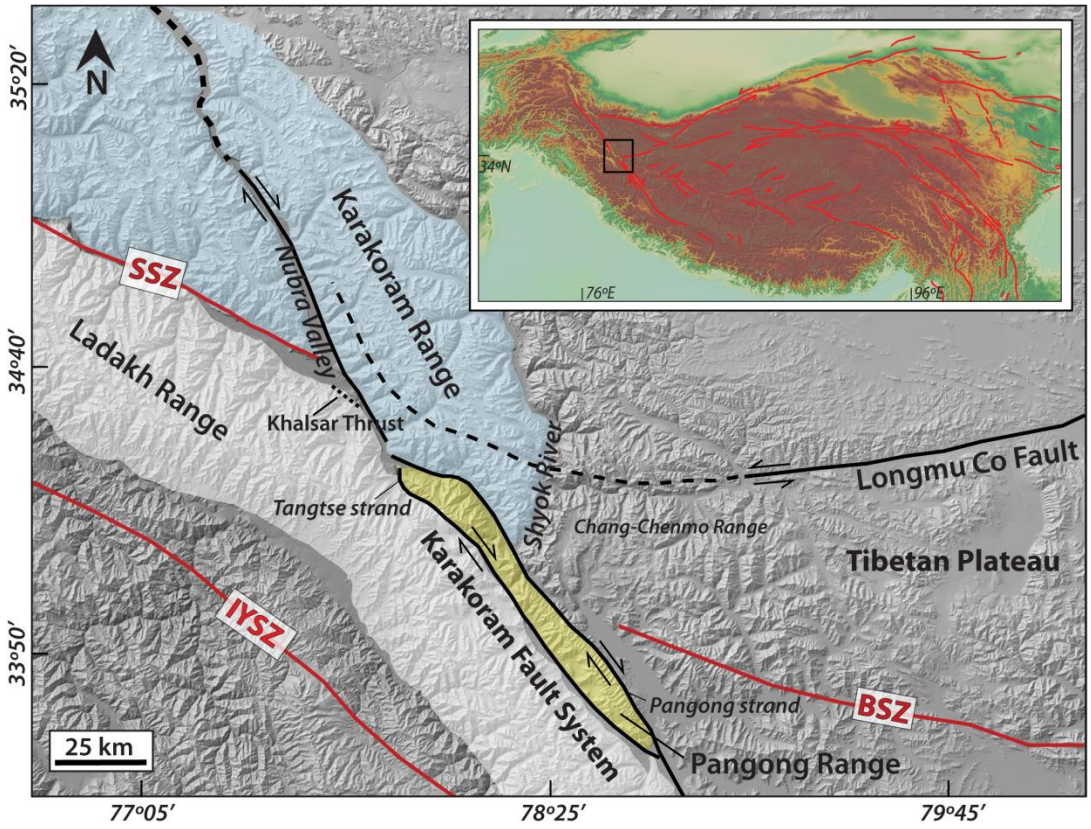

Figure 1. Tectonic map of major features of Ladakh region of northwest India over a hillshade DEM. Major faults are indicated by black lines and suture zones are indicated by red lines (SSZ - Shyok suture zone; IYSZ - Indus-Yarlung suture zone; BSZ - Bangong suture zone). The major mountain ranges discussed in this work have been shaded. Other structural provences and important locations are marked. Inset map shows transform faults within the Himalayan orogen (modified from Taylor and Yin, 2009). The study area is indicated by a black box.

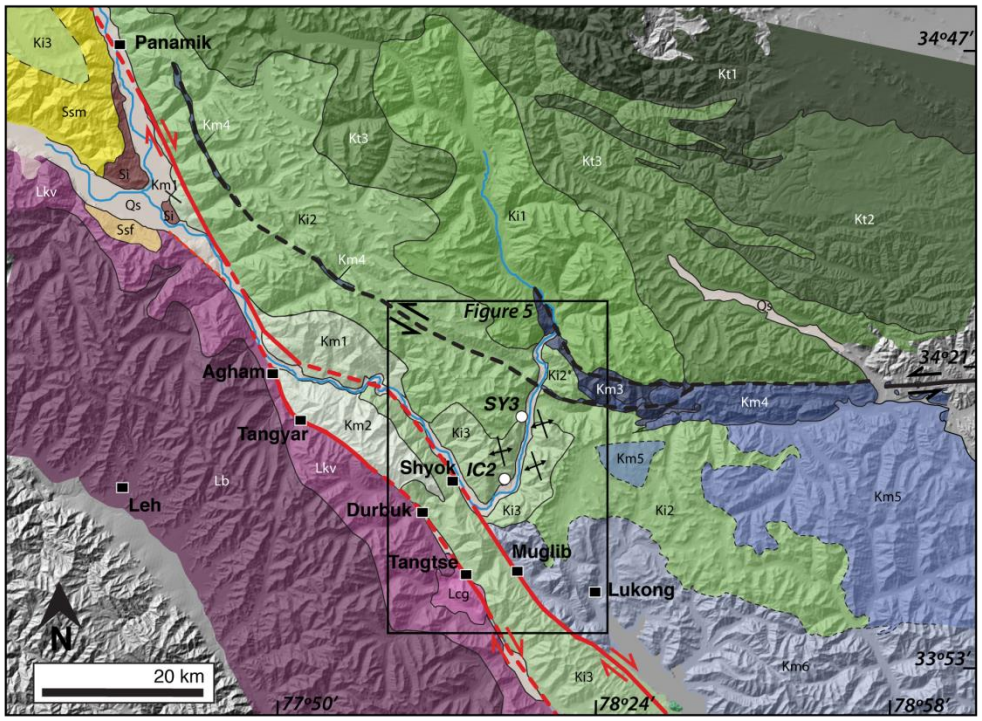

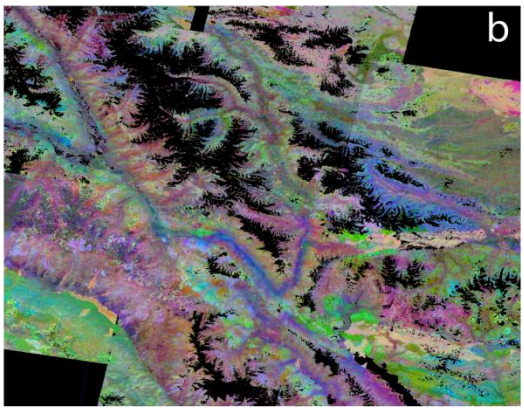

Karakoram Fault
Longmu Co Fault

Qs — Quaternary sediments

Ladakh Complex

- Lcg — Chilam granite
- Lkv — Khardung volcanic units
- Lb — Plutons of the Ladakh batholith

Suture Zone Complex

- Ssm — Saltoro molasse
- Ssf — Volcanic rocks
- Si — Intrusive igneous rocks

Karakoram Complex

Tethyan sedimentary domain

- Kt1 — Predominantly calcareous sedimentary rocks with some chert
- Kt2 — Predominantly volcaniclastic and clastic sedimentary rocks
- Kt3 — Predominantly clastic sedimentary rocks

Karakoram batholith and proximal country rocks

- Ki1 — Plutons interspersed with metasedimentary rocks
- Ki2 — Karakoram granitic rocks; gradational contact with Ki3
- Ki3 — Metasedimentary and metaigneous gneisses with granitic intrusions

Metamorphic domain

- Km1 — Metapelitic schists, volcanics and marbles
- Km2 — Schists, calc-silicates marble & amphibolite bands
- Km3 — Calcareous schists and calc-silicate gneisses, highly strained
- Km4 — Impure marbles, highly strained
- Km5 — Clastic metasedimentary rocks
- Km6 — Volcanoclastic and clastic sedimentary rocks with ophiolitic blocks and carbonate bands

Unmapped regions

Figure 2. a) Lithologic map of the Ladakh region created from a combination of field work and ASTER remote sensing data overlaid on a 30 m hillshade map. Black squares mark villages. White circles mark the location of samples collected for U-Pb geochronology. The units on the left correspond to Figure 2a. The black box shows the extent of Figure 5. b) ASTER decorrelation stretch 12-11-10 showing the same extent as the map in 2a. This stretch highlights differences in the amount of quartz present in the rocks. In this case pink indicates silicic rocks, blue indicates more mafic rocks and tan/peach shows carbonates. Various stretches were used while mapping to accentuate differences in mineral composition. The black areas are regions of snow, ice, water, clouds, or vegetation that have been removed. See Chapter 2 for additional information.

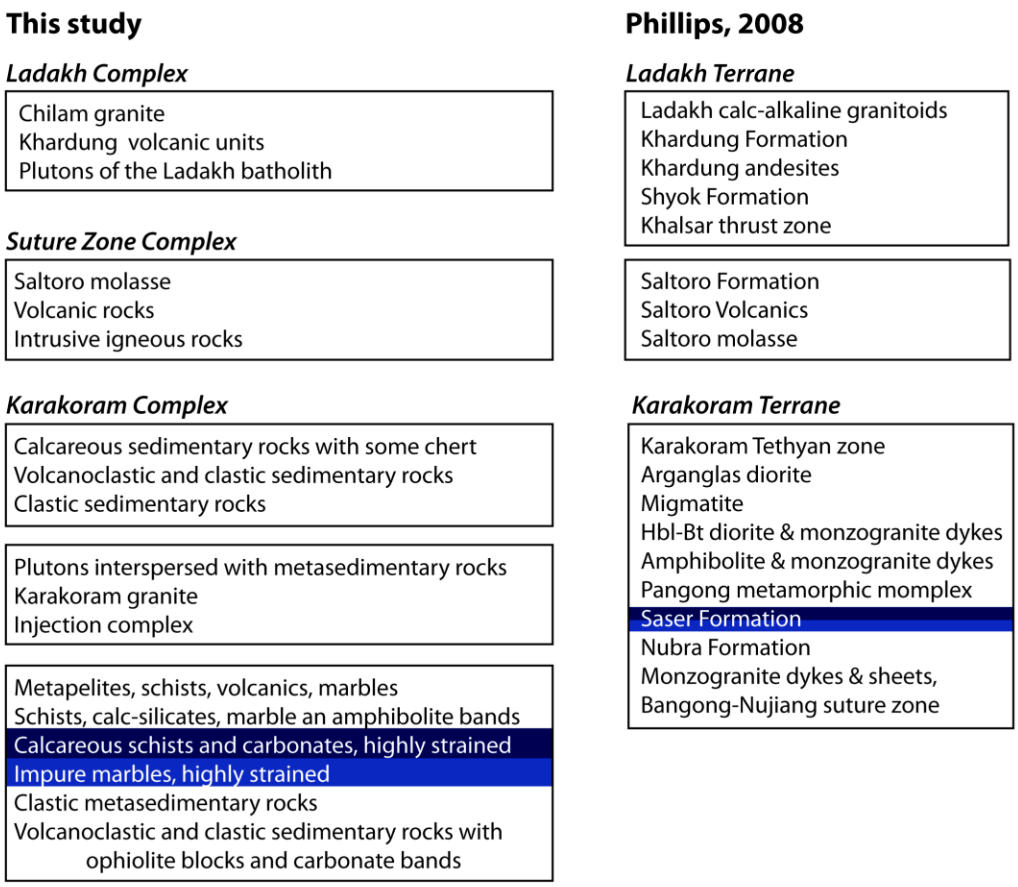

Figure 3. Correlation between units mapped in this study and units from the Phillips, 2008 map. The units associated with the trace of the Longmu Co fault have been highlighted in blue. See Figure 2 for additional information.

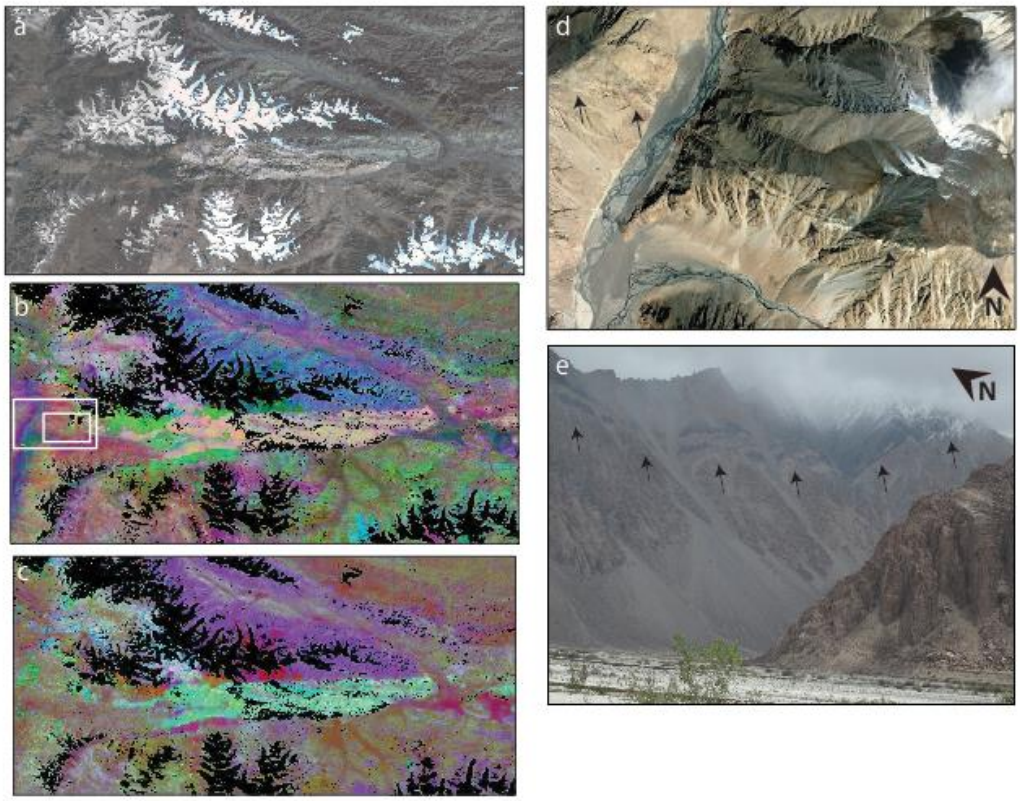

Figure 4. Stretched ASTER images, a Google Earth image and a field photo of the trace of the Longmu Co Fault. a) False color image for reference, b) 12-11-10 stretch. The peach/white unit is a carbonate tracer unit marking the Longmu Co fault system. The large white box shows the location of Figure 11d, the small white box shows the location of Figure 4e. c) 14-12-11 stretch of the same region. d) Google Earth image of the Longmu Co fault which is marked by the Km4 unit, indicated by arrows, e) Field photo of the Longmu Co fault in the same area as Figure 4d. Note the black and white banding of unit Km4 (marked by arrows).

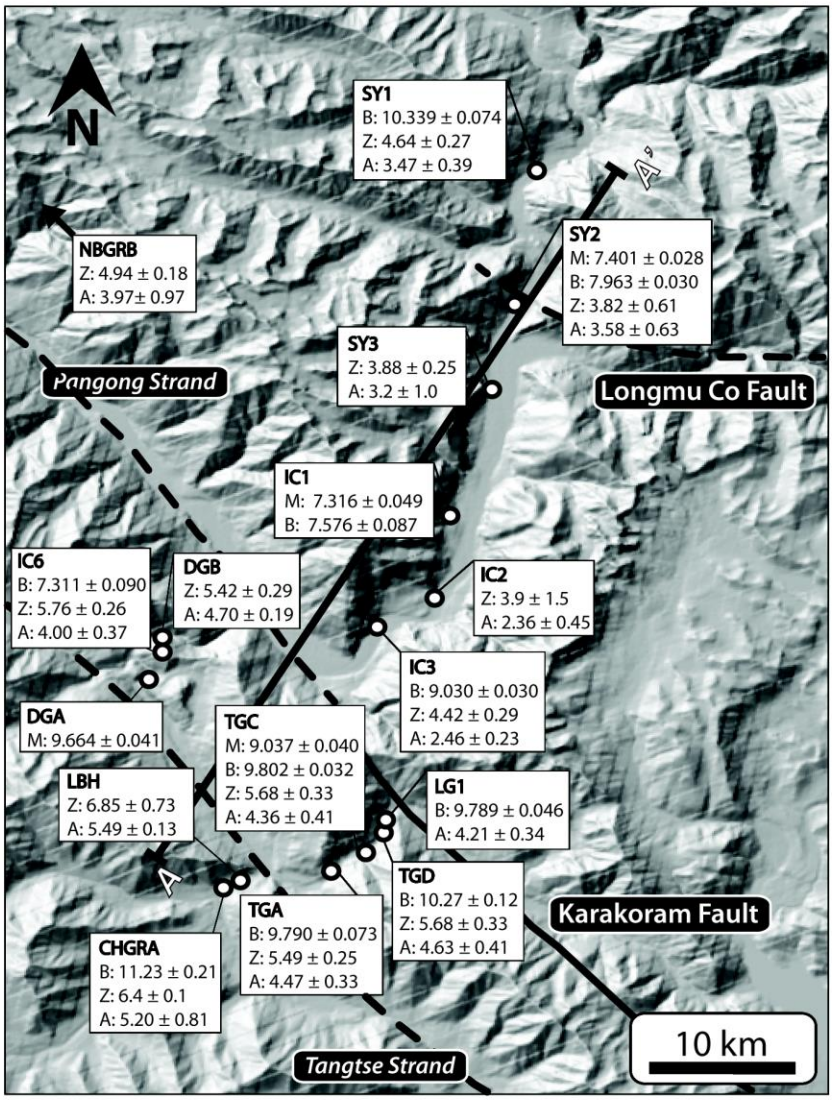

Figure 5. Hillshade showing the location of major faults and samples collected across the region. Sample names are in bold. The collection location of Sample NBGRB is off of the map (north of Panamik). Sample ages projected onto transect A - A″ and shown in Figure 9. M - Muscovite $^{40}Ar^{39}Ar$; B - Biotite $^{40}Ar/^{39}Ar$; Z - Zircon helium; A - Apatite helium. See Tables 2 and 3 for additional information.

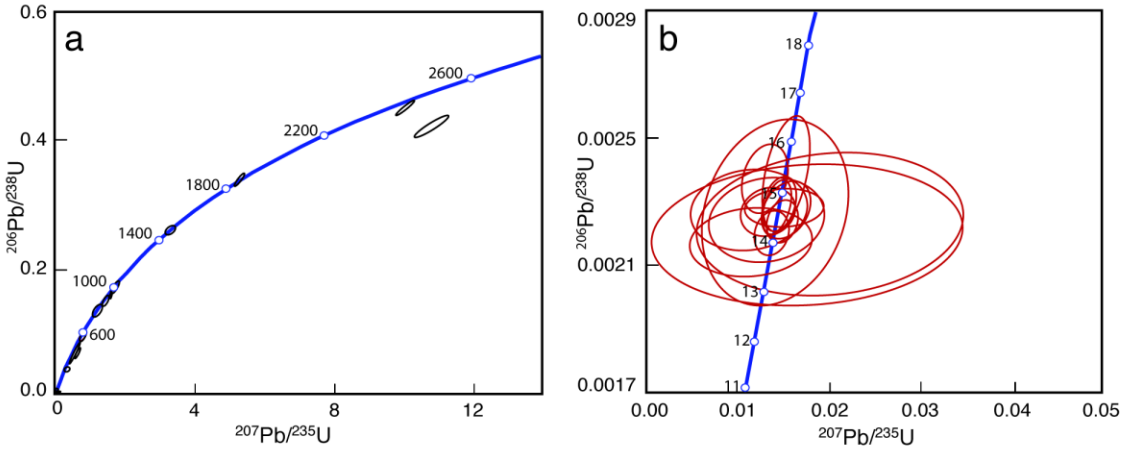

Figure 6. Sample SY3 U-Pb zircon data. a) Concordia plot of SY3 grain core measurements. Data point error ellipses are 68.3% confidence. b) Concordia plot of SY3 grain rim measurements. Data point error ellipses are 68.3% confidence

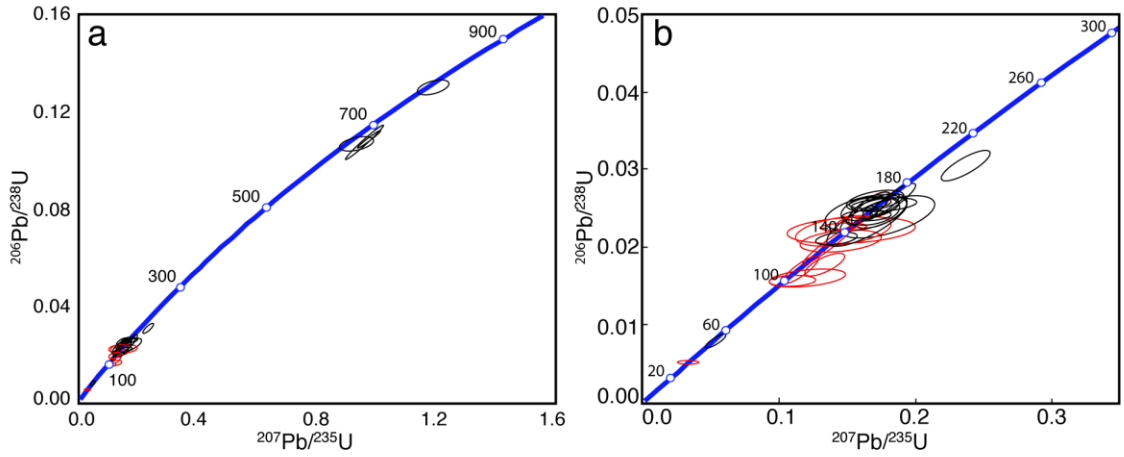

Figure 7. Sample IC2 U-Pb zircon data. Cores are plotted in black and rims are plotted in red. a) Concordia plot of IC2 grain measurements (cores and rims). Data point error ellipses are 68.3% confidence. b) Closer look at cluster of data at ca. 0.2 $^{207}Pb/^{235}U$ in concordia plot "a". Data point error ellipses are 68.3% confidence.

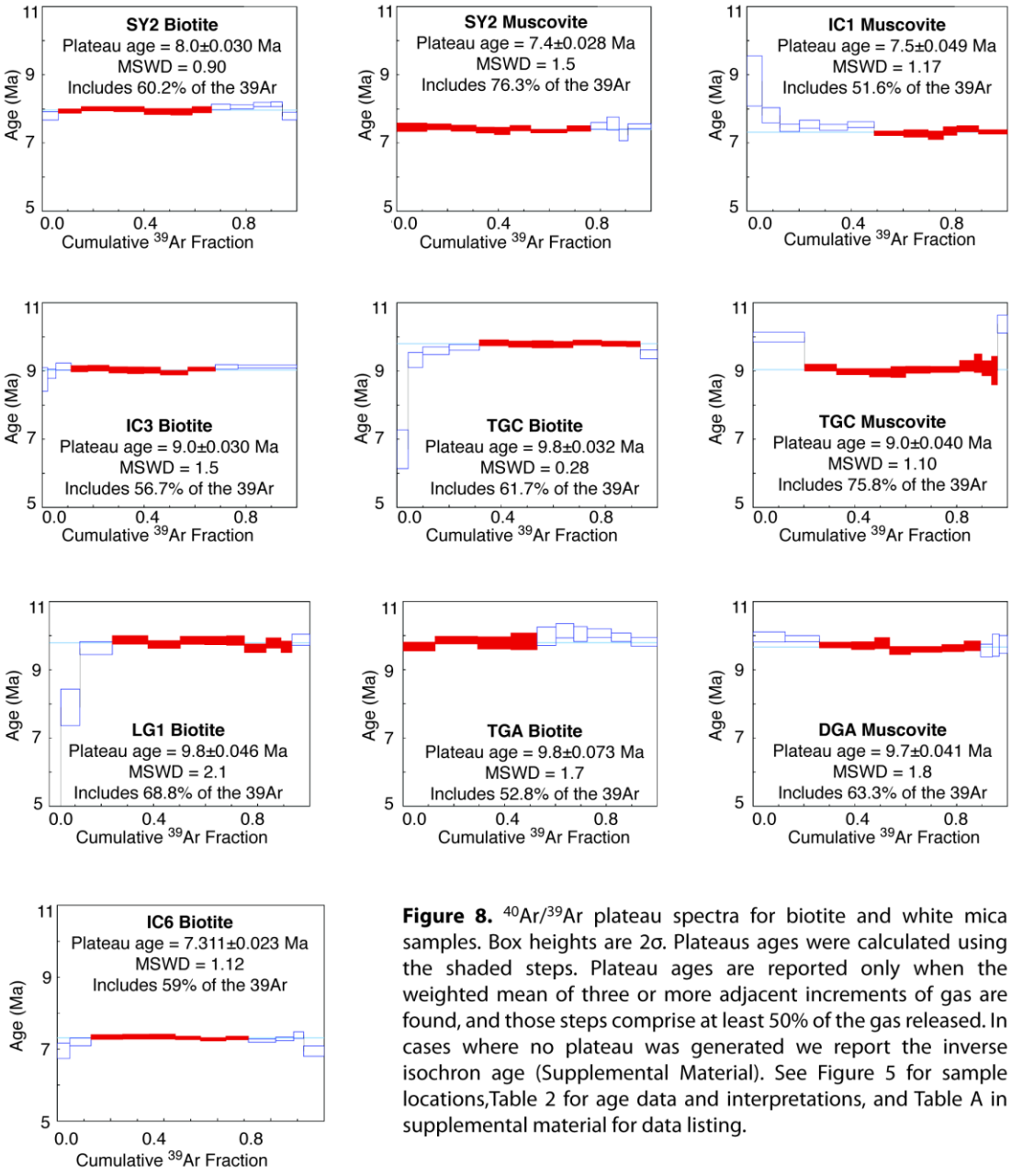

Figure 8. $^{40}Ar/^{39}Ar$ plateau spectra for biotite and white mica samples. Box heights are 2σ. Plateaus ages were calculated using the shaded steps. Plateau ages are reported only when the weighted mean of three or more adjacent increments of gas are found, and those steps comprise at least 50% of the gas released. In cases where no plateau was generated we report the inverse isochron age (Supplemental Material). See Figure 5 for sample locations,Table 2 for age data and interpretations, and Table A in supplemental material for data listing.

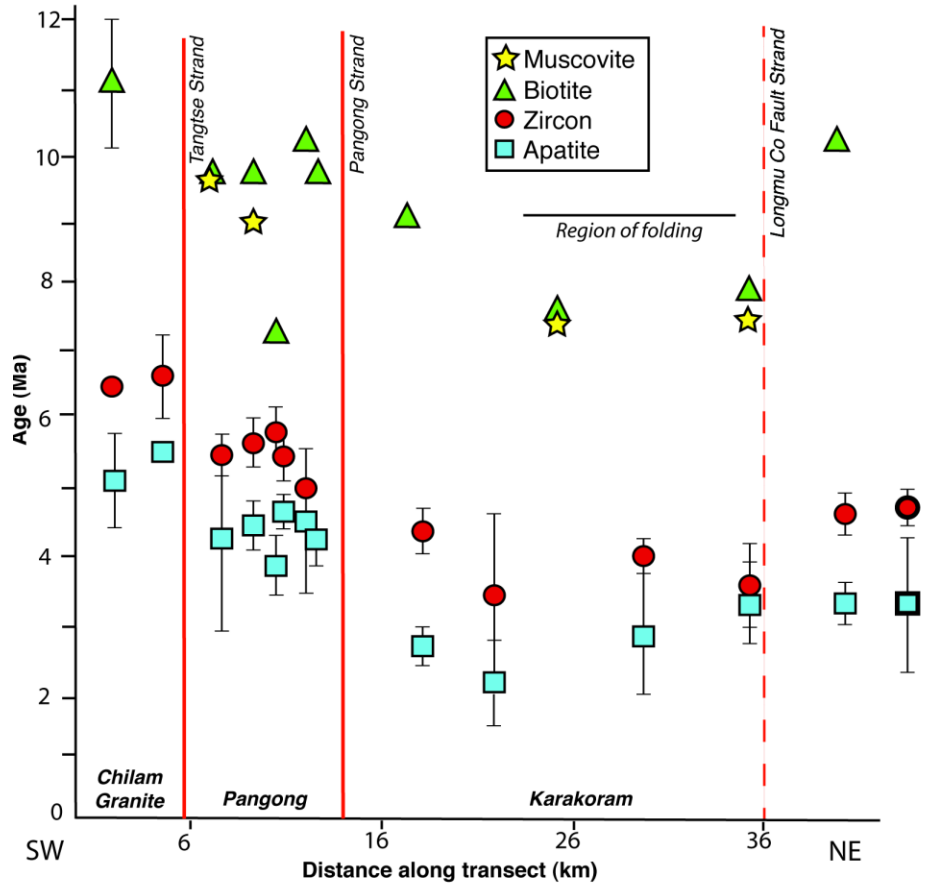

Figure 9. Sample ages and locations along transect A-A′ (from Figure 5). 2σ errors are indicated by error bars. Symbols with bolded outlines are from Sample NBGRB which is located within the Karakoram Range but 100 km northwest of the transect locaton. Solid red lines show approximate location of Karakoram Fault strands. Dashed red line indicates the location of the LCF where it crosses the Shyok River. Bold horizontal line shows location of east-west folding. Thermochronologic data from within all three ranges show discrete exhumation across each fault strand, consistent with vertical offset.

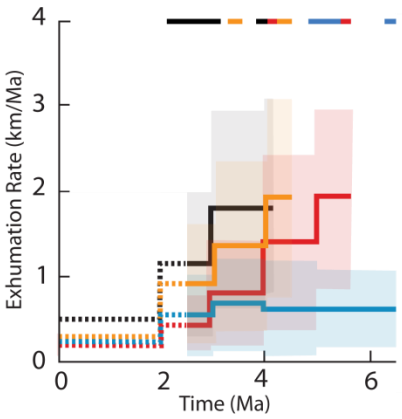

Figure 10. Modeled exhumation rates across the Karakoram fault system. Solid lines represent the mean exhumation rate, shaded regions represent 1 standard deviation of the mean for each time step. Each curve shows the exhumation of one representative sample from within each region; blue-Chilam Granite, red-Pangong Range, black-Karakoram Range. The thick colored lines at the top of the figure show the parts of the model that are constrained by ZrnHe, ApHe, or MsAr data (Tables 2 and 3). The exhumation rate in the Chilam Granite had already decreased by ca. 6.5 Ma, while rates within the Pangong and Karakoram Ranges stay high. At around 5 Ma, rates within the Pangong Range begin to slowly decline. At approximately 5 Ma the rocks to the north of the LCF start to decrease. Exhumation rates stay high within the Karakoram Range between the KFS and LCF systems until 3-4 Ma.

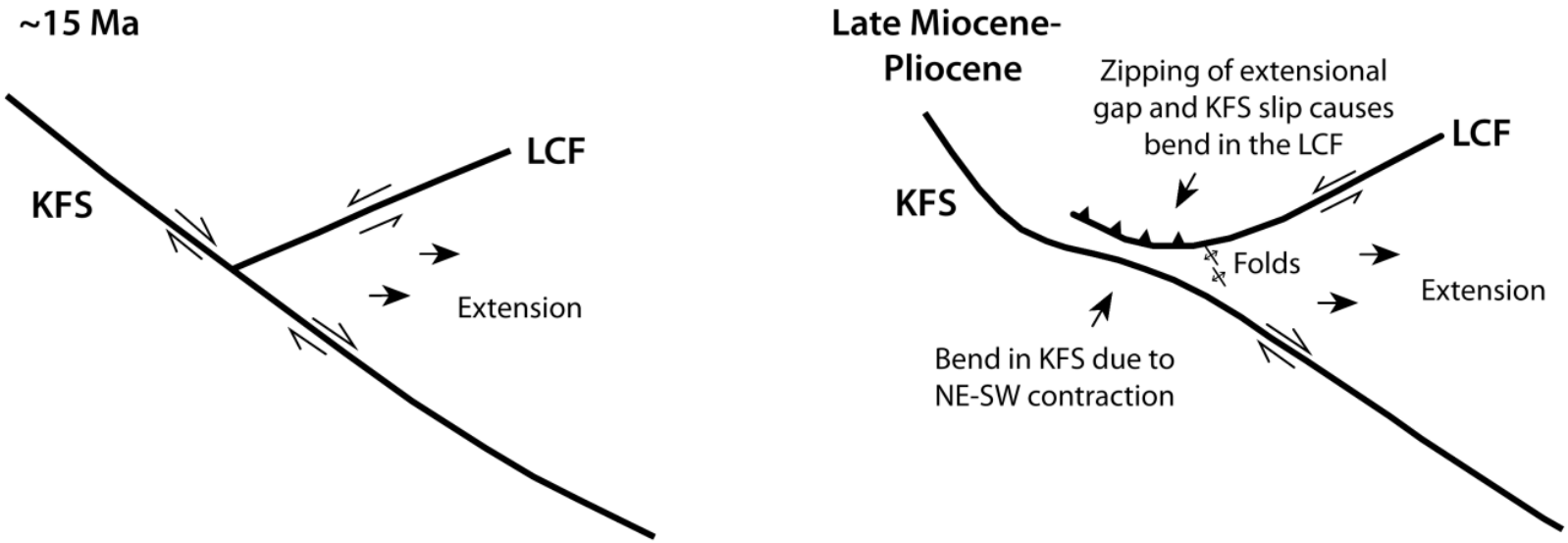

Figure 11. Schematic cartoon showing the evolution of the intersection of the Karakoram and Longmu Co faults from ca. 15 Ma until the present. At ca. 15 Ma. both fault systems initiated in response to east-west extension in central and southern Tibet. As extension continued, roughly north-south shortening closed the reulting gap between the two fault systems. This closure and subsequent shearing along the Karakoram fault system oroclinally rotated the Longmu Co fault. As a result of this change in orientation the Longmu Co fault proximal to the Karakoram fault is sinistral oblique. This obliquity has caused folding between the two fault systems. KFS - Karakoram fault system; LCF - Longmu Co fault.

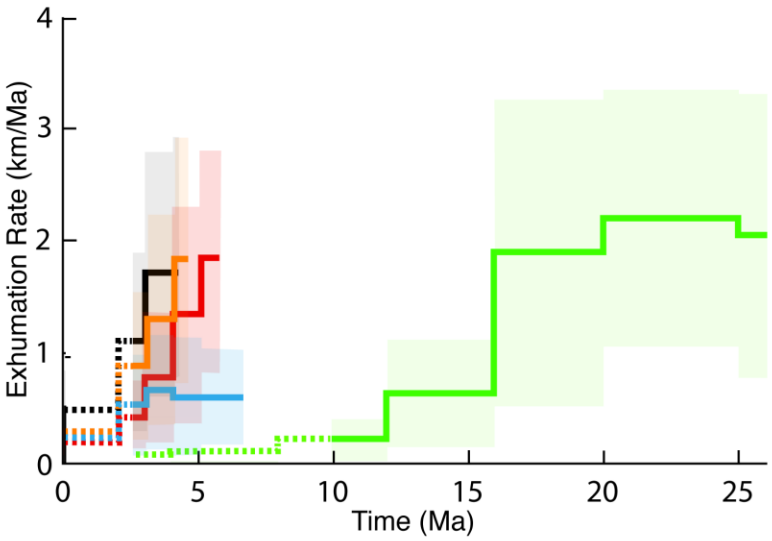

Figure 12. Modeled exhumation rates across the Ladakh-Pangong-Karakoram region. See Chapter 4 for Ladakh Batholith modeling information. Solid lines represent the mean exhumation rate, shaded regions represent 1 standard deviation of the mean for each time step. Each line is one representative sample from within each region; green-Ladakh Batholith, blue-Chilam Granite, red-Pangong Range, black-Karakoram Range, orange-Karakoram Range north of LCF. Dashes areas are unconstrained by data. Exhumation starts to decrease in the southwest in the Ladakh Batholith at ca. 16 Ma. Although we do not see the decrease in exhumation rate within the Chilam granite it is reasonable to assume that a decrease similar to what is observed in the Ladakh Range occurred pre-6.5 Ma. The decrease in exhumation rate then sweeps progressively northeastward into the Pangong and Karakoram Ranges. Exhumation decreases north of the LCF first, and finally begins to decrease between the two fault strands.

Table 1. Zircon U-Pb geochronologic analyses

Analysis	U[1] (ppm)	U/Th[1]	Isotope Ratios 206Pb* 207Pb*	±2s (%)	207Pb* 235U*	±2s (%)	206Pb* 238U	±2s (%)	error corr.	Apparent ages (Ma) 206Pb* 238U*	±2s (Ma)	207Pb* 235U	±2s (Ma)	206Pb* 207Pb*	±2s (Ma)	Best age[2] (Ma)	±2s (Ma)
SY3 Rim																	
1	1535	19.2	20.7041	38.5	0.0152	38.6	0.0023	3.4	0.09	14.70	0.50	15.3	5.9	114	915	14.69	0.49
2	2202	13.5	23.4995	29.7	0.0133	30.0	0.0023	4.3	0.14	14.60	0.63	13.4	4.0	-194	745	14.60	0.62
3	875	9.5	28.0092	75.4	0.0112	75.8	0.0023	7.3	0.10	14.7	1.1	11.3	8.5	-654	2136	14.7	1.1
4	2136	6.1	20.7198	14.5	0.0149	15.1	0.0022	4.0	0.27	14.40	0.58	15.0	2.2	112	343	14.40	0.58
5	540	14.3	17.2066	126.7	0.0176	127.4	0.0022	13.5	0.11	14.1	1.9	18	22	534	3104	14.1	1.9
6	2072	11.3	20.5631	22.2	0.0153	22.7	0.0023	4.8	0.21	14.70	0.71	15.4	3.5	130	524	14.69	0.71
7	1139	6.4	23.4185	63.4	0.0132	63.9	0.0022	7.9	0.12	14.5	1.1	13.3	8.5	-185	1620	14.5	1.1
8	541	5.3	21.9934	73.1	0.0142	75.1	0.0023	17.0	0.23	14.6	2.5	14	11	-30	1826	14.6	2.5
9	2230	6.0	21.6105	20.3	0.0152	23.1	0.0024	10.9	0.47	15.3	1.7	15.3	3.5	12	490	15.3	1.7
10	2682	9.6	16.9659	4.8	0.0388	17.1	0.0048	16.5	0.96	30.7	5.0	38.7	6.5	5765	105	30.7	5.0
11	2543	9.4	22.0223	17.2	0.0144	17.9	0.0023	5.3	0.29	14.80	0.78	14.5	2.6	-34	417	14.79	0.78
12	352	2.0	15.4068	96.0	0.0200	96.9	0.0022	13.3	0.14	14.4	1.9	20	19	771	2144	14.4	1.9
13	1110	7.9	26.2476	75.6	0.0114	75.9	0.0022	6.8	0.09	14.0	1.0	11.5	8.7	-478	2064	14.0	1.0
14	3161	13.6	22.2100	15.1	0.0142	15.9	0.0023	5.0	0.31	14.75	0.73	14.3	2.3	-54	368	14.75	0.73
15	2415	11.4	22.2095	18.5	0.0137	19.0	0.0022	4.2	0.22	14.18	0.59	13.8	2.6	-54	452	14.18	0.59
16	1929	17.5	24.9662	24.9	0.0131	25.6	0.0024	6.0	0.23	15.29	0.91	13.2	3.4	-347	643	15.28	0.91
SY3 Cores																	
1	51	1.7	14.9363	12.7	1.2070	15.9	0.1308	9.5	0.60	792	71	804	89	840	270	792	71
2	128	3.1	14.2628	5.5	0.6091	14.1	0.0630	13.0	0.92	394	50	483	54	930	110	394	50
3	66	1.0	10.7804	4.2	3.3011	5.6	0.2581	3.6	0.65	1480	48	1481	43	1483	80	1483	80
4	530	20.3	5.3722	2.2	10.8115	6.1	0.4212	5.6	0.93	2270	110	2507	56	2708	36	2708	36
5	105	0.7	8.7731	1.5	5.2977	3.9	0.3371	3.6	0.93	1873	58	1868	33	1864	26	1864	26
6	579	2.1	15.4851	2.4	0.5020	18.8	0.0564	18.7	0.99	354	64	413	64	761	50	354	64
7	680	9.0	14.9340	2.2	0.6649	15.1	0.0720	14.9	0.99	448	65	518	61	837	45	448	65
8	217	1.8	6.1828	0.7	10.0574	3.7	0.4510	3.6	0.98	2400	73	2440	34	2474	11	2474	11
9	184	1.9	15.3769	6.5	0.5480	11.0	0.0611	8.9	0.81	382	33	444	40	780	140	382	33
10	144	2.7	13.4932	4.1	1.6851	11.4	0.1649	10.6	0.93	984	97	1003	73	1044	82	1044	82
11	452	0.6	16.6406	2.1	0.7781	5.1	0.0939	4.6	0.91	579	25	584	23	607	46	579	25
12	68	1.4	14.0209	7.3	1.4497	11.0	0.1474	8.3	0.75	887	69	910	66	967	149	967	149
13	116	1.8	15.8467	9.3	0.7843	13.8	0.0901	10.2	0.74	556	54	588	61	710	200	556	54
14	183	2.4	16.6252	18.4	0.3201	20.0	0.0386	7.8	0.39	244	19	282	49	610	400	244	19
15	718	3.0	13.5207	0.50	1.5597	11.8	0.1530	11.8	1.00	920	100	954	73	1040.4	9.5	1040.4	9.5
16	1381	3.9	13.2548	0.40	1.6746	6.0	0.1610	6.0	1.00	962	54	999	38	1080.4	7.1	1080.4	7.1
IC2 Rims																	
1	642	1.4	20.1811	8.0	0.1174	15.9	0.0172	13.8	0.86	110	15	113	17	170	190	110	15
2	298	1.3	20.1982	143.6	0.1644	14.5	0.0241	5.0	0.35	153.4	7.6	155	21	170	320	153.4	7.6

3	223	1.1	20.1314	18.0	0.1755	18.5	0.0256	4.1	0.22	163.1	6.7	164	28	180	420	163.1	6.7
4	676	451.3	21.1211	31.9	0.0334	32.1	0.0051	4.1	0.13	32.9	1.3	33	11	70	760	32.9	1.3
5	270	1.1	21.0445	15.0	0.1701	16.5	0.0260	6.9	0.42	165	11	160	24	80	360	165	11
6	145	5.5	18.2587	28.1	0.1212	29.6	0.0161	9.3	0.31	102.6	9.4	116	33	400	630	102.6	9.4
7	373	1.0	19.6784	15.7	0.1617	17.0	0.0231	6.4	0.38	147.1	9.4	152	24	230	360	147.1	9.4
8	2040	0.7	20.1817	1.9	0.1511	10.4	0.0221	10.3	0.98	141	14	143	14	174	45	141	14
9	995	0.7	20.2390	5.4	0.1576	6.1	0.0231	2.8	0.47	147.5	4.1	149.0	8.4	170	130	147.5	4.1
10	302	1.4	19.5224	15.0	0.1644	23.9	0.0233	18.6	0.78	148	27	155	34	250	350	148	27
11	214	1.9	19.8521	25.6	0.1446	27.1	0.0208	9.1	0.33	133	12	137	35	210	600	133	12
12	110	1.1	20.1454	39.6	0.1525	40.8	0.0223	9.9	0.24	142	14	144	55	180	930	142	14
13	847	0.2	18.2998	9.1	0.1334	14.1	0.0177	10.8	0.76	113	12	127	17	400	200	113	12
14	1219	0.7	20.6439	6.0	0.1340	16.5	0.0201	15.4	0.93	128	20	128	20	120	140	128	20
15	1062	1.1	20.5207	6.7	0.1603	7.3	0.0239	2.9	0.39	152.0	4.3	151	10	140	160	152.0	4.3
16	1102	0.9	20.4537	2.2	0.1680	5.1	0.0249	4.6	0.90	158.7	7.2	158.0	7.4	143	51	158.7	7.2
17	257	35.7	19.6381	19.9	0.1097	20.6	0.0156	5.3	0.26	99.9	5.2	106	21	240	460	99.9	5.2
18	444	2.2	20.5656	13.4	0.1417	14.4	0.0211	5.5	0.38	134.8	7.3	135	18	130	320	134.8	7.3
19	1745	1.3	20.2478	3.1	0.1601	9.8	0.0235	9.3	0.95	150	14	151	144	166	72	150	14
20	1679	1.3	20.1358	3.6	0.1358	8.4	0.0198	7.7	0.91	126.6	9.6	129	10	179	83	126.6	9.6
21	336	1.6	21.0657	6.6	0.1659	11.6	0.0253	9.5	0.82	161	15	156	17	70	160	161	15
IC2 Cores																	
1	738	1.7	20.5317	11.6	0.0532	18.4	0.0079	14.3	0.78	50.8	7.2	53.0	9.4	130	270	50.8	7.2
2	399	0.7	18.4424	21.1	0.1787	26.0	0.0239	15.1	0.58	152	23	167	40	380	480	152	23
3	387	1.4	15.2807	1.4	0.9575	7.9	0.1061	7.8	0.98	650	48	682	39	789	30	650	48
4	975	0.7	20.0960	8.1	0.1707	11.7	0.0249	8.5	0.72	158	13	160	17	180	190	158	13
5	424	0.7	19.9613	6.5	0.1712	12.8	0.0248	11.1	0.86	158	17	160	19	200	150	158	17
6	254	0.7	20.8282	20.8	0.1626	24.0	0.0246	11.9	0.50	156	18	153	34	100	490	156	18
7	407	0.9	15.3789	1.6	0.9836	5.9	0.1097	5.7	0.96	671	36	695	30	775	33	671	36
8	529	0.8	20.0338	9.3	0.1718	10.6	0.0250	5.1	0.48	159.0	8.0	161	16	190	220	159.0	8.0
9	290	1.2	20.6137	9.8	0.1660	11.5	0.0248	6.0	0.52	158.0	9.3	156	17	120	230	158.0	9.3
10	790	0.7	19.8948	7.1	0.1747	7.6	0.0252	2.8	0.36	160.5	4.4	164	12	210	170	160.5	4.4
11	156	1.2	22.2848	21.3	0.1364	23.7	0.0220	10.5	0.44	141	15	130	29	-60	520	141	15
12	106	0.7	15.0539	4.9	1.1923	5.7	0.1302	3.0	0.53	789	22	797	32	820	100	789	22
13	136	1.6	15.7062	7.1	0.9365	8.0	0.1067	3.6	0.45	653	23	671	39	730	150	653	23
14	722	7.0	17.7843	5.6	0.2369	10.0	0.0306	8.3	0.83	194	16	216	19	460	120	194	16
15	303	1.0	21.2872	15.0	0.1461	15.2	0.0226	2.9	0.19	143.8	4.1	139	20	50	360	143.8	4.1
16	998	0.7	19.6243	6.7	0.1815	13.5	0.0258	11.7	0.87	164	19	169	21	240	160	164	19

Note: All uncertainties are reported at the 2σ level, and include only measurement errors. Systematic errors are as follows for $^{206}Pb/^{238}U$ and $^{206}Pb/^{207}Pb$, respectively, at 2σ level: 1.6% and 0.9% for sample TRD and 2.1% and 3.2% for sample TRE. Analyses conducted by LA-MC-ICPMS, as described by Gehrels et al. (2008). U/Pb and $^{206}Pb/^{207}Pb$ fractionation is calibrated relative to fragments of a large Sri Lanka zircon of 563.5±3.2 Ma (2σ). U decay constants and composition as follows: $^{238}U = 9.8485 \times 10^{-10}$, $^{235}U = 1.55125 \times 10^{-10}$, $^{238}U/^{235}U = 137.88$.

[1]U concentration and U/Th are calibrated relative to Sri Lanka zircon standard and are accurate to ~20%.

[2]Analyses with >20% uncertainty (2σ) in $^{206}Pb/^{238}U$ age are not included. Analyses with >20% uncertainty (2σ) in $^{206}Pb/^{207}Pb$ are not included, unless $^{206}Pb/^{238}U$ age is <500 Ma. Best age is determined from $^{206}Pb/^{238}U$ age for analyses with $^{206}Pb/^{238}U$ age <1000 Ma and from $^{206}Pb/^{207}Pb$ age for analyses with $^{206}Pb/^{238}U$ age >1000 Ma.

Reference

Gehrels, G. E., V. Valencia, and J. Ruiz (2008), Enhanced precision, accuracy, efficiency, and spatial resolution of U-Pb ages by laser ablation-multicollector-inductively coupled plasma-mass spectrometry, *Geochemistry, Geophysics, Geosystems*, *9*, Q03017, doi:10.1029/2007GC001805.

Table 2: 40Ar/39Ar step heating results

Sample	*Mineral*	*Latitude*	*Longitude*	*Elevation*	*Lithology*	*Plateau Date (Ma)*	*± (Ma)*	*MSWD*	*Integrated Date (Ma)*	*± (Ma)*	*Isochron Date (Ma)*	*± (Ma)*	*MSWD*	*40Ar/36Ar intercept*
SY1	biotite	34.3833	78.3064	3812	granite	-	-	-	10	0.08	**10.339**	**0.074**	8.5	288.5±8.0
SY2	biotite	34.317	78.2954	3790	granodiorite	**7.963**	**0.030**	0.9	8	0.09	8.129	0.088	2.1	290.9±6.1
	muscovite	34.317	78.2954	3790	granodiorite	**7.401**	**0.028**	1.5	7	0.09	-	-	-	-
IC1	biotite	34.209	78.2615	3701	granite	-	-	-	8	0.09	**7.576**	**0.087**	3.5	291.1±5.4
	muscovite	34.209	78.2615	3701	granite	**7.316**	**0.035**	1.2	7.3	0.12	-	-	-	-
IC3	biotite	34.153	78.2247	3641	granodiorite	**9.030**	**0.030**	1.5	9	0.07	9.122	0.097	4	291.7±6.1
IC6	biotite	34.1269	78.1101	3800	granite	**7.311**	**0.023**	1.1	7	0.09	7.333	0.079	2.8	295.0±5.0
TGA	biotite	34.0284	78.2028	4011	leucogranite	**9.790**	**0.073**	1.7	9.9	0.17	10.11	0.24	5.3	295.2±3.4
TGC	biotite	34.0389	78.2195	4017	leucogranite	**9.802**	**0.032**	0.3	9.7	0.14	9.93	0.12	1.3	291.7±5.1
	muscovite	34.0389	78.2195	4017	leucogranite	**9.037**	**0.040**	1.1	9	0.2	-	-	-	-
TGD	biotite	34.0541	78.2292	4065	leucogranite	-	-	-	10	0.14	**10.27**	**0.12**	5.5	292.2±2.1
LG1	biotite	34.6614	77.6178	-	granodiorite	**9.789**	**0.046**	2.1	10	0.3	10.21	0.19	3	293.7±4.7
DGA	Muscovite	34.1469	78.1159	3845	granite	**9.664**	**0.041**	1.8	10	0.12	10.10	0.20	13	305.9±9.7
CHGRA	biotite	34.6614	77.6178	3998	granite	-	-	-	10	0.4	**11.23**	**0.21**	5.7	289±18

Plateau, integrated and isochron age results are reported, when available.
All errors reported at 2 σ.
Preferred dates are in bold.
MSWD – mean square weighted deviation.
See Appendix B for additional information.

Table 3: Apatite and zircon (U-Th)/He data

Sample	Grain	Latitude	Longitude	Elevation	Lithology	4He*	± 2s	238U*	± 2s	232Th*	± 2s	Raw Date	± 2s	FT	^Corr Date	± 2s	Mean Date	± 2s
				(m)		(fmol)	(fmol)	(fmol)	(fmol)	(fmol)	(fmol)	(Ma)	(Ma)		(Ma)	(Ma)	(Ma)	(Ma)
SY1		34.3833	78.3064	3812	granite													
	a1					6.03	0.17	1285	23	1943	47	2.695	0.086	0.804	3.353	0.053	3.47	0.39
	a2					3.93	0.12	777	14	1509	28	2.704	0.090	0.748	3.613	0.060		
	a5					5.36	0.16	1511	25	1373	26	2.271	0.076	0.805	2.820	0.047		
	a6					2.38	0.12	563	10	556	10	2.67	0.14	0.772	3.454	0.089		
	z6					517	13	92900	1700	18200	170	4.13	0.12	0.849	4.860	0.071	4.64	0.27
	z7					498	12	86900	1500	21100	170	4.20	0.12	0.85	4.946	0.072		
	z8					172.0	4.3	32200	560	10100	88	3.87	0.11	0.823	4.697	0.069		
	z9					244.0	5.8	51000	900	11000	100	3.53	0.10	0.829	4.257	0.061		
	z10					250.0	6.1	50600	890	14100	120	3.60	0.10	0.813	4.423	0.065		
SY2		34.3170	78.2954	3790	granodiorite													
	a1					4.67	0.14	1265	23	1156	29	2.360	0.080	0.85	2.778	0.047	3.58	0.63
	a2					0.538	0.034	150.0	4.8	104.4	3.6	2.39	0.17	0.641	3.73	0.13		
	a4					0.290	0.026	100.0	6.0	57.6	2.4	1.98	0.21	0.599	3.30	0.18		
	a5					0.517	0.030	144.0	4.0	102.7	3.4	2.39	0.15	0.709	3.36	0.11		
	a6					1.550	0.072	323.0	6.2	205.9	5.2	3.24	0.16	0.73	4.44	0.11		
	a7					1.250	0.056	260.0	5.8	241.1	6.2	3.06	0.15	0.745	4.10	0.10		
	z6					99.9	2.5	23400	410	8180	240	3.056	0.092	0.8	3.821	0.057	3.82	0.61
	z7					183.0	4.5	53500	1200	15000	330	2.493	0.080	0.809	3.082	0.050		
	z11					167.0	4.1	27600	800	45000	910	3.41	0.11	0.75	4.547	0.075		
	z10					255.0	6.4	62500	1800	51600	1100	2.660	0.094	0.806	3.300	0.058		
SY3		34.2728	78.2821	3778	granite													
	a1					2.27	0.11	683	14	240.0	5.2	2.39	0.13	0.708	3.371	0.089	3.2	1.0
	a2					0.671	0.038	330.0	5.8	74.3	2.2	1.498	0.090	0.667	2.247	0.067		
	a3					2.18	0.11	619	12	33.1	1.6	2.70	0.14	0.697	3.88	0.10		
	z1					93.0	2.4	22900	360	3250	31	3.051	0.090	0.81	3.766	0.055	3.88	0.25
	z2					345.0	8.3	74700	1300	20000	170	3.369	0.096	0.859	3.921	0.055		
	z3					438	11	87900	1400	21400	180	3.65	0.10	0.832	4.390	0.063		
	z4					479	12	100000	1600	14800	120	3.58	0.10	0.902	3.971	0.056		
IC2		34.2093	78.2615	3767	diorite													
	a1					1.470	0.062	631	12	164.0	3.8	1.707	0.080	0.741	2.304	0.054	2.36	0.45
	a3					6.31	0.16	2920	55	586	12	1.599	0.050	0.848	1.886	0.030		
	a4					3.84	0.11	1290	25	204.0	4.4	2.226	0.074	0.791	2.814	0.047		
	a5					1.670	0.062	659	12	82.4	2.8	1.901	0.080	0.784	2.425	0.051		
	z1					39.0	1.1	6660	190	6210	130	3.73	0.14	0.747	4.998	0.091	3.9	1.5
	z2					135.0	3.4	25600	740	31300	640	3.19	0.11	0.791	4.037	0.068		
	z3					25.40	0.69	9070	260	6270	130	1.874	0.068	0.723	2.593	0.048		
IC3		34.1530	78.2247	3641	granodiorite													
	a2					0.993	0.048	377.0	8.2	18.6	2.0	2.02	0.11	0.819	2.464	0.065	2.46	0.23
	a4					3.31	0.11	1200	21	207	12	2.049	0.078	0.782	2.620	0.050		

	a5					1.440	0.060	483	10	79.4	4.4	2.23	0.10	0.769	2.900	0.067		
	z7					56.9	1.5	10000	220	7000	300	3.79	0.13	0.823	4.606	0.077	4.42	0.29
	z8					132.0	3.3	24300	440	15700	340	3.67	0.11	0.85	4.321	0.064		
	z9					74.7	1.8	15100	320	9900	270	3.34	0.10	0.823	4.057	0.064		
	z10					173.0	4.3	29100	680	16000	570	4.08	0.13	0.87	4.685	0.077		
NBGRB		34.7987	77.5319	3210	granite													
	a3					0.904	0.036	254.0	5.2	76.7	2.6	2.57	0.12	0.673	3.819	0.087	3.97	0.97
	a5					0.700	0.026	177.0	3.8	43.3	2.4	2.85	0.12	0.668	4.268	0.093		
	a6					1.270	0.044	435.0	7.8	152.0	3.6	2.063	0.080	0.731	2.823	0.055		
	z1					221.0	5.4	40800	630	8760	71	4.00	0.11	0.803	4.979	0.071	4.94	0.18
	z2					777	19	145000	2500	12000	100	4.07	0.12	0.807	5.046	0.075		
	z3					242.0	5.9	46900	780	6700	58	3.87	0.11	0.766	5.047	0.074		
	z4					228.0	5.5	44200	730	10800	100	3.78	0.11	0.809	4.676	0.068		
TGA		34.0284	78.2028	4011	leucogranite													
	a1					0.776	0.044	205.0	5.2	66.0	3.4	2.73	0.16	0.659	4.15	0.13	4.47	0.33
	a2					0.270	0.024	59.0	1.6	24.0	2.8	3.24	0.29	0.703	4.61	0.21		
	a3					1.110	0.054	300.0	6.0	74.8	4.6	2.72	0.14	0.702	3.878	0.099		
	a4					1.370	0.056	292.0	6.2	40.0	3.8	3.52	0.16	0.686	5.13	0.12		
	a5					0.678	0.030	161.0	5.6	54.6	4.4	3.02	0.17	0.66	4.58	0.13		
	z1					263.0	6.6	46900	850	15800	340	4.04	0.12	0.779	5.187	0.077	5.42	0.25
	z2					94.1	2.4	18700	370	3010	68	3.76	0.12	0.708	5.316	0.083		
	z3					255.0	6.1	44400	840	3390	71	4.37	0.13	0.76	5.748	0.086		
	z4					53.6	1.3	9640	230	3850	110	3.95	0.13	0.718	5.500	0.090		
TGC		34.0389	78.2195	4017	leucogranite													
	a2					2.68	0.16	669	13	120.0	2.6	2.98	0.18	0.738	4.04	0.12	4.36	0.41
	a3					4.23	0.12	877	20	155.0	7.0	3.59	0.13	0.762	4.709	0.085		
	a10					1.370	0.064	349.0	7.4	57.1	2.4	2.93	0.15	0.679	4.32	0.11		
	z1					290.0	6.9	42100	1100	5030	110	5.19	0.18	0.823	6.31	0.11	5.68	0.33
	z3					151.0	3.5	24100	530	5190	120	4.61	0.15	0.867	5.321	0.084		
	z10					216.0	5.2	33900	990	15400	320	4.47	0.16	0.826	5.409	0.098		
	z11					306.0	7.5	45600	1300	22600	470	4.66	0.17	0.832	5.60	0.10		
	z12					204.0	5.2	30500	890	19600	400	4.52	0.16	0.796	5.68	0.10		
TGD		34.0541	78.2292	4065	leucogranite													
	a3					5.48	0.19	1080	19	993	25	3.23	0.12	0.781	4.136	0.077	4.63	0.99
	a5					4.66	0.14	780	15	462	15	4.07	0.15	0.795	5.125	0.092		
	z5					191.0	4.6	33900	830	15600	420	3.95	0.13	0.827	4.778	0.077	5.04	0.28
	z6					368.0	8.9	53700	1600	39900	820	4.54	0.16	0.87	5.213	0.089		
	z8					223.0	5.5	36800	1100	12500	260	4.34	0.16	0.844	5.142	0.093		
LG1		34.6614	77.6178		granodiorite													
	a1					2.77	0.16	628	11	114.0	4.2	3.28	0.20	0.798	4.11	0.12	4.21	0.34
	a2					3.24	0.11	678	15	191.0	7.4	3.48	0.14	0.759	4.586	0.089		
	a3					3.37	0.11	747	14	98.4	3.6	3.39	0.12	0.78	4.349	0.078		
	a5					2.33	0.10	593	11	64.0	2.0	2.98	0.14	0.781	3.812	0.090		
DGB		34.1469	78.1159	3845	granite													
	a1					1.330	0.062	258.0	6.8	102.0	3.2	3.65	0.20	0.732	4.99	0.14	4.70	0.19
	a2					3.00	0.18	638	13	360	11	3.22	0.20	0.738	4.36	0.14		

	a3					1.130	0.050	231.0	5.2	118.0	4.6	3.39	0.17	0.703	4.82	0.12		
	a4					1.190	0.042	247.0	5.0	102.0	2.8	3.40	0.14	0.733	4.635	0.093		
	a5					1.130	0.058	225.0	4.8	158.0	5.4	3.35	0.18	0.727	4.60	0.13		
	z1					1040	25	189000	5500	20700	430	4.15	0.16	0.778	5.34	0.10	5.42	0.29
	z2					367.0	9.1	67500	2000	9410	210	4.08	0.16	0.714	5.71	0.11		
	z3					573	14	119000	3500	4430	94	3.71	0.15	0.71	5.22	0.10		
IC6		34.1269	78.1101	3800	granite													
	a1					0.441	0.032	108.0	2.8	37.7	3.0	2.92	0.23	0.765	3.82	0.15	4.00	0.37
	a3					2.09	0.14	375.0	7.6	571	13	3.19	0.22	0.806	3.96	0.13		
	a6					0.108	0.018	32.0	1.6	6.9	1.0	2.53	0.43	0.531	4.77	0.41		
	a7					0.309	0.034	103.0	2.2	53.9	3.0	2.07	0.23	0.602	3.44	0.19		
	z1					208.0	4.2	33200	670	11100	260	4.51	0.12	0.767	5.879	0.081	5.76	0.26
	z2					357.0	7.8	52500	1200	35200	720	4.56	0.14	0.787	5.798	0.086		
	z3					89.4	2.0	12600	270	5270	120	5.01	0.15	0.807	6.204	0.092		
	z4					68.7	1.4	10900	220	5710	150	4.36	0.12	0.749	5.825	0.081		
	z7					178.0	4.4	33200	960	5440	110	4.00	0.15	0.708	5.65	0.11		
	z8					170.0	4.2	33900	980	8670	180	3.66	0.13	0.704	5.195	0.095		
CHGRA		34.6614	77.6178	3998	granite													
	a1					3.82	0.14	389.0	7.0	1442	25	4.12	0.16	0.701	5.88	0.11	5.20	0.81
	a2					3.22	0.13	316.0	7.0	1486	42	3.80	0.17	0.684	5.56	0.12		
	a3					1.650	0.066	150.0	3.2	885	25	3.63	0.16	0.661	5.50	0.12		
	a4					4.73	0.13	449.0	7.4	2617	63	3.50	0.11	0.704	4.966	0.078		
	a5					0.731	0.036	133.0	3.0	437	14	2.43	0.13	0.655	3.715	0.097		
	a6					0.893	0.044	126.0	2.8	640	21	2.54	0.14	0.614	4.14	0.11		
	a8					6.28	0.17	391	11	2534	53	5.01	0.16	0.721	6.96	0.11		
	z9					379.1	9.0	49700	1100	49900	1500	4.83	0.14	0.771	6.261	0.094	6.4	0.1
	z10					243.6	6.0	32450	610	24200	690	4.99	0.15	0.768	6.500	0.097		
	z11					218.4	5.4	28890	520	23200	670	4.97	0.15	0.751	6.616	0.098		
	z15					117.3	2.9	17930	520	8390	170	4.60	0.17	0.729	6.31	0.11		
	z16					122.1	3.0	19640	960	8840	220	4.39	0.22	0.696	6.32	0.16		
LBH	a1	34.0258	78.1552	3961	granite	5.30	0.16	590	14	1667	42	4.24	0.14	0.774	5.473	0.094	5.49	0.13
	a2					7.10	0.20	814	16	2099	45	4.26	0.13	0.773	5.505	0.088		
	z1					1005	23	114000	3400	36130	900	6.41	0.23	0.862	7.43	0.14	6.85	0.73
	z2					536	13	92200	2700	28260	730	4.23	0.15	0.822	5.145	0.094		
	z3					1540	36	192700	5800	56200	1300	5.84	0.21	0.867	6.73	0.12		
	z5					883	20	98200	2300	41800	1100	6.38	0.20	0.849	7.52	0.12		
	z6					1397	32	143800	3300	102000	2800	6.50	0.20	0.862	7.55	0.12		
	z7					1061	26	132300	3900	49800	1000	5.75	0.21	0.846	6.80	0.12		
	z8					1231	29	150900	4400	66000	1400	5.78	0.21	0.858	6.73	0.12		

*Absolute measured abundances. 4He measurement used to calculate the "raw date," which was not corrected for the effects of 4He loss due to alpha particle recoil. The mean Fτ correction calculated following Farley et al. (1996) for apatite and Hourigan et al. (2005) for zircon.
^ The Fτ corrected date of the crystal. This age was recalculated with a Fτ corrected 4He measurement.

Table 4. Input parameters for 1-D therma1 modeling

Parameter	Input
Model thickness (km)	30
Thermal conductivity (W/m K)	2.5
Specific Heat Capacity (J/kg K)	800
Crustal density (kg/m^3)	2750
Mantle density (kg/m^3)	3200
Temp at base of the model (°C)	800
Temp at z=0 (°C)	5
Atmospheric lapse rate (°C/km)	6.5
Crustal volumetric heat production (uW/m^3)	2.5
e-folding depth of crustal heat production (km)	0
Mantle volumetric heat production (uW/m^3)	0.1

See Thiede and Ehlers (2013) for additional information

CHAPTER 6

CONCLUSIONS

The chapters above demonstrate the utility of using a variety of techniques to examine the spatial and temporal evolution of complex areas. Below, I summarize the major contribution of this work as well as opportunities for further, particularly in the Ladakh region.

1. Major contributions

The lack of accurate and comprehensive maps of the Ladakh region has been a hindrance to scientific inquiry in the area. The lithologic map created utilizing ASTER remote sensing images will thus be a significant aid to scientists working in the Ladakh region. Additionally, the location of major structures identified while making this map have implications for regional tectonics. For instance, our mapping of the continuation of the Longmu Co fault in India suggests that the LCF and the KFS may be acting as a conjugate fault pair, allowing the eastward extrusion of Tibet. This also implies that the Longmu Co fault may have initiated at around the same time as the Karakoram fault system at ca. 15 Ma. Our thermochronologic and exhumation rate studies between these fault systems and across the Ladakh Batholith show that a decrease in exhumation swept across the region from southwest to northeast starting at ca. 16 Ma. This is coincident with the onset of east-west extension in central and southern Tibet and indicates that this is a period of major structural reorganization in and around the Tibetan Plateau.

We have also contributed to the debate over late Quaternary slip along the KFS.

We have provided robust constraints for the slip rate on a second strand of the fault in the central region, implying that the partitioning of slip is more complex than previously believed. The time-integrated slip rate we determined is higher than the rate previously found in this region, which may indicate secular variations in slip rate. Additionally, it appears that one fault strand is dominant at a time. Our data suggest that the Pangong strand is currently dominant, but that the Tangtse strand was dominate pre-5.7 ka.

2. Opportunities for future work

2.1 Geologic mapping of the Ladakh region

In Chapter 2 we presented a comprehensive regional lithologic map created using ASTER remotely sensed images. Although this map is helpful for gleaning a broad understanding of major rock types in and around Ladakh, a regional geologic map will be even more useful. Starting with the lithologic map from Chapter 2 and drawing from previous mapping efforts (e.g. Phillips, 2008) and our own field observations we will carry this work forward and create a regional geologic map for publication in the Journal of Maps.

2.2 Additional slip rate studies along the central section of the KFS

Studies along the Tangtse strand of the KFS revealed a significant component of Quaternary slip that was previously unrecognized. This implies that the partitioning of slip along the central KFS where it bifurcates around the Pangong Range is more complex than previously thought. Further detailed studies of both strands, combining remotely sensed data and careful field investigation would likely identify additional

locations along the fault that could be used for slip rate studies. Information on fault slip in these additional locations would help clarify the spatial and temporal distribution of slip along the central section of the KFS. In particular, we identified a location along the Pangong strand that may be amenable to paleoseismic trenching. A trench along this strand could give constraints on the timing of the last few surface-breaking earthquakes, which would hint at the recurrence intervals of earthquakes along this strand of the fault. Also, our discovery of the low angle thrust fault near the northern terminus of the Pangong Range warrants further investigation. During our field studies, along-strike investigation of that feature to the north and northeast was impossible due to military restrictions. However, restrictions have recently been eased. Thus, detailed mapping of that fault contact around the tip of the Pangong Range and along the Shyok River may elucidate the fault behavior at the tip of the restraining bend.

2.3 Regional fault interaction and identification verification

Chapter 4 highlighted the importance of the interaction between the KFS and the LCF. In order to verify that the carbonate unit we correlated with the trace of the LCF using ATER imagery is actually the continuation of that fault system in India, more detailed fieldwork is necessary. For instance, more extensive field investigation of the Longmu Co fault where it crosses the Shyok River could provide insight into the overall sense of motion of the fault and and test the hypothesis that in this area the fault is sinistral-oblique. Additionally, this carbonate unit is accessable in a few remote locations in drainages along the Nubra Valley. Concentrated study of these outcrops could determine whether this is indeed the continuation of the LCF (sinistral motion) as we

posit, or if it is a secondary strand of the KFS (dextral motion) as suggested by Phillips (2008). It would be illustrative to map these regions in great detail to assess the degree of fabric development and determine if it is consistent with the implied strain in the shear zone.

2.4 U-Pb geochronology of the Karakoram Range

Finally, additional U-Pb geochronologic work within the Karakoram Range could provide better constraints on the temporal and spatial patterns of magmatic intrusion. Further sampling, particularly along the Shyok River, may provide additional evidence for the older episode of magmatism suggested by our work (IC2). Additionally, becausee the mid-Miocene age of sample SY3 closely correlates with the range of ages of the Baltoro Plutonic unit ~26-13 Ma (Searle et al., 1989, 1992; Parrish and Tirrul, 1989) and other Baltoro-type granites and leucogranites (Phillips et al., 2013), it supports the suggestion that post collisional granitoid formation was comagmatic from the Baltoro to the Pangong region (Searle et al., 1998; Searle and Phillips, 2007; Phillips et al., 2013). Determining the spatial extent of these young intrusions could lend insight into the post collisional processes responsible for regional magmatic generation.

3. References

Parrish, R. R., and R. Tirrul, 1989, U-Pb age of the Baltoro granite, Northwest Himalaya, and implications for monazite U-Pb systematics, Geology, 17, 1076–1079.

Phillips, R., 2008, Published Map. In Phillips, R., 2008, Geological map of the Karakoram fault zone, Eastern Karakoram, Ladakh, NW Himalaya, Journal of Maps, v 2008, 21-37.

Phillips, R.J., Searle, M.P. & Parrish, R.R. 2013. The geochemical and temporal evolution of the continental lithosphere and its relationship to continental-scale faulting: The Karakoram Fault, eastern Karakoram, NW Himalayas. Geochemistry Geophysics Geosystems, 14, 583-603.

Phillips, R.J., Searle, M.P. & Parrish, R.R. 2013. The geochemical and temporal evolution of the continental lithosphere and its relationship to continental-scale faulting: The Karakoram Fault, eastern Karakoram, NW Himalayas. Geochemistry Geophysics Geosystems, 14, 583-603.

Searle, M.P., Phillips, R.J., 2007. Relationships between right-lateral shear along the Karakoram fault and metamorphism, magmatism, exhumation and uplift: evidence from the K2–Gasherbrum–Pangong Ranges, north Pakistan and Ladakh., Journal of the Geological Society 164, 439–450.

Searle, M.P., Weinberg, R.F., Dunlap, W.J., 1998. Transpressional tectonics along the Karakoram fault zone, northern Ladakh: constraints on Tibetan extrusion. In: Holdsworth, R.E., Strachan, R.A., Dewey, J.F. (Eds.), Continental Transpressional and Transtensional Tectonics, 135. Geological Society, Special Publication, London, pp. 307–325.

Searle, M. P., and Rex, A. J., 1989, Thermal model for the Zanskar Himalaya: Journal of Metamorphic Geology, v. 7, p. 127–134.

Searle, M. P., M. B. Crawford, and A. J. Rex (1992), Field relations, geochemistry, origin

and emplacement of the Baltoro granite, central Karakoram, R. Soc. Edin. Trans., 83, 519–538.

APPENDIX A

SUPPLEMENTARY MATERIAL FOR CHAPTER 3

Refining Estimates of Quaternary Slip along the Karakoram fault system, Ladakh, northwest India

1. Cosmogenic Radionuclide Ages (CRN)

1.1 Depth Profiles

In 2004, Siame et al. showed that both denudation and exposure time could be determined within a CRN depth profile by employing a Chi-squared inversion model. Braucher et al., 2009 improved this model introducing Monte Carlo simulations. Using the methods outlined in Braucher et al., 2009 we generated 100 best-fit solutions from the range of possible ^{10}Be concentrations from within our depth profile. Each best-fit solution is the minimum median Chi-squared value. The median best-fit value of the 100 best-fit solutions is considered our preferred age, and we use the minimum and maximum values from those solutions as our acceptable age range. For this cosmogenic profile, the range of possible ages varied between 30.5 ka and 37.0 ka, and the median best-fit value was 33.9 ka.

Our model inputs are as follows; time = 5000 – 200000 yrs; erosion rate = 0 – 2 m/Myr; production rate of ^{10}Be = 70 atoms/g; inheritance = 1.47×10^{5} atoms/g; bulk density = 2.0 g/cm^2; decay constant of ^{10}Be = 4.99×10^{-7}/yr; attenuation length for spallation = 160 g/cm^2. For contribution from neutrons and muons we used the preferred values of Braucher et al. (2009).

Because inheritance was not calculated for this area, we chose to employ an inheritance value determined by Brown et al. (2002) on the other side of the Pangong

Range. Of the two inheritance values report by Brown and others we chose to use the higher inheritance value coupled with a low denudation rate in order to report the minimum surface ages and thus the maximum slip rate for this strand of the fault system.

1.2 Boulder Ages

Cosmogenic radionuclide production rate varies according to many factors, including latitude, longitude, altitude, and changes in the geomagnetic field (Gosse, 2001). Topographic or geometric barriers that may reduce the cosmic-ray exposure of a sample site, called the shielding factor, can also affect the amount of CRN produced in a sample. Additionally, the sample depth and density of the material through which the cosmogenic rays travel must be considered. Although there are various methods available for determining cosmogenic exposure ages, the CRONUS-Earth on-line calculator Version 2.2 (http://hess.ess.washington.edu/) provides an internally consistent, reproducible method for calculating these ages. Inputs to the CRONUS calculator are latitude, longitude, elevation, sample thickness and density, shielding correction, measured nuclide concentration and its related uncertainty. After the data are processed, CRONUS provides several different scaling methods which treat variation in production rate in different ways; we choose to use the Lal (1991)/Stone (2000) method due to its simplicity and broad use within the community. For additional information see Balco et al. (2008). For input values from this study see Table 1.

2. Fault Slip Rates and Uncertainties

Determining the slip rate on a fault system requires knowledge of the age of the offset feature as well as the total amount of offset, but both of these quantities have associated errors. In order to provide a rigorous assessment of displacement, age and slip rate values (and their associated uncertainties) we have used the probabilistic approach discussed in Zechar and Frankel (2009) for combining offset and marker age. We assume a Gaussian model for both age and offset uncertainty. We report the median values as our preferred interpretation as well as the upper and lower bounds at the 95% confidence interval. Probability density functions for age, displacement and slip rate are shown in supplemental Figures 1-3. These figures were generated using the code provided in Zechar and Frankel, 2009.

The CRN profile pit from the Q5 surface yielded a range of possible surface ages between 30.7 and 37.0 ka with a preferred age of 33.9 ka. However, since the adjacent, younger debris flow dominated surface only accrued 1-3 m of slip in the last 5.7 ka, we subtract both the amount of slip accommodated by that surface and the time over which it accumulated to find the most appropriate time-integrated slip rate for the offset Q5 surface during the period of interest. In other words, we subtract the 5.7 ka (over which time very little slip was accrued) from the preferred surface age of the feature (33.9 ka) to determine the amount of time over which most of the offset was produced (28.2 ka). We also subtract the amount of offset accrued over the past 5.7 ka (average of 2 m) from the total amount of offset recorded by the Q5 surface (160 m) in order to determine the amount of offset accumulated between 33.9 and 5.7 ka (158 m).

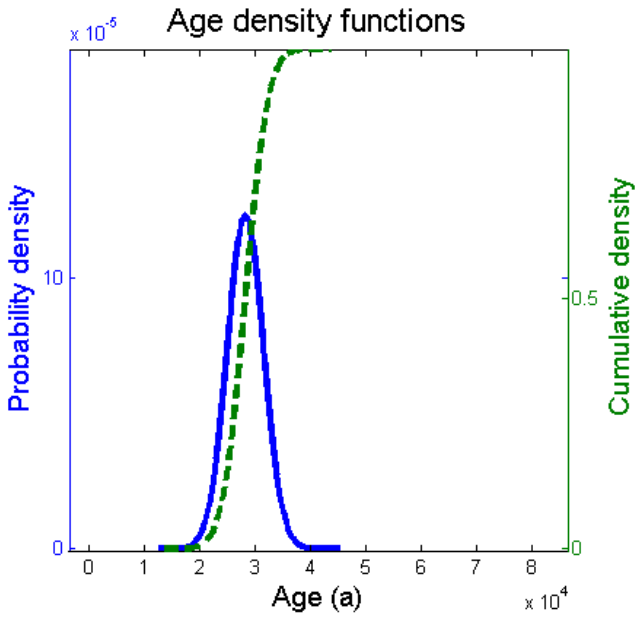

Figure A1. Probability density function of the age of the Q5 surface during the maximum time it was accruing offset. We have taken the preferred age of the Q5 surface (33.9 ka) with errors determined by the range of possible ages generated from the Braucher et al. (2009) model (30.7 – 37.0 ka) and subtracted the youngest offset debris flow age (5.7 ka) in order to get the duration of time over which the Q5 surface was accumulating the majority of offset. Mean: 28.2 ka; Mode: 28.2 ka; Median 28.2 ka and 95.5% bounds 28.2 +6.5/-6.5 ka.

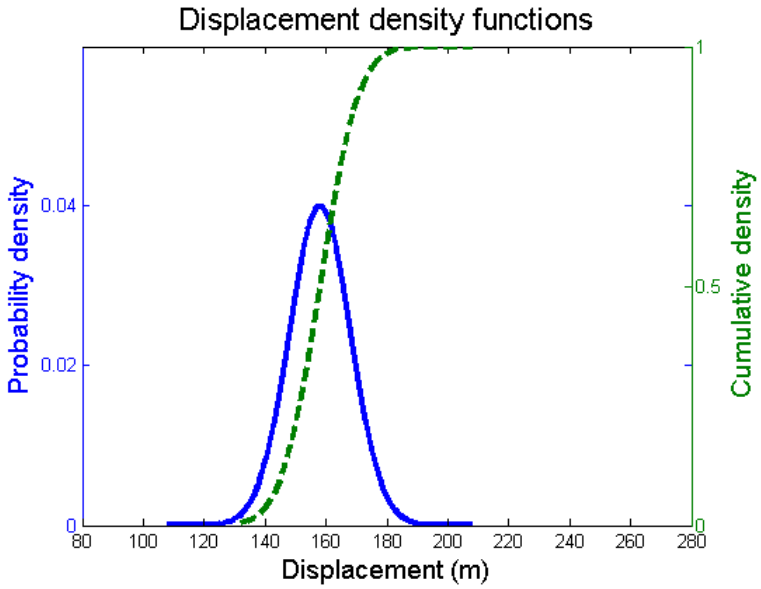

Figure A2. Probability density function of the amount of displacement of the Q5 surface over the time frame specified in Figure 1. We took the average of the offsets measured on debris flows (2 m) and subtracted that from the total amount of offset on the Q5 surface (160 m). Mean: 158.0 m; Mode: 158.0 m; Median and 95.5% bounds 158.0 +10.0/-10.0 m.

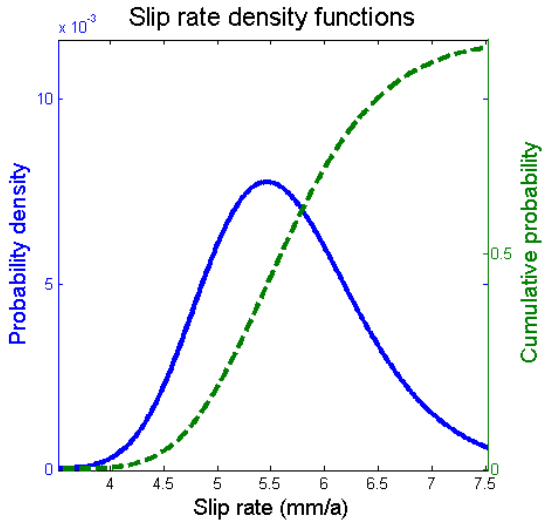

Figure A3. Probability density function of the slip rate over the time interval 33.9 ka – 5.7 ka. Mean: 5.7 mm/yr; Mode: 5.5 mm/yr; Median and 95.5% bounds: 5.6 +1.9/-1.2 mm/yr.

APPENDIX B

SUPPLEMENTARY MATERIAL FOR CHAPTER 5

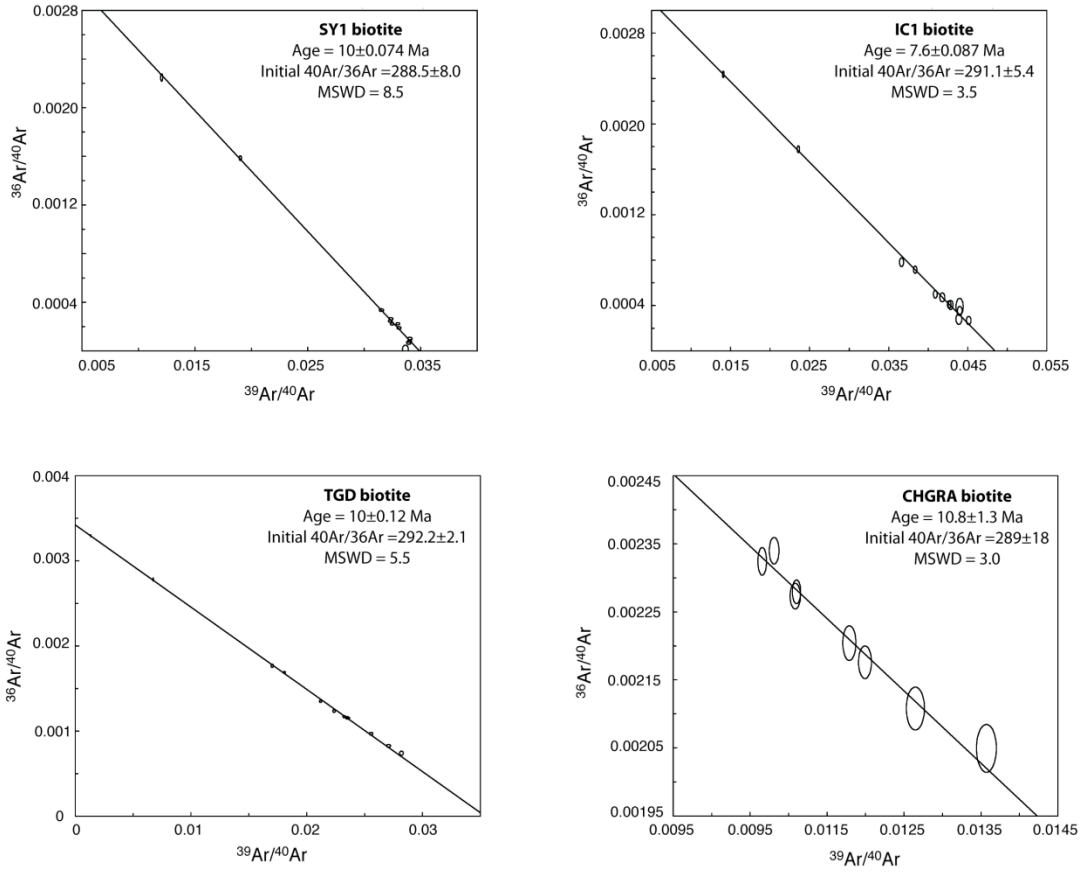

Supplementary Figure 1. Ar/Ar dating. Inverse isochron ages for biotite samples that did not form plateaus. Data point error ellipses are 2σ. See Figure 5 in Chapter 5 for sample locations. Results are summarized in Table 2.

Table A: $^{40}Ar/^{39}Ar$ step-heating data

Sample	Mineral	Latitude	Longitude	Elevation (m)	Lab ID#	Laser (W)	$^{40}Ar^*/^{39}Ar$	± 2s	$^{40}Ar/^{39}Ar$	± 2s	$^{38}Ar/^{39}Ar$	± 2s	$^{36}Ar/^{39}Ar$	± 2s
SY1	Biotite	34.383	78.306	3812	434-01A	3	27.91	0.31	52.55	0.25	0.02709	0.00072	0.08329	0.00086
					434-01B	3	28.56	0.18	31.73	0.16	0.01461	0.00045	0.01064	0.00030
					434-01C	4	28.69	0.15	30.96	0.13	0.01453	0.00036	0.00757	0.00022
					434-01D	5	28.76	0.14	30.81	0.12	0.01423	0.00037	0.00683	0.00023
					434-01E	5	28.30	0.15	30.33	0.13	0.01366	0.00033	0.00677	0.00023
					434-01F	6	28.47	0.16	30.90	0.14	0.01465	0.00033	0.00815	0.00028
					434-01G	6	28.52	0.16	30.24	0.14	0.01431	0.00038	0.00573	0.00027
					434-01H	7	28.46	0.16	29.37	0.14	0.01289	0.00042	0.00299	0.00026
					434-01I	8	28.69	0.15	29.40	0.13	0.01334	0.00039	0.00233	0.00024
					434-01J	9	28.84	0.17	29.46	0.14	0.01356	0.00045	0.00201	0.00035
					434-01K	10	29.59	0.32	29.72	0.19	0.01316	0.00098	0.00038	0.00087
					434-01L	15	27.80	0.69	82.93	0.56	0.0478	0.0012	0.1865	0.0022
SY2	Biotite	34.317	78.295	3790	*433-01A*	*3*	*21.70*	*0.34*	*51.74*	*0.29*	*0.03139*	*0.00073*	*0.10157*	*0.00090*
					433-01B	3	22.09	0.18	28.57	0.14	0.01642	0.00041	0.02184	0.00042
					433-01C	4	22.27	0.17	29.81	0.14	0.01766	0.00037	0.02544	0.00036
					433-01D	5	22.24	0.21	36.66	0.16	0.02147	0.00044	0.04873	0.00050
					433-01E	5	22.06	0.25	43.35	0.19	0.02598	0.00048	0.07198	0.00064
					433-01F	6	22.04	0.26	42.18	0.21	0.02473	0.00055	0.06807	0.00065
					433-01G	6	22.20	0.24	37.66	0.18	0.02252	0.00053	0.05220	0.00067
					433-01H	7	22.43	0.23	30.48	0.18	0.01842	0.00051	0.02713	0.00053
					433-01I	8	22.44	0.16	28.51	0.13	0.01645	0.00043	0.02048	0.00039
					433-01J	*9*	*22.63*	*0.17*	*27.00*	*0.13*	*0.01538*	*0.00052*	*0.01469*	*0.00043*
					433-01K	*10*	*22.65*	*0.19*	*25.66*	*0.11*	*0.01373*	*0.00061*	*0.01012*	*0.00053*
					433-01L	*15*	*21.68*	*0.31*	*47.01*	*0.24*	*0.02848*	*0.00074*	*0.08563*	*0.00093*
SY 2	White mica	34.317	78.295	3790	578-01A	4	7.58	0.13	14.770	0.057	0.01653	0.00046	0.02426	0.00043
					578-01B	5	7.591	0.086	9.068	0.037	0.01235	0.00048	0.00493	0.00027
					578-01C	5	7.549	0.090	9.149	0.037	0.01310	0.00041	0.00534	0.00028
					578-01D	5	7.493	0.090	8.230	0.035	0.01233	0.00046	0.00243	0.00028
					578-01E	5	7.47	0.11	8.299	0.039	0.01295	0.00052	0.00274	0.00034
					578-01F	6	7.555	0.081	8.494	0.030	0.01145	0.00041	0.00311	0.00026
					578-01G	7	7.469	0.050	8.332	0.023	0.01220	0.00033	0.00287	0.00015
					578-01H	8	7.541	0.080	8.773	0.034	0.01271	0.00042	0.00412	0.00025
					578-01I	9	7.62	0.10	8.204	0.030	0.01216	0.00053	0.00198	0.00031
					578-01J	9	7.69	0.19	12.049	0.059	0.01441	0.00068	0.01474	0.00063
					578-01K	11	7.35	0.17	8.151	0.046	0.01212	0.00067	0.00264	0.00056
					578-01L	15	7.606	0.073	7.798	0.031	0.01269	0.00039	0.00058	0.00022
IC1	Biotite	34.209	78.262	3683	431-01A	3	19.87	0.53	71.04	0.43	0.0478	0.0013	0.1731	0.0018
					431-01B	3	20.97	0.28	27.30	0.16	0.01927	0.00090	0.02134	0.00085
					431-01C	4	20.53	0.23	26.07	0.13	0.01922	0.00077	0.01866	0.00068
					431-01D	5	20.82	0.23	24.45	0.12	0.01897	0.00079	0.01221	0.00068

					431-01E	5	20.59	0.21	23.45	0.11	0.01825	0.00071	0.00958	0.00062
					431-01F	6	20.57	0.27	23.93	0.15	0.01796	0.00076	0.01129	0.00077
					431-01G	6	20.53	0.26	23.35	0.14	0.01664	0.00091	0.00948	0.00078
					431-01H	7	20.32	0.24	22.73	0.12	0.01614	0.00073	0.00806	0.00071
					431-01I	8	20.38	0.22	22.16	0.12	0.01657	0.00072	0.00594	0.00066
					431-01J	9	20.88	0.29	22.79	0.16	0.01629	0.00097	0.00637	0.00085
					431-01K	10	20.10	0.45	22.74	0.20	0.0161	0.0014	0.0088	0.0014
					431-01L	15	20.12	0.34	42.41	0.22	0.02998	0.00095	0.0754	0.0011
IC1	White mica	34.209	78.262	3683	*582-01A*	*4*	*9.07*	*0.76*	*56.38*	*0.42*	*0.0437*	*0.0019*	*0.1603*	*0.0028*
					582-01B	*5*	*8.03*	*0.23*	*18.80*	*0.10*	*0.01864*	*0.00070*	*0.03643*	*0.00078*
					582-01C	5	7.65	0.11	9.719	0.040	0.01266	0.00049	0.00698	0.00036
					582-01D	5	7.76	0.12	10.531	0.043	0.01403	0.00049	0.00933	0.00040
					582-01E	5	7.667	0.092	11.259	0.035	0.01407	0.00040	0.01212	0.00030
					582-01F	6	7.749	0.089	10.077	0.035	0.01319	0.00037	0.00783	0.00029
					582-01G	*7*	*7.485*	*0.068*	*8.745*	*0.032*	*0.01231*	*0.00038*	*0.00422*	*0.00021*
					582-01H	8	7.49	0.11	10.458	0.035	0.01350	0.00043	0.00998	0.00036
					582-01I	*9*	*7.43*	*0.13*	*8.925*	*0.041*	*0.01298*	*0.00056*	*0.00501*	*0.00041*
					582-01J	9	7.56	0.13	8.386	0.041	0.01225	0.00052	0.00273	0.00042
					582-01K	11	7.626	0.092	8.440	0.033	0.01239	0.00045	0.00269	0.00029
					582-01L	15	7.529	0.066	8.290	0.029	0.01261	0.00038	0.00250	0.00020
IC3	Biotite	34.153	78.225	3641	427-01A	3	24.18	0.97	115.60	1.01	0.0725	0.0019	0.3094	0.0037
					427-01B	3	24.63	0.37	43.40	0.27	0.02391	0.00083	0.0634	0.0011
					427-01C	4	25.23	0.28	37.62	0.22	0.02037	0.00062	0.04183	0.00069
					427-01D	5	25.05	0.25	34.24	0.21	0.01764	0.00052	0.03104	0.00055
					427-01E	5	25.10	0.24	38.11	0.19	0.02030	0.00051	0.04396	0.00056
					427-01F	6	24.96	0.25	39.56	0.19	0.02142	0.00057	0.04931	0.00064
					427-01G	6	24.92	0.28	37.40	0.21	0.02046	0.00053	0.04217	0.00069
					427-01H	7	24.93	0.25	34.47	0.19	0.01856	0.00057	0.03222	0.00062
					427-01I	8	24.72	0.19	34.11	0.15	0.01835	0.00040	0.03170	0.00044
					427-01J	9	25.02	0.16	31.06	0.13	0.01658	0.00042	0.02038	0.00035
					427-01K	10	25.20	0.18	31.47	0.15	0.01665	0.00049	0.02115	0.00039
					427-01L	15	25.24	0.12	34.24	0.10	0.01802	0.00030	0.03039	0.00026
IC6	Biotite	34.127	78.110	3800	422-01A	3	19.60	0.61	79.92	0.44	0.0551	0.0012	0.2041	0.0019
					422-01B	3	20.30	0.30	41.48	0.22	0.02912	0.00061	0.07160	0.00081
					422-01C	4	20.69	0.19	29.81	0.14	0.02099	0.00043	0.03079	0.00045
					422-01D	5	20.71	0.20	26.49	0.16	0.01917	0.00050	0.01947	0.00044
					422-01E	5	20.72	0.19	26.68	0.15	0.01948	0.00056	0.02007	0.00044
					422-01F	6	20.62	0.14	24.23	0.10	0.01778	0.00051	0.01215	0.00036
					422-01G	6	20.50	0.13	23.692	0.095	0.01723	0.00049	0.01071	0.00034
					422-01H	7	20.61	0.14	23.325	0.095	0.01703	0.00056	0.00912	0.00037
					422-01I	8	20.40	0.13	23.286	0.093	0.01678	0.00045	0.00969	0.00031
					422-01J	9	20.53	0.15	23.585	0.089	0.01781	0.00058	0.01026	0.00041
					422-01K	10	20.84	0.27	24.76	0.15	0.01876	0.00090	0.01320	0.00079
					422-01L	15	19.57	0.40	55.00	0.29	0.03766	0.00077	0.1198	0.0011
TGA	Biotite	34.028	78.203	4011	*497-01A*	*3*	*24.38*	*0.93*	*202.76*	*0.90*	*0.1265*	*0.0013*	*0.6036*	*0.0030*
					497-01B	3	28.19	0.38	74.74	0.30	0.04152	0.00062	0.1574	0.0011

					497-01C	4	28.75	0.33	71.21	0.26	0.04025	0.00056	0.14359	0.00086
					497-01D	5	28.50	0.52	111.06	0.42	0.06558	0.00077	0.2793	0.0014
					497-01E	5	28.64	0.71	152.95	0.62	0.0924	0.0011	0.4206	0.0021
					497-01F	6	29.08	0.78	152.28	0.68	0.0921	0.0013	0.4168	0.0025
					497-01G	6	29.55	0.61	104.81	0.53	0.0600	0.0011	0.2546	0.0019
					497-01H	7	29.26	0.64	85.35	0.53	0.0476	0.0011	0.1897	0.0020
					497-01I	8	29.35	0.37	60.00	0.28	0.03322	0.00065	0.1036	0.0010
					497-01J	9	28.98	0.36	51.12	0.28	0.02658	0.00064	0.0748	0.0010
					497-01K	*10*	*29.23*	*0.35*	*46.03*	*0.27*	*0.02302*	*0.00083*	*0.0568*	*0.0010*
					497-01L	15	28.60	0.38	67.01	0.33	0.03684	0.00070	0.1299	0.0010
TGC	Biotite	34.039	78.220	4017	*424-01A*	*3*	*18.2*	*1.5*	*312.90*	*1.53*	*0.1991*	*0.0021*	*0.9970*	*0.0054*
					424-01B	*3*	*25.40*	*0.59*	*93.79*	*0.46*	*0.0553*	*0.0010*	*0.2314*	*0.0018*
					424-01C	*4*	*26.13*	*0.30*	*52.33*	*0.24*	*0.02914*	*0.00053*	*0.08857*	*0.00077*
					424-01D	5	26.40	0.24	44.97	0.19	0.02305	0.00041	0.06274	0.00054
					424-01E	5	26.76	0.24	42.82	0.20	0.02290	0.00048	0.05426	0.00053
					424-01F	6	26.66	0.25	42.30	0.20	0.02204	0.00048	0.05284	0.00057
					424-01G	6	26.65	0.29	45.20	0.24	0.02485	0.00053	0.06270	0.00072
					424-01H	7	26.62	0.25	38.58	0.21	0.01998	0.00047	0.04040	0.00058
					424-01I	8	26.78	0.20	37.35	0.16	0.01904	0.00047	0.03568	0.00043
					424-01J	9	26.69	0.20	35.32	0.16	0.01814	0.00046	0.02914	0.00046
					424-01K	10	26.66	0.22	33.82	0.17	0.01755	0.00055	0.02417	0.00058
					424-01L	*15*	*25.84*	*0.34*	*54.62*	*0.27*	*0.03101*	*0.00069*	*0.09731*	*0.00092*
TGC	White mica	34.039	78.220	4017	584-01A	4	9.44	0.13	15.894	0.053	0.01595	0.00046	0.02178	0.00044
					584-01B	5	8.59	0.10	9.590	0.036	0.01260	0.00040	0.00328	0.00030
					584-01C	5	8.484	0.085	9.655	0.034	0.01236	0.00040	0.00391	0.00027
					584-01D	5	8.45	0.11	9.296	0.043	0.01274	0.00048	0.00279	0.00036
					584-01E	5	8.47	0.15	9.204	0.054	0.01241	0.00058	0.00236	0.00049
					584-01F	6	8.54	0.10	9.208	0.037	0.01204	0.00045	0.00223	0.00031
					584-01G	7	8.544	0.085	9.188	0.036	0.01210	0.00039	0.00214	0.00026
					584-01H	8	8.64	0.15	9.369	0.053	0.01124	0.00061	0.00243	0.00048
					584-01I	9	8.72	0.26	9.232	0.077	0.01180	0.00100	0.00175	0.00083
					584-01J	9	8.58	0.21	9.049	0.066	0.01184	0.00077	0.00164	0.00067
					584-01K	11	8.51	0.40	10.31	0.11	0.0128	0.0012	0.0062	0.0013
					584-01L	15	9.80	0.25	11.315	0.081	0.01390	0.00092	0.00522	0.00080
TGD	Biotite	34.054	78.229	4065	426-01A	3	19.75	3.34	752.38	4.21	0.4857	0.0043	2.479	0.014
					426-01B	3	26.43	0.75	148.73	0.59	0.0918	0.0011	0.4138	0.0022
					426-01C	4	27.68	0.24	55.30	0.20	0.02982	0.00043	0.09341	0.00059
					426-01D	5	28.13	0.20	43.04	0.16	0.02198	0.00042	0.05037	0.00047
					426-01E	5	27.92	0.19	42.37	0.16	0.02116	0.00042	0.04881	0.00042
					426-01F	6	28.34	0.22	47.19	0.19	0.02392	0.00053	0.06369	0.00055
					426-01G	6	28.36	0.24	44.72	0.17	0.02218	0.00048	0.05528	0.00065
					426-01H	7	28.00	0.22	42.58	0.18	0.02204	0.00045	0.04927	0.00052
					426-01I	8	27.89	0.22	39.11	0.18	0.01922	0.00045	0.03791	0.00051
					426-01J	9	27.90	0.24	36.94	0.20	0.01820	0.00059	0.03052	0.00053
					426-01K	10	27.69	0.26	35.48	0.17	0.01739	0.00072	0.02628	0.00072
					426-01L	15	28.07	0.34	58.76	0.28	0.03231	0.00064	0.10383	0.00093

LG1	Biotite	34.661	77.618		*496-01A*	*3*	*-38.6*	*7.4*	*1731.68*	*10.68*	*1.1400*	*0.0081*	*5.991*	*0.035*
					496-01B	*3*	*23.3*	*1.6*	*340.41*	*1.60*	*0.2145*	*0.0020*	*1.0731*	*0.0050*
					496-01C	*4*	*28.40*	*0.56*	*114.19*	*0.49*	*0.06774*	*0.00080*	*0.2902*	*0.0015*
					496-01D	5	29.11	0.37	70.98	0.29	0.03937	0.00058	0.14160	0.00094
					496-01E	5	28.71	0.34	61.81	0.28	0.03313	0.00057	0.11193	0.00086
					496-01F	6	29.08	0.35	62.22	0.29	0.03388	0.00074	0.11203	0.00091
					496-01G	6	29.06	0.36	59.15	0.32	0.03127	0.00080	0.10172	0.00094
					496-01H	7	29.06	0.41	56.35	0.35	0.03026	0.00072	0.0923	0.0011
					496-01I	8	28.39	0.36	62.95	0.30	0.03504	0.00076	0.1168	0.0010
					496-01J	9	28.85	0.45	64.77	0.32	0.03594	0.00085	0.1215	0.0013
					496-01K	10	28.52	0.50	61.00	0.37	0.0339	0.0011	0.1099	0.0015
					496-01L	15	29.13	0.48	79.58	0.40	0.04464	0.00078	0.1708	0.0014
DGA	White mica	34.054	78.229	4065	577-01A	4	9.65	0.14	15.060	0.055	0.01476	0.00050	0.01827	0.00047
					577-01B	5	9.606	0.085	11.045	0.041	0.01239	0.00039	0.00483	0.00026
					577-01C	5	9.428	0.080	10.918	0.037	0.01216	0.00042	0.00497	0.00025
					577-01D	5	9.41	0.11	10.719	0.047	0.01235	0.00048	0.00436	0.00035
					577-01E	5	9.48	0.16	10.572	0.057	0.01200	0.00067	0.00363	0.00051
					577-01F	6	9.27	0.11	10.315	0.045	0.01219	0.00052	0.00343	0.00036
					577-01G	7	9.301	0.084	10.034	0.038	0.01250	0.00038	0.00240	0.00026
					577-01H	8	9.34	0.10	10.155	0.042	0.01179	0.00050	0.00269	0.00032
					577-01I	9	9.40	0.14	10.736	0.055	0.01266	0.00060	0.00442	0.00044
					577-01J	9	9.27	0.18	10.017	0.056	0.01194	0.00066	0.00248	0.00058
					577-01K	11	9.42	0.32	10.345	0.079	0.01159	0.00099	0.0030	0.0010
					577-01L	15	9.44	0.25	10.143	0.074	0.01253	0.00094	0.00226	0.00082
CHGRA	Biotite	34.126	78.110	3998	*494-01A*	*3*	*-13.1*	*4.8*	*1114.72*	*5.18*	*0.7314*	*0.0046*	*3.817*	*0.016*
					494-01B	*3*	*24.1*	*1.2*	*249.38*	*1.14*	*0.1543*	*0.0016*	*0.7624*	*0.0039*
					494-01C	*4*	*28.78*	*0.59*	*117.16*	*0.55*	*0.0701*	*0.0010*	*0.2990*	*0.0018*
					494-01D	*5*	*30.45*	*0.46*	*89.86*	*0.37*	*0.05110*	*0.00076*	*0.2009*	*0.0013*
					494-01E	5	29.38	0.47	90.07	0.37	0.05040	0.00073	0.2053	0.0014
					494-01F	6	29.36	0.55	93.84	0.42	0.0535	0.0011	0.2181	0.0016
					494-01G	6	28.52	0.54	92.49	0.45	0.0524	0.0011	0.2164	0.0016
					494-01H	7	29.55	0.62	84.82	0.51	0.0468	0.0011	0.1870	0.0019
					494-01I	8	29.73	0.58	83.38	0.49	0.0472	0.0011	0.1814	0.0018
					494-01J	9	29.80	0.72	79.07	0.62	0.0416	0.0013	0.1667	0.0022
					494-01K	10	29.06	0.69	73.69	0.59	0.0407	0.0017	0.1510	0.0024
					494-01L	15	29.59	0.52	90.20	0.46	0.05056	0.00099	0.2050	0.0015

Sample	**Cl/K**	**^{39}Ar (fmol)**	**%^{40}Ar***	**%^{39}Ar**	**Date (Ma)**	**± 2s**	**J value**	**± 2s**
SY1	0.0019	5.88	53.14	6.20	10.06	0.11	2.0E-04	8.3E-07
	0.0021	8.45	90.09	8.91	10.298	0.065		
	0.0022	10.91	92.78	11.50	10.346	0.052		
	0.0022	11.33	93.45	11.94	10.370	0.050		

	0.0021	10.89	93.41	11.47	10.205	0.053		
	0.0022	10.27	92.21	10.82	10.265	0.058		
	0.0022	9.42	94.41	9.93	10.283	0.057		
	0.0021	8.17	96.99	8.61	10.261	0.056		
	0.0022	8.99	97.66	9.48	10.343	0.054		
	0.0022	5.50	97.99	5.80	10.399	0.063		
	0.0022	2.40	99.63	2.53	10.67	0.11		
	0.0022	2.67	33.54	2.81	10.03	0.25		
SY2	*0.0021*	*5.68*	*41.96*	*6.29*	*7.79*	*0.12*	2.0E-04	1.5E-06
	0.0021	8.15	77.40	9.03	7.936	0.064		
	0.0022	11.51	74.77	12.75	8.000	0.060		
	0.0021	10.84	60.70	12.01	7.988	0.074		
	0.0021	9.35	50.91	10.36	7.923	0.090		
	0.0020	7.65	52.29	8.48	7.919	0.092		
	0.0021	6.80	59.01	7.53	7.977	0.088		
	0.0022	6.67	73.68	7.39	8.058	0.081		
	0.0021	8.30	78.77	9.19	8.060	0.059		
	0.0021	*6.17*	*83.91*	*6.84*	*8.128*	*0.062*		
	0.0020	*4.02*	*88.34*	*4.45*	*8.136*	*0.067*		
	0.0021	*5.12*	*46.14*	*5.68*	*7.79*	*0.11*		
SY 2	0.0020	0.12	51.39	11.86	7.46	0.12	5.5E-04	1.4E-05
	0.0019	0.10	83.88	9.57	7.473	0.085		
	0.0020	0.10	82.68	9.84	7.432	0.089		
	0.0020	0.07	91.25	7.14	7.376	0.088		
	0.0021	0.06	90.21	6.09	7.35	0.11		
	0.0018	0.08	89.14	8.17	7.438	0.079		
	0.0020	0.14	89.83	14.28	7.353	0.049		
	0.0020	0.09	86.14	9.32	7.424	0.078		
	0.0020	0.06	93.08	6.37	7.50	0.10		
	0.0020	0.05	63.93	4.76	7.57	0.19		
	0.0020	0.03	90.36	3.46	7.23	0.17		
	0.0021	0.09	97.78	9.14	7.488	0.071		
IC1	0.0026	3.48	27.98	9.29	7.29	0.19	2.0E-04	1.5E-06
	0.0026	3.15	76.89	8.40	7.69	0.10		
	0.0027	3.88	78.84	10.36	7.533	0.083		
	0.0028	3.68	85.24	9.83	7.637	0.084		
	0.0028	3.64	87.93	9.71	7.554	0.076		
	0.0027	3.17	86.05	8.46	7.55	0.10		
	0.0025	2.88	88.00	7.69	7.53	0.10		
	0.0025	3.03	89.52	8.10	7.455	0.087		
	0.0026	3.06	92.08	8.17	7.476	0.082		
	0.0025	2.22	91.74	5.92	7.66	0.11		
	0.0024	1.45	88.51	3.86	7.38	0.16		
	0.0027	3.83	47.46	10.22	7.38	0.12		
IC1	*0.0023*	*0.06*	*16.08*	*5.82*	*8.82*	*0.74*	5.4E-04	1.8E-04
	0.0020	*0.07*	*42.77*	*6.88*	*7.81*	*0.22*		

	0.0019	0.08	78.87	7.49	7.44	0.11		
	0.0021	0.08	73.84	7.74	7.55	0.12		
	0.0020	0.11	68.21	10.61	7.458	0.089		
	0.0020	0.11	77.04	10.33	7.537	0.087		
	0.0019	*0.12*	*85.77*	*11.35*	*7.281*	*0.066*		
	0.0020	0.10	71.71	9.34	7.28	0.11		
	0.0020	*0.06*	*83.42*	*5.89*	*7.23*	*0.12*		
	0.0020	0.05	90.33	5.09	7.35	0.13		
	0.0020	0.09	90.56	8.31	7.418	0.089		
	0.0020	0.12	91.03	11.14	7.324	0.064		
IC3	0.0024	1.81	20.91	2.06	8.75	0.35	2.0E-04	1.0E-06
	0.0020	2.88	56.79	3.29	8.92	0.13		
	0.0021	5.20	67.13	5.94	9.13	0.10		
	0.0020	5.81	73.21	6.63	9.067	0.091		
	0.0020	7.24	65.91	8.28	9.085	0.085		
	0.0021	6.33	63.15	7.23	9.035	0.091		
	0.0021	5.65	66.68	6.45	9.02	0.10		
	0.0021	5.70	72.38	6.51	9.023	0.090		
	0.0021	9.46	72.53	10.80	8.948	0.067		
	0.0022	9.47	80.60	10.82	9.054	0.058		
	0.0021	7.73	80.15	8.83	9.123	0.065		
	0.0021	20.28	73.76	23.16	9.134	0.044		
IC6	0.0028	3.27	24.54	4.70	6.95	0.22	2.0E-04	1.7E-06
	0.0026	5.53	48.97	7.96	7.20	0.11		
	0.0026	8.27	69.46	11.89	7.335	0.067		
	0.0026	6.90	78.28	9.93	7.345	0.070		
	0.0027	6.80	77.76	9.77	7.348	0.069		
	0.0026	6.56	85.18	9.44	7.311	0.049		
	0.0026	6.59	86.64	9.48	7.271	0.047		
	0.0026	5.88	88.45	8.45	7.308	0.049		
	0.0025	7.11	87.71	10.22	7.234	0.045		
	0.0027	4.66	87.17	6.70	7.282	0.051		
	0.0027	2.60	84.25	3.74	7.390	0.094		
	0.0026	5.36	35.61	7.71	6.94	0.14		
TGA	*0.0022*	*6.65*	*12.03*	*8.53*	*8.37*	*0.32*	1.9E-04	1.4E-06
	0.0020	8.55	37.74	10.96	9.68	0.13		
	0.0022	11.35	40.39	14.56	9.87	0.11		
	0.0022	8.88	25.67	11.39	9.78	0.18		
	0.0023	6.97	18.73	8.94	9.83	0.24		
	0.0023	5.06	19.10	6.49	9.98	0.27		
	0.0021	4.72	28.20	6.05	10.14	0.21		
	0.0020	3.60	34.30	4.61	10.04	0.22		
	0.0023	6.44	48.93	8.26	10.07	0.13		
	0.0021	5.26	56.72	6.74	9.95	0.12		
	0.0021	*3.57*	*63.54*	*4.58*	*10.03*	*0.12*		
	0.0021	6.93	42.69	8.89	9.81	0.13		

TGC	*0.0020*	*3.72*	*5.83*	*4.33*	*6.70*	*0.57*	2.0E-04	1.6E-06
	0.0020	*4.82*	*27.09*	*5.61*	*9.33*	*0.22*		
	0.0021	*8.67*	*49.96*	*10.10*	*9.60*	*0.11*		
	0.0019	9.95	58.75	11.60	9.69	0.09		
	0.0021	9.63	62.54	11.22	9.825	0.087		
	0.0020	7.75	63.07	9.03	9.789	0.092		
	0.0022	6.91	59.00	8.05	9.78	0.11		
	0.0021	6.56	69.05	7.64	9.772	0.092		
	0.0021	9.38	71.76	10.93	9.833	0.073		
	0.0021	8.23	75.63	9.59	9.799	0.075		
	0.0022	4.52	78.89	5.27	9.789	0.081		
	0.0022	*5.68*	*47.34*	*6.62*	*9.49*	*0.13*		
TGC	0.0020	0.14	59.48	20.26	9.99	0.14	5.4E-04	1.8E-04
	0.0020	0.09	89.80	12.56	9.10	0.10		
	0.0020	0.09	88.03	12.87	8.983	0.090		
	0.0021	0.06	91.10	8.47	8.95	0.12		
	0.0020	0.04	92.25	5.81	8.97	0.16		
	0.0020	0.07	92.88	9.70	9.04	0.10		
	0.0020	0.08	93.18	11.45	9.05	0.09		
	0.0018	0.04	92.40	5.79	9.15	0.16		
	0.0019	0.02	94.58	3.01	9.23	0.27		
	0.0019	0.03	94.94	3.78	9.08	0.22		
	0.0020	0.02	82.70	2.32	9.01	0.42		
	0.0022	0.03	86.75	3.98	10.38	0.26		
TGD	0.0035	3.15	2.63	3.18	7.20	1.21	2.0E-04	1.9E-06
	0.0024	6.50	17.77	6.55	9.62	0.27		
	0.0021	13.18	50.07	13.29	10.076	0.088		
	0.0021	13.54	65.40	13.65	10.240	0.072		
	0.0020	12.43	65.95	12.54	10.165	0.068		
	0.0020	9.37	60.09	9.45	10.316	0.082		
	0.0020	8.94	63.45	9.02	10.322	0.087		
	0.0022	7.65	65.81	7.71	10.194	0.080		
	0.0020	7.91	71.35	7.97	10.152	0.079		
	0.0021	5.83	75.59	5.88	10.157	0.086		
	0.0021	4.01	78.10	4.04	10.080	0.093		
	0.0022	6.68	47.79	6.73	10.22	0.12		
LG1	*0.0027*	*3.28*	*-2.23*	*4.46*	*-13.17*	*2.53*	1.9E-04	2.2E-06
	0.0022	*5.37*	*6.84*	*7.29*	*7.90*	*0.54*		
	0.0022	*9.25*	*24.88*	*12.55*	*9.63*	*0.19*		
	0.0022	10.03	41.03	13.60	9.87	0.13		
	0.0020	9.14	46.48	12.40	9.74	0.11		
	0.0022	6.95	46.77	9.42	9.86	0.12		
	0.0021	6.18	49.16	8.38	9.86	0.12		
	0.0022	5.05	51.60	6.85	9.86	0.14		
	0.0022	6.13	45.12	8.32	9.63	0.12		
	0.0022	4.20	44.56	5.70	9.78	0.15		

	0.0022	3.07	46.77	4.17	9.67	0.17		
	0.0021	5.07	36.61	6.88	9.88	0.16		
DGA	0.0019	0.09	64.18	12.65	9.96	0.15	5.7E-04	2.3E-05
	0.0019	0.09	87.12	13.43	9.910	0.087		
	0.0019	0.09	86.50	12.60	9.727	0.082		
	0.0019	0.06	87.93	9.12	9.71	0.11		
	0.0019	0.04	89.82	5.85	9.78	0.16		
	0.0019	0.06	90.04	8.23	9.56	0.12		
	0.0020	0.08	92.87	12.33	9.60	0.09		
	0.0019	0.06	92.15	8.76	9.64	0.11		
	0.0020	0.04	87.74	6.41	9.70	0.14		
	0.0019	0.03	92.74	4.67	9.57	0.18		
	0.0019	0.02	91.27	2.67	9.72	0.33		
	0.0020	0.02	93.28	3.28	9.74	0.26		
CHGRA	*0.0026*	*4.68*	*-1.17*	*7.70*	*-4.64*	*1.70*	2.0E-04	7.8E-04
	0.0019	*5.21*	*9.66*	*8.57*	*8.50*	*0.44*		
	0.0024	*7.37*	*24.57*	*12.12*	*10.15*	*0.21*		
	0.0023	*7.69*	*33.90*	*12.66*	*10.74*	*0.16*		
	0.0020	8.07	32.63	13.27	10.36	0.17		
	0.0021	5.92	31.30	9.73	10.36	0.19		
	0.0020	4.95	30.84	8.14	10.06	0.19		
	0.0020	3.76	34.85	6.19	10.43	0.22		
	0.0022	3.72	35.67	6.13	10.49	0.20		
	0.0017	2.73	37.70	4.50	10.51	0.25		
	0.0021	1.82	39.44	2.99	10.25	0.24		
	0.0020	4.86	32.82	8.00	10.44	0.18		

Instrument sensitivity - 1.66E-20 mol/cps
Steps in italics were disregarded when creating plateau dates.

Subject Categories: 0372; 0484; 0799